Dissertation submitted to the Faculty of the
Virginia Polytechnic Institute & State University
in partial fulfillment of the requirements for the degree of

Doctor of Philosophy
in
Electrical Engineering

Active Antenna Bandwidth Control Using Reconfigurable Antenna Elements

Nathan P. Cummings

Virginia Tech Antenna Group
Bradley Department of Electrical & Computer Engineering
Blacksburg, Virginia 24061-0111

Committee Members:

Warren L. Stutzman, Chair
Christopher A. Beattie
Gary S. Brown
William A. Davis
Timothy Pratt

December 8, 2003
Blacksburg, Virginia

Keywords: Reconfigurable Antennas, Bandwidth Control

Active Antenna Bandwidth Control Using Reconfigurable Antenna Elements

Nathan P. Cummings

(ABSTRACT)

Reconfigurable antennas represent a recent innovation in antenna design that changes from classical fixed-form, fixed-function antennas to modifiable structures that can be adapted to fit the requirements of a time varying system. Advances in microwave semiconductor processing technologies have enabled the use of compact, ultra-high quality RF and microwave switches in novel aspects of antenna design. This dissertation introduces the concept of reconfigurable antenna bandwidth control and how advances in switch technology have made these designs realizable. Specifically, it details the development of three new antennas capable of reconfigurable bandwidth control. The newly developed antennas include the reconfigurable ring patch, the reconfigurable planar inverted-F and the reconfigurable parasitic folded dipole. The relevant background work to these designs is described and then design details along with computer simulations and measured experimental results are given.

Acknowledgments

I would first like to thank Dr. Warren L. Stutzman for serving as my committee chairman and as my advisor during both my M.S. and Ph.D. degrees. His generous direction, encouragement, advice and support have been invaluable throughout my graduate education. I would like to thank Dr. William A. Davis, Dr. Gary S. Brown, Dr. Tim Pratt and Dr. Christopher A. Beattie for serving on my committee. I want to give special thanks to Dr. Davis the time and advice he has graciously given to me while working with the Virginia Tech Antenna Group.

I would like to thank all the members of VTAG that I have worked with during my time spent with the group. The opportunity to interact, both in and out of the lab, with such a talented and diverse group of individuals has been extremely enlightening. Additionally, I am indebted to Randall Nealy for the assistance he has given me in antenna construction and measurement.

Finally, and most importantly, I would like to thank my parents–Patrick and Susan Cummings–along with the rest of my family. The limitless patience and support they have given me during my pursuit of this degree is infinitely appreciated.

Contents

List of Figures

List of Tables

Chapter 1

Introduction

1.1 Motivation

The recent advent of microelectromechanical system (MEMS) components into microwave and millimeter wave regimes has opened new and novel avenues of antenna technology development. High quality, miniature RF switches provide the antenna designer with a new tool for creating dynamic radiating structures. The antenna is beginning to be seen as a component or sub-system that may be intelligently altered in-situ to meet operational goals.

This dissertation discusses a comprehensive investigation of reconfigurable antennas with a primary focus on antenna bandwidth control. The problem motivation is to investigate the use of new RF switch technology to actively and intelligently change the operating bandwidth of an antenna. The key design objectives that are considered in the bandwidth control design problem include: high degree of bandwidth control, minimization of active switching components and an overall reduction in antenna design complexity.

1.2 Executive Summary

From a systems standpoint, antennas have historically been viewed as static and passive devices with time-constant characteristics. Once an antenna design is finalized, its operational characteristics remain unchanged during system use. However, the recent advent of microelectromechanical system (MEMS) components into microwave and millimeter wave applications has opened new and novel avenues of antenna technology development. High quality, miniature RF switches provide the antenna designer with a new tool for creating dynamic radiating structures that can be reconfigured during operation. MEMS switches are of particular interest because they offer broadband operation, low insertion loss and high contrast between active states. In the near future the antenna will evolve as a component that will offer intelligence that alters itself in-situ to meet operational goals. This development is similar to the introduction of viable field programmable gate arrays for integrated circuit logic in the late 1980s.

While the method of antenna operation is evolving, its role in communication systems still remains the same. The task that an antenna must perform is fundamentally that of a radiator and thus the metrics by which antennas operate and are measured are still intact. Gain, bandwidth, polarization, antenna feature size, etc. are still the realizable quantities of interest. But now the introduction of dynamic radiating structures has given the antenna designer an additional degree of freedom to meet these design goals. This dissertation discusses a comprehensive investigation of reconfigurable antennas with a primary focus on dynamic impedance bandwidth control. The essence of the problem is to use new RF switch technology to actively and intelligently change the operating band and bandwidth of an antenna. The overall objective of bandwidth control is to change only the antenna impedance bandwidth and not significantly affect any other radiating characteristics characteristics of the antenna. By maintaining all other performance characteristics, predictable antenna behavior can be ensured regardless of the impedance bandwidth. The objectives that are considered in the bandwidth control design problem include: high degree of bandwidth control, minimization of active switching components, and an overall reduction in antenna design complexity.

Successful completion of this research effort will have several key impacts on both theoretical antenna analysis and practical antenna design. Thorough understanding of the operation and design of reconfigurable antennas is necessary for development of new and innovative antenna designs and applications, a increased maturity level in the understanding of reconfigurable antenna elements then leads to practical applications.

The ability to control the operating band of an antenna system can have many useful applications. Systems that operate in an acquire-and-track configuration would see a benefit from active bandwidth control. In such systems a wide band search mode is first employed to find a desired signal then a narrow band track mode is used to follow only that signal. Utilizing active antenna bandwidth control, a single antenna would function for both the wide band and narrow band configurations providing the rejection of unwanted signals with the antenna hardware. This ability to move a portion of the RF filtering out of the receiver and onto the antenna itself will also aid in reducing the complexity of the often expensive RF processing subsystems.

This project will also have beneficial implications for communication systems that operate in hostile signal environments. Military communication systems in particular can be subject to intentional jamming signals. Active bandwidth control will provide an additional layer of protection. Performing RF signal rejection at the antenna level can prevent damaging or interfering signals from ever reaching sensitive internal components.

Though antenna bandwidth control is fundamentally a frequency domain topic, the potential exists for extension into time domain antenna design. The recent publication of the FCC part 15 standard for ultrawideband systems has spawned a renewed interest in time-domain antenna development. In many time-domain systems, transmit pulse shaping is a critical aspect of antenna operation. The antenna frequency domain bandwidth has a direct impact on the time-domain response and thus plays a key role in pulse shaping [1].

There has also been a recent move to increased integration between the antenna radiating elements and the underlying RF subsystems. The goal of single chip radio solutions is to package all RF components, including the antenna, on one generic chip. The ability to reconfigure an integrated on-chip antenna will be required to achieve

generic operation for single chip solutions.

MEMS and PIN diode switches have already been used to a limited extent to create reconfigurable antenna geometries. The focus of current reconfigurable antenna research has been limited primarily to beam steering and multiple band frequency selection scenarios. The reconfigurable Vee dipole antenna [2] uses MEMS actuators to vary the pitch angle of a Vee dipole antenna to change the beam shape. The reconfigurable tapered slot array [3] achieves beam steering via a different manner but also with MEMS switches. It consists of an array of tapered slot antennas whose slot lengths can be changed by altering the state of MEMS switches placed along the length of each slot. Computer simulation and hardware verification of these antennas and others have shown the viability of RF MEMS switches for antenna applications.

Work performed at Virginia Tech includes investigation and analysis of several preliminary bandwidth reconfigurable designs. The present research has been limited to antenna elements only, but arrays are popular realizations and are being intensively investigated elsewhere. The reconfigurable parasitic dipole and the reconfigurable microstrip patch have been studied extensively with computer simulation as preliminary designs. Three original encouraging designs have also been developed. The reconfigurable folded dipole, the reconfigurable planar inverted-F (PIFA), and the reconfigurable ring patch show all excellent bandwidth control capabilities.

The concept of bandwidth control through reconfigurable antennas is introduced and explained in this dissertation. The primary contributions to the field however, are the new reconfigurable antenna designs. These designs include the reconfigurable folded dipole, the reconfigurable stacked dipole, the reconfigurable PIFA and the reconfigurable ring patch. Additionally, detailed analysis and explanation of how the antennas operate is presented through mathematical calculation and measurements.

Three broad methods have been identified for achieving reconfigurable of antenna designs and operation. These three methods are total geometry morphing, matching network morphing and smart geometry reconfiguration. *Total geometry morphing* is implemented though a large array of switchable sub-elements. These sub-elements are combined to form the desired radiating structure. *Matching network morphing* modifies only the feed structure or impedance matching network of the antenna while

the radiating structure remains constant. The *smart geometry reconfiguration* method modifies only critical parameters of the antenna radiating structure to achieve the desired bandwidth control.

Each of these methods have been examined and the important aspects are detailed here. The total geometry morphing method has the advantage of being highly reconfigurable. It gives wide control over many antenna characteristics and the level of parameter control is limited only by sub-element granularity. It has the obvious disadvantage of being extremely complex. A large number of sub-elements, switches and control lines are required to implement reconfigurable geometries. The impedance network method has the advantage of being extremely simple to implement because the number of switching components is kept to a minimum. Its disadvantage is the level of parameter control is extremely limited.

The solution method that has been selected is the smart geometry reconfiguration method. This method is desirable because of its lower overall antenna complexity. A high level of parameter control can be obtained but with considerably fewer control elements than the total geometry method. This method does exhibit the constraint that the level of parameter control is ultimately limited by the electrical characteristics of the geometry. It also requires that the behavior of the antenna must be well understood in order to implement a reconfigurable antenna geometry.

1.3 Dissertation Overview

This dissertation is organized into three parts. The first part consists of the first two chapters and is a review of previous work and necessary background information. The motivation and overview of the dissertation is presented in Chapter 1. A review of several different antenna geometries which form the basis for the reconfigurable antenna designs is included in Chapter 2. It provides an introduction and analysis of piecewise wideband antennas which forms the foundation upon which the reconfigurable antenna concept is built. Chapter 2 also includes a description of the current state of reconfigurable antenna research.

The second part of the dissertation is contained in Chapters 3. It provides an expanded and detailed analysis of the reconfigurable antenna concept. It also expands the description of reconfigurable antenna technology including various methodologies for achieving antenna reconfiguration along with the physical components used in reconfigurable antennas.

Chapters 4, 5 and 6 present the results of specific investigations using simulations and experimental methods. The original antenna designs for achieving bandwidth reconfiguration are presented. Chapter 4 presents the reconfigurable ring patch antenna. Various geometries for achieving the bandwidth reconfiguration and control for the ring patch are presented. The investigation of the reconfigurable ring patch includes computer simulations performed with IE3D, Fidelity and HFSS along with an analysis of the measured prototype antennas. Chapters 5 and 6, present similar analyses for the reconfigurable planar inverted-F and the reconfigurable folded dipole antennas. Conclusions are then presented in Chapter 7.

Chapter 2

Previous Work

This chapter presents a review of the previous work performed related to the subject of reconfigurable antennas and background information for the new designs developed in this dissertation. Sections 2.1-2.3 present conventional antenna designs germane to the new antennas developed. Section 2.4 gives an overview of the current state of reconfigurable antennas.

2.1 Ring Patch Antenna

The ring patch antenna is a modification of the ubiquitous rectangular microstrip patch antenna [4, 5, 6]. Figure 2.1 shows the layout of the ring patch antenna. The ring patch is an attractive element because it can offer a significant reduction in antenna size over the solid microstrip patch antenna. Like the microstrip patch, the ring patch is characterized by the length and width of its metal radiator along with the height of the metal layer above the ground plane and the dielectric constant of the substrate material. The ring patch antenna consists of a planar dielectric substrate material with of a radiating patch on one side and a ground plane on the other. The ring patch differs from the rectangular patch due to the removal of a section of material, $W_2 \times L_2$, from the center of the patch. The patch is fed against the ground at the point (F_x, F_y) and common feed methods are the microstrip line, coaxial probe, and proximity coupled feeds. Figure 2.1 shows a coaxial probe feed to the ring radiator.

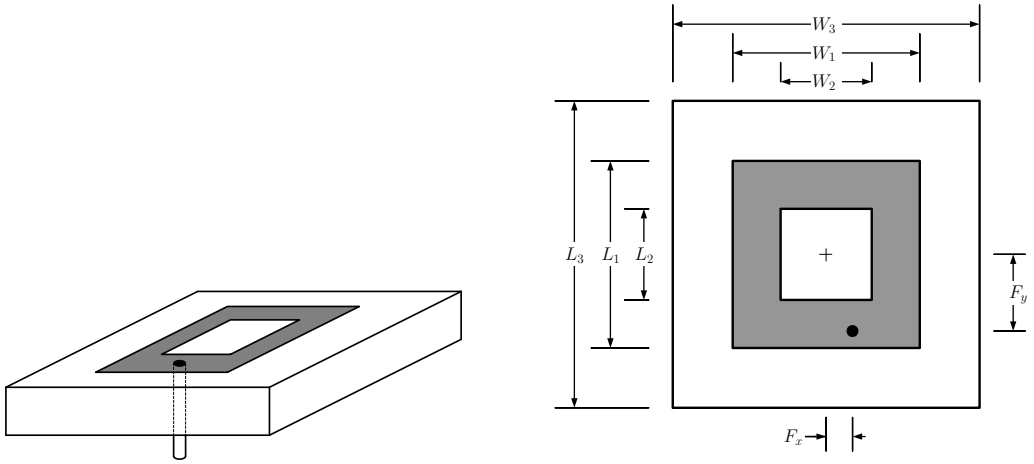

(a) antenna overview (b) antenna dimensioning

Figure 2.1 Ring microstrip patch antenna

Analysis of the ring patch antenna typically begins with an examination of the rectangular microstrip patch antenna. A charge distribution is developed between the underside of the patch metalization and the ground plane when the patch is excited. The electrical behavior can be visualized as two magnetic surface currents flowing along the radiating patch edges normal to the feed line. These magnetic currents are the result of the fringing fields along the radiating edges. In order to maintain real-valued input impedances, the microstrip patch antenna is normally operated near resonance. An approximate value for the length of a resonant half-wave patch is [7]

$$L \approx 0.49 \frac{\lambda}{\sqrt{\epsilon_r}} \tag{2.1}$$

where λ is the free-space wavelength and ϵ_r is the relative dielectric dielectric constant of the media. Removing the center section of the patch and thus creating the ring patch has the effect of increasing the resonant length of the antenna and lowering its operating frequency. The ring patch lies functionally between a microstrip patch and a wire loop radiator above a ground plane [8]. Thus, the resonant length of the patch is between that of the patch and the loop: $\lambda_{eff}/4 < L_2 < \lambda_{eff}/2$, where λ_{eff} is the effective wavelength in the dielectric medium. As more metal is removed from the microstrip patch, it becomes the printed loop and the resonant length L increases.

The area of the removed section also affects the input impedance and impedance

bandwidth of the antenna. The real part of the impedance increases as the removed metal area is increased [9]. For a fixed ring outer perimeter the impedance can go from a few hundred ohms, for small area of removal, to a few thousand ohms for a large area of removal [8]. The impedance bandwidth decreases as the subtracted area increases. The bandwidth varies between a few percent for the solid microstrip patch to less than a 1% for the ring patch with ring width ratio $W_2/W_1 = 0.7$.

Several methods exist for improving both the input impedance and bandwidth of the ring patch antenna. One of the most common methods is stacking additional radiators above the ring patch [10, 8]. Attempts have been made using both solid and ring stacked radiators with bandwidth increases from 6%-10% being reported [9].

2.2 Planar Inverted-F Antenna (PIFA)

The planar version of the inverted-F antenna, the planar inverted-F antenna (PIFA), is a popular antenna for reduced size environments. Figure 2.2 shows the general structure of the planar inverted-F antenna. The PIFA can be viewed a modification of the wire-form inverted-F antenna (IFA) [11]. The wire horizontal radiating element of the IFA is replaced by a plate and results in an increase in bandwidth. Some variations of the PIFA also replace the vertical shorting wire of the IFA with a vertical strap or plate to further enhance the bandwidth performance. A flush mounted PIFA extends in height approximately 1/20 of a wavelength as opposed to a conventional 1/4 wavelength monopole. The unobtrusive design of the PIFA makes it ideally suited for mobile and handheld situations where accidental damage to the antenna via unintentional contact with other objects is avoided. The PIFA offers very high radiation efficiency and adequate bandwidth for mobile applications in a compact antenna. A bandwidth of 10% can be realized with the PIFA.

The increased complexity of the PIFA structure over the IFA and monopole brings an associated increase in complexity of the PIFA design and analysis. The size and aspect ratio of the top radiating plate, the height of the plate above the ground plane, the size and position of the shorting plate, and the feed point location all have considerable impact on the electrical performance of the antenna. Several

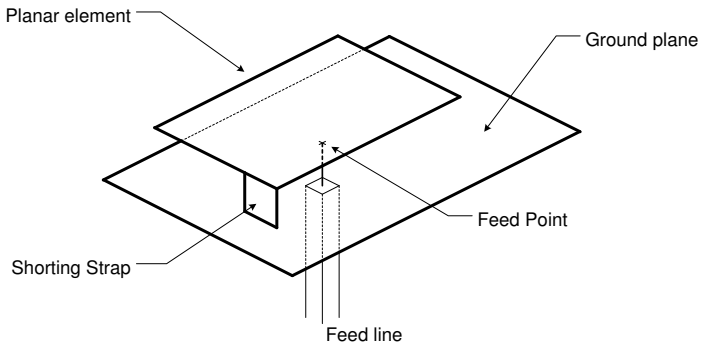

Figure 2.2 Basic geometry of the planar inverted-F antenna.

guidelines exist to determine the appropriate antenna dimensions based on the desired performance. The size of the radiating top plate can be calculated approximately using [12]

$$\lambda_{center} = 4(L + W) \tag{2.2}$$

where L and W are, respectively, the length and width of the plate. The resonant frequency is also influenced by the aspect ratio of the top plate (W/L) and the width of the shorting plate, S, in relation to the width of the top plate. Figure 2.3 shows how the current flow on the top plate varies with different top plate and shorting plate configurations [13]. In general, a greater top plate aspect ratio will result in a lower resonant frequency for a given grounding strap width. However, when the top plate aspect ratio is greater than unity ($W/L > 1$) and the difference in top plate and shorting plate lengths is equal to the top plate length ($W - S = L$), there is an inflection point in the resonant frequency. The resonant frequency of the antenna then increases with increasing aspect ratio. The current on the top plate generally flows to the open-circuit edge on the long side of the top plate when $W - S < L$. However, when $W - S > L$ the current flows to the open circuit edge along the short side of the top plate [13]. This change in current flow direction results in an effective reduction in electrical path length. Consequently, there is an inflection point in the resonant frequency. The change in current direction be seen for the square top plate case ($W = L$) with narrow shorting plate ($S << W$); the current flows almost equally along the both the W and L dimensions.

The impedance bandwidth of the PIFA is also affected by the design of the

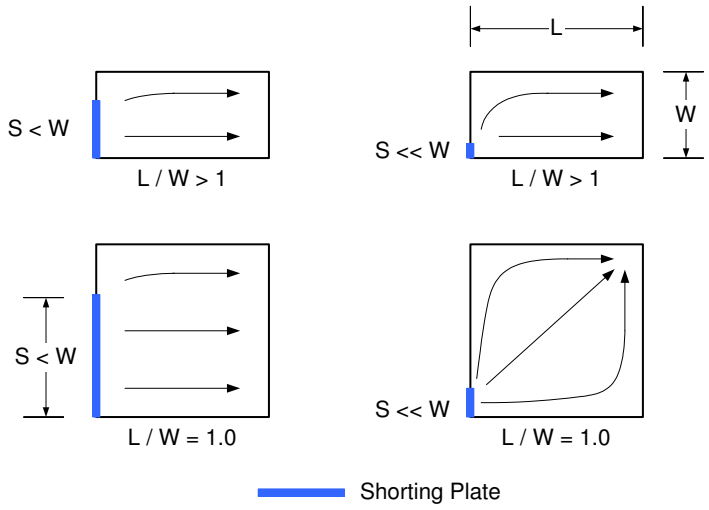

Figure 2.3 Surface current on PIFA top plate for various aspect ratios, L/W, and grounding strap widths, S.

structure. The height, H, of the radiating top plate above the ground plate and the shorting plate width, S have the greatest influence on PIFA bandwidth. In general, the bandwidth increases with both increasing top plate height and increasing shorting plate width. However, as the height of the top plate approaches the length of the grounding strap, $H \approx S$, the height also begins to influence the resonant frequency. The resonant frequency then given from [13]

$$\lambda_{center} = 4(L + W + H). \tag{2.3}$$

PIFA bandwidth is greatest when the shorting plate is the same width as the top plate ($S = W$). As the width of the grounding strap decreases, the relative bandwidth of the PIFA decreases. The bandwidth of a PIFA with the grounding strap width much less than the width of the top plate ($S/W \leq 0.1$) can be reduced to below 1%.

There are several procedures available for designing PIFAs and many different PIFA layouts may satisfy the same design criteria. One particular design of a cellular PIFA is given by [14] and is re-analyzed here for clarity. The design of Figure 2.4 has a radiating top plate that is 6.40 cm long and 2.29 cm wide. The height of the top plate is 1.78 cm and the shorting strap is equal in width to the top plate. The metal strips used in the simulation are 60 mils thick and the probe feed is model as a single

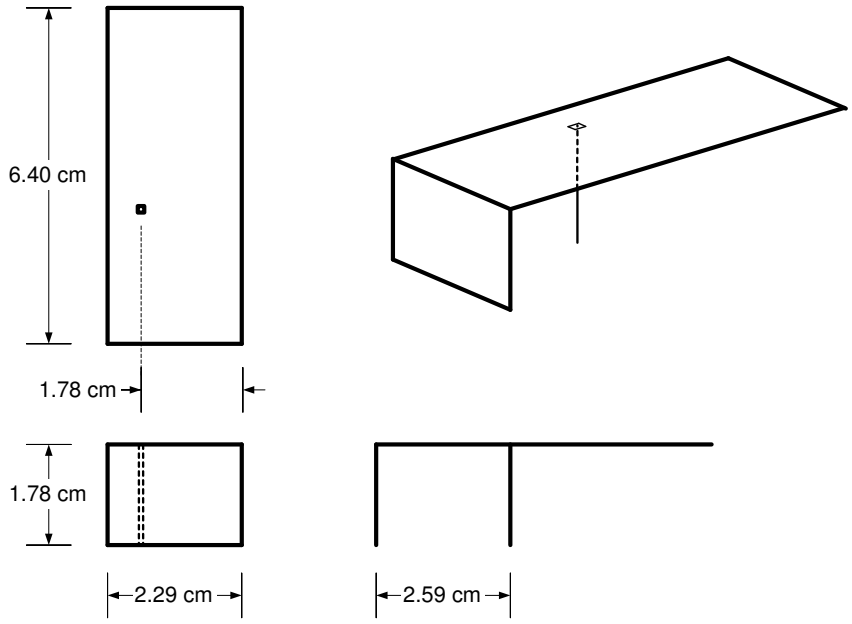

Figure 2.4 Typical PIFA designed for operation near cellular band.

strip 1.6 mm wide. The antenna is simulated over an infinite ground plane with the moment method package IE3D. The PIFA of Figure 2.4 shows and excellent impedance match to 50 Ω at 1 GHz. The 2:1 VSWR bandwidth in Figure 2.5 shows an impedance bandwidth of over 8%.

Further conventional PIFA modifications have been investigated to improve the antenna radiation performance [11, 12, 15, 16, 17, 18]. One particular modification is a PIFA with a partial shorting plate. This shorted PIFA was designed for operation on a handset was demonstrated to have 8 to 12% bandwidth [19]. This antenna, however, has an appreciable amount of radiation in the broadside direction as well as the horizontal plane.

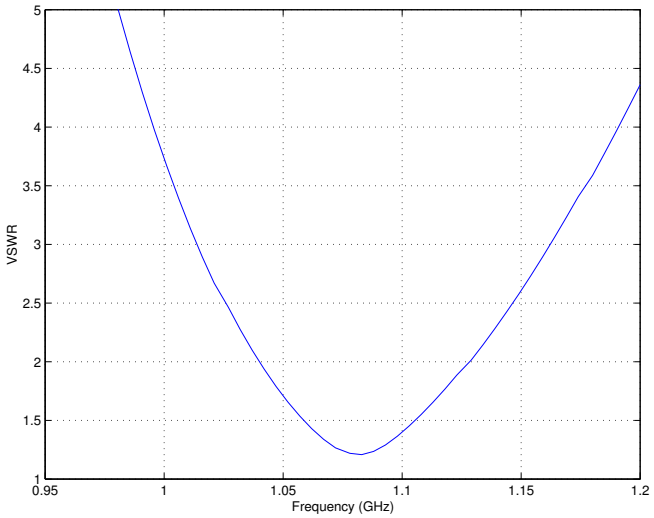

Figure 2.5 VSWR versus frequency for the PIFA of Figure 2.4 calculated using the moment method code IE3D.

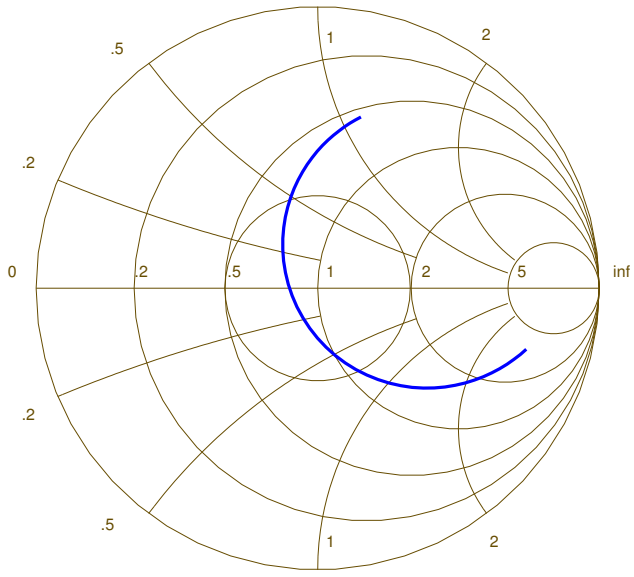

Figure 2.6 Input reflection coefficient for the PIFA of Figure 2.4 calculated using the moment method code IE3D.

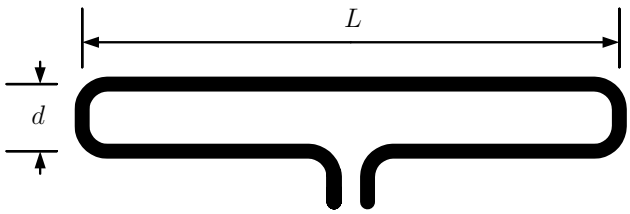

Figure 2.7 The geometry of the wire-form folded dipole antenna.

2.3 Folded Dipole Antenna

The folded dipole is a popular wire antenna and has been studied thoroughly since the 1960s [7, 20, 21]. The antenna is attractive due to its favorable input impedance qualities and simple construction. The input impedance of the folded dipole is higher than that of an equivalent half-wave dipole and it also has a larger impedance bandwidth than the typical wire half-wave dipole. The geometry of the folded dipole is shown in Figure 2.7. The antenna is formed by joining two equal length parallel dipoles at the ends and feeding it from the center of one dipole. In general, the diameters of the two parallel dipoles need not be equal. The folding of the dipole produces two parallel currents of equal magnitude and in opposite direction.

Analysis of the folded dipole can be accomplished by viewing the excitation of the folded dipole as the superposition of two modes: a symmetrical mode having equal driving voltages and an asymmetrical mode having equal but opposite driving voltages [21, Sec. 3.3]. Figure 2.8 illustrates the decomposition of the two modes. The equivalent impedance of the symmetric mode is given by

$$Z_r = \frac{V}{(1+a)I_r} \tag{2.4}$$

where the term $(1+a)$ is the impedance step-up ratio and relates the radiuses of the parallel dipoles. This step up ratio is detailed in [21, Sec. 3.3] and is given by

$$a = \frac{\cosh^{-1}\frac{\nu^2-\mu^2+1}{2\nu}}{\cosh^{-1}\frac{\nu^2+\mu^2-1}{2\nu\mu}}. \tag{2.5}$$

The terms ν and μ relate the ratios of the two diameters to the parallel dipole separation

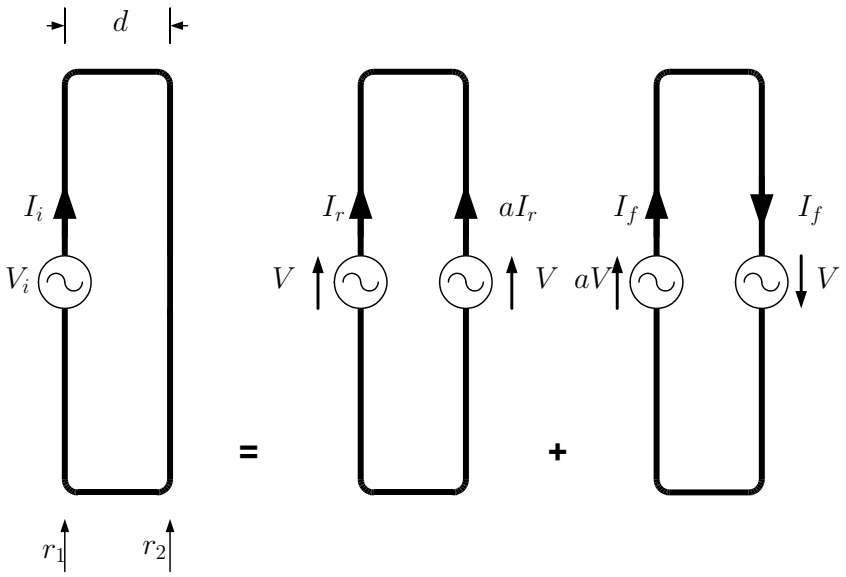

Figure 2.8 Network representation of the decomposition of the folded dipole.

distance d and are given from

$$\nu = \frac{d}{r_1}, \qquad \mu = \frac{r_2}{r_1}. \tag{2.6}$$

The asymmetrical mode can be viewed as a shorted transmission line of length equal to the folded dipole length, L, and its impedance is given by

$$Z_f = \frac{(1+a)V}{2I_f} = jZ_0 \tan \beta L/2 \tag{2.7}$$

where Z_0 is the characteristic impedance of the transmission line. The expression for the input impedance is then obtained by combining Z_r and Z_f and is

$$Z_i = \frac{(1+a)V}{I_r + I_f} = \frac{2(1+a)^2 Z_r Z_f}{(1+a)^2 Z_r + 2Z_f}. \tag{2.8}$$

For the special case of the half-wave folded dipole ($L = \lambda/2$) with equal radius arms ($r_1 = r_2$) Equation 2.8 reduces to

$$Z_i = 4Z_{dipole}. \tag{2.9}$$

The input impedance of a half-wave dipole is roughly 70 Ω thus the input impedance of the folded dipole is 280 Ω [7].

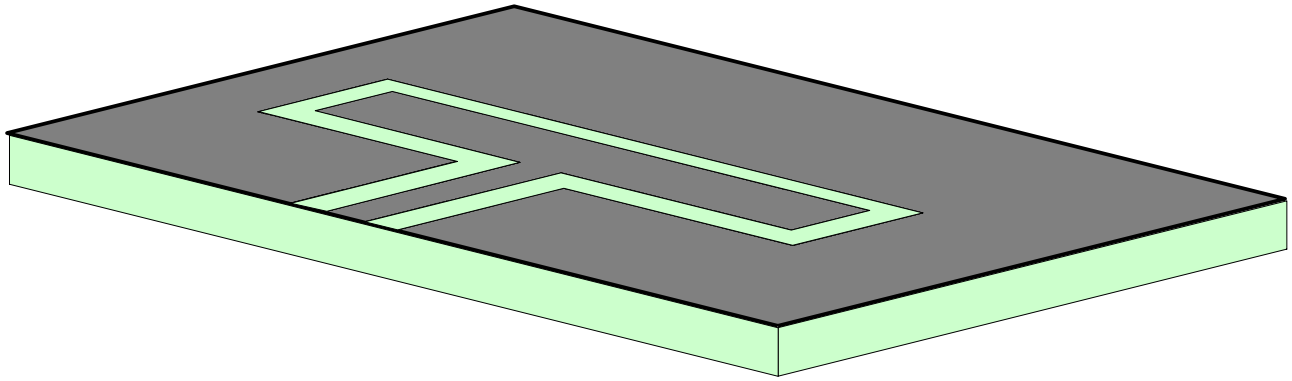

Figure 2.9 The printed folded-slot dipole antenna.

The printed slot folded dipole in Figure 2.9 is a variation on the wire form of the folded dipole [22, 23, 24, 25, 26]. It is constructed by etching a slot on a metallized substrate in the shape of a folded dipole. The printed version is an attractive alternative due to the rugged nature of printed antenna technology. The printed slot also lends well to use with coplanar waveguide feed networks. The input impedance of the printed slot antenna may be obtained by applying Babinet's principle to the geometry [22]. Babinet's principle views a thin slot in an infinite ground plane as the compliment to a dipole in free space. This gives an expression for the impedance of the half-wave folded dipole slot as

$$Z_{slot} = \frac{Z_{fs}}{4Z_{dipole}} \tag{2.10}$$

where the free space impedance is given by $Z_{fs} \approx 377\ \Omega$ and the half-wave folded dipole impedance is again $Z_{dipole} \approx 70\ \Omega$. This results in a $Z_{slot} \approx 500\ \Omega$. As expected, the radiation patterns of the folded dipole and folded slot antenna are similar to those of the half-wave dipole.

2.4 Reconfigurable Antennas

This section gives a survey of previous and current research involving reconfigurable antennas. Reconfigurable antennas are a relatively recent phenomena in antenna design. The late 1990s marks the transition into viable reconfigurable antenna design and there has been a rapid increase in the number of literature references containing recon-

figurable designs and applications since that time. The current literature is divided into a few broad categories of reconfigurable antennas. Most reconfigurable antennas can be classified as either reconfigurable elements designs, fragmented apertures designs or reconfigurable arrays designs.

2.4.1 Reconfigurable Elements

Reconfigurable elements represent antennas that radiate with one or few primary radiating elements. That primary element is reconfigured via switches or some other variable element to provide parameter control. The antennas listed in this subsection all function in this manner (lumped reconfigurable elements).

2.4.1.1 Planar Reconfigurable Slot

The reconfigurable slot antenna presented in [27] is an electronically tunable planar VHF slot antenna. It consists of a microstrip fed resonant slot structure loaded with a series of PIN diode switches. The resonant frequency of operation is selected by varying the length of the radiating slot and thus changing its electrical length. The length of the slot is altered by biasing the PIN diode switches along the slot length. It is capable of operating at four different frequencies in the band from 500 to 900 MHz.

2.4.1.2 MEMS Reconfigurable Vee

The MEMS reconfigurable Vee antenna is a printed antenna that uses dynamic actuators to alter the radiation characteristics of the antenna. Figure 2.10 shows the geometry of the reconfigurable Vee antenna. The antenna presented in [28, 2, 29] uses MEMS actuators to alter geometry of the Vee dipole. Push-pull actuators connected to the dipole arms enable reconfiguration of the Vee pitch angle. Each arm of the Vee is independently controlled, allowing the antenna to both steer the antenna beam and alter the beam shape. Symmetrical movements of the Vee actuators result in a widening and narrowing of the Vee angle, α, and thus widens and narrows the main beam. The main beam may be steered off broadside by moving each Vee actuator by

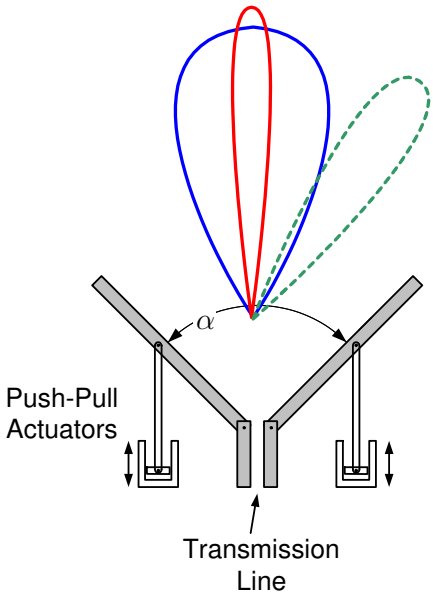

Figure 2.10 The reconfigurable Vee-dipole antenna.

different distances.

The antennas presented in [2, 29] were fabricated using a three layer polysilicon surface micromachining process. Two versions were detailed, a 3 GHz version and a 17.5 GHz version, and were shown to offer a considerable amount of dynamic reconfigurability. The antennas demonstrated 48° of main beam shift from broadside.

2.4.1.3 Reconfigurable Dime and Q-dime Antennas

The dime antenna [30, 31, 32] and its constituent q-dime element are broadband multi-layered stacked circular patches. Figure 2.11 shows the basic geometry of the dime antenna. The dime antenna is constructed as either a single monolithic element or as a combination of four quarter dime (q-dime) elements. The antennas are electrically small (radius $< 0.2\lambda$ and height $< 0.5\lambda$) and volumetric in nature to achieve the size reduction. Broadband operation is accomplished by creating two degenerate modes via two cylindrical radiating slots in the patch structures. MEMS switches located within the geometry of the the patches allow the antenna to alter the working frequency of the design. The switches are successively turned on to tune the frequency of the antennas.

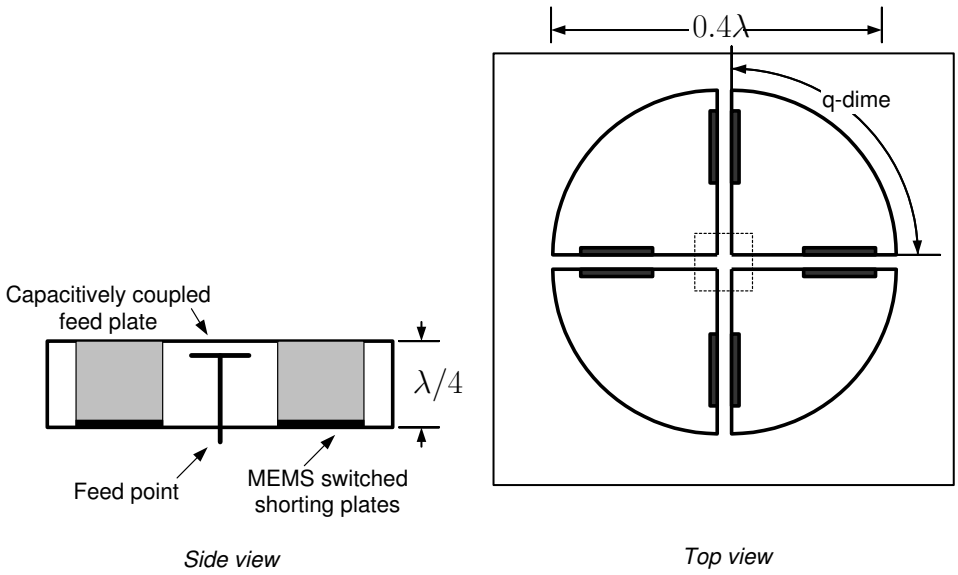

Figure 2.11 Geometry of the proximity coupled reconfigurable dime antenna composed of four quarter-dime stacked patch antennas.

The antennas are also able to control polarization and radiation pattern shape by activating the MEMS switches.

2.4.1.4 Reconfigurable Leaky Mode Patch

The antenna presented in [33], [34] is a combination of normal microstrip patch antenna and a leaky-wave antenna. Leaky-wave radiation is facilitated by the presence of higher order modes on microstrip structures [35]. The antenna is shown in Figure 2.12 and consists of a high-order mode launcher connected to a length of X-band leaky-mode microstrip antenna. The mode launcher is composed of a microstrip impedance transformer, 180° phase shifter and an even-mode suppressor. The leaky-mode antenna is then connected via MEMS switches to a conventional C-band microstrip patch antenna. When the MEMS switches are deactivated the antenna operates as a conventional patch antenna. Activating the switches causes the patch structure to become part of the leaky-mode structure and the antenna radiates as a leaky-mode antenna.

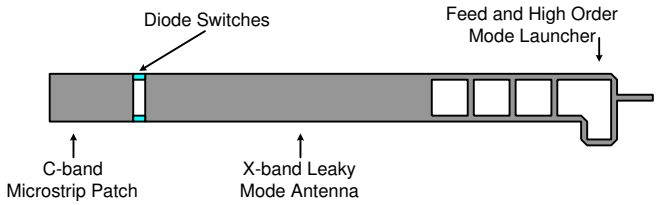

Figure 2.12 The reconfigurable leaky mode patch antenna.

2.4.1.5 MEMS Mechanical Beam Steering

The antenna system presented in [36] addresses the problem of scan loss inherent to electronically steered antennas. Scan loss is a broadening of array main beam and the associated reduction of array gain seen as the main beam is steered off broadside. The system overcomes this loss by steering the antenna *electromechanically* via a MEMS structure as opposed to a strictly electrical scan as in a phased array. The antenna system presented has a V-band radiating patch antenna element. It uses a MEMS fabricated element platform with two degrees of rotational freedom to facilitate the main beam scanning. The MEMS antenna system is capable of scanning the main beam over 60° with no measured scan loss.

2.4.1.6 Stacked Reconfigurable Bowtie

The stacked reconfigurable bowtie antenna [37] consists of a dual layer arrangement of unequal size balanced microstrip bowtie elements. Figure 2.13 shows the geometry of the stacked reconfigurable bowtie antenna. The individual bow ties are situated on mixed dielectric layers above a ground plane and the bowtie geometries are designed for 3.1 GHz and 8 GHz operation. Each bowtie layer is constructed on top of a mixed layer dielectric consisting of a thick polymer layer ($\epsilon_r \approx 3.0$) over a thin foam layer ($\epsilon_r \approx 1.0$). This layered dielectric arrangement provides both upper and lower operating bands with nearly 25% bandwidth. The smaller high-frequency bowtie layer is stacked on top of the larger low-frequency bowtie layer. The low-frequency antenna acts as a virtual ground plane for the high frequency antenna when the antenna is operating in the high-frequency mode. Several sets of MEMS switches are present under the ground

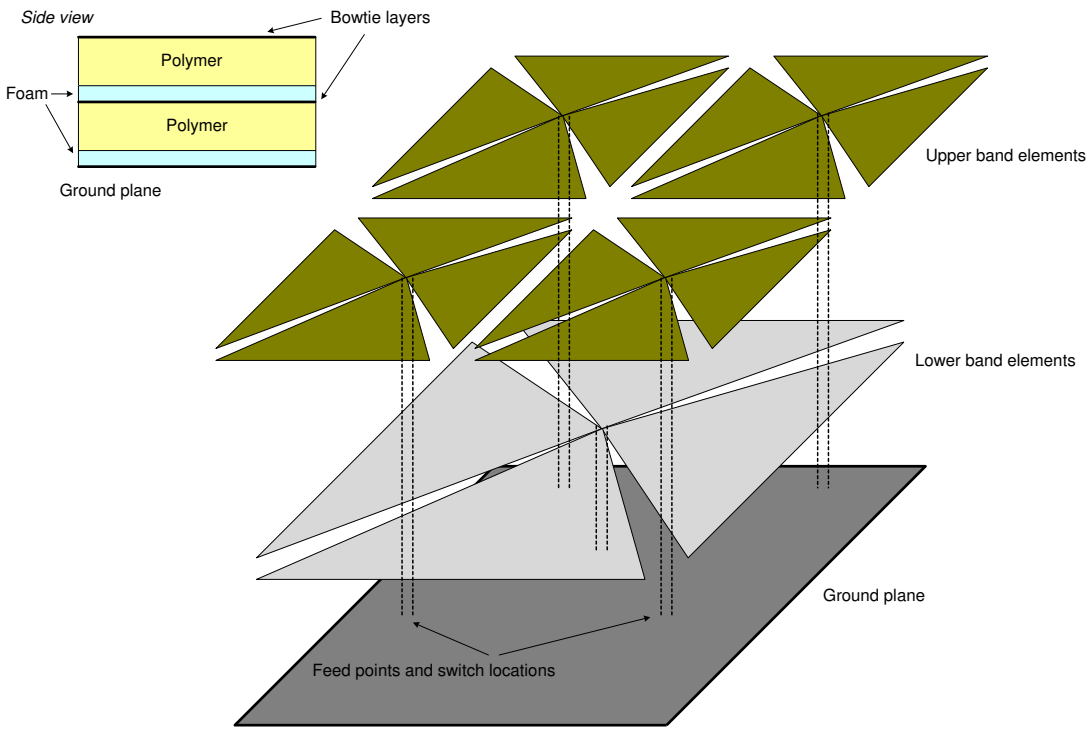

Figure 2.13 The reconfigurable stacked bowtie antenna.

plane and control the antenna band selection. A set of MEMS switches connects each of the bowtie feeds to the main antenna feed while an additional set of switches connects the bowtie feeds to the ground plane. The upper bowtie is activated by closing the appropriate set of switches and enabling the high frequency feeds. The lower bow ties are then grounded via the low-frequency MEMS switches and the larger bow ties act as a ground plane for the high-frequency elements. Conversely, in the low-frequency mode the lower elements are activated by closing the appropriate set of switches and enabling the low-frequency feeds. The upper bow ties are then disabled by disconnecting the MEMS switches for the high-frequency feeds. In this low-frequency configuration, the upper bow ties act as floating parasitic radiators for the lower elements and increase the operating bandwidth of the lower elements.

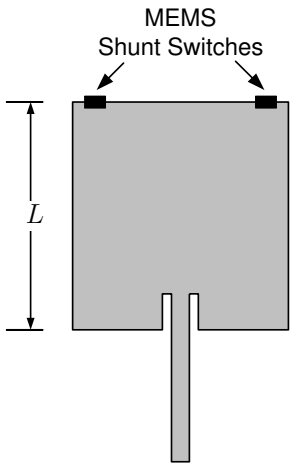

Figure 2.14 The reconfigurable microstrip patch antenna.

2.4.1.7 Reconfigurable Patch

The patch described in [38] uses a conventional microstrip patch antenna with the addition of two MEMS controllable shorting elements. Figure 2.14 illustrates the geometry of the reconfigurable patch antenna. The antenna is fed through a conventional microstrip line. The MEMS switches are positioned at the far end of the microstrip patch. The patch operates at its nominal frequency when the MEMS switches are in the off state. As with other rectangular microstrip patches, frequency of operation is determined by the length L, the edge parallel to the microstrip feed. When the MEMS actuators are turned to the on state, they add a capacitance in shunt with the input impedance of the patch. This added capacitance has the effect of lowering the resonant frequency of the antenna. The antenna presented was designed to operate at 25 GHz. A frequency reduction of 1.6% was achieved with the MEMS switches in the "on" state.

2.4.2 Distributed Radiators

The second broad class of reconfigurable antennas are the distributed radiators. This class represents antennas that radiate primarily by combining sub-elements together to form a larger discontinuous radiating structure. They are frequently referred to as

fragmented apertures or microswitch arrays because the radiating structure is formed from a subset of elements from a large array of elements. The operation of this class of antennas is distinct from conventional arrays because the individual elements that make up the radiator effectively radiate as a single unit with a single feed. The elements or, more precisely, sub-elements do not act as autonomous radiating structures. The sub-elements control the current distribution on the aperture of the structure and thus control the radiation properties of the antenna. It is the combination of these sub-elements which allows the overall structure to radiate. The reconfigurable nature of the switch elements allows the antenna to change its functionality by activating and deactivating specific switches.

The micro-switched fragmented aperture [39, 40, 41] developed by Georgia Tech Research Institute (GTRI) has been studied extensively. The aperture investigated by GTRI consists of small metallic conducting pads connected by MEMS switches. The MEMS switches are activated by control chips that are placed on or near the radiating aperture. Each control chip directs either a single switch or a small functional cell of switches. A bowtie dipole has been simulated and tested in the fragmented aperture. The bowtie geometry has shown promising results in its ability to control radiation characteristics such as polarization and operational frequency.

The GTRI fragmented aperture has also been configured to radiate via a genetic algorithm structure search [39]. An array test bed was created that allowed a computer routine to automatically generate the radiating structure based on a desired radiation characteristic. The search routine evaluated the fitness of the radiation performance of a previous generation and generated the next generation of aperture structure. The large number of sub-elements present in the fragmented aperture has made optimization routines such as genetic algorithms particularly well suited to antenna design.

The MEMS switched reconfigurable antenna presented in [42] is very similar in layout and operation to the GTRI fragmented aperture. The antenna consists of a 3×3 array of patches connected with MEMS switches. This reconfigurable patch module is used a building block for larger conformal antenna structures. A dual L/X-band prototype antenna was constructed using ideal open/closed switches in place of functional MEMS switches. The antenna was able to achieve 1.2% bandwidth and

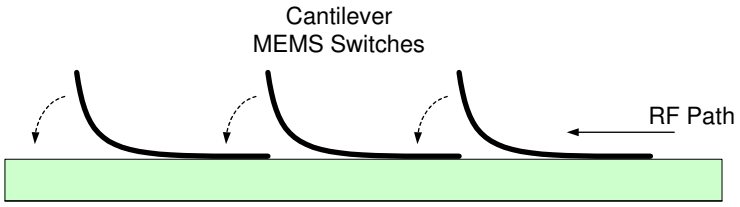

Figure 2.15 The MEMS cantilever RF switch used in the microswitch array.

acceptable radiation patters for the L-band operation and greater than 7% bandwidth for X-band operation.

The reconfigurable microswitch array presented in [43, 44] extends the concept of the reconfigurable pad presented in [39] and [42]. The microswitch antenna differs from the previous examples because it omits the conducting pad portion of the antenna. It uses MEMS switches to form both the switch and the conducting elements for the antenna. Figure 2.15 shows the cantilever MEMS switch that acts as both the RF switch and the radiating structure. The removal of the conducting pad allows the switches to be placed much closer together and thus gives the antenna more reconfigurability by allowing more switches to be placed in the same physical space. The reference [43] presents results from the design of a reconfigurable microstrip patch. Two promising configurations of the patch were tested—a 10 GHz version and a 20 GHz version.

The self-structuring antennas (SSA) introduced in [45] also achieve parameter reconfigurability in a distributed radiator manner. This method differs slightly from the previous distributed radiator configurations presented. The SSA uses a predefined network of radiating wires connected together with RF microswitches.

2.4.3 Reconfigurable Arrays

The first two categories of reconfigurable antennas presented deal strictly with radiating elements. The third category covers reconfigurable antenna arrays. Antenna arrays can employ reconfigurable design aspects in several methods. Dynamic reconfigurable elements can be used instead of conventional fixed antennas as the array elements. Or the array can use conventional fixed elements and the feed section phase-controllers

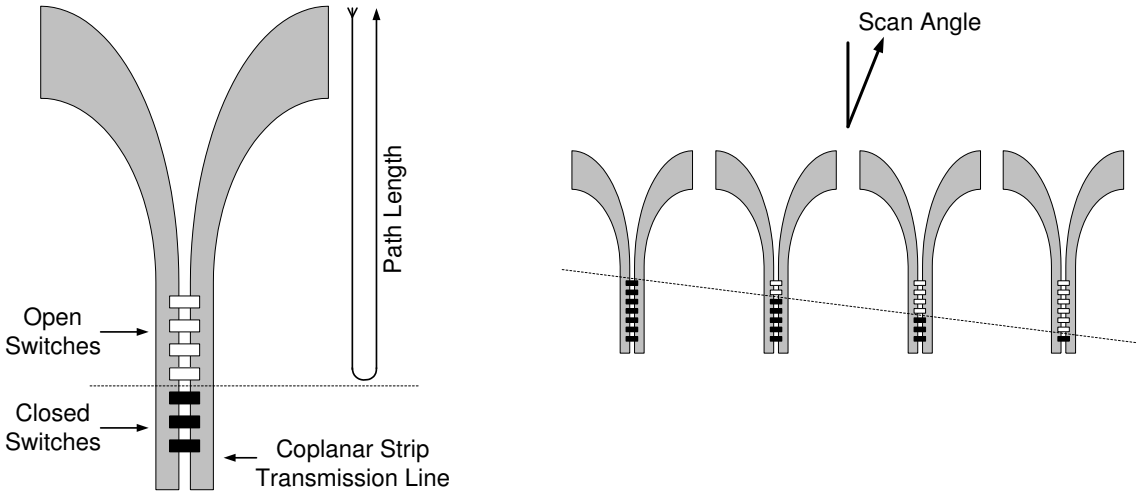

(a) Flared notch with reconfigurable feed section.

(b) Array showing beam steering with reconfigurable feed section.

Figure 2.16 The reconfigurable flared notch array element with time-delay beam steering.

might employ reconfigurable elements.

A reflective reconfigurable aperture that uses an array of fixed flared-notch antennas is presented in [3], [46], [47]. The flared notch antennas have MEMS switches placed along the notch feed section that allows the length of the feed section to be changed. This alteration of feed length introduces a time delay in the received energy. The time delay in the individual array elements allows the array to be electromechanically steered. Figure 2.16 illustrates the antenna. Figure 2.16(a) shows the array element with MEMS switches for phase control and Figure 2.16(b) shows how these elements are combined in the array to perform beam scanning.

A reconfigurable array design based on TEM horn elements is presented in [48]. The array was designed to achieve an effective bandwidth of 10:1 over the 2-20 GHz range. To attain the 10:1 bandwidth the array uses MEMS switches to control the antenna ground plane. A switchable reflective/transmissive ground screen was numerically demonstrated to offer the necessary reflective control. The ground screen was constructed from $\lambda/10$ spaced wires connected together with MEMS switches. The

MEMS switches allow the screen inter-element spacing to be varied, and consequently, the screen can be configured such that it is transparent or opaque to selected frequencies.

A method is presented in [49] for control of reconfigurable array antennas. The method requires phase-only control of quantized phase shifters that is directly applicable to use with MEMS phase shifters. A 150,000 element space-based radar is presented in [50] that uses MEMS phase shifters. The weight of the electronically scanned array was reduced by employing the MEMS phase shifters in place of conventional phase shifters.

Chapter 3

Reconfigurable Antennas and Technology

This chapter presents the concept of reconfigurable antennas and details the emerging technologies that make reconfigurable antennas possible. First, a description of the methodologies available for designing reconfigurable antennas is presented. Then a description of the physical switch technologies and how they can be utilized for antenna design. Their electrical characteristics are described and the mathematical models used in simulating the switches in an RF environment are presented.

From a systems standpoint, antennas have historically been viewed as static devices with time-constant characteristics. Once an antenna design is finalized, its operational characteristics remain unchanged during system use. However, the recent advent of microelectromechanical system (MEMS) components into microwave and millimeter wave applications has opened new and novel avenues of antenna technology development. High quality, miniature RF switches provide the antenna designer with a new tool for creating dynamic radiating structures that can be reconfigured during operation. MEMS switches are of particular interest because they offer broadband operation, low insertion loss and high contrast between active states. In the near future the antenna will evolve as a component that will offer intelligence that alters itself in-situ to meet operational goals. This development is similar to the introduction of viable field programmable gate arrays for integrated circuit logic in the late 1980s.

While the method of antenna operation is evolving, its role in communication systems still remains the same. The task that an antenna must perform is fundamentally that of a radiator and thus the metrics by which antennas operate and are measured are still intact. Gain, bandwidth, polarization, antenna feature size, etc. are still the realizable quantities of interest. Only now the introduction of dynamic radiating structures has given the antenna designer an additional degree of freedom to meet these design goals.

3.1 Reconfigurable Antenna Methodologies

This section details the methodologies identified for designing reconfigurable antennas. It describes each method and illustrates the strengths and weaknesses associated with each. Example designs are presented for each method.

Classical non-reconfigurable design methods have dominated antenna engineering for the majority of antenna design history. To make the transformation from fixed element operation to reconfigurable antenna design requires a suitable conversion in design methodology. The short existence of reconfigurable has produced two primary design methods: total geometry morphing and matching network morphing. A third method is also identified and expanded in this dissertation—smart geometry reconfiguration. Thus, three broad methodologies have been identified for achieving reconfigurable antenna designs and operation.

Total geometry morphing represents the most structurally complicated of the methods. It is implemented though a large array of switchable sub-elements which are combined to form the desired radiating structure. Matching network morphing is the simplest of the methods and modifies only the feed structure or impedance matching network of the antenna while the radiating structure remains constant. The smart geometry reconfiguration method lies between the other two in its structural implementation complexity. It modifies only critical parameters of the antenna radiating structure to achieve the desired range of reconfigurable control.

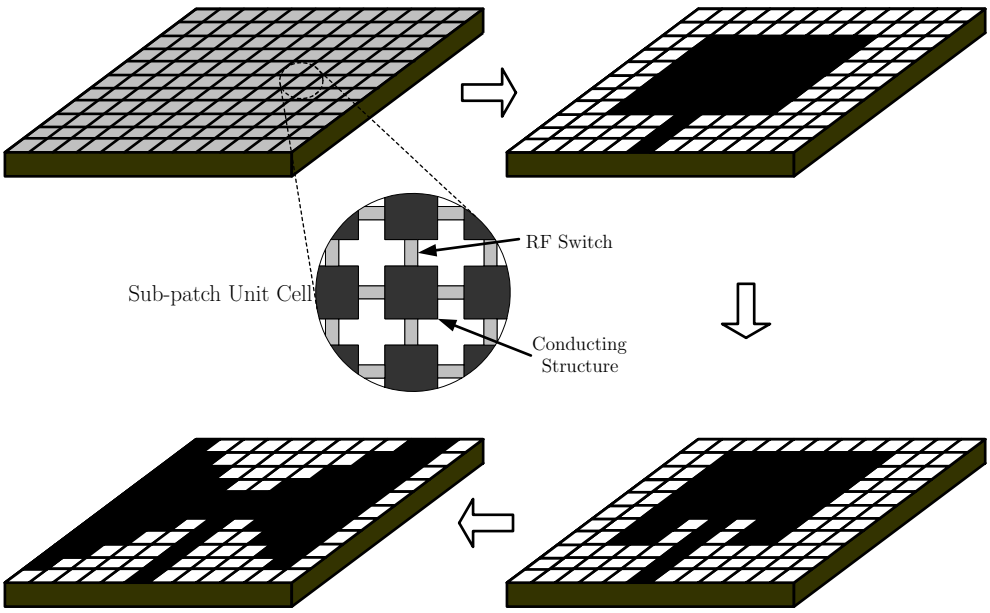

Figure 3.1 The total geometry morphing method of reconfigurable antenna design.

3.1.1 Total Geometry Morphing Method

The total geometry morphing method achieves reconfigurable operation by switching a large array of interconnected sub-elements. The sub-elements are connected together via RF switches and are typically less than $\lambda/20$ in size. Because the sub-elements are much less than a wavelength in size they do not form efficient radiating elements individually. However, switching together multiple adjacent sub-elements results in an aggregate structure that forms the desired radiator. This sub-element arraying allows considerable flexibility in forming the radiator. The geometry of the aggregate radiating structure can take a wide variety of forms depending on the desired application. The reconfigurable antennas designed via this method are often referred to in the literature as distributed radiators because the total radiating structure is distributed over many smaller structures.

Figure 3.1 illustrates the concept of the total geometry morphing method. The example is a reconfigurable microstrip patch antenna consisting of a large grid of switched microstrip sub-patches that are available on the dielectric substrate. These sub-patches do not represent individual microstrip patch antennas themselves but act

as actively reconfigurable conducting structures. The detailed blow-up in Figure 3.1 shows a single functional unit cell for the composite antenna. These unit cells illustrates the concept of the sub-patch conducting structure. Each unit cell consists of a small conducting patch of metal and four RF microswitches. The switches provide the RF conduction path to the nearest neighboring unit cell. The composite antenna is then constructed by activating the necessary switches to form then antenna. In this example the structure is first configured to form a conventional rectangular microstrip patch antenna. Next, several of the sub-patches along the length of the microstrip feed are switched to the off state. This moves the effective feed point for the patch antenna closer to the center of the patch and alters the input impedance of the patch. Finally, the unit cells are configured to form a bow-tie patch antenna which has different radiation characteristics than the rectangular patch.

The total geometry morphing method has the obvious advantage of providing a large amount of antenna reconfigurability. The array of sub-elements provides a large level of flexibility in composing the aggregate antenna. Because of the flexibility in configuring the antenna, a wide range of control over many antenna characteristics is offered by employing this method. Thus, a single reconfigurable platform could be used for a large number of applications. System operation over multiple frequency bands, with variable radiation pattern characteristics and selective polarization is possible with a single reconfigurable platform. Likewise, the layout of the sub-element array pattern is not limited to two dimensional planar microstrip geometries. Surface conformal and three dimensional geometries also represent viable configurations.

The highly flexible nature of total geometry morphing dictates the primary difficulty with implementing this method. The extreme complexity involving numerous individual components to necessary to realize the geometries is inherent in this method. A large number of sub-elements, switches and control lines are required to implement the reconfigurable geometry. This leads directly to geometry and component management issues. A large number of active components also means there are a large number of points of failure. Recent advancements in RF MEMS switches have been the driving force behind much the reconfigurable antenna designs. As with any mechanical switch, MEMS devices are susceptible to reliability issues due to mechanical fatigue. Thus,

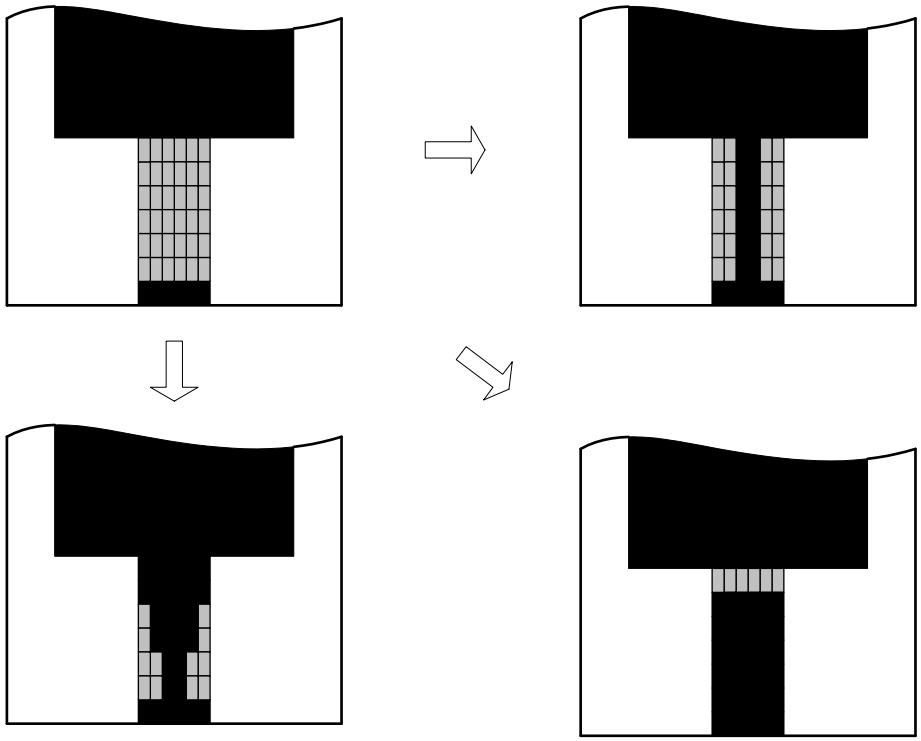

Figure 3.2 Microstrip feed configurations for impedance matching of reconfigurable antenna design.

any structure which depends explicitly on the reliable operation of these switches will be subject to performance degradation in the case of switch failure.

3.1.2 Matching Network Morphing Method

The matching network morphing method represents the simplest of the three techniques for achieving reconfigurable antenna operation. In this method, the actual radiating structure remains constant and only the feed or impedance matching section of the antenna is reconfigured. Like the total geometry method, this method is often employed with microstrip geometries because of the relative ease in placing RF switches on planar structures. In the case of microstrip feed lines, there are typically 10 or more sub-elements in the transverse direction across the width of the microstrip line for adequate parameter control. They are on the order of $\lambda/20$ in length along the longitudinal direction.

Figure 3.2 illustrates one implementation of the matching network morphing method. In this example a microstrip patch antenna is edge fed by a reconfigurable microstrip line. The reconfigurable microstrip line consists of a small array of switchable microstrip sub-elements. Each of these sub-elements may be switched on or off by activating one of the miniature RF switches that form the interconnections between the sub-elements and compose the overall microstrip structure. The width and length of the feed line is altered to change the impedance of the microstrip. The grey boxes represent inactive sub-elements and the block boxes represent active sub-elements.

The top left configuration in Figure 3.2 shows the microstrip patch antenna and the available microstrip feed lattice. The top right sub-element arrangement shows the feed configured as a narrow microstrip line having a characteristic impedance. The patch antenna operates in a radiation mode that is specified by this feed configuration. The bottom two arrangements in Figure 3.2 show the microstrip feed line configured in two other possible formations. These variations in feed impedance then excite different radiation modes in the microstrip patch antenna.

The matching network morphing technique carries the distinct advantage of being extremely simple to implement in practice. The only component of the antenna that is changed is the feed network and thus the complexity of the design is minimized. As a result, the number of physical switching components is kept to a minimum and switch reliability becomes less of an issue. Conversely, this method exhibits the disadvantage of limited antenna reconfigurability. The antenna operation is varied only through changes in matching. Consideration is not given to other critical radiation characteristics. Because the principal radiation mode is altered by the impedance, the electrical performance characteristics are likely to change as well.

3.1.3 Smart Geometry Reconfiguration

The final identified method of reconfigurable antenna design is smart geometry reconfiguration. Falling between total geometry morphing and the matching network morphing method in both the amount of achievable parameter control and system complexity, this method modifies only critical parameters of the antenna radiating

structure to achieve the desired reconfigurable performance. It can be implemented with considerably fewer control elements than the total geometry method and thus has the advantage of reduced design complexity. However, with a thorough understanding of the underlying antenna design and careful design consideration it can yield a high level of reconfigurability and antenna parameter control. The primary disadvantage of this method is that the underlying physics of the particular antenna must be known in order to take advantage of minor geometry modifications to achieve the reconfigurable goal. Additionally, the amount of reconfigurability is ultimately limited by the electrical characteristics of the antenna geometry.

3.2 Antenna Switch Technologies

This section gives a brief overview of the current state of RF switches available for use in antenna systems. It includes switches have been used in both classical antenna systems and more recent reconfigurable implementations. In particular it explores conventional mechanical switches, PIN diodes, and FET switches, and MEMS switches and makes recommendations of candidates for use in reconfigurable antenna designs.

The fundamental role of a switch or relay is a device to make or break an electric circuit. In static and quasi-static regimes, a switch operates simply as either a conduction path or a break in the conduction path. However, switch operation in an RF system will include additional electrical properties. Switch resistance, capacitance and inductance along the RF signal path must be included in the analysis of the system. In RF antenna systems, switch function typically entails controlling and directing the flow of RF energy along a desired RF path. Traditionally, this path may include any of the RF subsystems leading to the antenna feed distribution network as well as the antenna feed and, in the case of arrays, any power distribution network. The introduction of reconfigurable antennas has also added the antenna itself to the list of places where switches are utilized to control the direction and flow of RF current.

Irrespective of the type of switch used, there are several important characteristics that must be evaluated for all RF switch applications and particularly reconfigurable antenna designs. The selection of switch type depends fundamentally on the switching

speed required by the application and the switched signal power level. Other critical parameters to consider in the selection of RF switches include impedance characteristics, switch biasing and activations conditions, package and form factor, and switch cost.

The usable speed that a switch can toggle between states in an RF signal path is actually composed of three complementary mechanisms: transition time, switch rate and transient behavior. Switch transition time measures the speed at which the switch can alternate between on and off states. For RF applications, this is typically defined as the time required for the RF power level to change from 10% to 90% for an on transition or 90% to 10% for an off transition [51]. The switch rate represents the speed at which the switch can respond to a control signal. It measures how long after sending a signal to the switch will the output state change. This is normally defined as the time between the appearance of 50% of the control voltage and 90% of the RF output level. Switch transient behavior represents the exponentially decaying signal components seen on the switch due to the physical change in switch state. Transients are often manifested by large, quickly decaying voltage spikes at the RF input and output. Transients may contain both electromechanical and electromagnetic in nature. Electromechanical transients are caused by the mechanical movement of the switching component while electromagnetic transients represent energy exchange between electric and magnetic fields in the switch components.

The power handling capability of a switch measures how well the switch will pass the RF signal level from switch input to output. An ideal switch would pass all signal levels through linearly with no distortion. However, real switches tend to have a upper limit to which signals will pass linearly. Above this level, input signals become compressed and are passed in a non-linear manner. This maximum signal level is typically used as a measure of switch performance. Often the 1 dB compression point is specified to indicated the input level at which the output sees 1 dB of compression from linear switch operation.

Impedance issues relating to switch characterization are also described by several related quantities. The overall impedance matching of the switch, insertion loss, isolation, and series resistance are all related to switch impedance performance. For

maximum power transfer, the switch should be match with the transmission paths to which it is connected. Impedance mismatches in RF components result in undesirable reflections which degrade system performance. Insertion loss is directly related to impedance matching and provides a measure of the transmission efficiency. Insertion loss is given for the conduction or on-state of the switch and is normally specified by the S-parameter coefficient *S21* in decibels. Efficient on-state switch transmission requires small insertion losses. Also specified by the S-parameter transmission coefficient *S21* is switch isolation. Isolation is defined for the non-conduction or off-state and represents the coupling between the input and output points. A high level of isolation is necessary to block RF energy from propagating through the switch when it should be off. The contrast between insertion loss and isolation provides a quick measure of the quality of the switch. Switches with high contrast function more like ideal switches than lower contrast switches. Switch bandwidth can also be considered an impedance property because the available bandwidth is often limited predominantly by device resistances and reactances.

3.2.1 Mechanical Switches

Due to their large size conventional mechanical switches are not practical for reconfigurable antenna applications. However, they have been used extensively in high power RF applications. Mechanical switching is normally accomplished by breaking the conducting path of a transmission line within the switch. The electrical performance of mechanical switches are often much better than those of solid state switches. Insertion losses of less than 0.1 dB and isolations of over 70 dB are common [51]. The excellent matching characteristics and high power handling capabilities make them the only suitable alternative for many applications such as broadcast systems. Next to their large size however, the other major drawback of mechanical RF switches is long transition times associated with mechanically actuating a switch. The moving switch components parts have a mechanical resonant frequency that naturally limit the speed at which the switch can change states. Typical switching speeds for mechanical switches are on the order of 2 ms [51].

3.2.2 PIN Diode Switches

The PIN diode switch is a popular in microwave circuit applications due to its fast switching times and relatively high current handling capabilities. Conventional electromechanical RF switches are inherently speed limited devices due to inertial and contact potential effects. The PIN diode can operate at speeds orders of magnitude faster than mechanical switches and can be placed in packaging measuring a fraction the size of mechanical RF switches. The PIN diode along with other solid state switches utilize a semiconductor junction as the RF control element which accounts for the increase in switch speed and reduction in package size. Switching speeds of less than 100 ns are typical. An important quality for RF applications is the fact that it can behave as an almost pure resistance at RF frequencies. This resistance may be varied over a range of approximately 1 Ωto 10 kΩby biasing with a dc or low frequency current [52]. The bias current required for on state operation is normally on the order 10 mA.

Construction of the P-I-N diode consists of two semiconductor regions–a p-type and a n-type–separated by a resistive intrinsic region. The presence of this resistive intrinsic layer distinguishes it from a normal pn diode and is responsible for its unique properties [53]. Forward biasing the diode introduces electron-hole pairs into the I-intrinsic region. These charge pairs reduce the resistance of the region because they have a finite lifetime and do not recombine immediately. The charge density of the intrinsic region along with its geometry determine the diode conductance. The conductance is proportional to the stored charge, Q_d, which is related to the dc bias current, I_d by

$$Q_d = \tau I_d \tag{3.1}$$

where τ is the carrier lifetime. The resistance of the I region is then expressed as

$$R_s = \frac{W^2}{(\mu_N + \mu_P)Q_d} \tag{3.2}$$

where W is the intrinsic region width, μ_N is the electron mobility and μ_P is the hole mobility. Combining equations (3.1) and (3.2) leaves an expression for device resistance based on bias current

$$R_s = \frac{W^2}{(\mu_N + \mu_P)\tau I_d}. \tag{3.3}$$

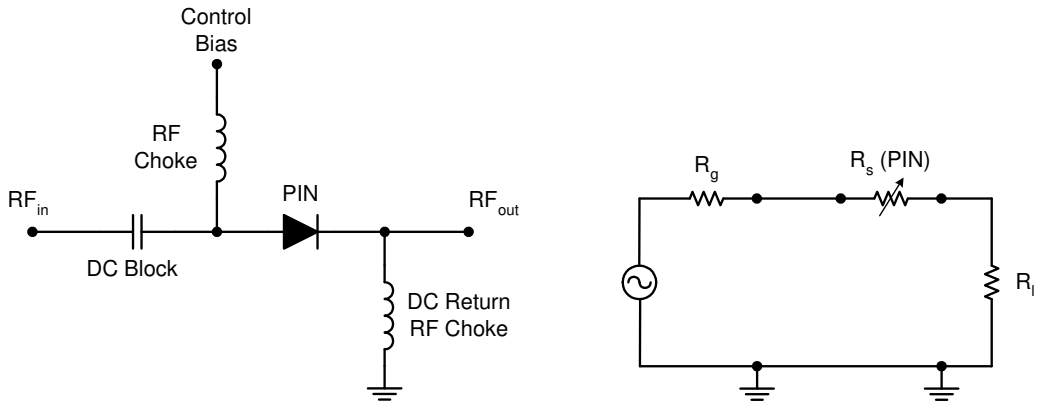

(a) PIN diode switch circuit

(b) Ideal equivalent RF circuit representation

Figure 3.3 Series PIN diode RF switch model.

The low frequency limit of useful application is determined by the carrier lifetime [52]. At frequencies lower than $f_0 = 1/2\pi\tau$ the RF signal modulates the stored charge just as the DC bias thus causing the PIN diode to behave as a normal *pn* diode [53].

When used in an RF circuit application having a system characteristic impedance, Z_o, the switch transfer functions for the circuit descriptions of Figures 3.3 and 3.4 are given by [52]

$$\left|S_{21}\right|^{-1}_{series} = 20\log_{10}\left[1 + \frac{R_{diode}}{2Z_o}\right] \tag{3.4}$$

$$\left|S_{21}\right|^{-1}_{shunt} = 20\log_{10}\left[1 + \frac{Z_o}{2R_{diode}}\right] \tag{3.5}$$

Need plot of the isolation and loss for typical PIN diodes that ties together all these equations.

3.2.3 Field Effect Transistor Switches

Before the emergence and common application of gallium arsenide field effect transistors (GaAs FET) as microwave switches in the mid 1980s, the PIN diode was primarily the only high speed alternative available. However, advances in semiconductor processing techniques and design innovations have moved GaAs FETS as well as other

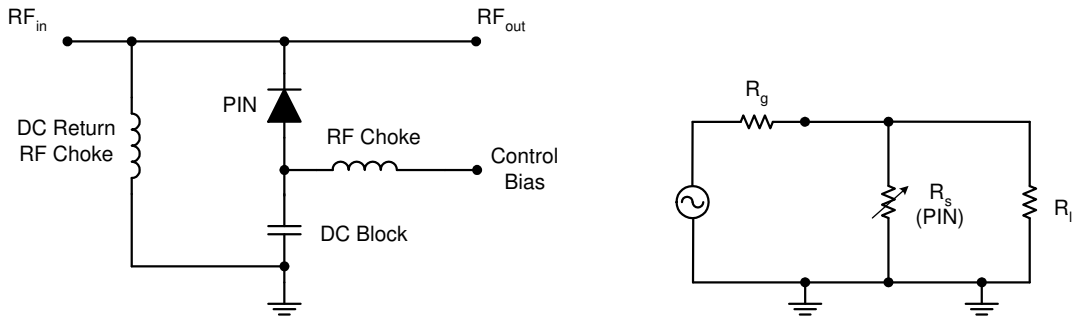

(a) PIN diode switch circuit

(b) Ideal equivalent RF circuit representation

Figure 3.4 Shunt PIN diode RF switch model.

microwave monolithic integrated circuit (MMIC) transistors into popular use for RF switch applications. The first use of FETs as microwave switches was reported by Liechti in 1976 [54].

FET switches possess a number of characteristics that make them more attractive than PIN diode switches. First, control biasing is isolated from the RF signal path. Thus, only minimal choke separation is required to ensure no dc leaks into the RF signal. Second, the biasing power requirements are much lower for FET switches than for PIN diodes. Gaspari reports [55] the possibility of zero dc power dissipation in biasing the switch. Typically however, the gate bias current is less than 10 μA. The third key advantage of FETs over PIN diode switches is switching speed. Large electron mobility and drift velocity in GaAs devices translates directly to very fast operating switches. FETs can typically switch on the order of a few nanoseconds while PIN diodes are normally limited to a hundred nanoseconds. This combination of lower power draw and fast switching speed makes the FET switch tends to have much faster switching speeds and much lower bias current requirements compared to a corresponding PIN diode switch.

Common FET switches are generally based on MOSFET or MESFET technology and like the PIN diode switch, the FET switch is a three terminal device. Figures 3.5(a) and 3.4(a) show typical FET switch configurations for both series and shunt orientations. The bias voltage at the FET gate terminal provides the switch control.

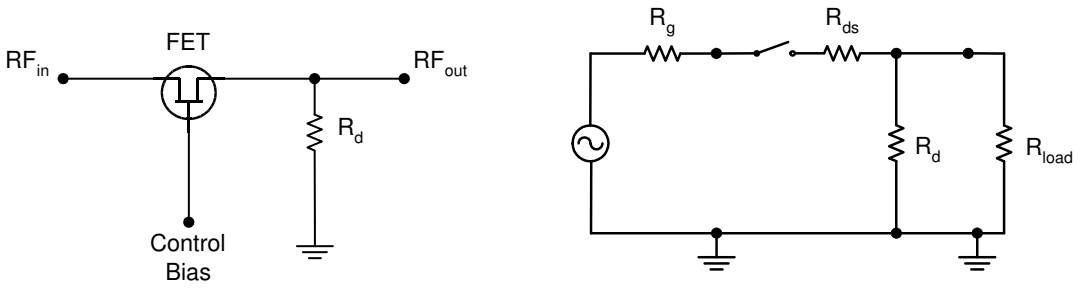

(a) FET switch circuit

(b) Ideal equivalent RF circuit representation

Figure 3.5 Series field effect transistor RF switch model.

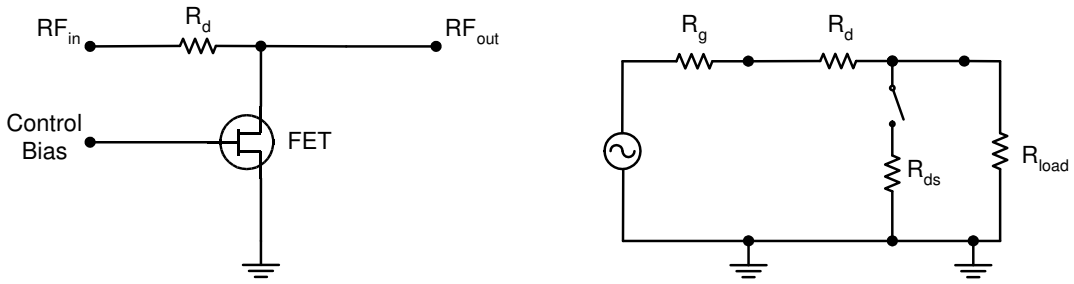

(a) FET switch circuit

(b) Ideal equivalent RF circuit representation

Figure 3.6 Shunt field effect transistor RF switch model.

Switching the gate voltage between zero and greater than the device pinch-off voltage toggles the switch between its on and off states. RF FET switches tend to operate over a broader bandwidth than PIN diode switches but the associated insertions losses for FET switches are comparatively higher than PIN diode implementations. FET switch tend to suffer from increased insertion losses at frequencies over 1 GHz and reduced isolation in the off state. Typically 1-2 dB of insertion loss and 20 to 25 dB of isolation in the off state is seen at these higher frequencies.

3.2.4 MEMS Switches

As previously described, conventional PIN diode and FET switches have seen limited use in RF and microwave antenna design. However, specific disadvantages make them unsuitable for reconfigurable antenna design where a large number of switches may employed and individual device losses have a cumulative impact on overall antenna performance. Device deficiencies including narrow bandwidth, comparatively low isolation and high insertion loss, and finite power consumption make them unattractive for use in many reconfigurable applications. Additionally, the non-linear nature of solid-state semiconductor switches always has the potential to introduce undesirable inter-modulation products into the RF signal path. RF microelectromechanical systems (MEMS) have moved the forefront of reconfigurable antenna design because of their potential to overcome the limitations imposed by conventional RF switches. RF MEMS switches have been shown to exhibit excellent and consistent switching characteristics over an extremely wide range of operational frequencies. Additionally, their large isolation and low insertion loss characteristics result in a switch that is very close to an ideal switch for RF applications. This switch contrast ratio coupled with very low actuation power consumption, small feature size and extremely wide bandwidth makes MEMS switches ideally suited to reconfigurable antenna applications.

MEMS are microscopic electronic devices fabricated using existing semiconductor process technologies that typically include a mechanical moving component. Surface micromachining has been the most important fabrication method for MEMS but other processes such as bulk micromachining, fusion bonding and LIGA (lithography, electroplating and molding) are frequently used [56]. Surface micromachining can be viewed as a three dimensional lithographic process and involves depositing various patterns of thin films on a substrate. Free-standing or suspended structures are created by applying patterns of sacrificial film layers below non-sacrificial or 'release' layers [57]. Selective etching of the sacrificial layers then leaves a suspended film which is capable of mechanical actuation.

Active MEMS devices can function as variable capacitors, resistors and inductors; filters; resonators and switches. However, for reconfigurable antenna applications, the MEMS RF switch is the most important MEMS device. As with other RF switch tech-

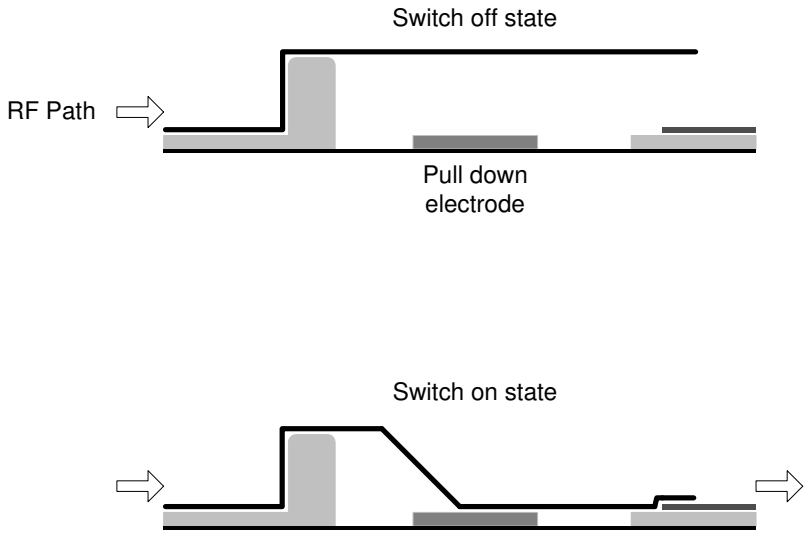

Figure 3.7 Cantilever style RF MEMS series switch layout in both on and off states.

nologies, RF MEMS switches normally are designed in either series or shunt topologies. Shunt switches are commonly used with coplanar waveguide structures and function by shorting the RF signal path to the coplanar ground lines. A movable MEMS shunting bridge is placed between the ground lines and suspended above the signal trace. Activating the switch pulls the shorting bridge down and it into contact with the signal line which shorts the RF signal path [58].

Series MEMS switches are favorable for use in microstrip topologies and one configuration is illustrated in Figure 3.7. This is the so-called cantilever switch because the moving part is suspended above the microstrip transmission line like a cantilever beam. In the absence of a control voltage, the beam remains suspended above the microstrip transmission line and the switch is in the off state. When a control voltage is applied to the pull-down electrode, the cantilever beam is brought into contact with the microstrip line and completes the transmission path. The switch is then in the on state and acts as a continuous microstrip transmission line. The off state isolation the simple dc-contact series MEMS switch is can be derived from its transmission coefficients and is given by [59]

$$S_{21} = \frac{2j\omega C_u Z_0}{1 + 2j\omega C_u Z_0} \tag{3.6}$$

where C_u is the up state (off) capacitance of the switch and Z_0 is the characteristic

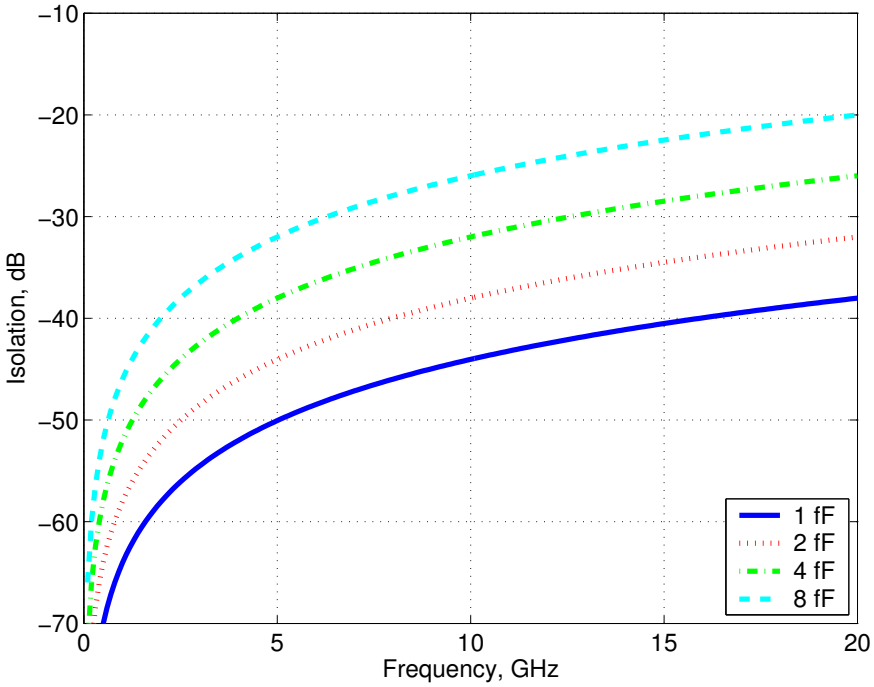

Figure 3.8 Isolation versus on state capacitance for a typical dc-contact MEMS series switch given from (3.6) calculated using MATLAB.

impedance of the transmission line. The up state capacitance is a result of two mechanisms: the coupling between the open ends of the transmission line and the coupling between the cantilever beam and the transmission line. There is only a small inductive term due the short length of switch and can be neglected [59]. Thus the isolation becomes a dependent only on the up state capacitance. This capacitance is typically very small and results in quite high isolation values even at high frequencies. Figure 3.8 compares switch isolations for realistic values of C_u.

When the device is in the down position (on state) the insertion loss is dominated by the contact resistance of the switch, R_s. This term represents the resistance between the switch beam and the transmission line. R_s is a function of switch contact area, the amount of force applied to hold the switch down and the metal contact quality [60]. The transmission coefficient expression for the switch reduces to

$$S_{21} = 1 - \frac{R_s}{2Z_0} \tag{3.7}$$

where the contact resistance of the switch and is typically less than 1 Ω. This yields

on state insertion losses of less than 0.1 dB [61, 62]. The performance of dc-contact series switches is very close to an ideal RF switch over a very large bandwidth.

The advantages that MEMS switches offer over current PIN diode or FET RF switches are as follow:

Wide Bandwidth Similar to conventional mechanical switches, the bandwidth of RF MEMS switches is quite large. Unlike solid state which rely on a semiconductor junction, the conduction path is based on metal to metal contact. The upper limit on frequency of operation is normally restricted by reduced device isolation in the off state. RF MEMS switches have been reported to operate with high reliability from dc to 110 GHz [63].

High Isolation The attenuation between input and output ports of the switch when in the *off* state is isolation. The small switch contact area and air gap filling of metal contact switches produces very little electromagnetic coupling between switch points while in the off state. Consequently, the off state capacitance of MEMS switches are in the femto-farad range. DC-contact switches operating at less than 60 GHz can achieve isolations of 50-60 dB while higher frequency capacitive switches produce acceptable isolation up to 100 GHz [64].

Low Insertion Loss The attenuation between input and output ports of the switch when in the *on* state is insertion loss. Small on state capacitances and very low contact resistance facilitate very low insertion loss characteristics for MEMS switches. Insertion losses of less than 0.1 dB can be achieved for switches up to 40 GHz [61, 65].

Low Power Consumption Many RF MEMS switches are actuated using electrostatic mechanisms which consume almost no power and offers several critical advantages. The first and most obvious result is that total system power is minimized which is critical for portable applications. The second result of very low power consumption is one of potentially greater significance. One of the primary concerns in designing highly integrated reconfigurable antennas is to what degree do the dc bias and control lines

effect the performance of the RF structure by coupling from the RF portions of the antenna to the bias sections. Because almost no power is required to bias the switch, control lines may be created with high impedance materials and thus provide poor conduction paths for RF energy. This fact can be used to minimize and or eliminate any antenna performance degradation from the bias section.

Linearity The quality of the signal passed through the switch is measured by its linearity. Switches which pass signals without distortion or the introduction of harmonics are said to be highly linear. The linearity of MEMS switches can be as much as 50 dB better than that of solid-state switches. This results in very low intermodulation products in switching operations [64].

There are also critical disadvantages of RF MEMS switches compared to PIN diodes and FET switches. Though none are considered insurmountable, it is necessary to identify the characteristics of MEMS switches that could potentially cause problems for reconfigurable antenna applications.

Slow Switching Speed Switching speed is one aspect where MEMS switches lag behind PIN diode and FET switches in performance significantly. Because MEMS are inherently mechanical in nature they are subject to inertial forces and bound by structural resonant frequencies. The fastest electrostatic topologies switch in 2-40 μs whereas PIN diode switches can operate in the nanosecond range [51].

Low Power Handling One of the biggest limitations that MEMS switches currently face is power handling capability–most cannot reliably handle more than 200-500 mW of power [66]. This number however, has increased by a factor of ten in just two years and current research is targeted at improving the power capabilities [67].

High Actuation Voltage Typical dc-contact MEMS switches require 20-80 V for electrostatic actuation [68]. This can present a problem for portable devices where high voltage signals may not be readily available and up-converters would be needed to provide adequate switching potential. Low voltage switches are being developed to

help mitigate this problem and devices have been produced which require as little as 6 V [69].

Low Reliability Reliability considerations have been another major stumbling block for widespread use of MEMS switches. Current designs have demonstrated only 40 billion switching cycles [64]. While this may appear to be a very large number of switch toggles, many systems require switches capable of withstanding over 200 billion cycles.

Packaging Considerations MEMS switches are inherently moving devices and thus are susceptible to environmental contamination and physical contact. Special attention must be given to the protective packaging used to shield the components and hermetic sealing is an essential part of the package assembly. Packaging also has an impact on device size, performance and cost.

Table 3.1 provides a summary comparison for the RF switches identified for use in reconfigurable antenna designs.

Table 3.1 RF switch comparison summary

	Mechanical relay	PIN diode	FET	MEMS
Insertion loss at 1 GHz (dB)	0.25	0.5–1.0	0.5–1.0	< 0.1
Isolation at 1 GHz (dB)	70	20–40	40	> 40
Switching speed (s)	$2 \cdot 10^{-3}$	$650 \cdot 10^{-9}$	10^{-9}–10^{-8}	10^{-6}
Bandwidth (MHz)	dc–1200	20-2000	?	dc–100000
Actuation voltage (V)	100–200	3–5	5–50	3–30
Bias current (μA)	1–2	10^4	< 10	< 10

3.3 Switch Modeling for Reconfigurable Antenna Applications

This section presents the methods available for analyzing reconfigurable antennas that incorporate RF MEMS devices as switching elements. Modeling effort limitations leave two practical ways exist to model the MEMS switches using conventional field solvers: as non-ideal reactive switches or as ideal on/off switches. A brief overview of field solver capabilities is presented along with the two possible modeling methods. A simple reconfigurable dipole antenna is then simulated using both methods and the results are compared.

3.3.1 Antenna Field Simulators

The task of accurately modeling microwave circuits containing intricate MEMS components is critical for predicting antenna behavior. In the past 20 years, EM field simulators have become the most common type of tool for designing and simulating antennas. A wide variety of field solver techniques exist including moment method (MoM), finite element method (FEM), finite difference time domain (FDTD), finite integration technique (FIT) and transmission line modeling (TLM). Though the specific details of each approach are different, all field solvers solve Maxwell's equations to determine the antenna's electrical properties. Fundamentally, field solvers take a microscopic approach to calculating the antenna design problem and work by subdividing the problem space into smaller pieces referred to as cells. Cell size is typically based on many conditions and is highly dependent on the particular solver formulation used, but in all cases, the guided wavelength is critical. Several other cell discretization parameters include direction of field propagation, material properties, and geometrical discontinuities. Consequently, the numerical size of the total field problem is directly related to the resolution of the geometry discretization. Field solvers are an excellent choice for antenna design because it is possible to include all electromagnetic effects from first principles without having to include compensation terms which are often required in circuit theory or other model approximations methods.

The small feature size of RF MEMS devices compared to typical operating wavelengths presents an immediate problem for normal field solvers. Most solvers require a minimum number of cells per geometric feature to converge with at the correct solution. Proper discretization of the MEMS device in the presence of the entire antenna geometry forces a prohibitively large number of unknowns. It is often impractical to model both the MEMS device and the antenna in the same simulation. As a result, the approach that is taken to model the reconfigurable antenna must be modified. From the field simulator standpoint there is a clear tradeoff between modeling accuracy and modeling effort. Modeling effort encompasses both the amount of time required to define the the problem and the amount of time required to numerically find the solution. Ideally the modeling effort should be minimized while the modeling accuracy is maximized.

3.3.1.1 IE3D Solution Formulation

The commercial moment method package IE3D [14] is the primary simulation tool used in this dissertation for studying reconfigurable antennas. As with any package, care must be taken to ensure that the computed models reflect the actual behavior of the antenna. IE3D is a full-wave, frequency-domain simulation package that utilizes a laterally-open moment method engine capable of simulating arbitrary metalization geometries. Its primary formulation is an integral equation obtained through the use of Green's functions. Both the electric current on metallic structures and the magnetic current representing field distributions on metallic apertures can be modeled.

The solution to a general electromagnetic scattering problem, assuming a conducting structure S in a dielectric environment, requires finding resulting current $\mathbf{J}(\mathbf{r})$ on S, induced by the incident field $\mathbf{E_i}(\mathbf{r})$. The induced field will create a secondary field to satisfy the boundary conditions on the surface. The induced field is distributed on the conducting surface and the boundary condition is given from [14]

$$\mathbf{E}(\mathbf{r}) = Z_s(\mathbf{r})\mathbf{J}(\mathbf{r}), \tag{3.8}$$

where $\mathbf{r} \in S$, $\mathbf{E}(\mathbf{r})$ is the total tangential field on S, $\mathbf{J}(\mathbf{r})$ is the current distribution on S, and $Z_s(\mathbf{r})$ is the surface impedance of the conductor.

IE3D uses a mixed potential integral equation (MPIE) based solution formulation. Thus it retains all vector and scalar components of the Green's function in all calculations. This allows the placement of metal in arbitrary directions. The solver itself, however, is referred to as a 2.5 dimension solver–while the field solutions depend on three spatial dimensions, the sources are confined to planes with only two spatial dimensions and dielectrics must be layered and homogeneous. This results in a simplification of the problem space but comes at expense of problem generality. The resulting Green's function formulation for 2.5D codes requires dielectrics to be infinite in lateral extent but of arbitrary height or thickness. This formulation makes 2.5D solvers particularly suited for planar geometries such as microstrip and multi-layer structures. When the structure is in a layered dielectric, the total field can be then written as [14]

$$\mathbf{E}(\mathbf{r}) = \mathbf{E}_i(\mathbf{r}) + \int_S \mathbf{G}(\mathbf{r}|\mathbf{r}') \cdot \mathbf{J}(\mathbf{r}')ds, \tag{3.9}$$

where $\mathbf{G}(\mathbf{r}|\mathbf{r}')$ is the dyadic Green's function for the dielectric environment and $\mathbf{E}_i(\mathbf{r})$ is the incident field on the conducting surface. Replacing Equation (3.8) into Equation (3.9) gives the integral equation

$$Z_s(\mathbf{r})\mathbf{J}(\mathbf{r}) = \mathbf{E}_i(\mathbf{r}) + \int_S \mathbf{G}(\mathbf{r}|\mathbf{r}') \cdot \mathbf{J}(\mathbf{r}')ds. \tag{3.10}$$

The incident field, $\mathbf{E}_i(\mathbf{r})$, and the surface impedance are specified from the problem and the Green's function is derived from the solver setup. The unknown to be solved for is the current distribution, $\mathbf{J}(\mathbf{r})$.

It is assumed that the current distribution can be represented by a complete set of known basis functions

$$\mathbf{J}(\mathbf{r}) = \sum_{n=1}^{\infty} I_n \mathbf{B}_n(\mathbf{r}), \tag{3.11}$$

where the I_n terms represent the unknown expansion coefficients. Substituting Equation (3.11) into Equation (3.10) gives

$$Z_s(\mathbf{r}) \sum_{n=1}^{\infty} I_n \mathbf{B}_n(\mathbf{r}) = \mathbf{E}_i(\mathbf{r}) + \sum_{n=1}^{\infty} I_n \int_S \mathbf{G}(\mathbf{r}|\mathbf{r}') \cdot \mathbf{B}_n(\mathbf{r})ds'. \tag{3.12}$$

Equation (3.12) can be converted into matrix form by the Galerkin's method as [14]

$$S_m \int_S ds \mathbf{E}_i(\mathbf{r}) \cdot \mathbf{B}_n(\mathbf{r}) = S_m S_n I_n \left\{ \int_S ds Z_s(\mathbf{r}) \mathbf{B}_m(\mathbf{r}) \cdot \mathbf{B}_n(\mathbf{r}) + \int_S ds \int_S ds' \mathbf{B}_m(\mathbf{r}) \cdot \mathbf{G}(\mathbf{r}|\mathbf{r}') \cdot \mathbf{B}_n(\mathbf{r}') \right\} \tag{3.13}$$

This formulation Equation (3.13) enforces Equation (3.12) with a complete set of testing functions that are the same as the basis functions. The formulation of a complete set of basis functions for Equation (3.13) necessarily requires an infinite number of terms and must be truncated in order to calculate. The truncation of a continuous equation involves a mathematical projection of the solution onto finite-dimensional subspaces. These subspaces are defined by the basis and testing functions. For antenna purposes, it is convenient to represent this projection as the familiar Kirchoff's network formulation given by [7]

$$\sum_{n=1}^{N} Z_{mn} I_m = V_m, \qquad m = 1, 2, \ldots, N \tag{3.14}$$

where

$$Z_{mn} = \int_S ds Z_s(\mathbf{r}) \mathbf{B}_m(\mathbf{r}) \cdot \mathbf{B}_n(\mathbf{r}) + \int_S ds \int_S ds' \mathbf{B}_m(\mathbf{r}) \cdot \mathbf{G}(\mathbf{r}|\mathbf{r}') \cdot \mathbf{B}_n(\mathbf{r}') \tag{3.15}$$

and

$$V_m = \int_S ds \mathbf{E}_i(\mathbf{r}) \cdot \mathbf{B}_n(\mathbf{r}). \tag{3.16}$$

Equation (3.14) is often written in the compact formulation

$$[Z_{mn}][I_m] = [V_m], \tag{3.17}$$

where the matrices $[Z_{mn}]$, $[I_m]$, and $[V_m]$ are referred to as generalized impedance, current and voltage matrices, respectively [7]. The solution of Equation (3.14) gives the current distribution for the structure. With the current distribution solved, it is a relatively simple matter to calculate the S-parameters, radiation patterns and other quantities for the structure.

Accurate convergence of the numerical approximation in Equation (3.14) requires that the major components of the actual solution be within the finite dimensions of the approximation. The discretization of the problem geometry into a mesh structure dictates the basis functions. IE3D implements a triangular and rectangular mixed meshing scheme to form a non-uniform discretization mesh. The package discretizes the geometry to be simulated using its non-uniform mesh based on the specified number of cells per wavelength. The simulations performed in subsequent sections use a minimum of 15 cells per wavelength. This discretization value has been shown to give a good balance between high simulation accuracy and reasonable solution times.

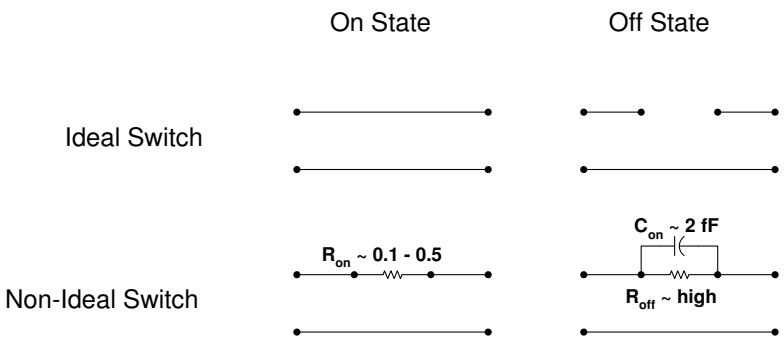

Figure 3.9 Comparison of ideal and non-ideal transmission line circuit model switches [59].

3.3.2 Modeling Methods

A considerable amount of effort and research has gone into accurately predicting the electrical behavior of RF MEMS switches [70, 71, 72]. One of the most compelling reasons for using MEMS in antenna applications is that they have shown to approximate, to a very good degree, ideal switches. This allows us to forego the nearly impossible task (at present) of a complete field simulation of an entire antenna structure including all the minute details of the MEMS switches. Thus, reconfigurable antenna modeling can be performed using a less complex approach with simplified equivalent switch switches in place of the actual MEMS structures.

Two options are examined to model reconfigurable antennas in a simplified manner. The first approach taken is called the reactive switch model and treats the RF switch as a non-ideal component. Electrically the switch is modeled with lumped elements. The on-state consists of a small series resistance, R_{on}, in the switch transmission line path. R_{on} is the switch contact resistance and is normally between 0.1 and 0.5 Ω. The specific value chosen for R_{on} depends on the actual switch to be used. The off-state is modeled as a large series resistance, R_{off}, in parallel with a small capacitance, C_{off}. The off-state capacitance is generally quite small (1-2 fF) and is describe in more detail in Section 3.2.4. Incorporating the reactive switch model can be rather cumbersome if large numbers of switches are to be used. Placing a discrete component within the model requires the insertion of a port at the physical switch location in

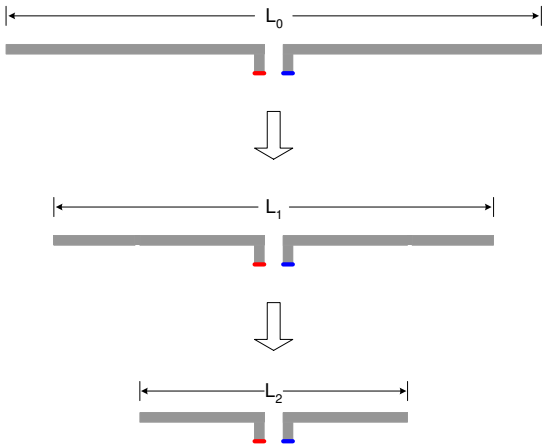

(a) Multiple frequencies of interest normally requires multiple elements

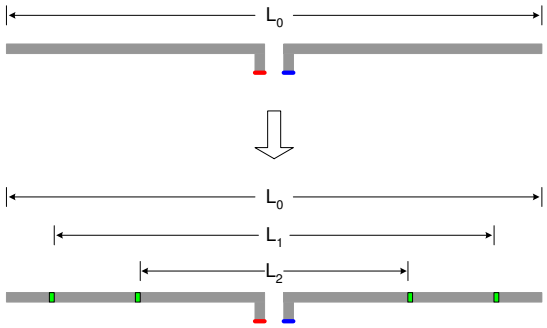

(b) Dipole with constructed with variable length arms via RF switches

Figure 3.10 Multi-band dipole antenna with three resonant lengths: L_0, L_1 and L_2.

the geometry definition. IE3D performs the field calculations based on the specified geometry and port details and upon completion, the S-parameter data for the structure is available. The task of adding the switch properties now becomes solving a circuit based model. The switch electrical properties are added to the S-parameter data and the final solution to the problem is obtained after post-processing is complete.

This model takes into account the well understood behavior of the reactive properties of MEMS switches [59]. The second approach will model the MEMS switches as ideal elements and will only include the reactive characteristics intrinsic to the discontinuities caused by the presence of the switch itself. Figure 3.9 depicts the two models in terms of equivalent transmission lines.

3.3.3 Switch Simulation Method Comparison

The antenna to be examined as a case study is the canonical multi-band dipole. This antenna is attractive for many applications where it is desirable to have a single antenna that can be dynamically reconfigured to operate on multiple frequency bands. Essentially it is a dipole with variable length arms and thus has a modifiable center frequency. It consists of a linear array of sub-elements connected together via RF

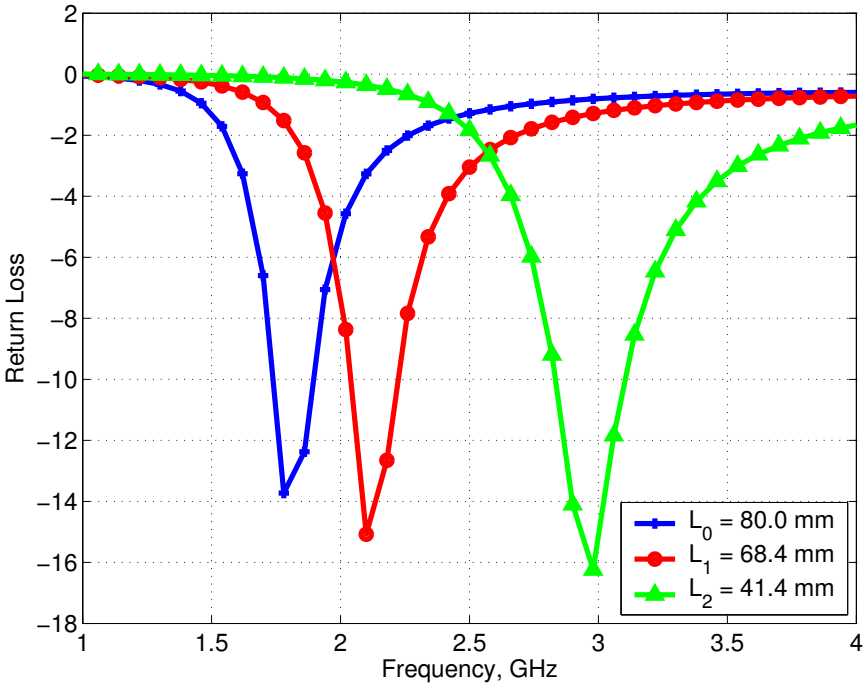

Figure 3.11 Return loss as a function of frequency for dipole antennas of Figure 3.10 with arm lengths of 80.0 mm, 68.4 mm and 41.4 mm simulated using IE3D.

switches. The resulting antenna behaves like a dipole with its arm length determined by the number of switches in the on-state. The desired frequency of operation determines the number of elements to switch together. Figure 3.10(a) illustrates the concept of the multi-band dipole. The single antenna reconfigurable version is shown in Figure 3.10(b). The antenna examined has arm lengths of 80 mm, 68.4 mm and 41.4 mm which correspond to resonant frequencies of 1.8 GHz, 2.1 GHz and 3.0 GHz. As a reference example, Figure 3.11 shows the calculated return losses for three separate dipoles of these lengths and how the bandwidths of each element overlap.

The geometries of the reconfigurable dipoles to be simulated with IE3D are shown in Figure 3.12. Figure 3.12(a) shows the dipole geometry with ideal switches and Figure 3.12(b) shows the geometry with the non-ideal reactive switches. The geometries of the two models are the same except for the switch definitions. Both models are printed dipole elements with major arm length, $L_0 = 80$ mm. The higher frequency dipole element lengths are 68 and 41 mm and the conductor strip width is 1 mm. The antennas are center fed with differential ports. The differential feed port consists

of a parallel wire transmission line 1.5 mm in length. The ideal switch model in Figure 3.12(a) uses removable metal patches to simulate the MEMS switches. A patch length of 0.3 mm is used and is representative of typical MEMS switch dimensions. To place a switch in the off state, the patch is deleted from the geometry, leaving a gap of 0.3 mm along the length of the arm. Figure 3.12(b) shows the dipole with non-ideal reactive switches. The antenna dimensions are the same as those of the ideal-model. IE3D has several schemes available for defining ports and port selection is dependent on the particular geometry of interest [14]. The *vertical localized* port scheme was chosen here due to the switch geometries. A vertical localized port is placed at each edge of the switch antenna junctions instead of metal patches to represent the MEMS switches. Each switch is represented by a pair of ports. Consequently, the model requires a total of eight ports to properly simulate the four switches.

The calculated return loss for the two switch modeling methods are compared in Figure 3.13. The three switch states corresponding to the three resonant lengths are shown for both methods. When the antennas are operating in the lowest frequency state, all six switches are in the on state and the effective dipole length is 80 mm. Operation in the middle frequency band requires the distal set of switches to be in the off or open position and the proximal switches to be in the on position. This results in an effective antenna length of 68 mm. The highest frequency band corresponding to a dipole length of 41 mm has all switches in the off position. The return loss figures show very close agreement between the two methods. There is almost no noticeable difference in the plots for the two lower frequency bands. For the high frequency configuration, there is a slight shift upwards in the resonant frequency for the non-ideal case. The results from this study show that modeling the MEMS switches as ideal components yields results very close to those of the non-ideal model. The additional effort required to describe the reactive components does not greatly impact the end result primarily because the MEMS switches do behave very much as if they were ideal switches.

Figure 3.14 summarizes the methods available for simulating reconfigurable in the presence of RF switches. The complete model which performs a full electromagnetics analysis on both the antenna structure and the RF switch structure is currently considered impractical due to the large problem size required to model the switches. This

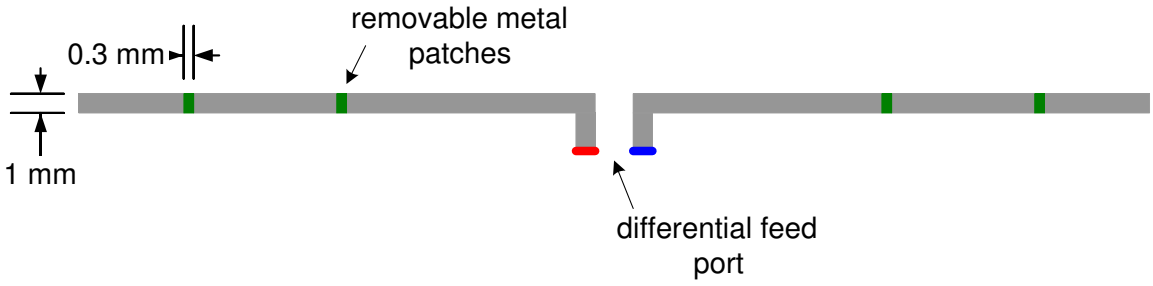

(a) ideal switches modeled with removable metal patches

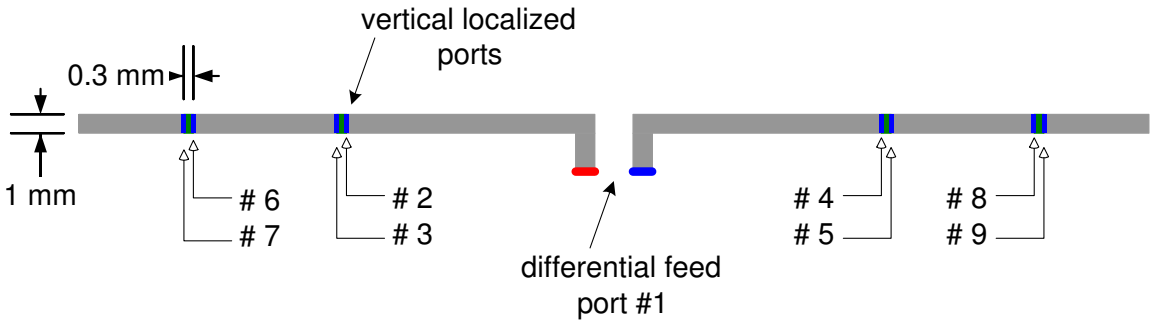

(b) non-ideal reactive switches modeled with multiple ports

Figure 3.12 IE3D models for the reconfigurable dipole including RF switches.

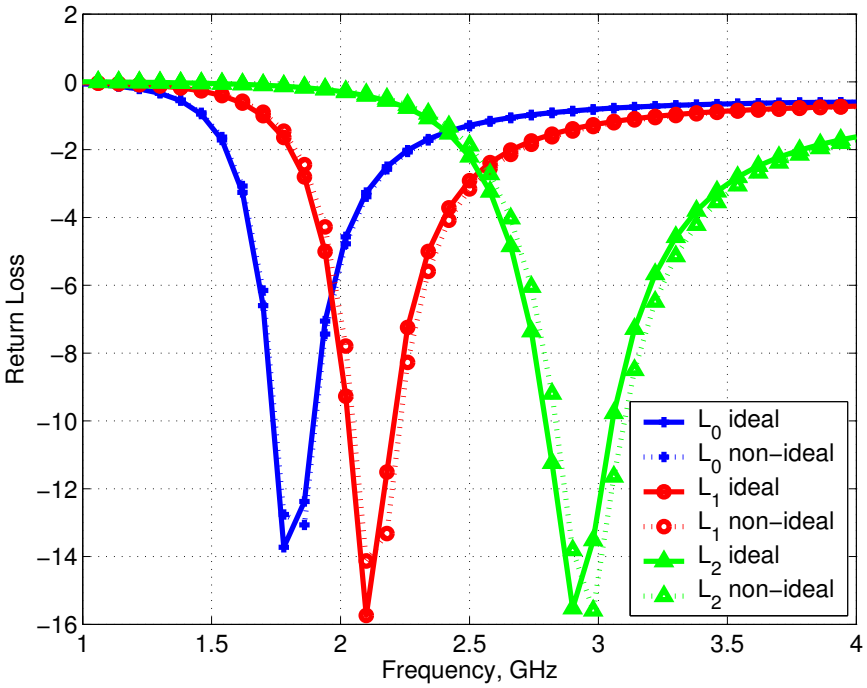

Figure 3.13 Computed return loss as a function of frequency for the frequency agile dipole antenna of Figure 3.12 simulated using IE3D. The ideal switch model is from Figure 3.12(a) and the non-ideal model is from Figure 3.12(b).

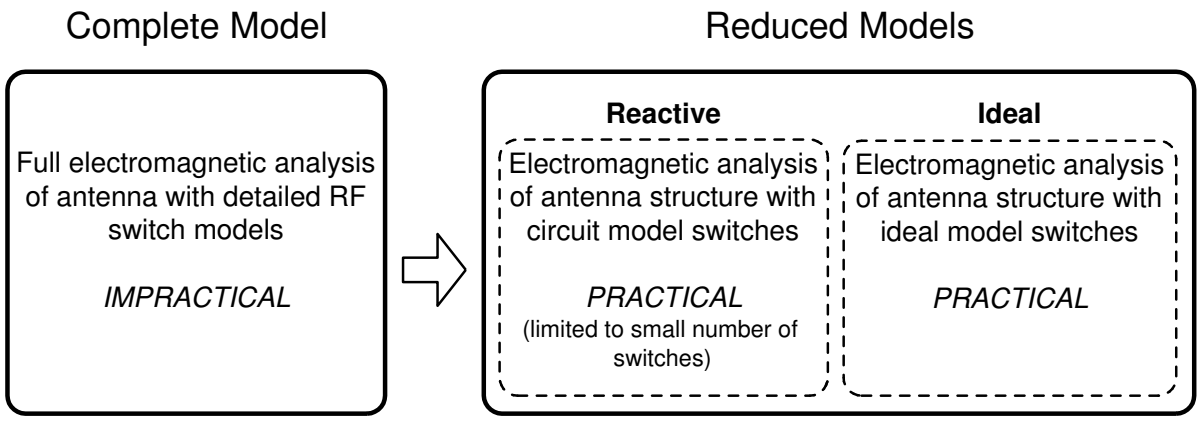

Figure 3.14 Reconfigurable antenna modeling comparison.

leaves the reduced models which represent the switches in a more manageable manner. The non-ideal model treats the switches as reactive elements requires additional port structures in the model. It also requires the additional step of post processing to include switch the effects within the model and is practical for reconfigurable antennas with only a small number of switches (less than 10). The ideal model is the only method currently practical for antennas with a relatively large number (greater than 10) of switches. There is no post processing needed to include the switch effects and toggling between switch states is performed simply by adding or removing metal patches.

Chapter 4

Analysis and Measurement of Reconfigurable Ring Patch

This chapter presents the design and analysis of the reconfigurable ring patch antenna. The newly developed reconfigurable ring patch patch antenna achieves an adjustable bandwidth of up to 15% while maintaining constant performance over the other electrical characteristics. The antenna structure is shown along with an explanation of its operation. Analysis of its bandwidth controllable behavior, computer simulations and measured results are also presented.

4.1 Introduction

The microstrip patch antenna has become one of the most commonly used antenna types in the last 20 years for a broad assortment of applications, including hand-held, automotive and aircraft applications. Its popularity is due to a number of factors: unobtrusive and low profile shape, rugged form factor, and low construction cost. In general, the microstrip patch antenna consists of a patch of metalization suspended over a grounded substrate. The substrate height is normally much less than the operational wavelength ($h < \lambda/20$) and is responsible for the very low-profile device form factor. The low-profile comes at the expense of bandwidth. The microstrip patch is a resonant antenna, and in its basic form has only a few percent bandwidth [7]. By increasing the

structure complexity, bandwidth can be increased considerably.

There is a wide array of geometric variations on the general microstrip patch antenna. The ring patch antenna is one variant of the conventional microstrip patch that has favorable radiation characteristics for a number of applications. Ring patches can be designed for both linear and circular polarization and typically have a single main beam in the broadside direction. During the investigation of the conventional ring patch antenna it was determined that the impedance bandwidth of the antenna could be altered by varying the width of the microstrip ring. These findings lead to the invention of the reconfigurable ring patch antenna with parasitic matching plate (RRPA). This antenna performs similar to the ring patch antenna but with the ability to control the bandwidth of operation. The new antenna is describe in detail in this chapter.

4.2 Antenna Structure

This section presents the reconfigurable ring patch antenna geometry. The geometry of the reconfigurable ring patch antenna is shown in Figure 4.1. It is a two layer, probe-fed, printed patch antenna designed to operate at a nominal center frequency of 2.5 GHz. The primary feature of the RRPA is the ring patch layer. The printed ring patch is similar to a solid microstrip patch except that a central portion of the metal is removed to create a ring. The ring layer located 1.575 mm above the ground plane and is situated on a substrate with a dielectric constant of 2.35. The ring layer is responsible for controlling the reconfigurable bandwidth of the antenna and will be detailed in Section 4.2.1. There is a second parasitic radiating structure above the ring layer which improves the impedance matching characteristics. It is a 47 mm long square patch located 4.9 mm above the ring layer. The parasitic patch is supported with a foam block to approximate the dielectric constant of air ($\epsilon_r \approx 1$). The antenna is fed via a standard through-hole probe feed located 11.5 mm from the center of the patch along the centerline. In order to operate properly the antenna must be placed over a ground plane.

The square annular ring patch operates similar to the annular ring microstrip

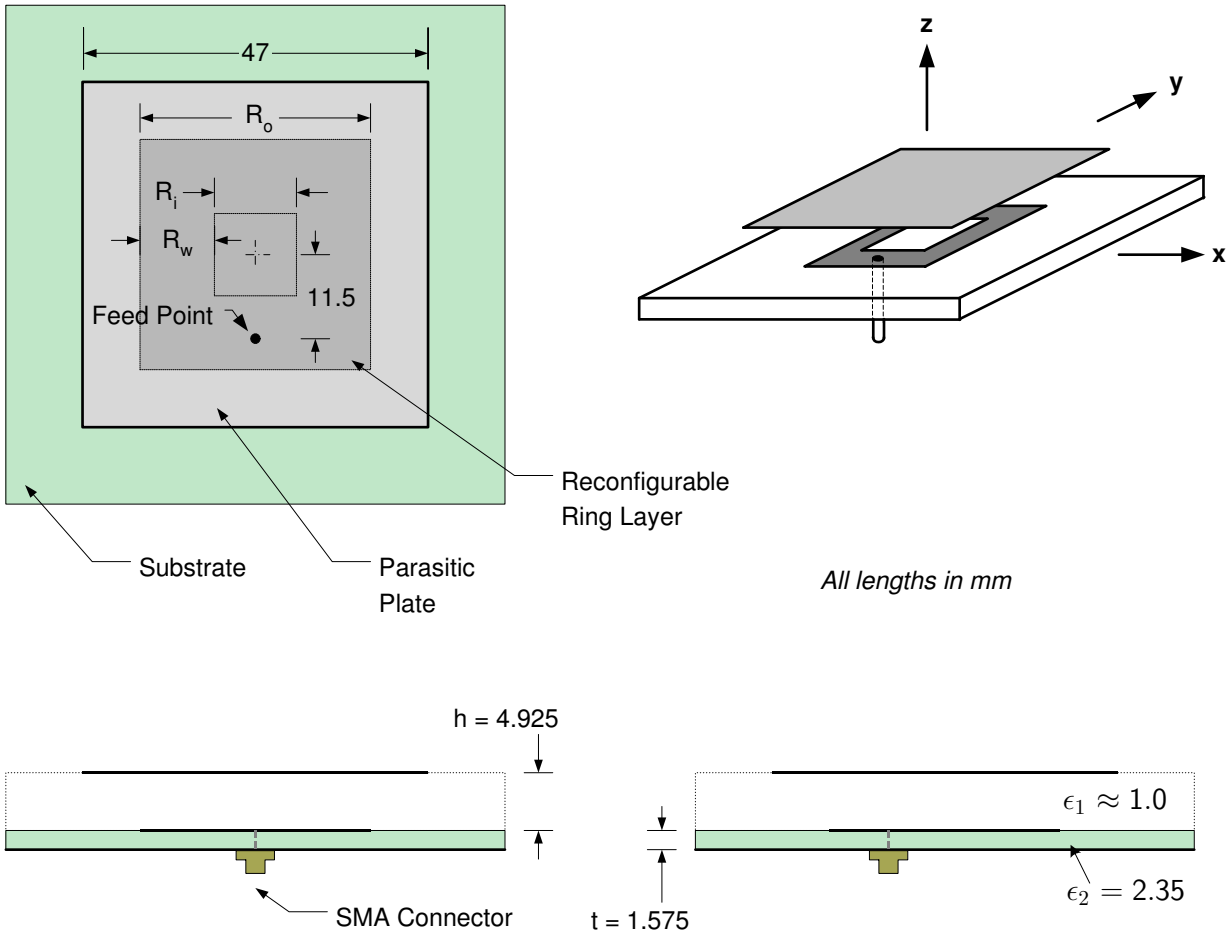

Figure 4.1 Geometry of the reconfigurable ring patch antenna that operates at 2.5 GHz, units are in mm.

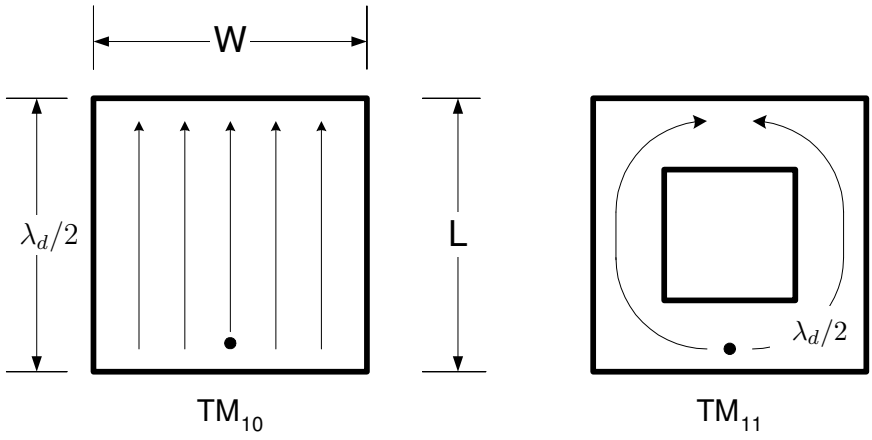

(a) rectangular (square) patch (b) square ring patch

Figure 4.2 Difference in current path length for rectangular patch and square ring patch. The guided wavelength is $\lambda_d = \lambda/\sqrt{\epsilon_r}$, where ϵ_r is the dielectric constant of the substrate.

patch antenna [73, 8] shown in Figure 4.2(b). The ring patch behaves electrically as an intermediate between a ground plane backed loop and a solid microstrip patch shown in Figure 4.2. The square ring patch evolved from the ring patch when Mink [74] found that the resonant frequency of a conventional patch could be reduced considerably by removing a portion of metal from the center of the patch turning it into an annular structure. The dominant modes for the rectangular MSA and the rectangular ring are shown in Figure 4.2. It can be seen from Figure 4.2 that for equal sized patch antennas, the ring structure forces the current to take a longer path and decreases the frequency of operation. The average path length traveled by the current in the square ring is longer than that of the square ring.

Similar to the rectangular microstrip patch, the ring patch can be viewed as radiating via equivalent magnetic currents caused by fringing electric fields present at the patch edges. These fringing fields act as radiating slots and, through equivalence, can be viewed as magnetic currents. Ring resonators tend to excite TM_{mn} modes with the TM_{1n} $(n = 2, 4, \dots)$ being suitable for antenna applications due to favorable efficiency and bandwidth characteristics [75]. Polarity of the magnetic current can be determined from the fringing fields at the edge of the patch. Figure 4.3 shows that the

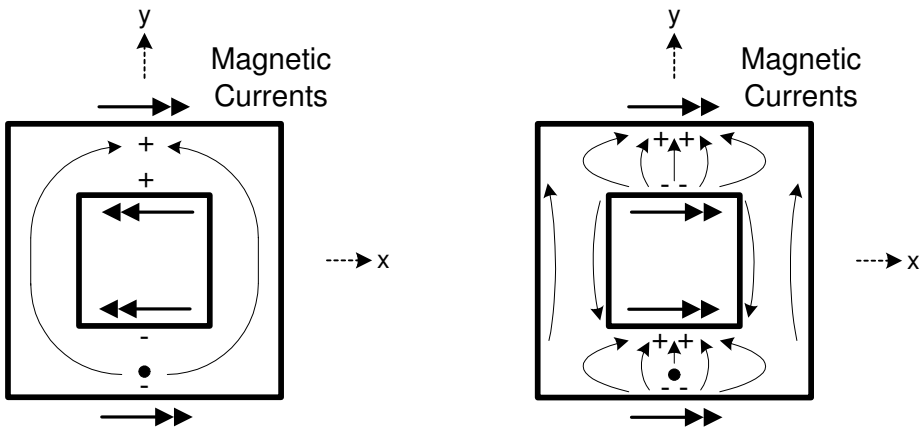

(a) TM_{11} (b) TM_{12}

Figure 4.3 Equivalent magnetic currents for TM_{11} and TM_{12} modes on the square ring patch.

TM_{11} mode has opposing direction magnetic currents on the inner and outer edge of the ring while the TM_{12} mode has magnetic currents with the same polarity. When the equivalent magnetic sources are of the same polarity, they interfere constructively and are suitable for radiation.

Antenna impedance bandwidth of the square ring is determined primarily by the width of the square ring, R_w. R_w is the width of the patch metalization measured along the x-axis and is defined by

$$R_w = \frac{R_o - R_i}{2} \tag{4.1}$$

where R_o is the outer ring dimension and R_i is the inner dimension as shown in Figure 4.1. The separation of adjacent antenna modes is determined by the ring width. The outer ring dimension R_o limits the lower end of the operational frequency while the inner dimension, R_i, controls the upper end. When the ring width is small ($R_w < \lambda_g/10$ where λ_g is the guided wavelength defined by $\lambda_g = \lambda_0/\sqrt{\epsilon_r}$), the modes are closely spaced and the antenna operates with effectively one radiation mode. However, as the ring width increases the single TM_{12} mode spreads into two degenerate TM modes.

An investigation was conducted using IE3D to determine the usable limits of

on ring width, R_W. The ring dimensions were studied for the ring patch antenna with solid, continuously varying ring widths in the patch layer. The results obtained from this investigation are used in the subsequent sections to develop the discrete ring states for the reconfigurable ring patch antenna geometry. The inner and outer ring dimensions (R_o and R_i) were varied together and all antenna geometry parameters were held constant to explore the effect of ring width on antenna impedance bandwidth. Figure 4.4 shows the calculated VSWR for ring widths of 4 to 11 mm. Provided R_w does not become too large, it is possible to use mode separation behavior to selectively increase or decrease the bandwidth of the antenna without adversely affecting the other antenna electrical properties. It can be seen that the radiation mode splits into two modes when $R_w > 8$ mm ($0.1\lambda_g$). Figure 4.5 shows the antenna bandwidth versus ring width aspect ratio, R_o/R_i. The plot shows that antenna bandwidth gets larger with increasing ring width. Bandwidth increases up to a maximum value and then begins to drop back down. Above an aspect ratio of 2.6, the two radiation modes become distinct and begin diverging resulting in an overall reduction in antenna bandwidth. Table 4.1 summarizes electrical performance of the ring patch antenna from Figure 4.1 based on different ring widths simulated using IE3D.

Table 4.1 Electrical performance based on ring width of the ring patch antenna simulated using IE3D.

Ring width R_w (mm)	Inner dimension R_i (mm)	Outer dimension R_o (mm)	Bandwidth 2:1 VSWR (%)	Minimum VSWR
4	9.25	13.25	-	2.5
5	8.75	13.75	-	2.1
6	8.25	14.25	5.0	1.5
7	7.75	14.75	8.6	1.2
8	7.25	15.25	11.4	1.2
9	6.75	15.75	15.7	1.3
10	6.25	16.25	11.8	1.3
11	5.75	16.75	3.1	1.2

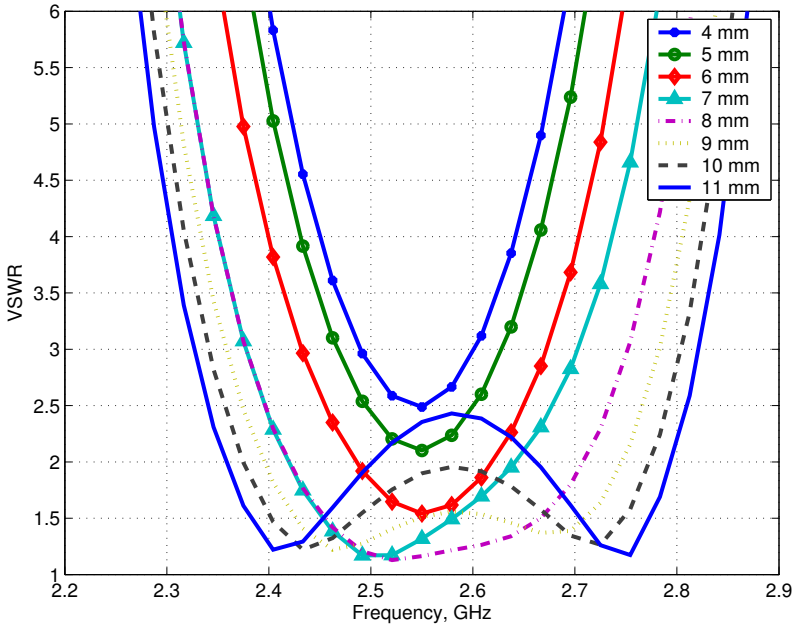

Figure 4.4 VSWR versus frequency of the ring patch antenna of Figure 4.1 for various ring widths, R_w, computed using IE3D.

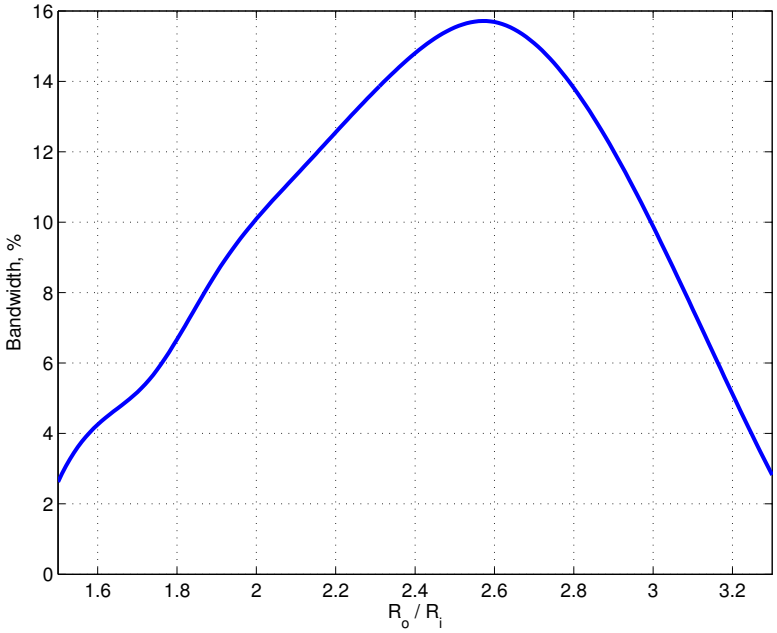

Figure 4.5 Bandwidth versus ring width aspect ratio, R_i/R_o, of the ring patch antenna of Figure 4.1 computed using IE3D.

4.2.1 The Reconfigurable Ring Patch Antenna

Specific discrete ring widths are selected for several antenna bandwidth values based on the ring width investigation performed in Section 4.2. Six ring widths have been chosen to achieve discrete bandwidth states from 0% (effectively off) to 15% (maximum bandwidth). These ring width states are used in the subsequent work to accomplish the desired reconfigurable performance. Table 4.2 summarizes the ring widths chosen to achieve the selectable bandwidth behavior along with the estimated bandwidth values based on the ring width investigation in Section 4.2.

Table 4.2 Discrete ring widths for selected antenna bandwidth states based on simulations from Section 4.2.

State	Ring width R_w (mm)	Inner dimension R_i (mm)	Outer dimension R_o (mm)	Bandwidth 2:1 VSWR (%)
A	10.10	6.20	16.30	15
B	8.98	6.76	15.74	13
C	7.86	7.32	15.18	11
D	6.74	7.88	14.62	9
E	5.62	8.44	14.06	5
F	4.50	9.00	13.50	0

The design task becomes how to physically vary the width of the ring to achieve the desired reconfigurable operation. With the limits on the ring width defined from Figure 4.4 and listed in Table 4.2, the solid layer ring is replaced by a new structure with reconfigurable components. The ring is reformed as a single smaller solid ring with a series of thin concentric rings on the inside and outside connected together via MEMS switches as shown in Figure 4.6. The electrical width of the ring is varied by selectively activating the interconnecting switches between the concentric rings and a variable impedance bandwidth of 0–15% is obtained.

The ring layer is replaced by a solid ring 4.5 mm in width having inner and outer dimensions of R_i = 18 mm and R_o = 27 mm respectively. The feed point remains the same at 11.25 mm from the patch center which results in a mean ring diameter R = 45 mm, or roughly $\lambda_g/4$ for 2.55 GHz. To facilitate bandwidth control, the inner and outer portions of the solid ring are replaced with concentric strip rings connected

together with RF switches. Figure 4.6 shows the layout of the rings and switches. The strips are 0.36 mm wide and their length depends on their location within the ring layer. The inner ring strips have a length of 12.4 mm and the outer strips have a length of 31.88 mm. Following the switch modeling procedures from Section 3.3, the switches are chosen to be 0.2 mm square. There are switches are placed at the corners and the middle of the strips to ensure that in the on-position the connected sections act as solid rings. They function in groups so the ring size changes in a symmetric fashion, for example, the outer and inner rings switch together.

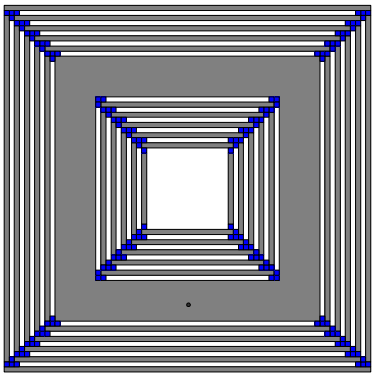

(a) state A, $R_w = 10.10$ mm

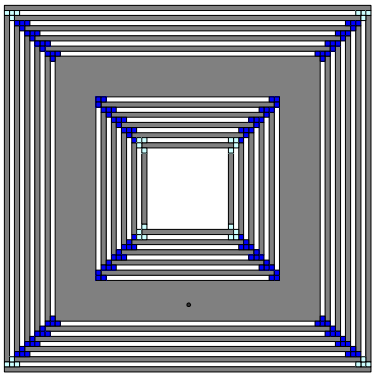

(b) state B, $R_w = 8.98$ mm

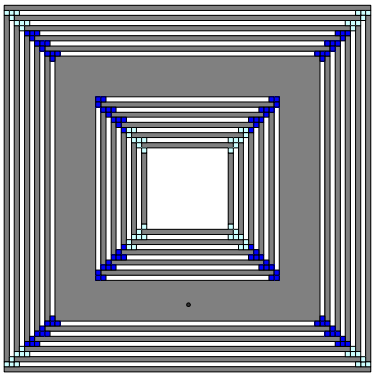

(c) state C, $R_w = 7.86$ mm

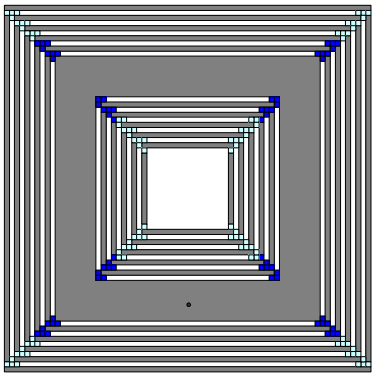

(d) state D, $R_w = 6.74$ mm

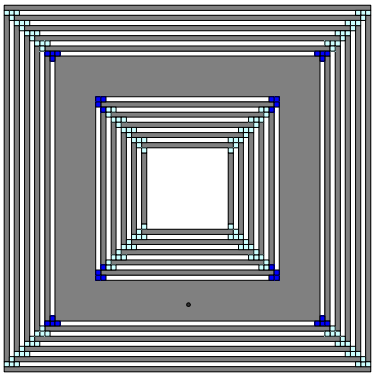

(e) state E, $R_w = 5.62$ mm

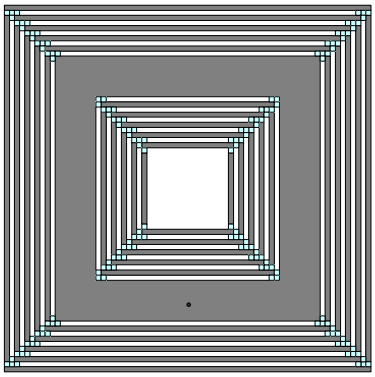

(f) state F, $R_w = 4.50$ mm

Figure 4.6 Reconfigurable ring patch active layer switch configuration states. Switches in *on* position are shown in dark and switches in *off* position are shown in light.

4.3 Simulation of Reconfigurable Ring Patch

This section presents the computer simulations performed on the reconfigurable ring patch antenna (RRPA) developed in the previous section. The commercial code IE3D was the primary simulation tool used for studying the RRPA. IE3D is a full-wave, frequency-domain simulation package that utilizes a laterally-open moment method engine capable of simulating arbitrary metalization geometries. It is referred to as a 2.5 dimension solver because the field solutions can depend on three spatial dimensions while the sources are confined to planes with only two spatial dimensions. This results in a simplification of the problem space but comes at expense of problem generality. The resulting Green's function formulation for 2.5D codes requires dielectrics to be infinite in lateral extent but of arbitrary height or thickness. This formulation makes 2.5D solvers particularly suited for planar geometries such as microstrip and multi-layer structures. A primary concern however with using a 2.5D solver on realistic patch antennas is the finite lateral extent of the antenna substrate. Hardware models will, of course, have substrate and ground plane layers of finite extent, leading to some deviation from 2.5D code simulation results. Experience indicates this deviation is small for most microstrip patch antenna simulations provided that the ground plane is at least two wavelengths in extent for relatively thin substrates.

Figure 4.7 shows the computed input impedance for the antenna switch states of Figure 4.6. The real part of the impedance varies between 35 and 100 Ω and the imaginary part is 0 Ω at 2.5 GHz indicating a very good match to 50 Ω. The reactance plots clearly show why switch state A offers the largest bandwidth. The section of the plot centered at 2.5 GHz remains near 0 Ω reactance over the widest bandwidth for state A and least for state F. Figure 4.8 shows the corresponding VSWR for the switch states referenced to 50 Ω. State F just slightly dips below the 2:1 level indicating that any further reduction in ring width, R_w will result in a VSWR above 2:1. It can also be seen for state A there is a slight reduction in the upper frequency limit. This is in contrast to the behavior of the 10 mm solid ring patch from Section 4.2 that did not exhibit this diminished upper frequency. This behavior is attributed to the fixed ring width used in the reconfigurable version. At higher frequencies the rings and switches appear electrically larger resulting in a decreased operational frequency. A

ring width that varies progressively larger toward ring extremes would mitigate this effect. However, this would require the use of variable switch sizes in the antenna design. Table 4.3 summarizes the computed 2:1 VSWR impedance bandwidth and geometry parameters for the antenna switch states of Figure 4.6.

Table 4.3 Impedance bandwidth performance and reconfigurable ring geometry for the RRPA with switch states of Figure 4.6 computed using IE3D

State	Ring width R_w (mm)	Center frequency f_o (GHz)	Bandwidth 2:1 VSWR (%)	Minimum VSWR
A	10.10	2.498	15.0	1.05
B	8.98	2.530	13.4	1.10
C	7.86	2.533	11.7	1.20
D	6.74	2.530	9.1	1.10
E	5.62	2.515	5.6	1.45
F	4.50	2.503	0.6	1.95

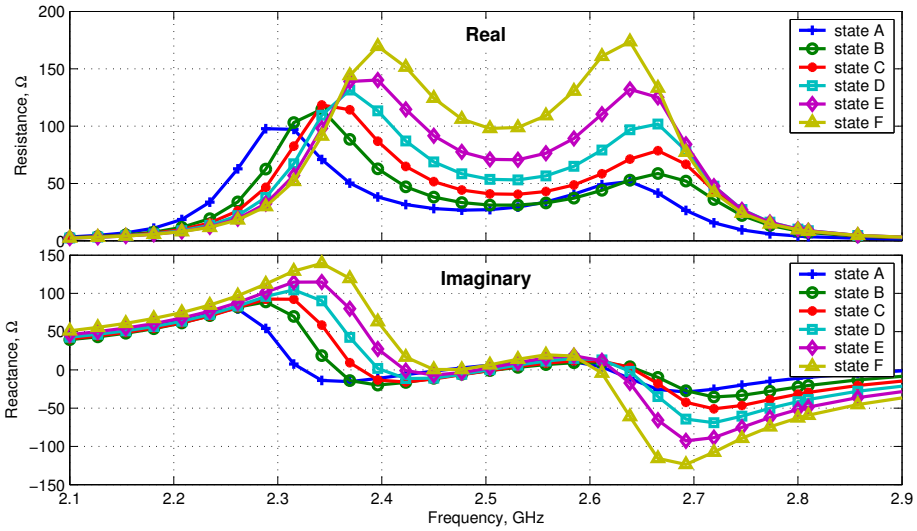

Figure 4.7 Input impedance versus frequency of the reconfigurable ring patch antenna for switch states of Figure 4.6 simulated using IE3D.

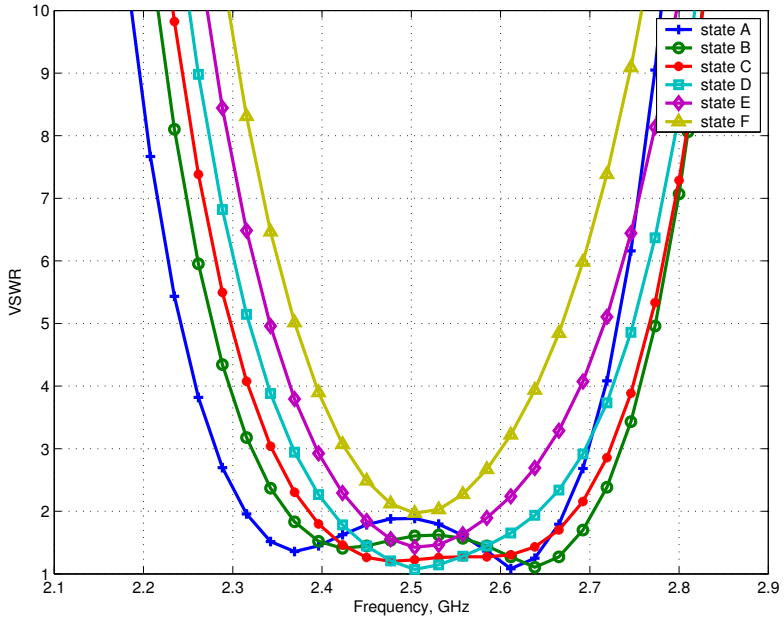

Figure 4.8 VSWR versus frequency of the reconfigurable ring patch antenna for switch states of Figure 4.6 simulated using IE3D.

4.4 Experimental Results for RRPA

The prototype RRPA of Figure 4.9 was constructed and its electrical performance characteristics were measured in order to verify the theoretical and simulated results. The prototype antenna is composed of two halves, the lower ring patch section and the upper parasitic patch section. The lower section contains the ring layer and ground plane plus the feed. The ring layer was printed on Rogers RT/Duroid 5870 [76] which has a dielectric constant of 2.35. The overall substrate size was 4.5 by 6 inches with the copper left on the lower side for the ground plane. A hole was drilled through the ring layer metalization, substrate and ground plane to accommodate the probe feed. A standard SMA flange connector was used as the feed with the pin inserted through the hole in the antenna substrate. The feed pin was then soldered to the ring layer and the SMA flange was soldered to the ground plane. The other half of the assembly was consisted of the 47 mm parasitic radiating plate and its support structure. The parasitic plate was cut from a 15 mil copper blank. A $30 \times 30 \times 5$ mm block of RohaCell HF31 foam was attached to the parasitic plate with double-sided tape. The HF31 material is a closed-cell polymethacrylimide rigid foam produced by Röhm Composites [77] which has a dielectric constant of 1.05 and a negligible loss tangent (< 0.0002) at 2.5 GHz.

To achieve the six antenna switch states without the actual switches, six ring layers were constructed to mimic the presence of the MEMS switches. Figure 4.10 shows the six ring patch layers that were constructed corresponding to the reconfigurable antenna switch states of Figure 4.6.

4.4.1 Impedance Measurements

All measurements of the RRPA were performed at the Virginia Tech Antenna Group's antenna test facility. Impedance measurements were made using an HP8510C vector network analyzer. The measurement unit consists of the printed antenna under test and the ground plane mounting fixture. The AUT was mounted on a 4λ circular ground plane. The ground plane was made from a 16 inch diameter stainless steel pizza-pie plate. A small hole was cut in the center of the plate to accommodate the antenna SMA connector and feed cable. The test unit was then mounted on

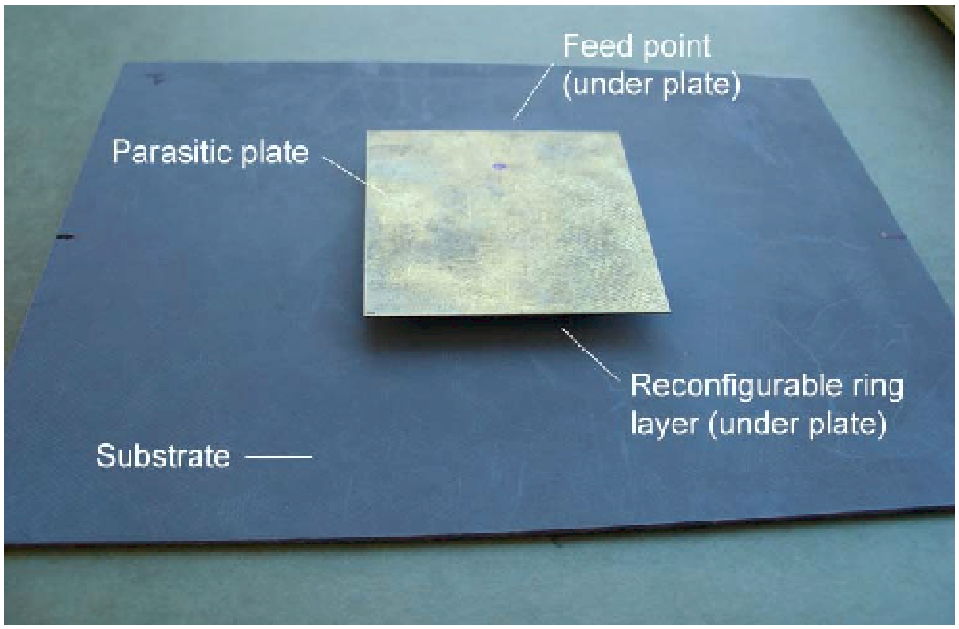

Figure 4.9 Hardware test model of the reconfigurable ring patch antenna with ring layer geometries specified in Table 4.2.

the near-field scanner AUT positioner inside the anechoic chamber to minimize any external disturbances. While the impedance measurements were being performed, the AUT positioner was pointed toward the closed chamber door to further reduce any unwanted reflections and maintain repeatability between measurements. RF absorber was placed around the metal AUT tower to minimize any reflections from the mounting fixture. Considerable effort was taken to minimize any unwanted reflection in the test environment and to ensure repeatability between antenna measurements. Before the final impedance measurements were performed, the setup was validated by measuring the input impedance of a known 2.4 GHz $\lambda/4$ monopole antenna. The S-parameter values and input impedance values obtained from this measurement confirmed that the measurement setup provided a suitable test environment.

The measured impedance data is plotted along with the respective IE3D simulated results for each antenna switch state. The measured impedance referenced to 50 Ω is shown in Figure 4.11. Reasonable agreement was obtained between the measured and simulated data. The resistance peaks away from the center frequency are slightly higher in the measured case. However, around the frequency of interest, 2.5 GHz, the

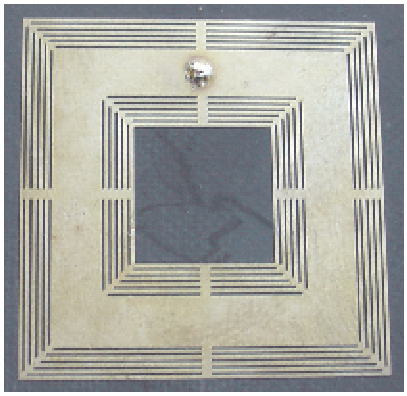

(a) Switch state A

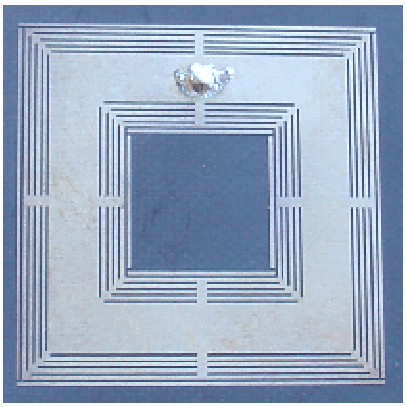

(b) Switch state B

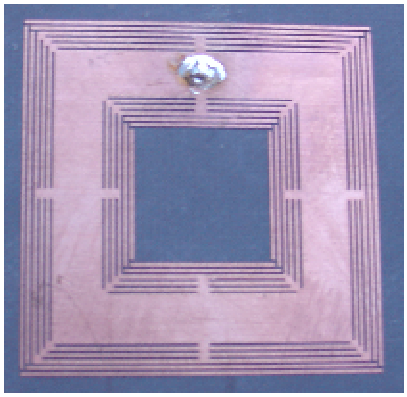

(c) Switch state C

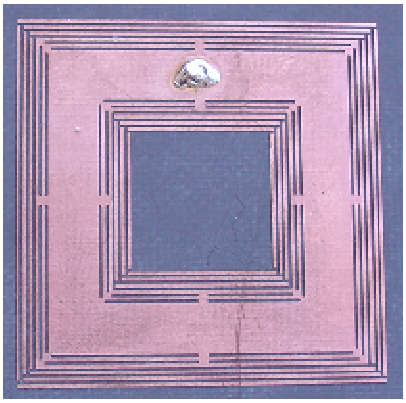

(d) Switch state D

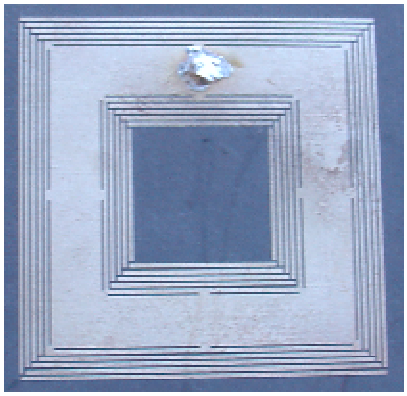

(e) Switch state E

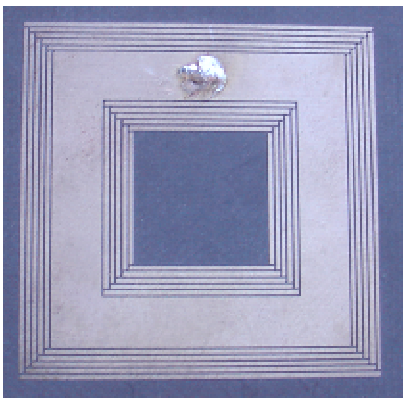

(f) Switch state F

Figure 4.10 Hardware models for each of the switch states of Figure 4.6.

measured resistance and reactance for all switch states is very similar to the computed values. This indicates that that the design is somewhat sensitive to manufacturing tolerances off resonance. The height, h, of the parasitic plate has a significant impact on the input impedance and the process of hand sanding the foam support block was the most prone to manufacturing tolerance errors and most likely contributed to the slight measurement differences.

Figure 4.12 shows the measured VSWR for all states compared to the computed values. There is a small overall upward shift in the center frequency noted for all switch states in comparison to the simulated antenna. However, the total 2:1 VSWR impedance bandwidths are very close to the computed values for all switch states. Figure 4.13 compares the VSWR for all switch states on the same graph. It is noted that the reduction in upper frequency limit seen in simulated state A also appears in the measured data. The associated return loss for all switch states is shown in Figure 4.14. Table 4.4 provides a summary of the measured and simulated 2:1 VSWR performance of the RRPA.

Table 4.4 Summary of the measured and simulated 2:1 VSWR impedance bandwidth performance for the RRPA.

	Bandwidth 2:1 VSWR (%)		Center Frequency f_o (GHz)		Minimum VSWR	
State	measured	simulated	measured	simulated	measured	simulated
A	13.3	15.0	2.52	2.50	1.05	1.05
B	11.0	13.4	2.54	2.53	1.10	1.10
C	8.0	11.7	2.54	2.53	1.35	1.20
D	4.5	9.1	2.51	2.53	1.70	1.10
E	0	5.6	2.52	2.52	2.05	1.45
F	0	0.6	2.52	2.50	2.52	1.95

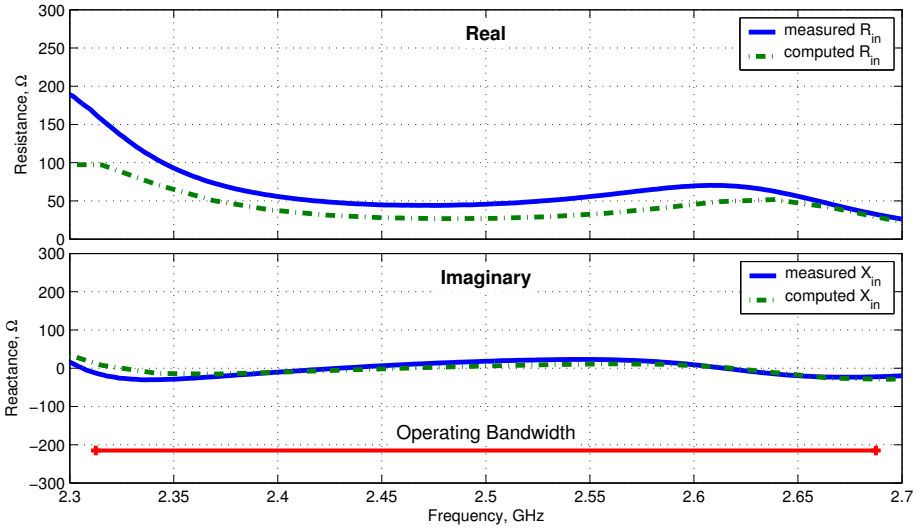

(a) switch state A

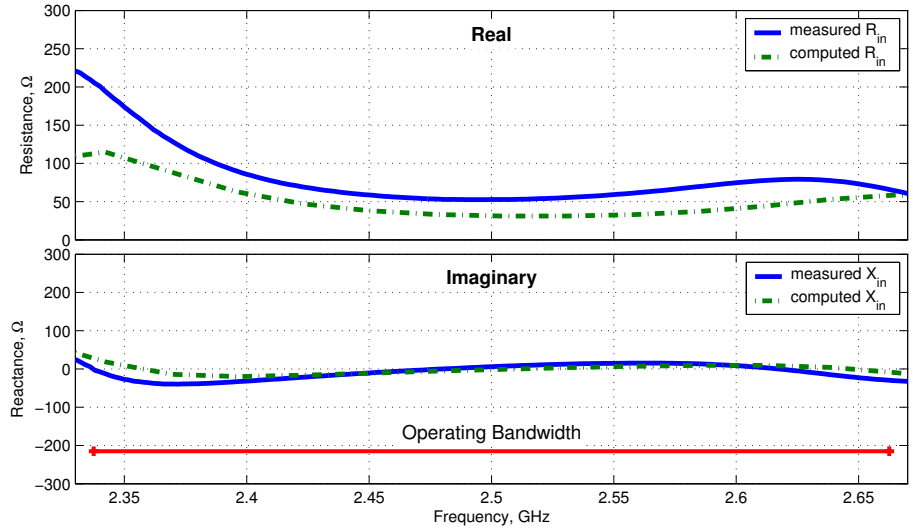

(b) switch state B

Figure 4.11 Measured and simulated input impedance for the ring patch.

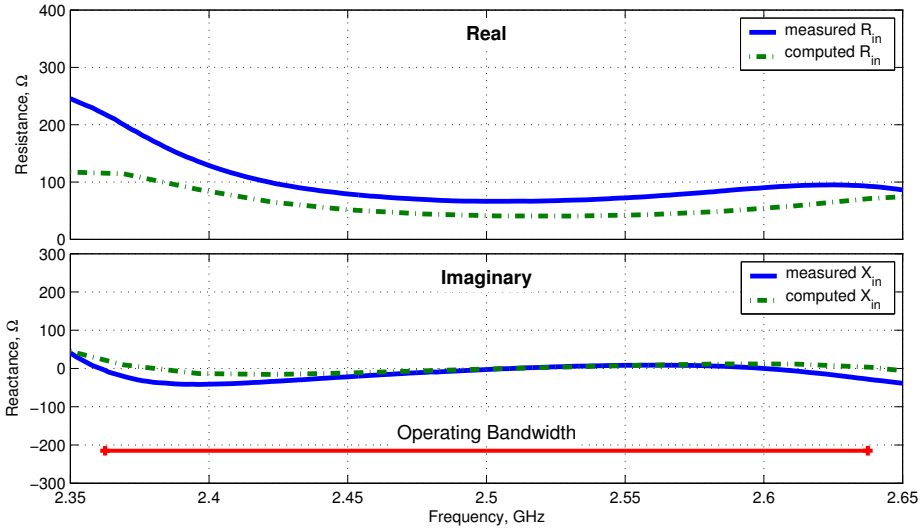

(c) switch state C

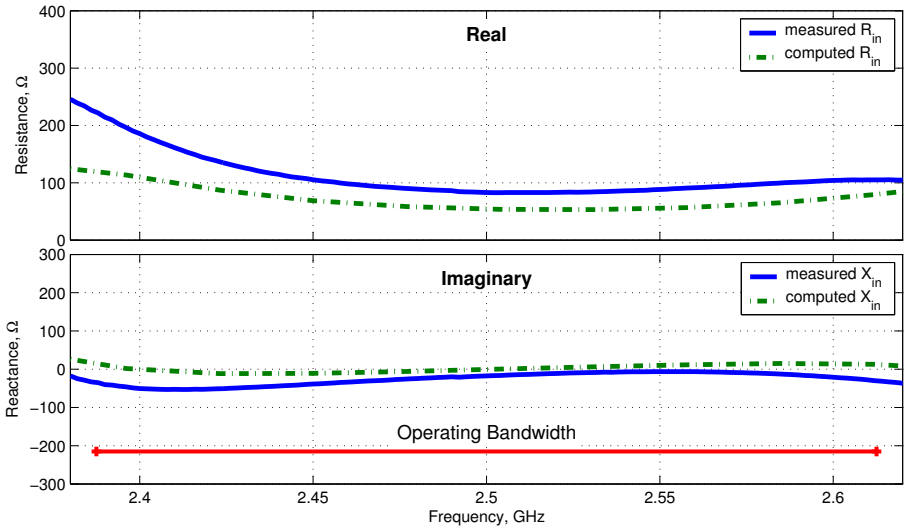

(d) switch state D

Figure 4.11 Measured and simulated input impedance for the ring patch (cont.)

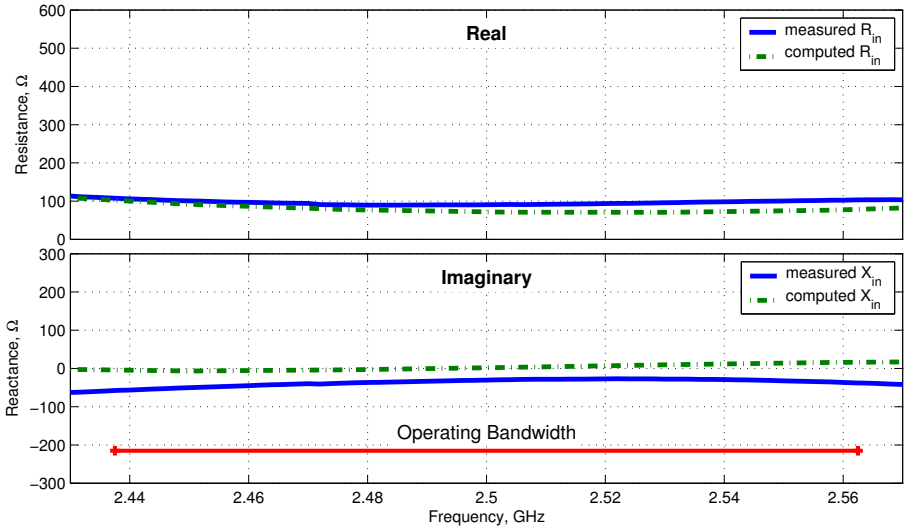

(e) switch state E

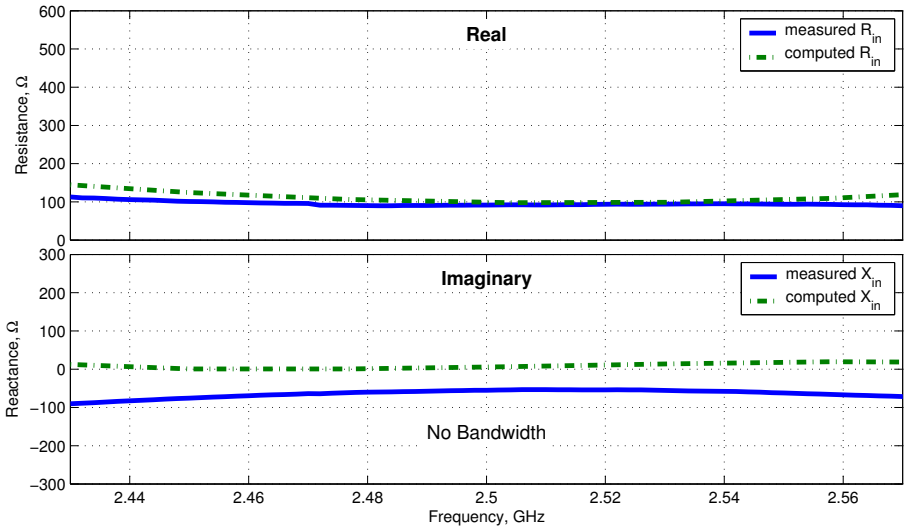

(f) switch state F

Figure 4.11 Measured and simulated return loss for the ring patch (cont.)

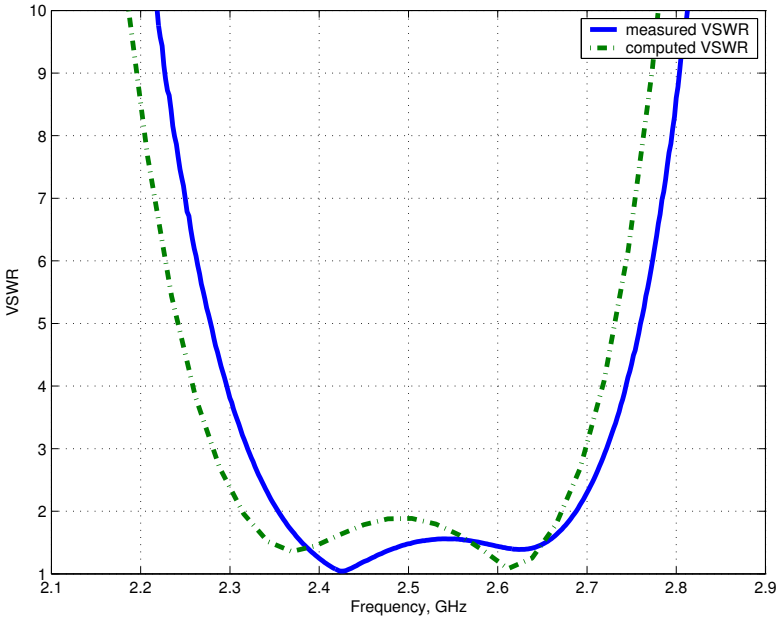

(a) switch state A

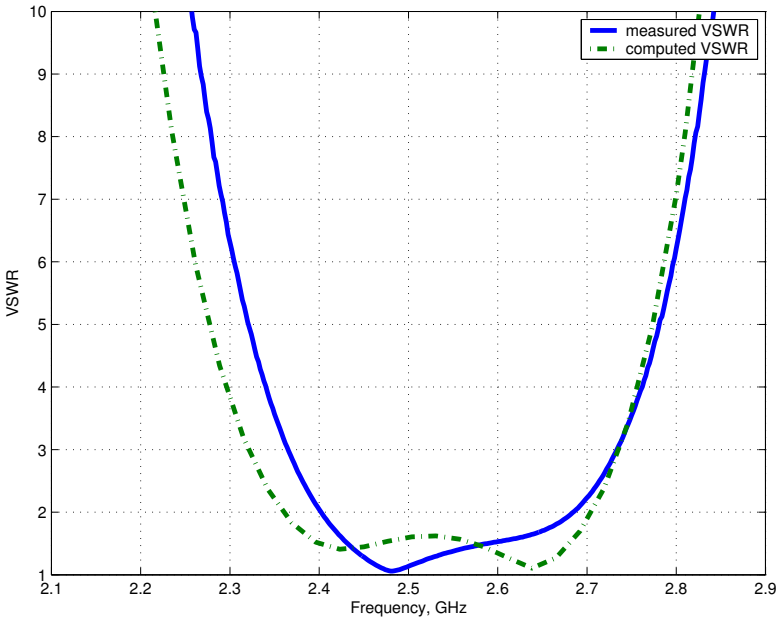

(b) switch state B

Figure 4.12 Measured and simulated voltage standing wave ratio for the ring patch antenna.

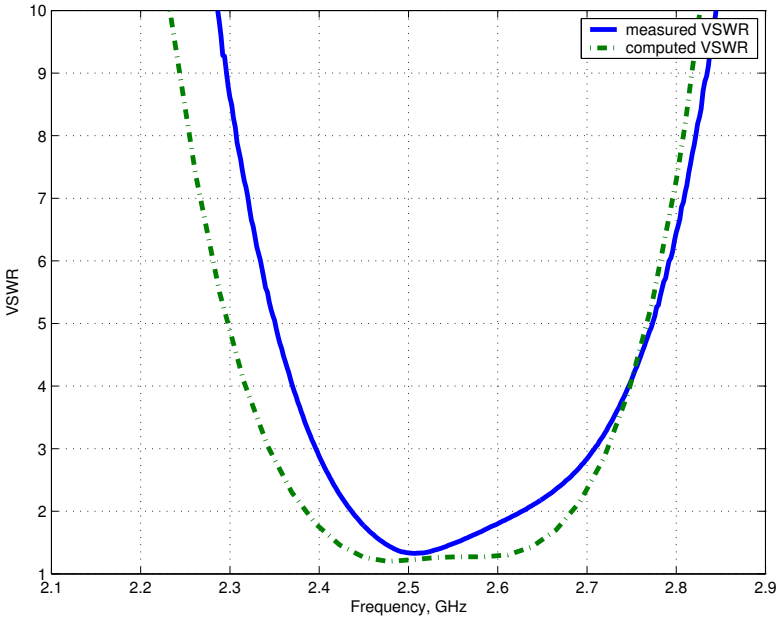

(c) switch state C

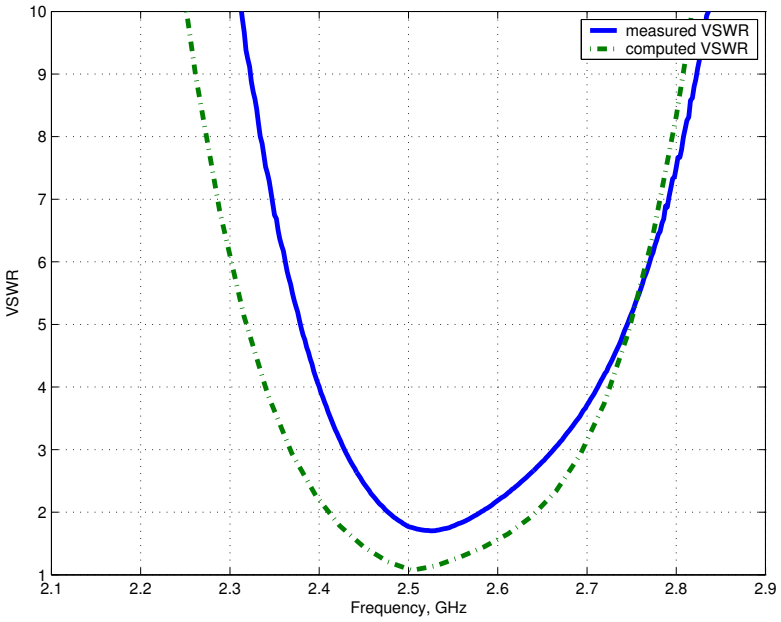

(d) switch state D

Figure 4.12 Measured and simulated voltage standing wave ratio for the ring patch antenna (cont.)

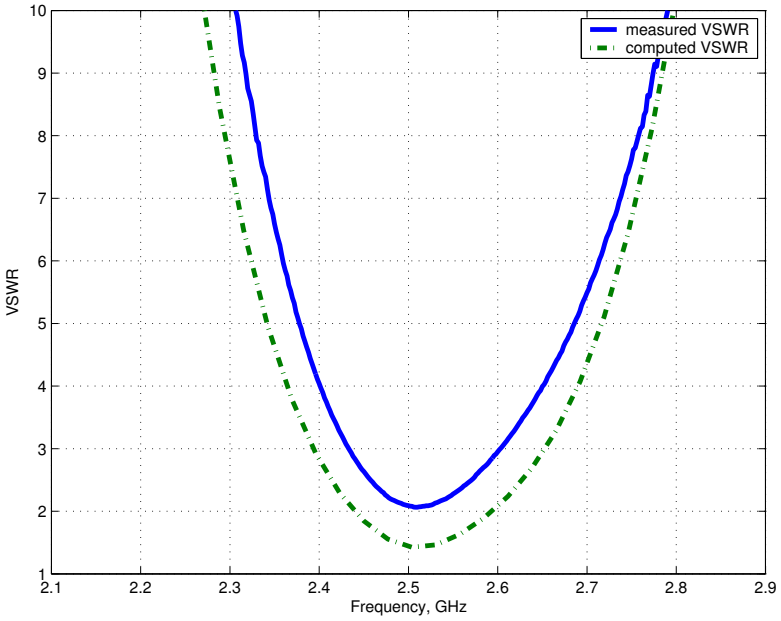

(e) switch state E

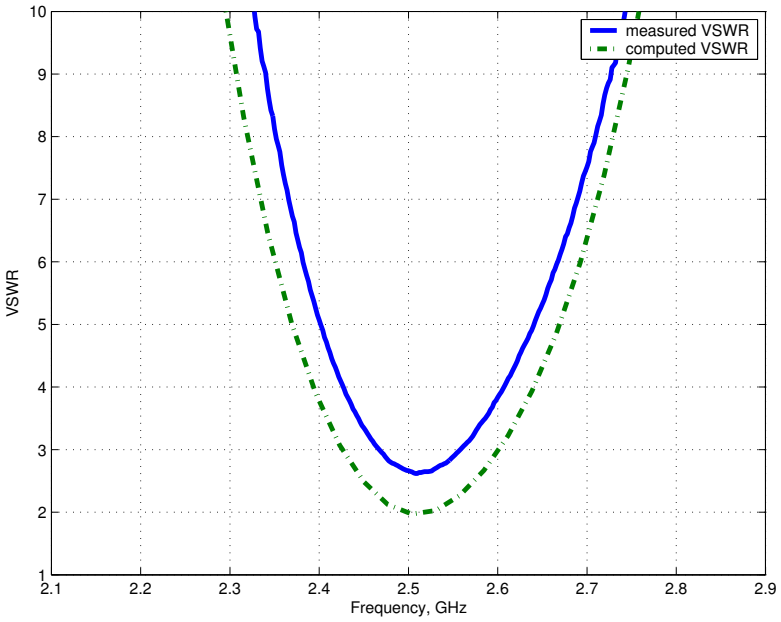

(f) switch state F

Figure 4.12 Measured and simulated voltage standing wave ratio for the ring patch antenna (cont.)

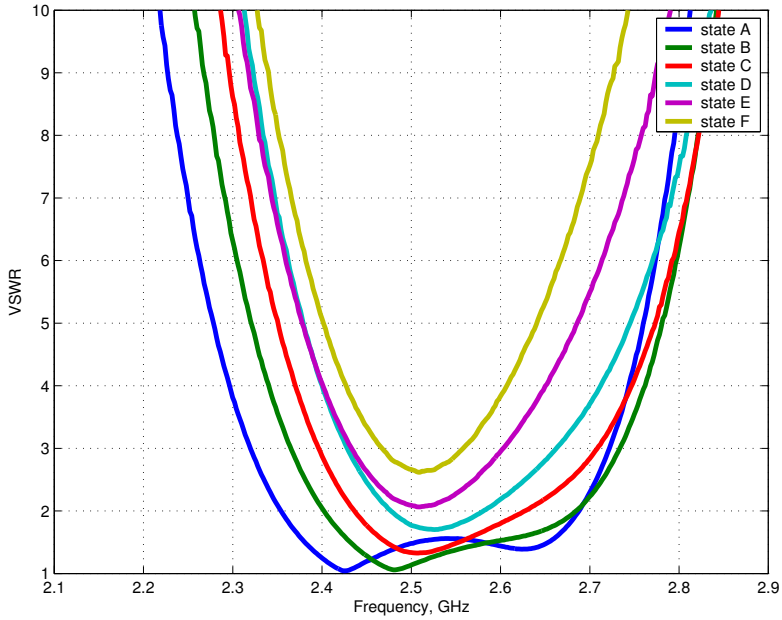

Figure 4.13 Measured voltage standing wave ratio for the ring patch in all states.

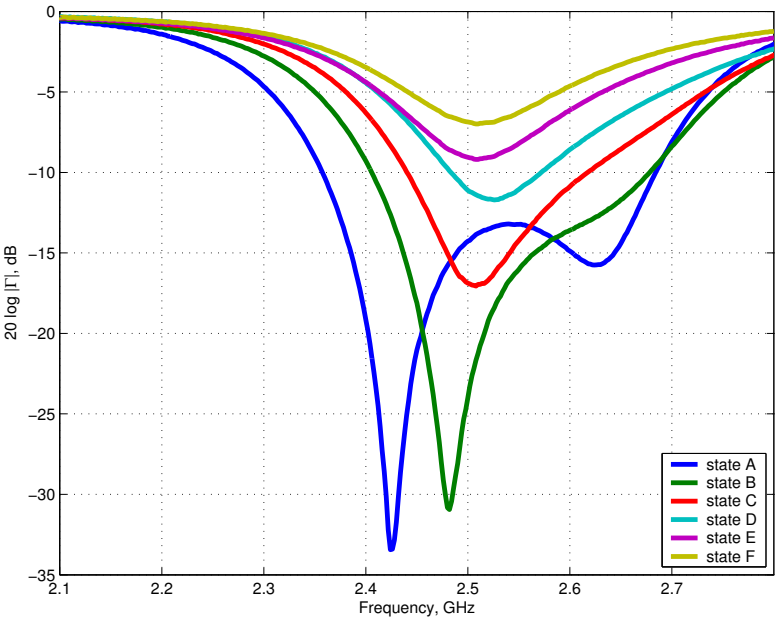

Figure 4.14 Measured return loss for the ring patch in all states.

4.4.2 Pattern Measurements

Radiation patterns were measured in the VTAG indoor anechoic chamber using the near-field measurement system. The pattern measurements were made using the same pie-plate ground plane test fixture that was used in the impedance measurements presented in Section 4.4.1. However, for the pattern measurements the AUT was connected to the near-field scanner through the AUT positioner. Additional RF absorber was placed behind the test antenna and around the AUT tower to minimize any reflection from the test equipment. A spherical scan was performed with the near-field scanner and the results for selected pattern cuts are presented here compared to the simulated patterns. Prior to performing the final pattern measurements of the AUT, the setup was validated by measuring the radiation patterns of a known 2.4 GHz $\lambda/4$ monopole antenna. The radiation patterns obtained from this validation measurement confirmed that the measurement setup provided a suitable test environment.

The patterns were made at several frequencies and the results for 2.5 GHz are presented here. Similar to the rectangular microstrip patch, the RRPA has a broad, unidirectional beam in the boresight (z-axis) direction. This is the expected pattern behavior arising from the x-directed, equivalent magnetic surface currents on the patch edges described in Figure 4.3(b). As was predicted by the simulations, the radiation pattern behavior of the antenna remains nearly constant from one switch state to the next. This is a desired behavior of the antenna in order to maintain predictable performance while selecting the antenna bandwidth. The principal plane elevation cuts are shown in Figure 4.15. The elevation E-plane ($\phi = 90°$) cut is slightly broader than the H-plane ($\phi = 0°$) pattern cut which is expected from the surface currents. The elevation patterns remain nearly constant over all six switch states showing only 0.04 dB variation from the maximum directivity of 9.18 dB. The measured elevation patterns show a small amount of high-frequency diffraction ripple for low elevation angles behind the ground plane ($-90° < \theta < 90°$). This ripple is a result of the finite nature of the measured ground plane and arises from diffraction currents along the edge of the circular ground plane. The diffraction effects are not seen in the simulated patterns because a infinite ground plane was assumed in the simulations. Figures 4.16 and 4.17 show the measured azimuth patterns. The ground plane edge diffraction is

again visible in Figure 4.16 for $\theta = 80°$; this conical pattern cut corresponds to the elevation angle around the ground plane. As with the elevation patterns, there is very little deviation in the patterns between the each state and good agreement to the simulated performance. Figures 4.18, 4.19 and 4.20 re-plot the directivity patterns for each switch state on the same graph to illustrate those pattern consistency over all bandwidth states.

Due to the difficulty in measuring the gain for electrically small antennas, absolute gain measurements were not made. However, the close agreement between computed and measured performance for pattern and impedance leads to a high level of confidence in the predicted gain obtained from the IE3D simulations even though absolute gain was not measured. In the absence of gain standard measurements, the near-field measurement software reports only directivity measurements.

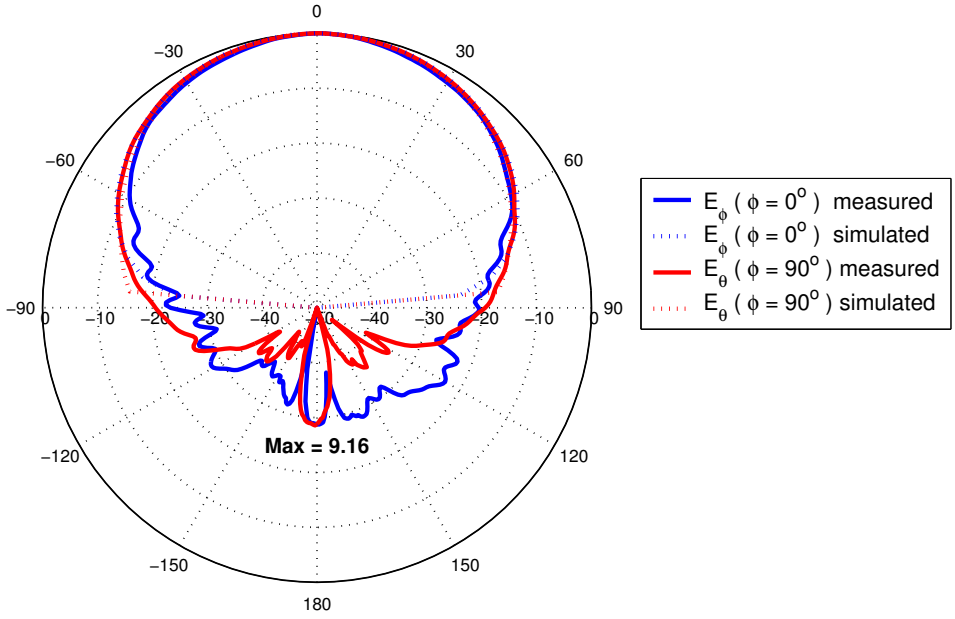

(a) switch state A

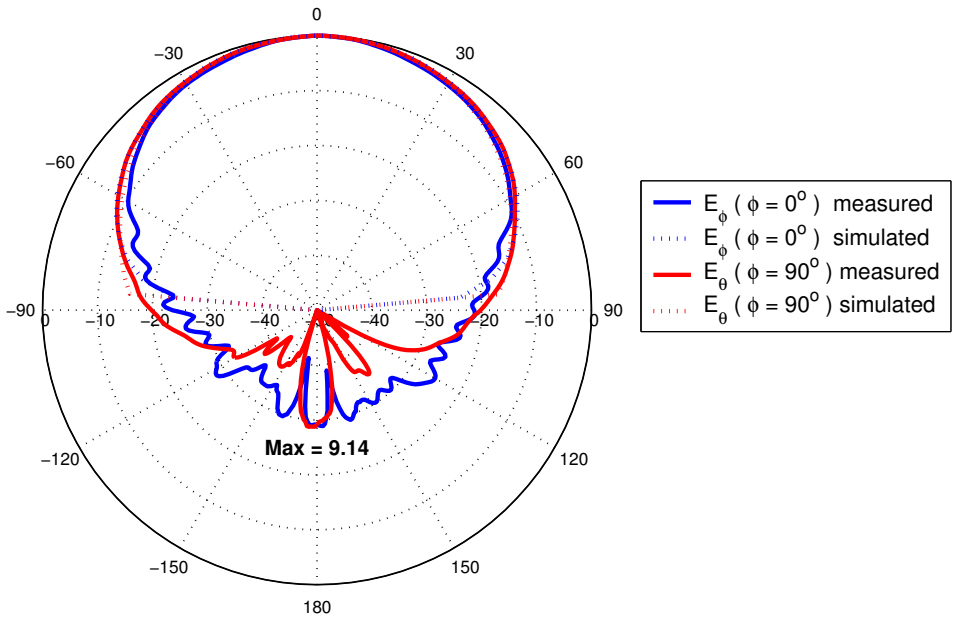

(b) switch state B

Figure 4.15 Measured and simulated elevation radiation patterns in the principal planes for the RRPA.

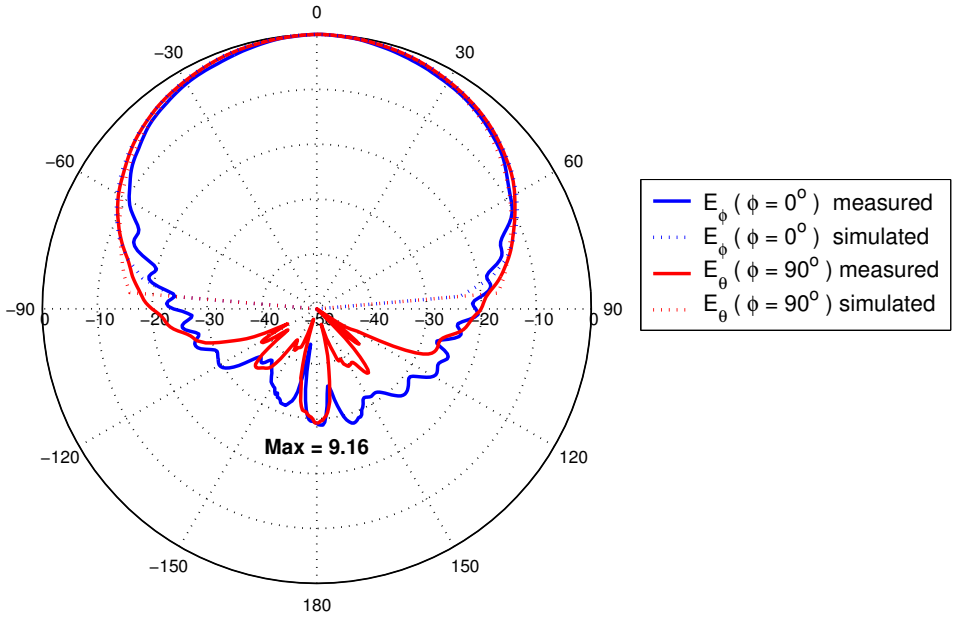

(c) switch state C

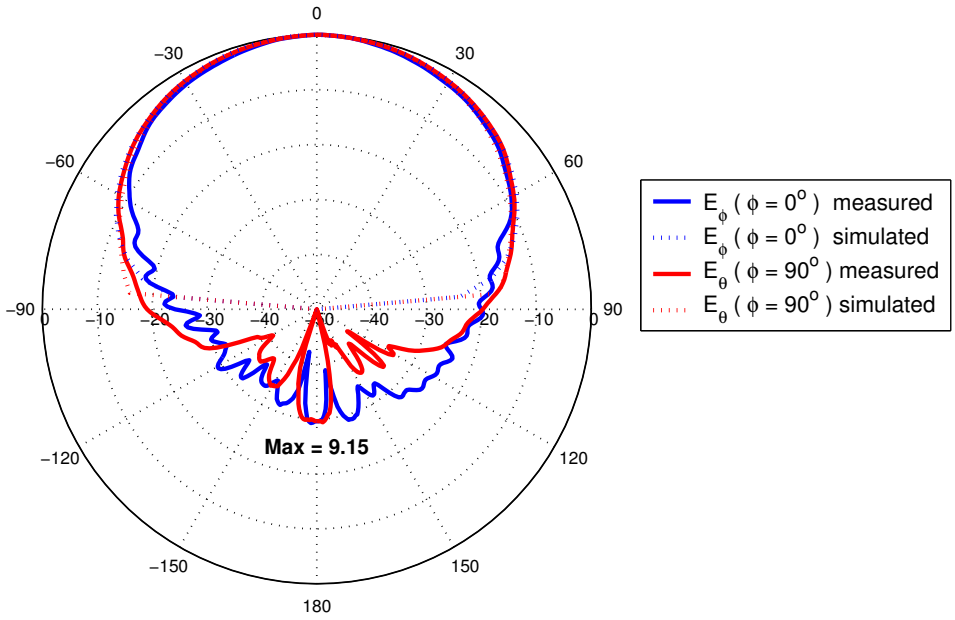

(d) switch state D

Figure 4.15 Measured and simulated elevation radiation patterns in the principal planes for the RRPA (cont.)

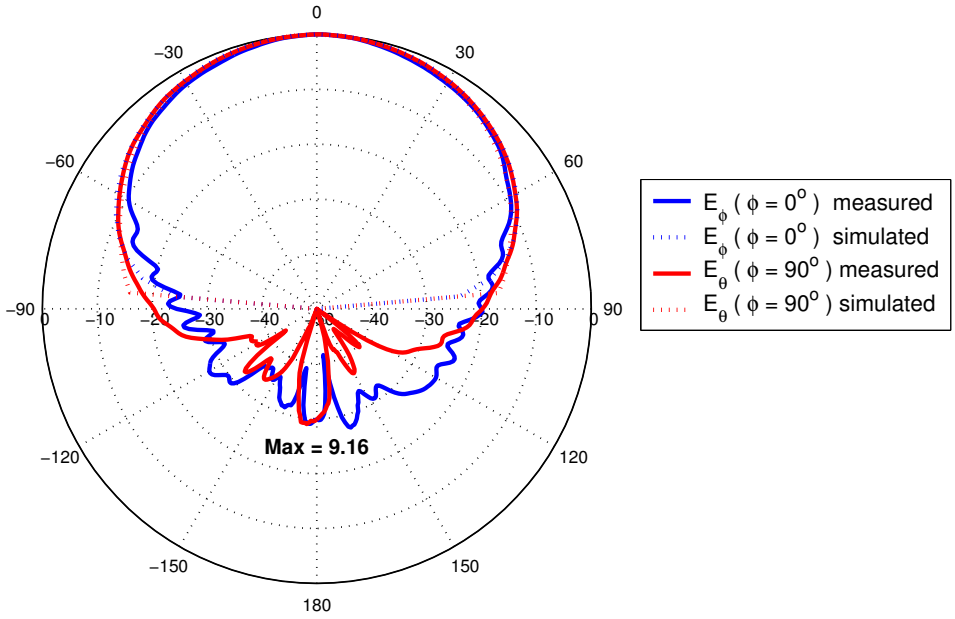

(e) switch state E

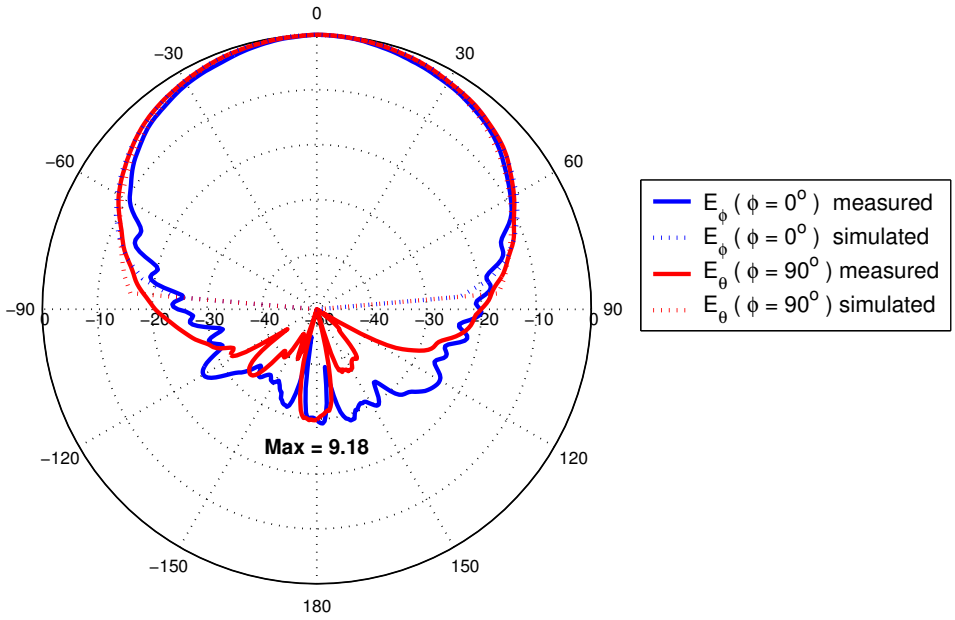

(f) switch state F

Figure 4.15 Measured and simulated elevation radiation patterns in the principal planes for the RRPA (cont.)

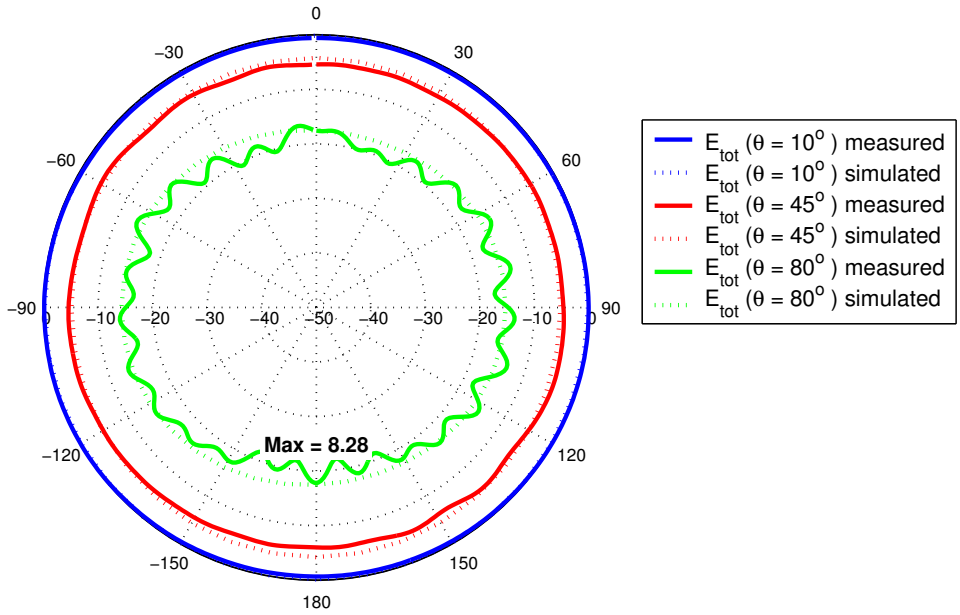

(a) switch state A

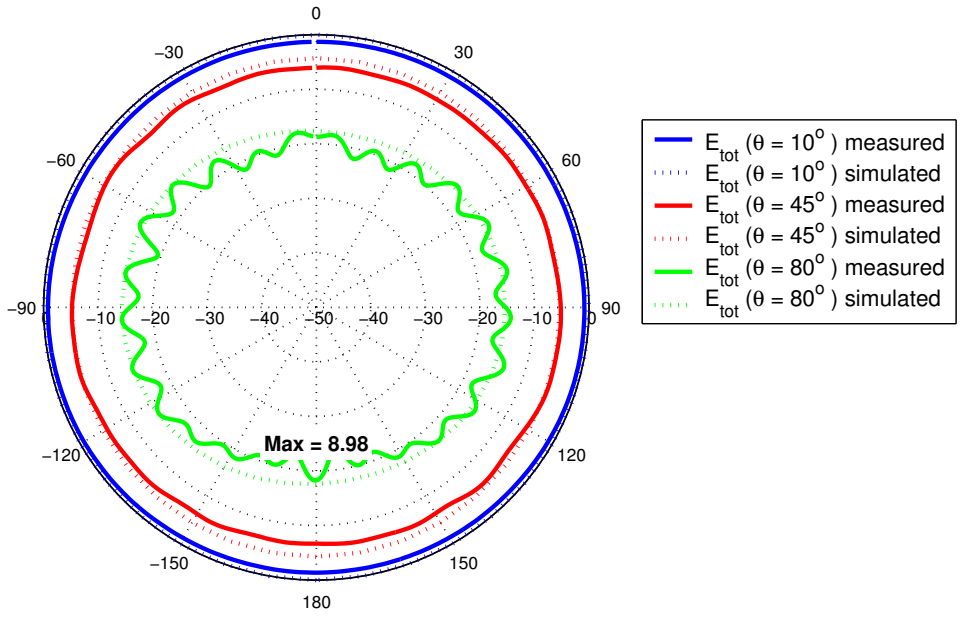

(b) switch state B

Figure 4.16 Measured and simulated conical E_{total} radiation patterns for the RRPA.

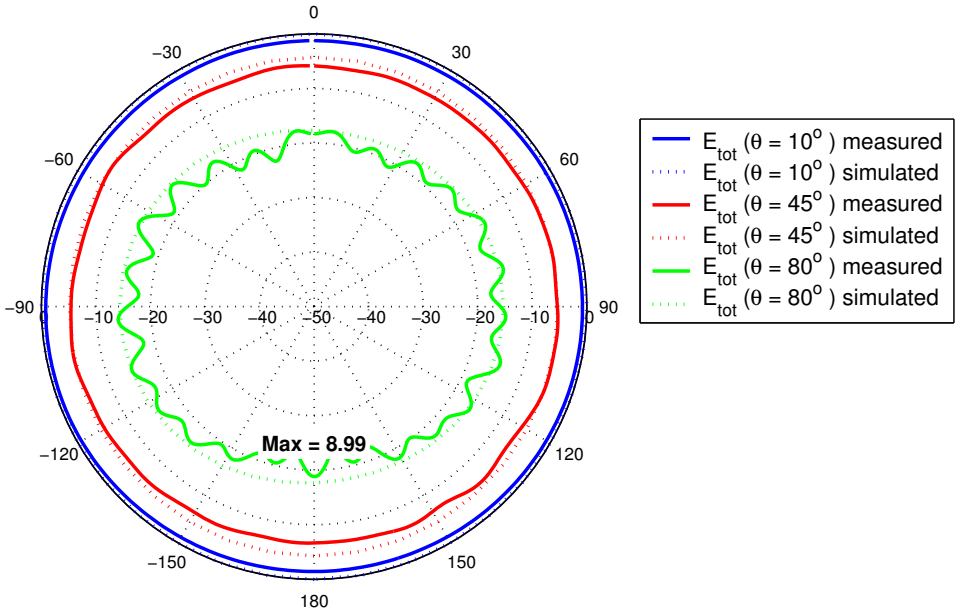

(c) switch state C

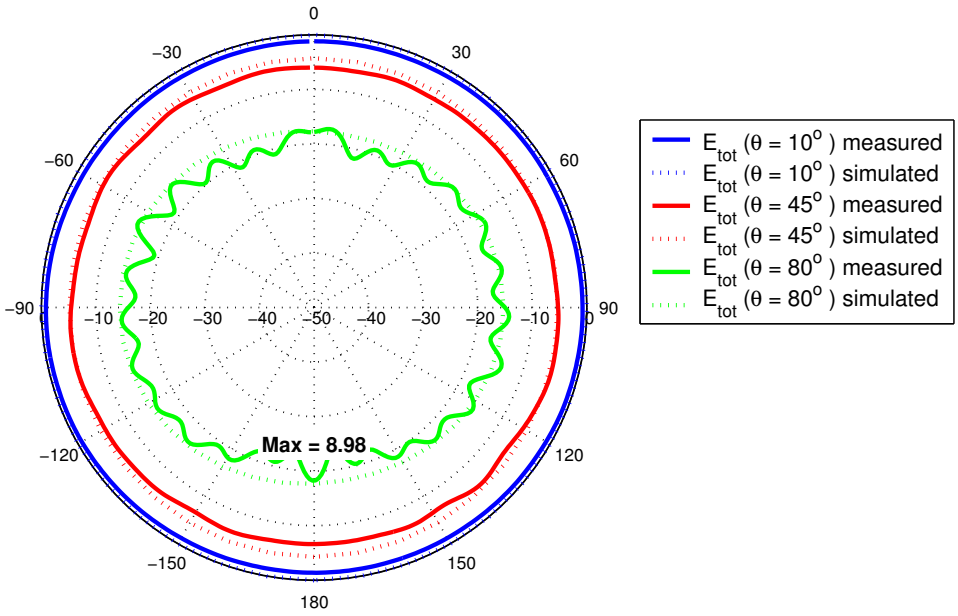

(d) switch state D

Figure 4.16 Measured and simulated conical E_{total} radiation patterns for the RRPA (cont.)

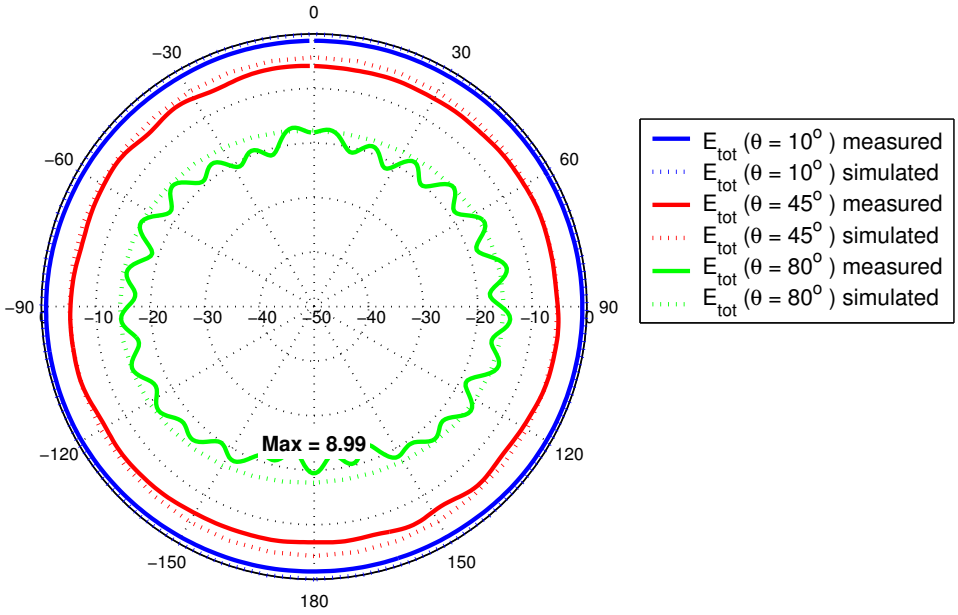

(e) switch state E

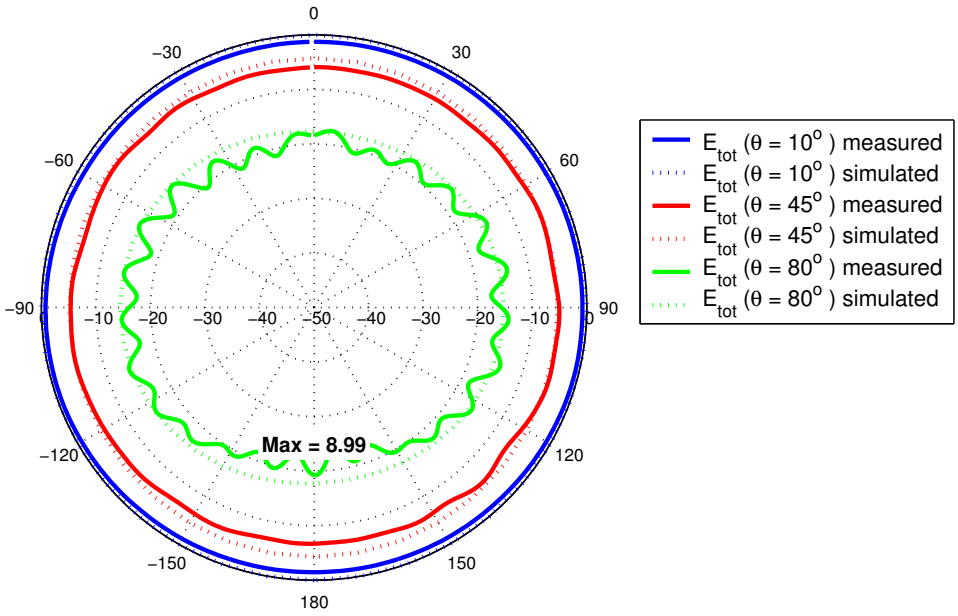

(f) switch state F

Figure 4.16 Measured and simulated conical E_{total} radiation patterns for the RRPA (cont.)

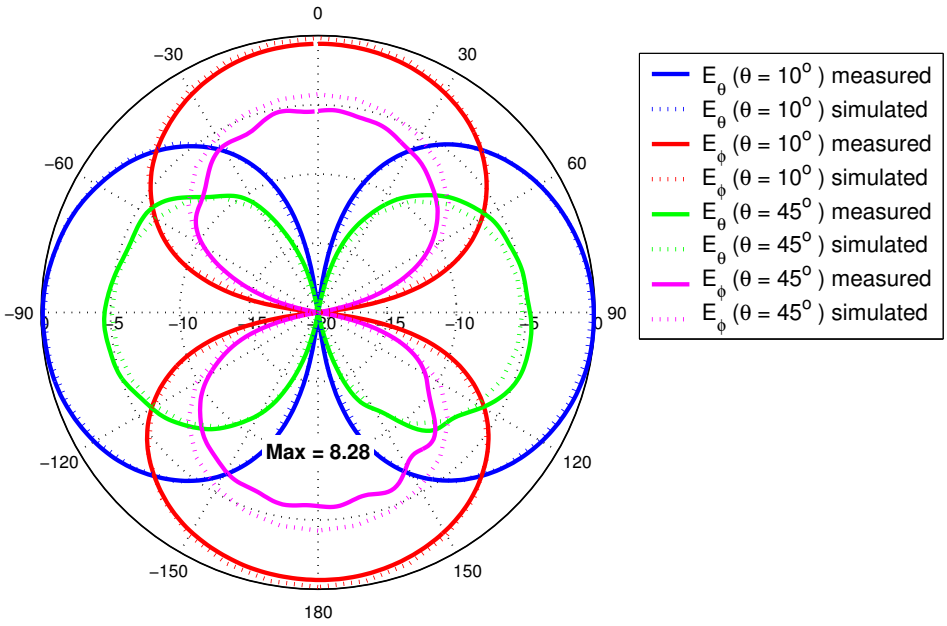

(a) switch state A

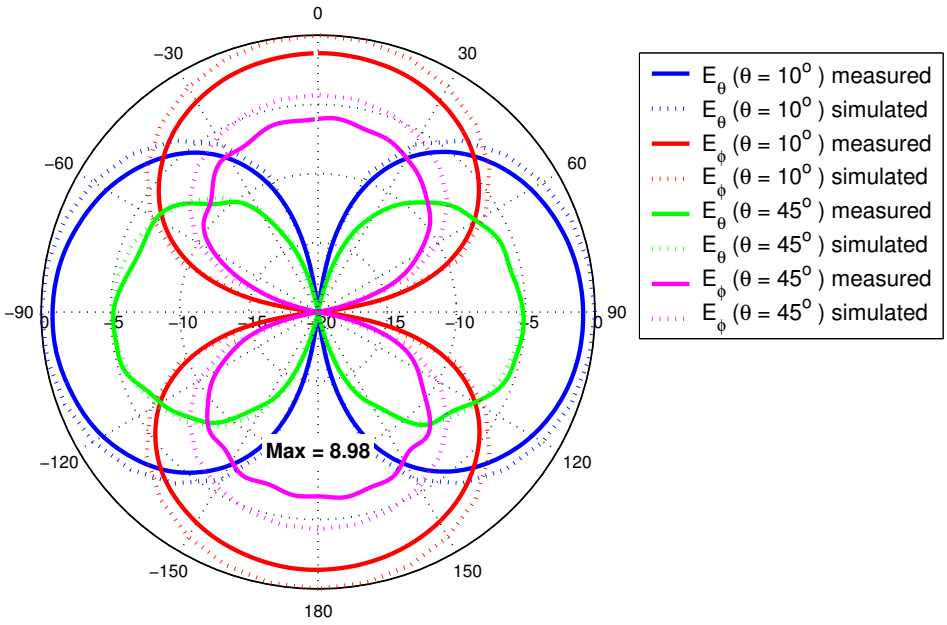

(b) switch state B

Figure 4.17 Measured and simulated conical E_θ & E_ϕ radiation patterns for the RRPA.

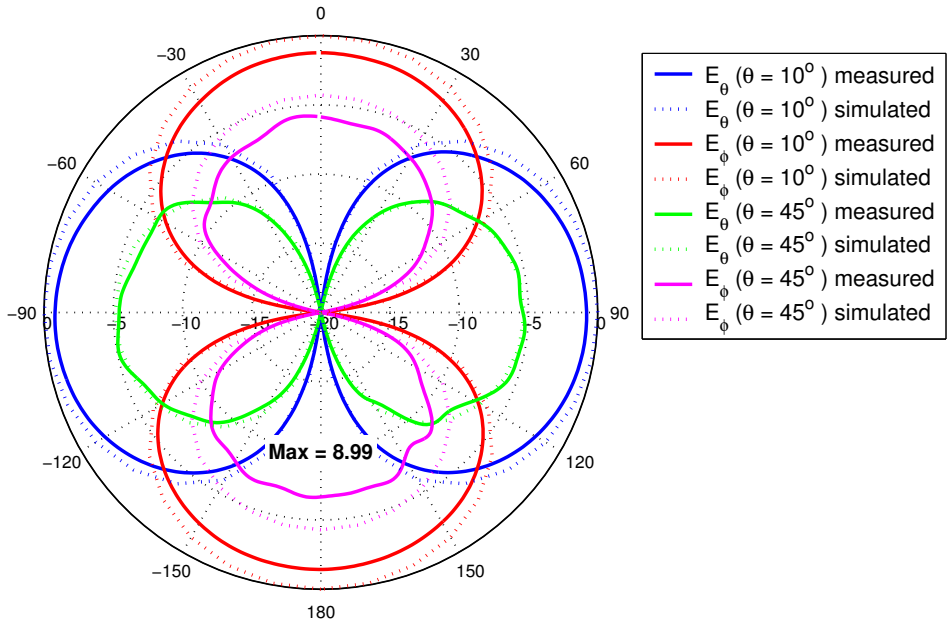

(c) switch state C

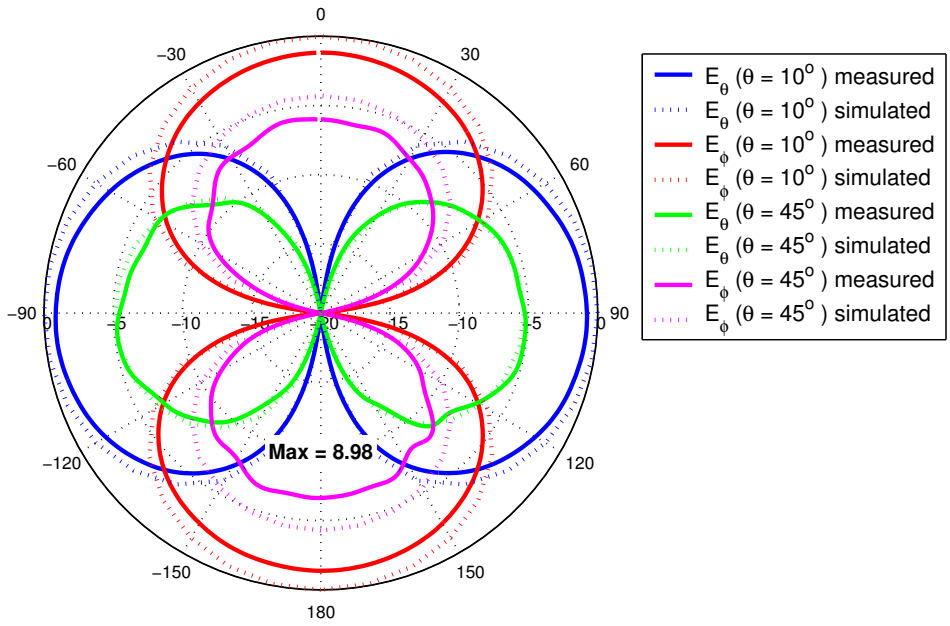

(d) switch state D

Figure 4.17 Measured and simulated conical E_θ & E_ϕ radiation patterns for the RRPA (cont.)

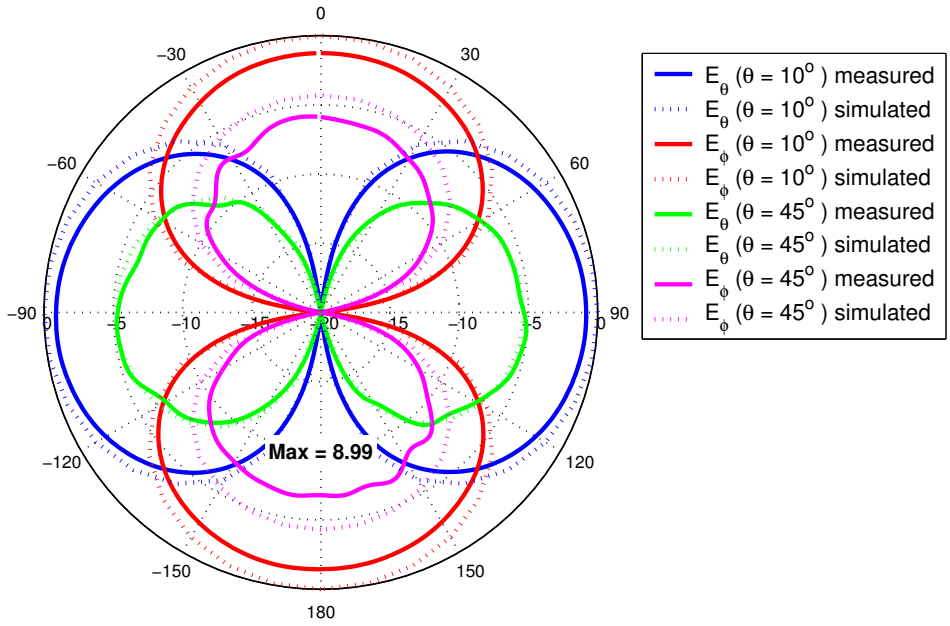

(e) switch state E

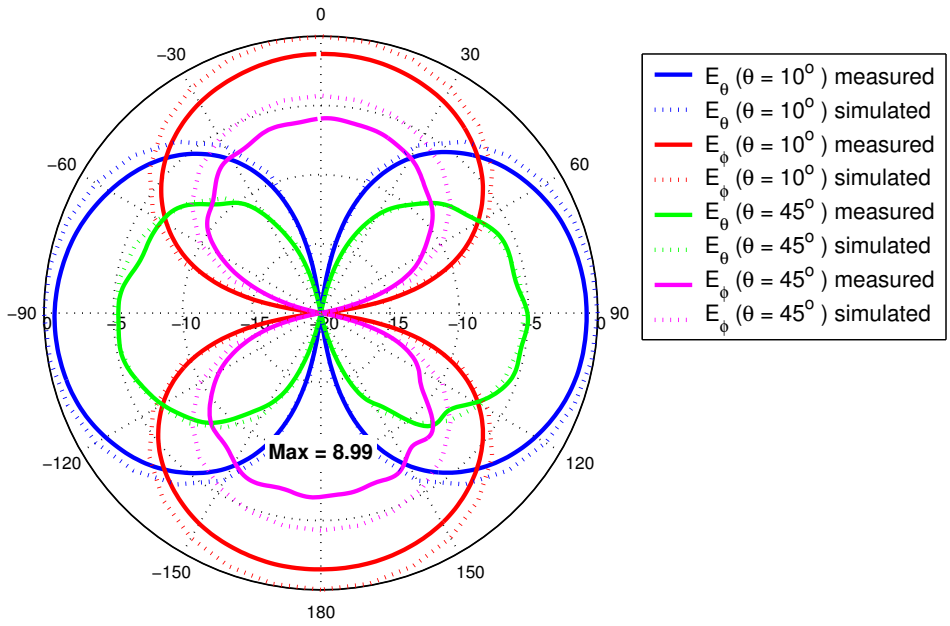

(f) switch state F

Figure 4.17 Measured and simulated conical E_θ & E_ϕ radiation patterns for the RRPA (cont.)

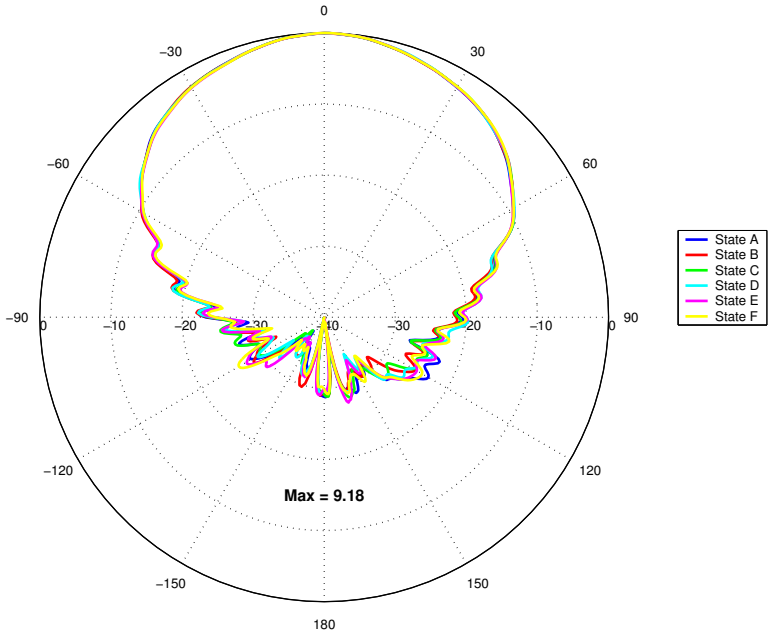

(a) E_θ ($\phi = 90°$)

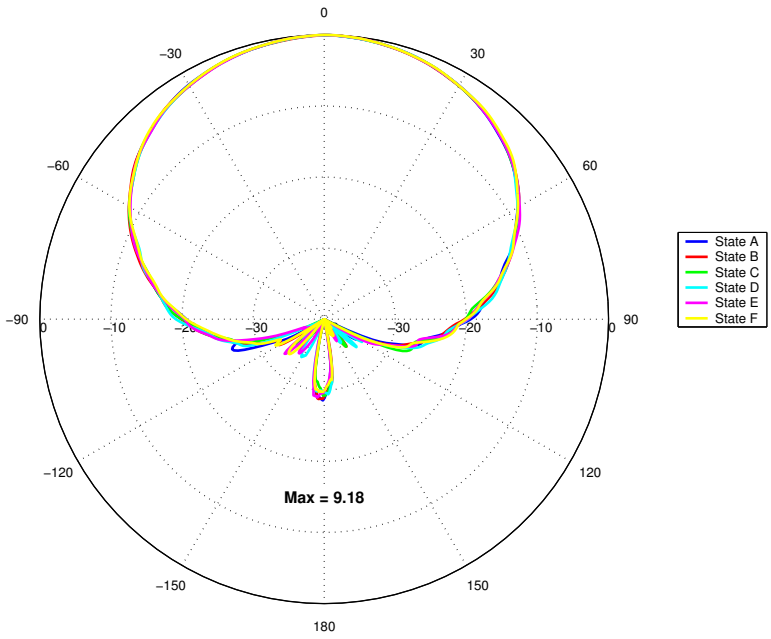

(b) E_ϕ ($\phi = 0°$)

Figure 4.18 Comparison of measured elevation radiation patterns in the principal planes for all switch states of the RRPA.

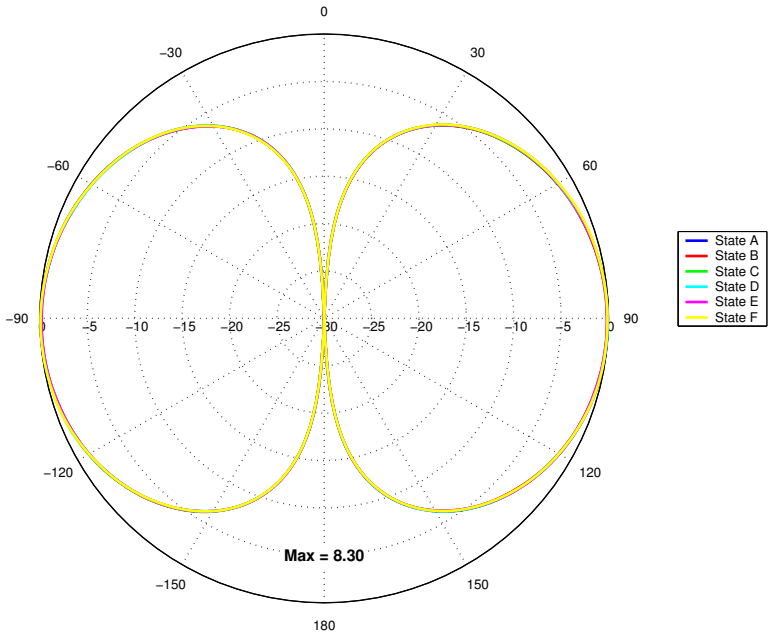

(a) E_θ ($\theta = 10°$)

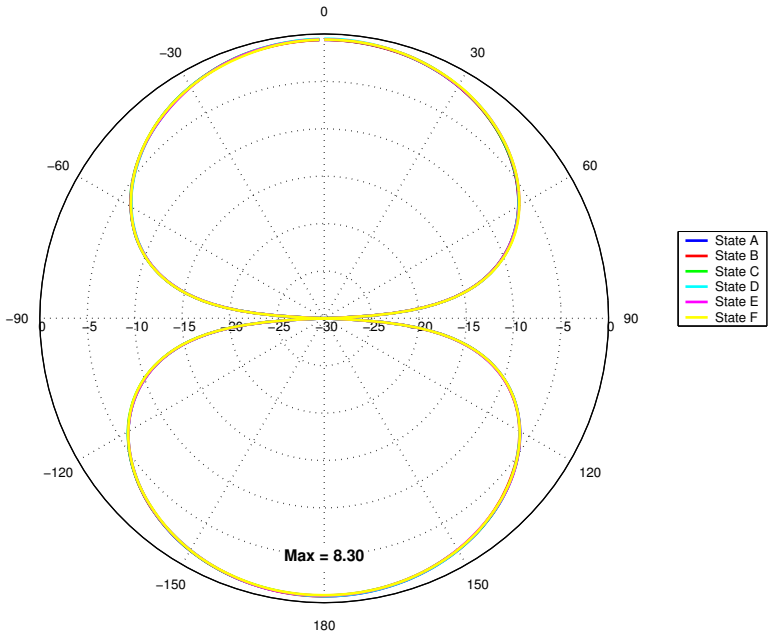

(b) E_ϕ ($\theta = 10°$)

Figure 4.19 Comparison of measured conical radiation patterns for all switch states of the RRPA.

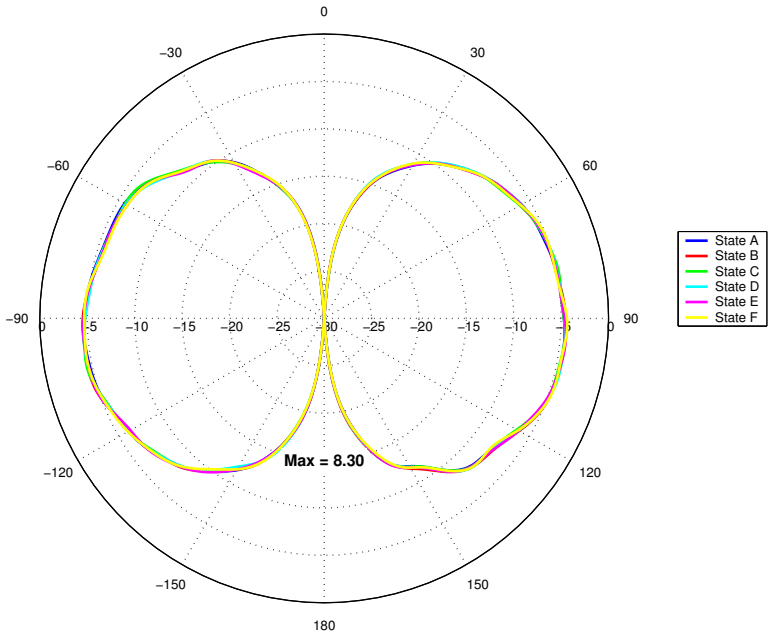

(a) E_θ ($\theta = 45°$)

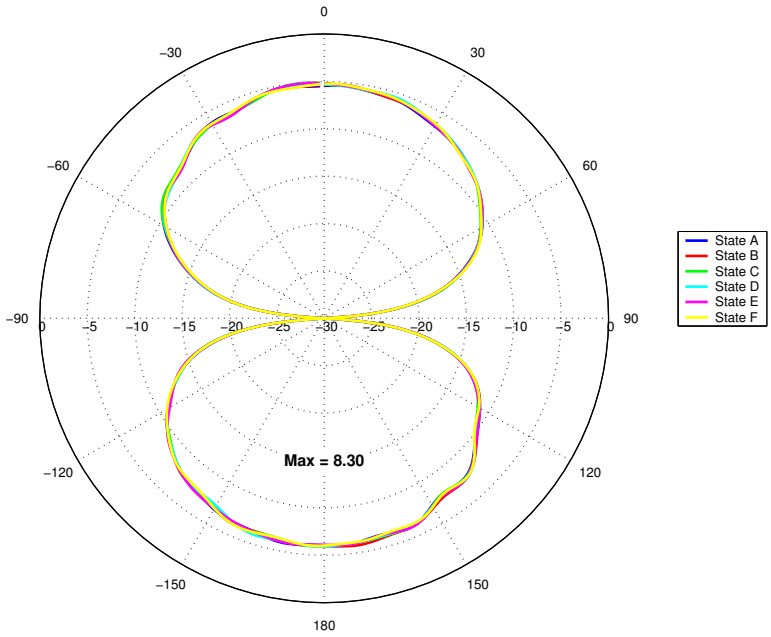

(b) E_ϕ ($\theta = 45°$)

Figure 4.20 Comparison of measured conical radiation patterns for all switch states of the RRPA.

4.5 Summary

The development, design, computer simulation and measurement of the reconfigurable ring patch antenna was presented in this chapter. The RRPA can be viewed as an extension to the classical square or annular ring patch with bandwidth controllable behavior. A total of 80 RF switch locations were incorporated into the design to achieve the desired reconfigurable bandwidth performance. A selectable bandwidth of 0-15% was attained with minimal impact other antenna radiation characteristics. Table 4.5 summarizes the selectable bandwidth characteristics of the RRPA. The measured antenna performance was shown to be very similar to the computed performance and demonstrates that the antenna indeed provides the desired bandwidth control.

Table 4.5 Selectable bandwidth performance for the reconfigurable ring patch antenna with switch states of Figure 4.6.

	Center Frequency	Minimum	Bandwidth 2:1 VSWR	
State	f_o (GHz)	VSWR	(MHz)	(%)
A	2.50	1.05	375	15.0
B	2.53	1.10	340	13.4
C	2.53	1.20	295	11.7
D	2.53	1.10	230	9.1
E	2.52	1.45	140	5.6
F	2.50	1.95	15	0.6

Chapter 5

Analysis and Measurement of Reconfigurable Planar Inverted-F

This chapter presents the design and analysis of the reconfigurable planar inverted-F antenna. The newly developed antenna achieves an adjustable bandwidth of up to 16% while maintaining constant performance over other electrical characteristics. The antenna structure is presented along with an explanation of its operation. The methods used for controllable bandwidth are given, an analysis of its bandwidth controllable behavior is detailed and finally measured results are presented for the antenna.

5.1 Introduction

The planar inverted-F antenna (PIFA) is a very popular solution for compact and embedded mobile devices. Its small size, light weight and low production cost coupled with very favorable radiation characteristics have made it particularly appealing for consumer level personal communication devices such as cell phones and PDAs. The PIFA and its variations have also become popular because of their ability to overcome one of the primary limitations inherent to low-profile antennas—narrow bandwidth. Compact antenna bandwidth is typically limited by impedance matching issues within the system where the antenna must be favorably matched to 50 Ω. Whereas conventional microstrip patch antennas are usually limited to a few percent bandwidth [7],

conventional PIFA designs without complicated matching or tuning schemes have been shown to offer 10% bandwidth [13]. The gain and pattern characteristics for common PIFAs are also very favorable for personal communication devices. Mobile devices typically require omnidirectional patterns in the azimuthal direction because the position of the user relative to the base station is normally not known. The PIFA radiation pattern is omni or near-omnidirectional in most cases and 1-4 dB peak gain is common. These attractive radiation characteristics are accomplished within antenna packages normally less than $\lambda/4$ in length and $\lambda/10$ in height.

Numerous literature sources describe geometric variations on the basic PIFA design for achieving specific performance enhancements [13, 15, 12]. Antenna size reduction, pattern manipulation, and bandwidth improvement are common design goals. Several studies have reported the effects of ground plane size on the impedance properties of the PIFA [78, 79]. During the investigation of conventional PIFA designs and the ground plane effects, it was determined that the PIFA impedance bandwidth could be altered by changing the ground plane size and aspect ratio. These findings lead directly to the invention of the reconfigurable planar inverted-F antenna (RPIFA) which is presented here. The RPIFA performs similar to a conventional PIFA but with the ability to control the bandwidth of operation. It achieves bandwidth adjustable behavior by altering the ground plane length via RF switching elements.

5.2 Antenna Structure

This section presents the reconfigurable planar inverted-F antenna geometry. The PIFA is an example of a small antenna that is operated over an electrically small finite ground plane. The geometry of the newly developed RPIFA is shown in Figure 5.1. The antenna consists of a rectangular top radiating plate suspended via two posts above a finite ground plane. The top plate is 26 mm long, 34 mm wide and at a height of 11 mm above the ground plane. The top plate is positioned 5 mm away from the edge of the ground plane and centered along the y-axis. The ground plane contains the reconfigurable portion of the antenna and has an envelope that is 117.5 mm long and 42 mm wide corresponding to $0.6\lambda \times 0.2\lambda$. The details of the ground plane are

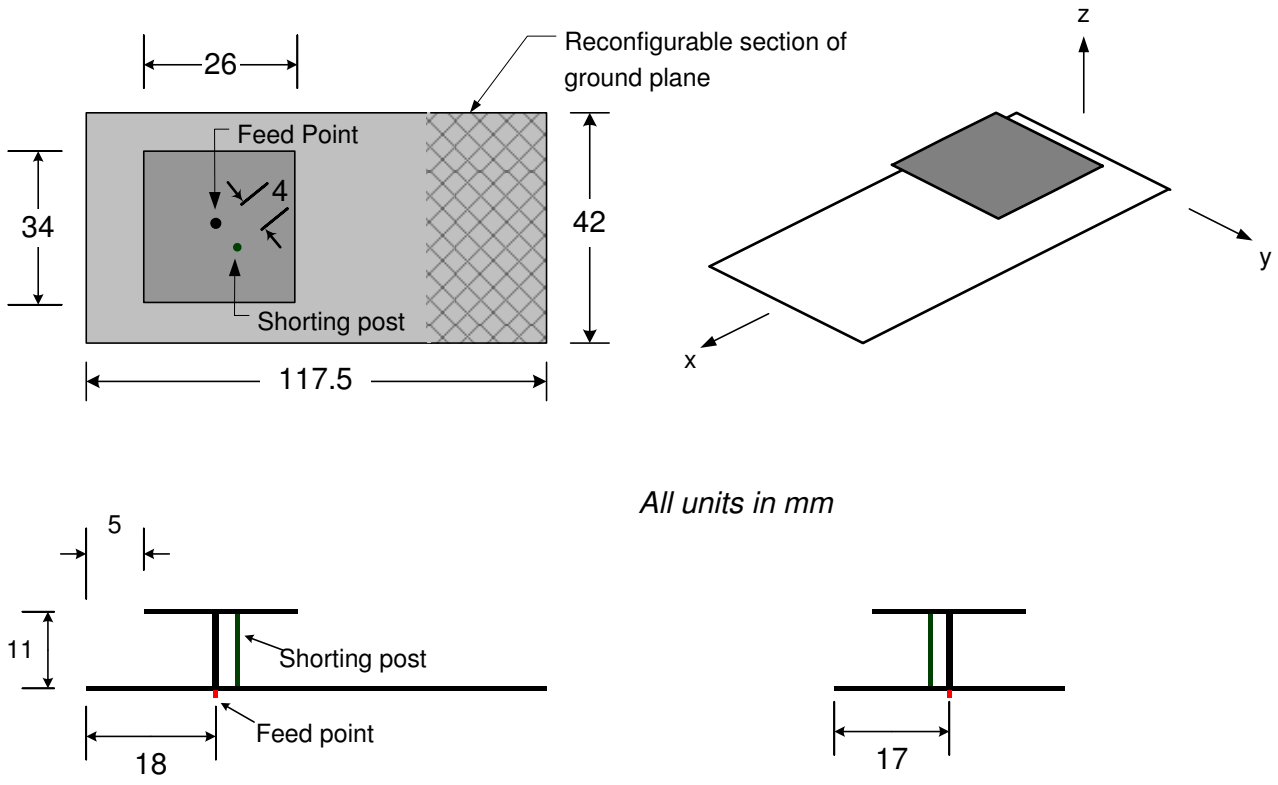

Figure 5.1 Geometry of the reconfigurable planar inverted-F antenna that operates at 1.5 GHz. Units are in mm.

presented in Sections 5.2.1 and 5.2.2. The antenna is fed from the underside of the ground plane with the feed pin consisting of a standard through hole type feed having a pin diameter of 1.27 mm. The feed point is 18 mm from the ground plane back edge along the x-axis. It extends through the ground plane vertically and is connected to the center of the top plate. The second feature that supports the top plate is the shorting post which connects the top plate to the ground plane and has a diameter of 0.7 mm. The shorting post is located 4 mm away from the feed pin at 45° from the x-axis.

5.2.1 Ground Plane Influence On Bandwidth

While conventional PIFA designs offer relatively large impedance bandwidths, new broadband communication applications have forced designers to create novel methods for widening the bandwidth [13]. Common approaches employed for increasing the bandwidth include increasing the height of the radiating top plate above the ground plane, varying the position and width of the shorting post, altering the aspect ratio of the top plate and the inclusion of parasitic or dielectrically loaded elements. PIFA variations utilizing these modifications have demonstrated single-band bandwidths as high as 40% [79] several have been described that offer dual [12, 18] and triple band behavior [80]. While these techniques provide mechanisms for modifying the PIFA bandwidth, none provide a convenient manner for use with reconfigurable antenna components such as planar RF switches. Additionally, bandwidth enhancement via these methods typically comes at the expense of other electrical characteristics; pattern and polarization purity are often sacrificed for impedance bandwidth enhancements.

Several studies have been performed on the effects of ground plane size on small antennas [81, 82, 83, 84] and a very limited number of sources exists on PIFA ground plane effects [79, 85]. A parametric study was performed by Huynh [85] that provides a detailed description of ground plane size effects on a canonical edge-strap shorted PIFA configuration. It was found, for a square top plate and square ground plane, that the relative bandwidth increases with increasing ground plane dimensions for small ground planes less than one wavelength in size. The bandwidth increases from 4% for a ground plane of 0.2λ to 10% for a ground plane of 1.0λ. However, the impedance bandwidth does not grow unbounded for increasing ground plane sizes. Once the ground plane size reaches about one wavelength in extent the bandwidth oscillates around 8%—the relative bandwidth for the same PIFA with an infinite ground plane. Huynh [85] also reported that the ground plane size can have a marked influence on antenna gain. Very small ground planes ($L < 0.5\lambda$) tend to have small peak gain values of around 1 dB and as the ground plane size reaches 0.65-0.75 λ the peak gain tends to flatten out at around 4 dB.

The results presented in [79, 85] provide a starting point for the bandwidth reconfigurable PIFA design. While it was shown that the ground plane size can have

a large effect on all radiation parameters, careful attention to the top plate design and shorting post configuration along with judicious ground plane envelope selection can result in the desired bandwidth control without significant impact on other radiation properties. The selection of an elongated ground plane and top plate form, as opposed to a square shape, results in currents that are primarily directed in the longitudinal direction. Thus, the input impedance can be varied by altering only the length of the ground plane.

An investigation was conducted using IE3D to quantify the effects of ground plane length, L, on antenna bandwidth for the geometry of Figure 5.1. The results obtained from this investigation are used in the subsequent sections to develop discrete ground plane length states for the reconfigurable antenna geometry. The ground plane length was varied while its width, $W = 42$ mm, was kept constant. All other PIFA dimensions were held constant as well: top plate height, $H = 11$ mm; width, $u = 34$ mm; and length, $v = 26$ mm. Figure 5.2 shows the calculated VSWR for ground plane lengths of 50 to 130 mm. The curves shown in solid represent ground plane lengths where the the center frequency remains fixed at 1.53 GHz and the VSWR is less than 2:1. The ground plane lengths shown by these solid curves represent lengths that are suitable for the subsequent reconfigurable design. It can be seen that ground plane lengths less than 130 mm yield VSWR plots which are within the 2:1 criteria. However, when the ground plane length falls below 85 mm, the center frequency, f_0 begins to move away from 1.53 GHz. Figure 5.3 plots the computed bandwidth as a function of ground plane length, L, for the RPIFA shown in Figure 5.1. The bandwidth behavior is similar to that seen in [85] as the bandwidth initially increases with ground plane length and then decreases. Table 5.1 summarizes the electrical performance of the PIFA from Figure 5.1 based on different ground plane lengths simulated using IE3D. Note that the bandwidth peaks at 18% for a ground plane length of L= 80 mm. This maximum bandwidth is slightly larger than the maximum bandwidth of 10% reported by Huynh [78].

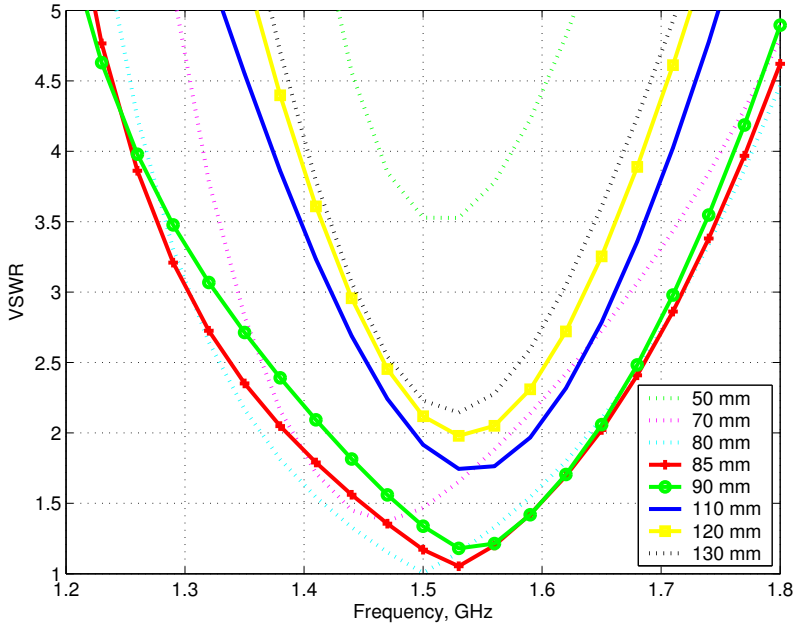

Figure 5.2 VSWR versus frequency of the planar inverted-F antenna of Figure 5.1 for various ground plane lengths, L, computed using IE3D.

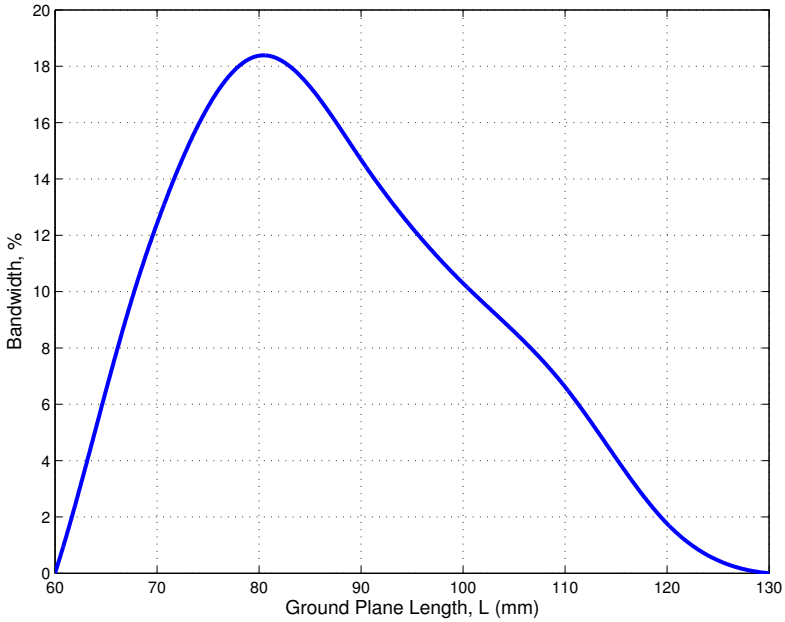

Figure 5.3 Bandwidth versus ground plane length for the geometry in Figure 5.1 computed using IE3D.

Table 5.1 Electrical performance based on ground plane length, L, for the PIFA of Figure 5.1 simulated using IE3D.

Ground plane length, L		Center frequency	Minimum	Bandwidth
(mm)	(wavelengths)	f_0 (GHz)	VSWR	2:1 VSWR (%)
50	0.255	1.52	3.49	-
60	0.306	1.49	2.28	-
65	0.332	1.48	1.77	6.5
70	0.357	1.48	1.37	12.4
80	0.408	1.5	1.01	18.4
85	0.434	1.53	1.05	17.3
90	0.459	1.54	1.17	14.7
100	0.510	1.54	1.44	10.3
110	0.560	1.54	1.73	6.6
120	0.612	1.54	1.98	1.8
130	0.663	1.53	2.14	-
140	0.714	1.51	2.16	-

5.2.2 The Reconfigurable Planar Inverted-F Antenna

Specific discrete ground plane lengths were selected for several antenna bandwidth values based on the ground plane length investigation performed in Section 5.2.1. Five ground plane lengths were chosen to achieve discrete bandwidth states from 0% (effectively off) to 17% (maximum bandwidth.) These ground plane lengths are used in the subsequent sections to accomplish the desired reconfigurable bandwidth performance. Table 5.2 summarizes the discrete ground plane lengths, L, selected to achieve the bandwidth controllable behavior along with the predicted bandwidth values based on the ground plane length investigation in Section 5.2.1.

Table 5.2 Discrete ground plane lengths for selected antenna bandwidth states based on simulations from Section 5.2.1.

	Length		Bandwidth
State	(mm)	(wavelengths)	2:1 VSWR (%)
A	85.0	0.43	17
B	91.7	0.47	15
C	98.1	0.50	10
D	104.5	0.53	7
E	117.5	0.60	0

To determine a suitable method for altering the length of the ground plane a second numerical investigation was performed. Figure 5.4 shows the average current distribution on the ground plane of antenna from Figure 5.1 computed using IE3D. Along the length of the structure, the current is primarily constrained to the long edges of the ground plane. The fact that the current on the ground plane is located along the edge of the conductor will be exploited to achieve the reconfigurable bandwidth goal.

The ground plate is replaced by a five smaller ground plate sections separated by 0.3 mm gaps as shown in Figure 5.5. The ground plate section on the radiative feed end of the antenna is 85 mm long. The three ground plate strips closest to the feed end are 6.1 mm long and the outer strip is 12.7 mm long. The larger segment is required at the outer end of the ground plate because the current intensity decreases away from the feed, thus having a reduced impact on performance. Figures 5.6(a)-5.6(e) show the

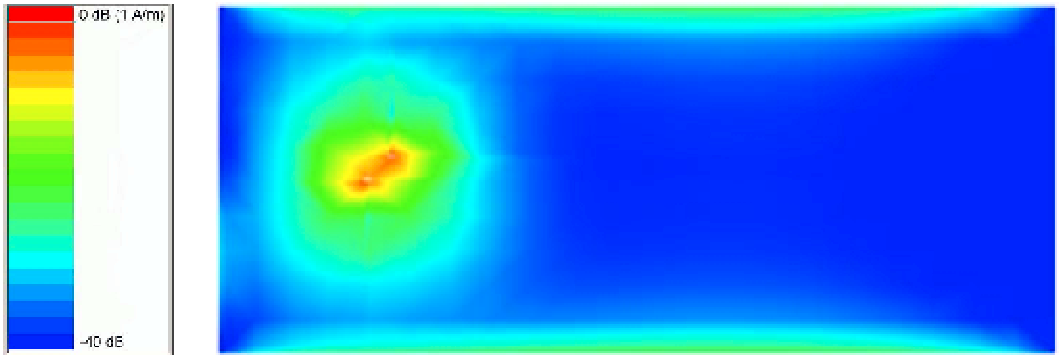

(a) scale (b) current on ground plane

Figure 5.4 Average current distribution on RPIFA ground plane computed using IE3D.

layout of the ground plate switches and detail the discrete switch states. The switches span the 0.3 mm gap separating the ground plate section and when activated connect adjacent sections. A set of switches are also placed along the ground plane central axis and ensure continuity of the current gradient across the width of the ground plane. This prevents current loops on the ground plane strip sections.

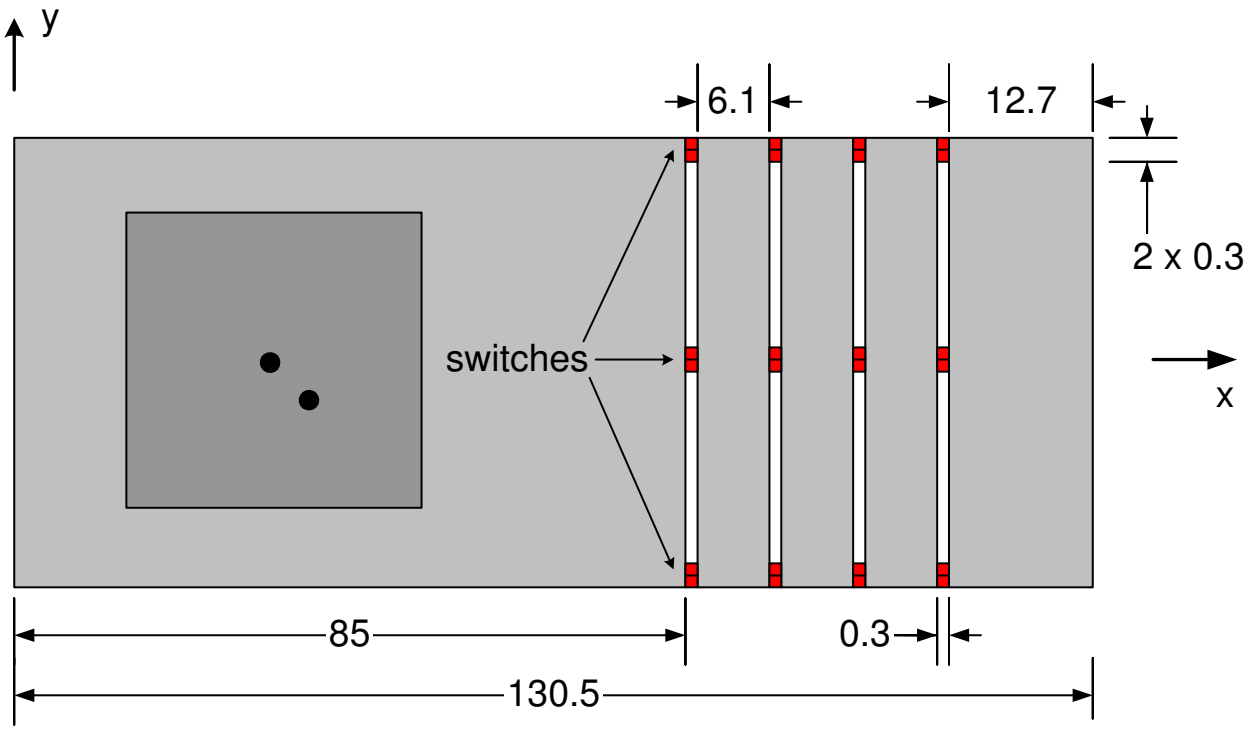

Figure 5.5 Reconfigurable planar inverted-F with active ground plate and RF switch locations.

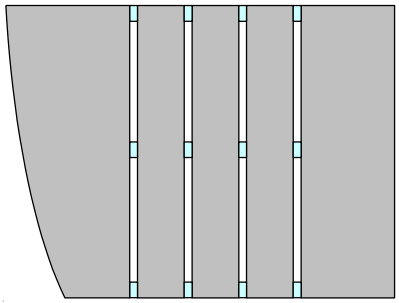

(a) state A, $L = 85.0$ mm

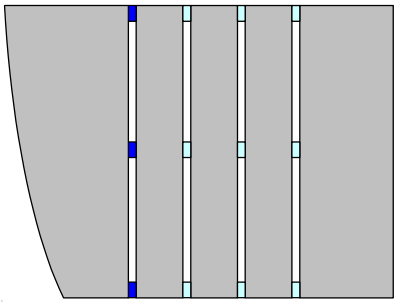

(b) state B, $L = 91.7$ mm

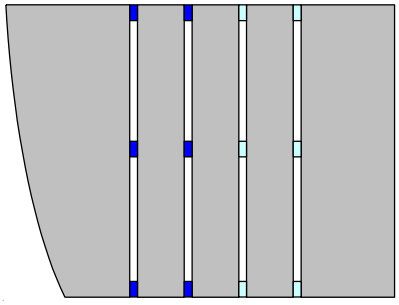

(c) state C, $L = 98.1$ mm

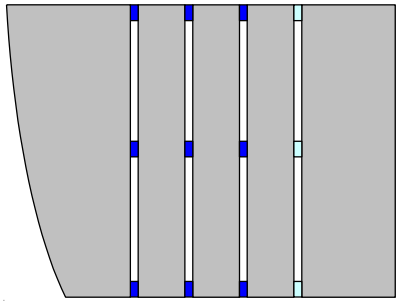

(d) state D, $L = 104.5$ mm

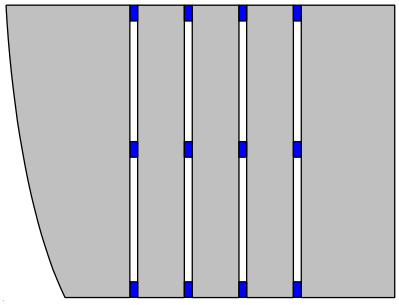

(e) state E, $L = 117.5$ mm

Figure 5.6 Reconfigurable PIFA active layer switch configuration states. Switches in *on* position are shown in dark, switches in *off* position are shown in light.

5.3 Simulation of RPIFA

The commercial code IE3D was the primary simulation tool used for studying the RRPA. IE3D is a full-wave frequency-domain package utilizing a laterally-open moment method engine capable of simulating arbitrary metalization geometries and was described in Section 4.3. The simulation model of the RPIFA does not contain dielectric components thus it is not subject to the 2.5 dimensional substrate caveat of finite extent substrates as was seen in the ring patch model. There is however, a small section of dielectric material used in the feed post of the prototype antenna that will be ignored for now.

Figure 5.7 shows the computed input impedance for the antenna switch states of Figure 5.5. The real part of the impedance varies between 25 Ω for state E and and 50 Ω for state A, while the imaginary part is between -18 Ω and -5 Ω. This provides a very close match to 50 Ω at the design frequency of 1.53 GHz. The desired antenna bandwidth control is facilitated primarily by altering the real part of the input impedance as seen in Figure 5.7. Figure 5.8 shows the corresponding VSWR for the switch states referenced to 50 Ω. As was predicted from Figure 5.3, the largest bandwidth is seen with the ground plane in state A. The ground plane length in state A is 85 mm, or 0.44 λ, and results in a relative antenna bandwidth of 15.4 %. Table 5.3 summarizes the computed 2:1 VSWR impedance bandwidth and geometry parameters for the RPIFA with switch states of Figure 5.6.

Table 5.3 Impedance bandwidth performance and reconfigurable ground plate geometry for the RPIFA with switch states of Figure 5.6 computed using IE3D

State	Ground plate R_w length, L (mm)	Center frequency f_o (GHz)	Bandwidth 2:1 VSWR (%)	Minimum VSWR
A	85.0	1.53	15.8	1.13
B	91.7	1.54	12.4	1.30
C	98.1	1.54	9.4	1.51
D	104.5	1.54	5.1	1.76
E	117.5	1.53	0	2.10

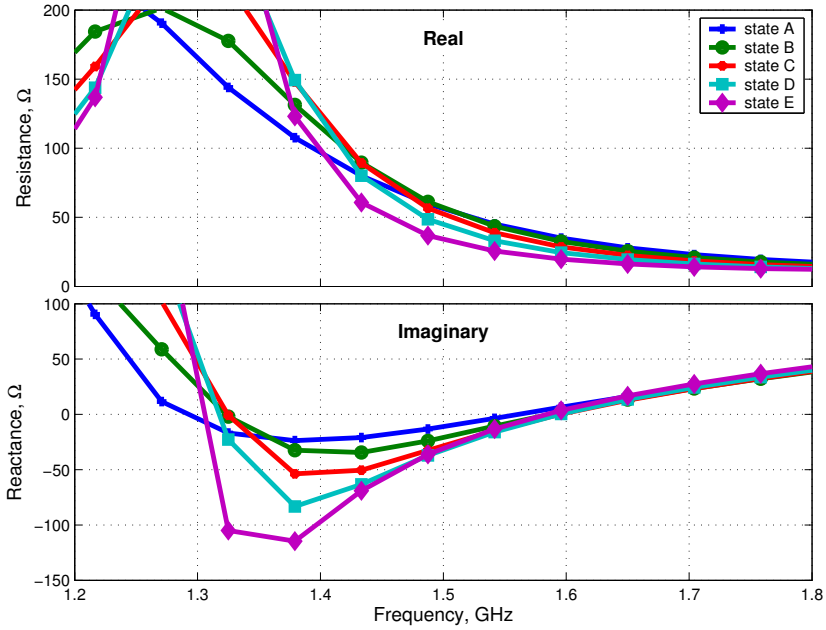

Figure 5.7 Input impedance versus frequency of the reconfigurable planar inverted-F antenna for switch states of Figure 5.6 simulated using IE3D.

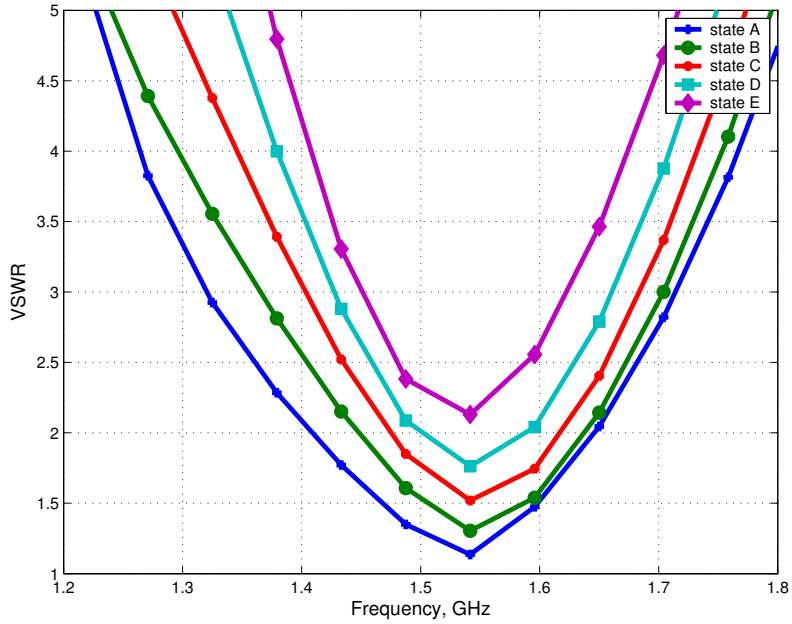

Figure 5.8 VSWR versus frequency of the reconfigurable planar inverted-F antenna for switch states of Figure 5.6 simulated using IE3D.

5.4 Experimental Results for RPIFA

The prototype RPIFA of Figure 5.9 was constructed and its electrical properties were measured in order to verify the theoretical and simulation results. The top plate and 42×85 mm ground plate section were constructed from standard 25 mil hobby brass. The ground plate strip sections were constructed with 30 mil hobby brass. The ground plate sections were attached to a 76×45 cm piece of 62 mil RT/Duroid 5870 for mechanical support. The sections were attached to the Duroid with common double sided tape. Figure 5.10 shows a side view of the antenna feed end. An extended length SMA connector was used as the antenna feed. This connector has the same body dimensions as a standard SMA connector with the center-pin and the dielectric sleeve extended 0.65 inches and 0.59 inches respectively. The Teflon (PTFE) extended dielectric sleeve is visible in the figure next to the shorting post. The dielectric sleeve provides a convenient structural support for the RPIFA top plate. Teflon has a dielectric constant of 2.0, thus the presence of the sleeve impacts the electrical performance of the antenna slightly. The measured center frequency of a preliminary RPIFA prototype antenna was slightly lower than the simulated results from Section 5.3. Loading effects of the dielectric and the resulting decrease in measured antenna operating frequency were compensated by reducing the height of the top plate. The compensated height was experimentally determined to be 2 mm less than the simulated design. The height of the top plate, H, was 9 mm for the final measured prototype RPIFA. The shorting post is also visible in Figure 5.10. The post was made from hobby stock brass rod with a diameter of 1.27 mm. The post was soldered to both the top plate and the ground plate as seen in Figure 5.10.

To achieve the five antenna ground plate lengths, small strips of copper used as substitutes for the MEMS switches. The copper strips were soldered to the ground plate sections at the switch locations to simulate *on* switch states. The solder locations are visible in Figure 5.9 and correspond to the switch locations specified in Figure 5.5. The copper strips were made from standard copper tape and were approximately 0.6 mm wide. The tape switches were sufficiently long enough (2 mm) to both span the 0.3 mm gap separating the ground plate sections and provide enough metal to metal contact for good solder joints. Figure 5.11 gives a close-up view of one copper tape switch

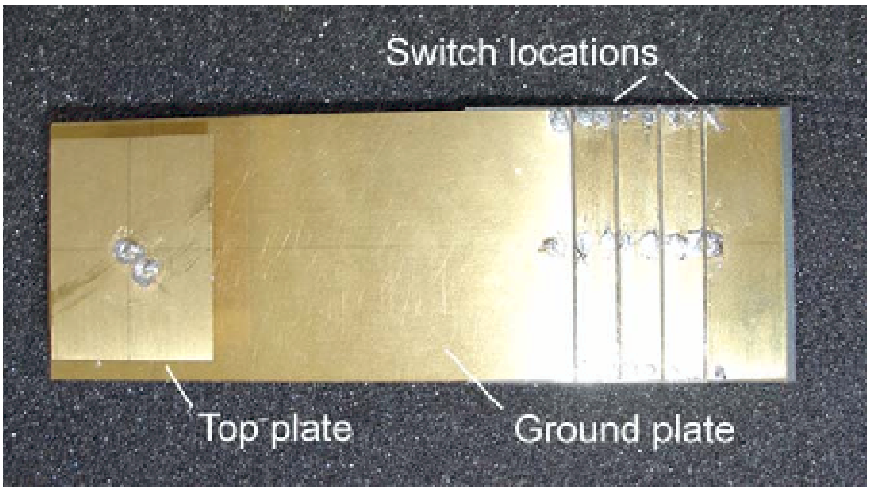

Figure 5.9 Hardware test model of the RPIFA with switch states specified from Figure 5.6.

connecting adjacent ground plate strip sections.

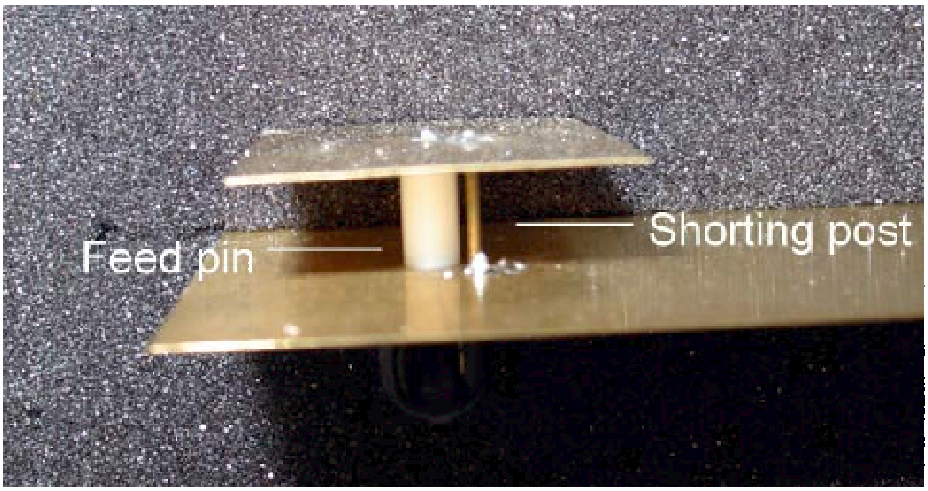

Figure 5.10 Feed end of RPIFA hardware test model showing dielectric sleeve and shorting post.

Figure 5.11 Close-up of copper tape RF switch for RPIFA hardware test model.

5.4.1 Impedance Measurements

All measurements of the RPIFA were performed at the Virginia Tech Antenna Group's antenna test facility. Impedance measurements of the RPIFA were made using an HP8510C vector network analyzer. The measurement unit consisted of the antenna under test (AUT) and a PVC mounting fixture. The AUT was secured to the PVC fixture and then mounted to the near-field scanner AUT positioner inside the anechoic chamber to minimized external disturbances. While the impedance measurements were being performed, the AUT positioner was pointed toward the closed chamber door to further reduce any unwanted reflections and maintain repeatability between measurements. RF absorber was placed around the metal AUT tower and behind the PVC fixture to minimize any reflections from the tower and mounting fixture. Considerable effort was taken to minimize any unwanted reflection in the test environment and to ensure repeatability between antenna measurements. Before the final impedance measurements were performed, the setup was validated by measuring the input impedance of a known 1.5 GHz $\lambda/4$ monopole antenna. The S-parameter values and input impedance values obtained from this measurement confirmed that the measurement setup provided a suitable test environment.

The measured impedance data is plotted along with the respective IE3D simulated results for each switch state ground plane configuration. The measured input impedance referenced to 50 Ω is shown in Figure 5.12. Acceptable agreement is seen between the measured and simulated data, particularly around the design frequency of 1.53 GHz. The reactance plots show very good agreement for all states over most of the measured bandwidth. In all switch states, the simulated reactance tends be slightly higher than the measured reactance at the lower frequencies. The measured resistance plots follow the same general curves as the simulated data for all states. However, the measured resistances are slightly higher than the computed values at the lower frequencies and somewhat lower at the higher frequencies. The net effect of this minor divergence in impedances at the higher frequencies can be seen in the VSWR plots. Figures 5.13(a) - 5.13(e) show the measured VSWR compared to the computed VSWR for all antenna states. Above the center frequency, the measured VSWR levels do not increase as quickly as the computed values for all antenna states.

The measured bandwidths are slightly larger than the predicted values, most likely due to loss mechanisms caused by the PTFE sleeve that is present in the experimental antenna but not in the computed model. There is also a small amount of high order ripple in the measured VSWR plots, particularly at the higher frequencies. Measured ripple of this type is often caused by connector mismatch or external reflections. Figure 5.14 shows a comparison of the five measured VSWR values. Because of the ripple on the measured VSWR curves, the comparison plot is not as clean as the computed plot, however the trend of increasing bandwidth with decreasing ground plane length is present. Figure 5.15 re-plots a comparison of the measured impedance data as return loss for all switch states. Again, the bandwidth control is visible for each ground plane switch state. Table 5.4 gives a summary of the measured and simulated 2:1 VSWR impedance bandwidth performance of the RPIFA.

Table 5.4 Summary of the measured and simulated 2:1 VSWR impedance bandwidth performance for the RPIFA.

	Bandwidth 2:1 VSWR (%)		Center Frequency f_o (GHz)		Minimum VSWR	
State	measured	simulated	measured	simulated	measured	simulated
A	16.0	15.8	1.55	1.53	1.40	1.13
B	13.4	12.4	1.56	1.54	1.45	1.30
C	8.5	9.4	1.57	1.54	1.65	1.51
D	6.4	5.1	1.57	1.54	1.75	1.76
E	1.3	0	1.54	1.53	1.95	2.10

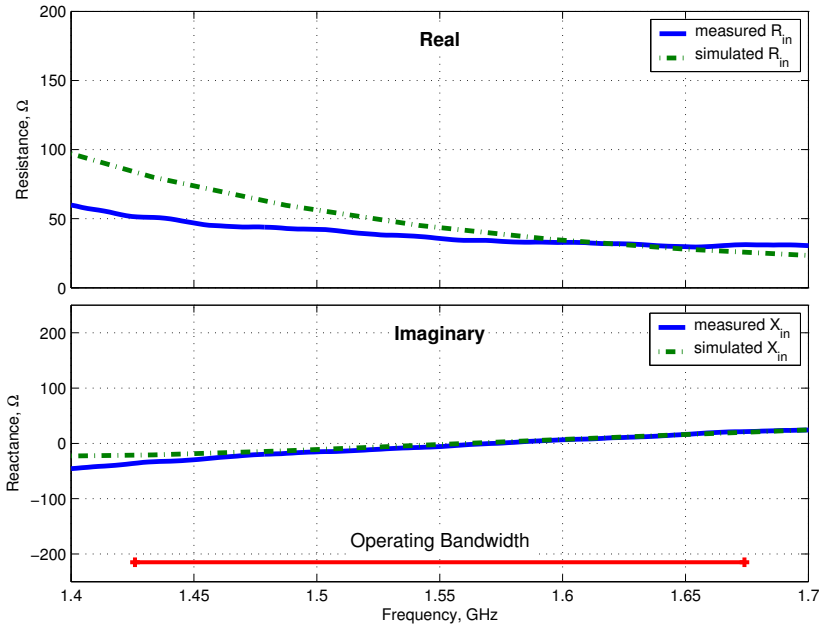

(a) switch state A

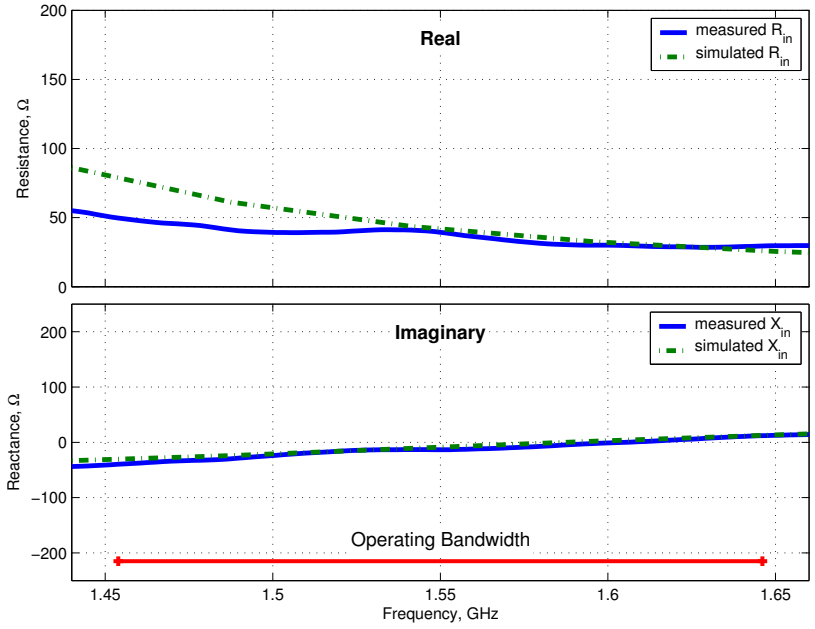

(b) switch state B

Figure 5.12 Measured and simulated input impedance for the reconfigurable PIFA.

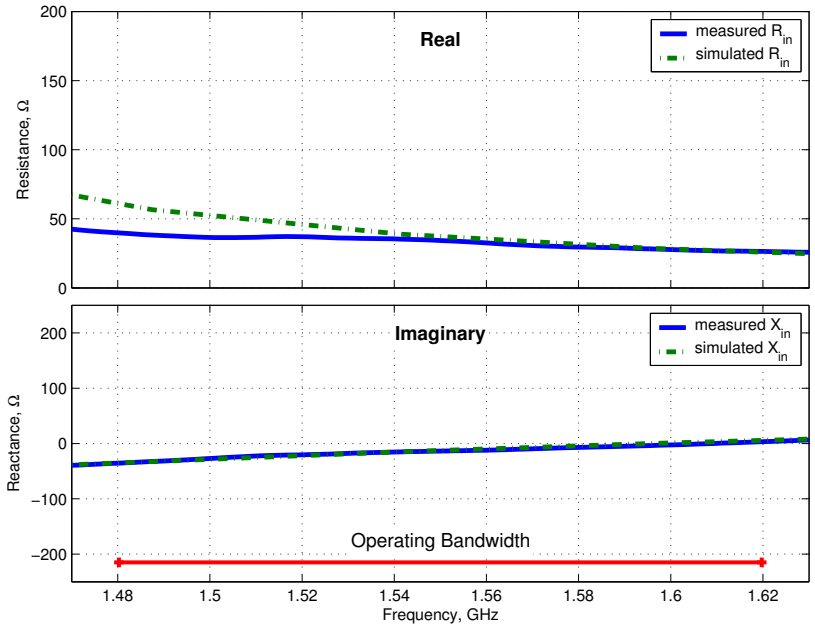

(c) switch state C

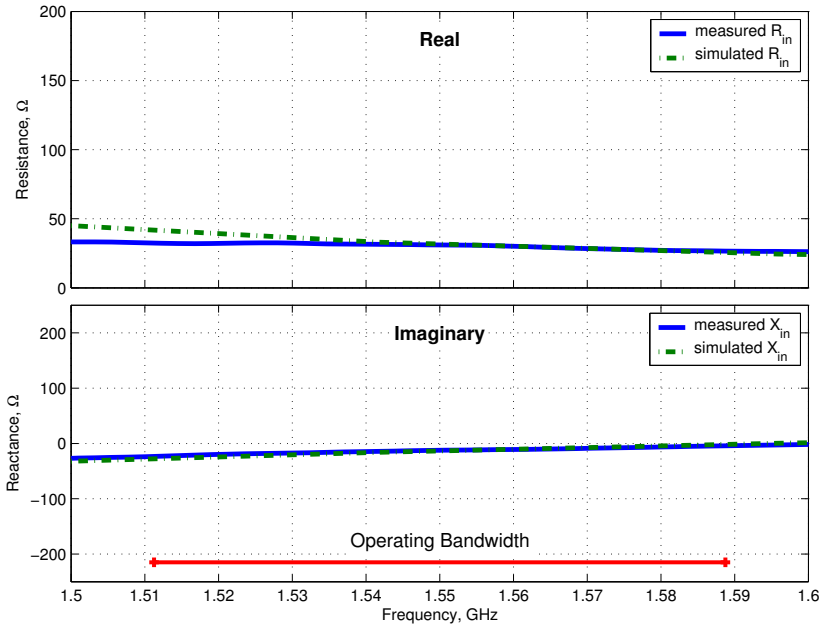

(d) switch state D

Figure 5.12 Measured and simulated input impedance for the reconfigurable PIFA (cont.)

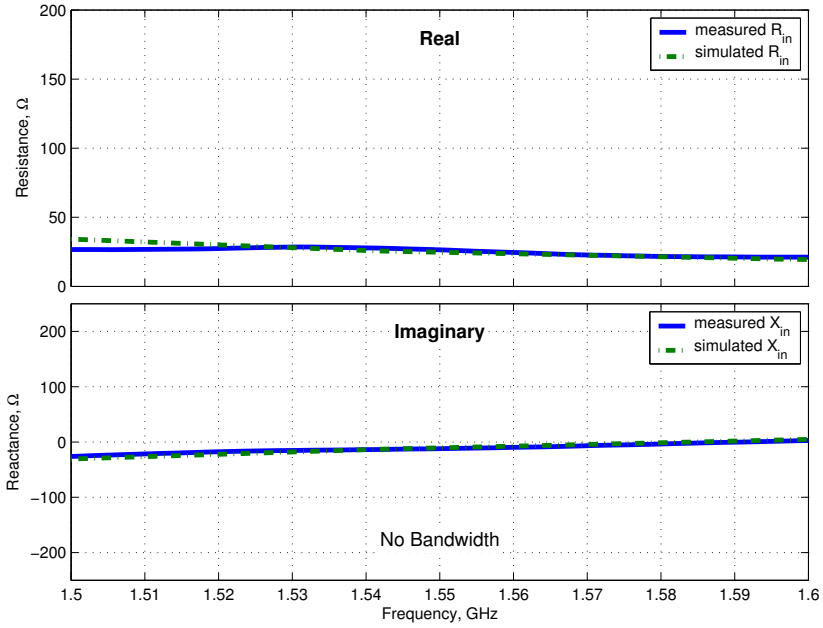

(e) switch state E

Figure 5.12 Measured and simulated input impedance for the reconfigurable PIFA (cont.)

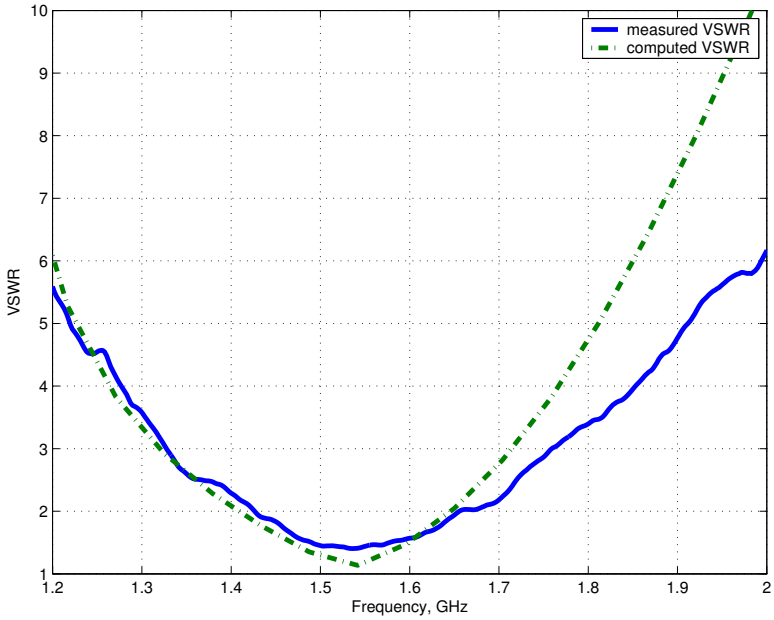

(a) switch state A

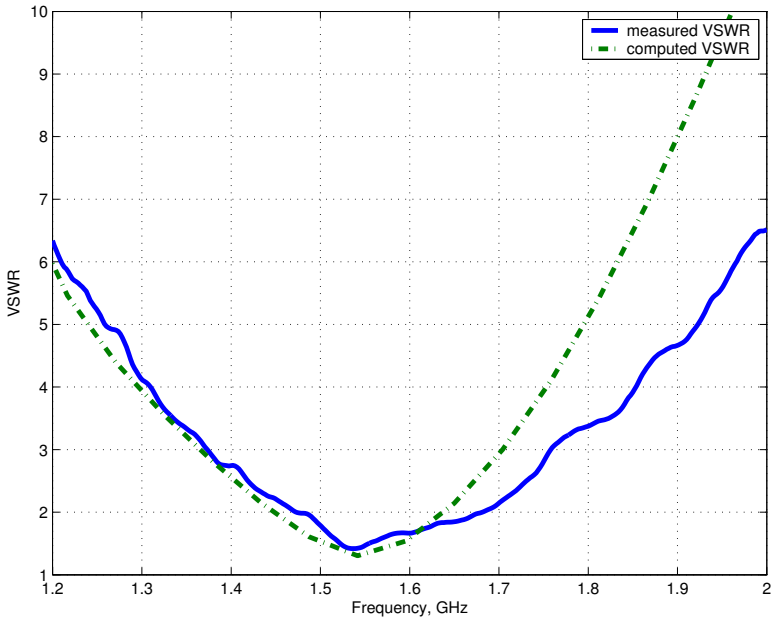

(b) switch state B

Figure 5.13 Measured and simulated voltage standing wave ratio for the reconfigurable PIFA.

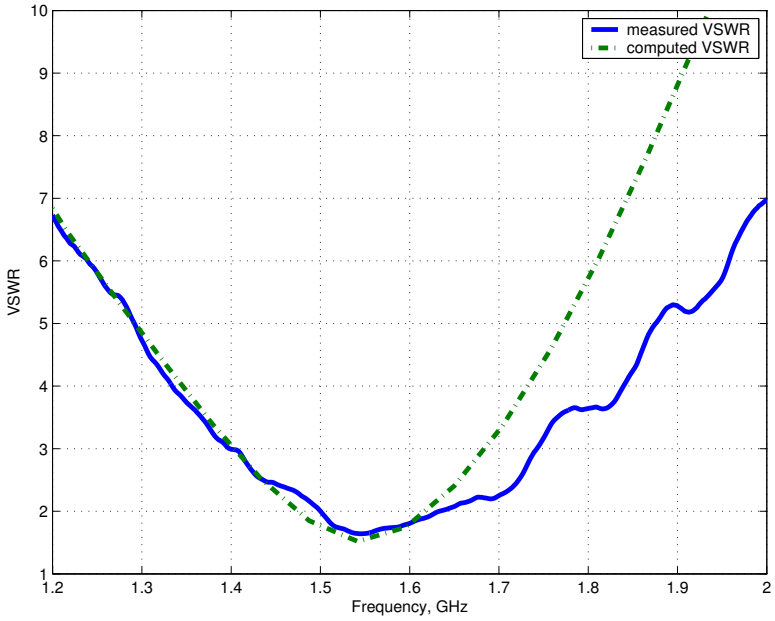

(c) switch state C

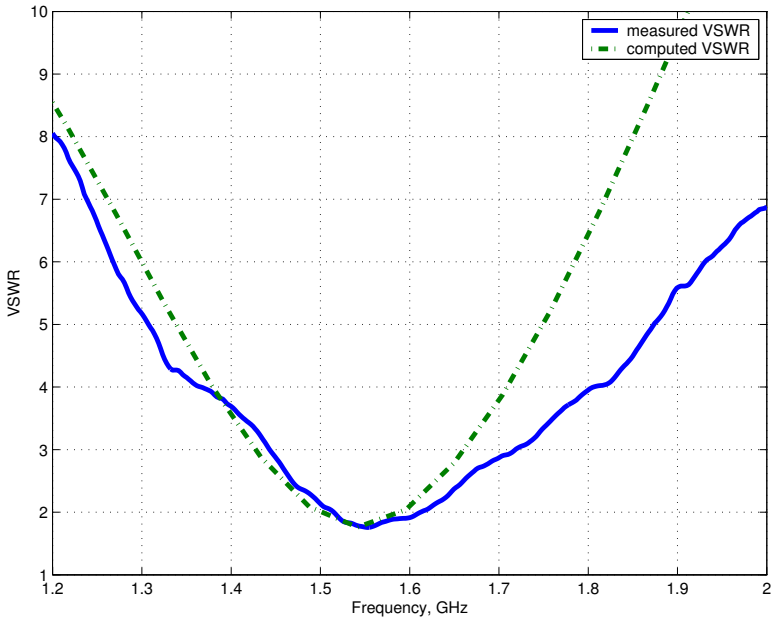

(d) switch state D

Figure 5.13 Measured and simulated voltage standing wave ratio for the reconfigurable PIFA (cont.)

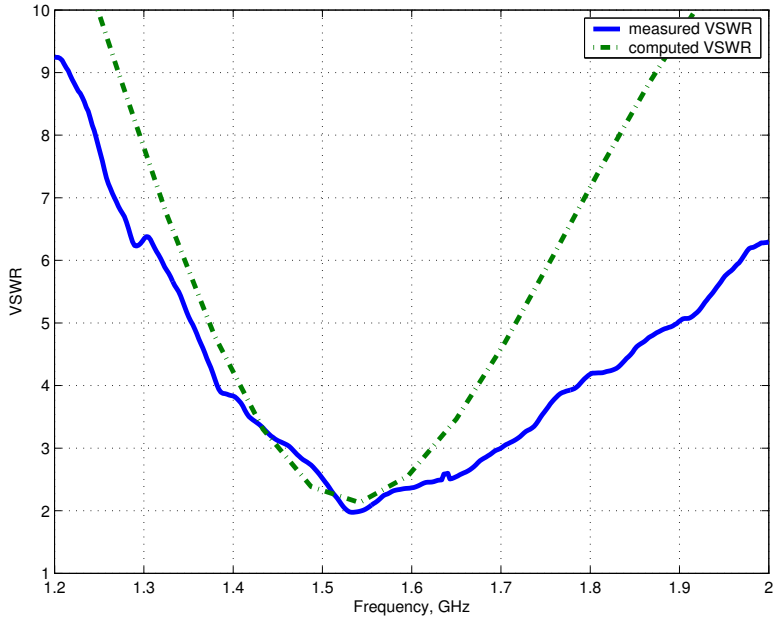

(e) switch state E

Figure 5.13 Measured and simulated voltage standing wave ratio for the reconfigurable PIFA(cont.)

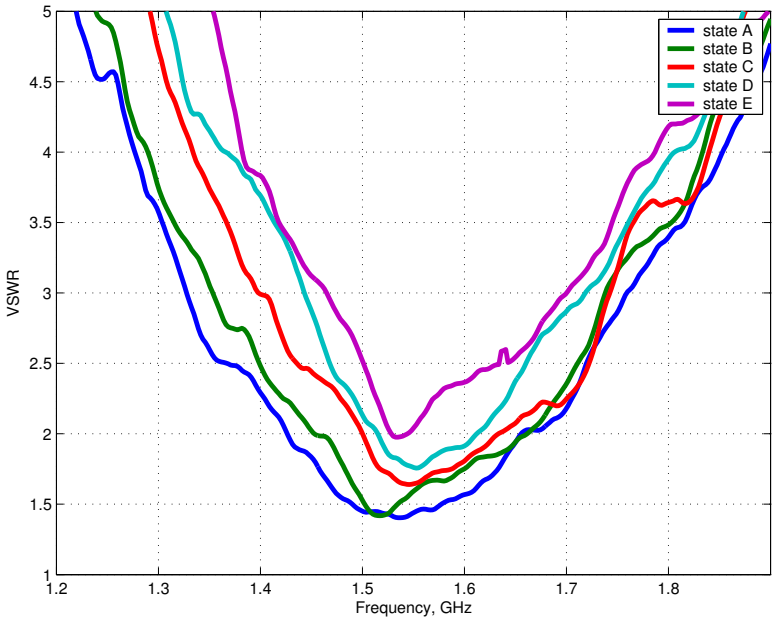

Figure 5.14 Measured voltage standing wave ratio for the reconfigurable PIFA in all states.

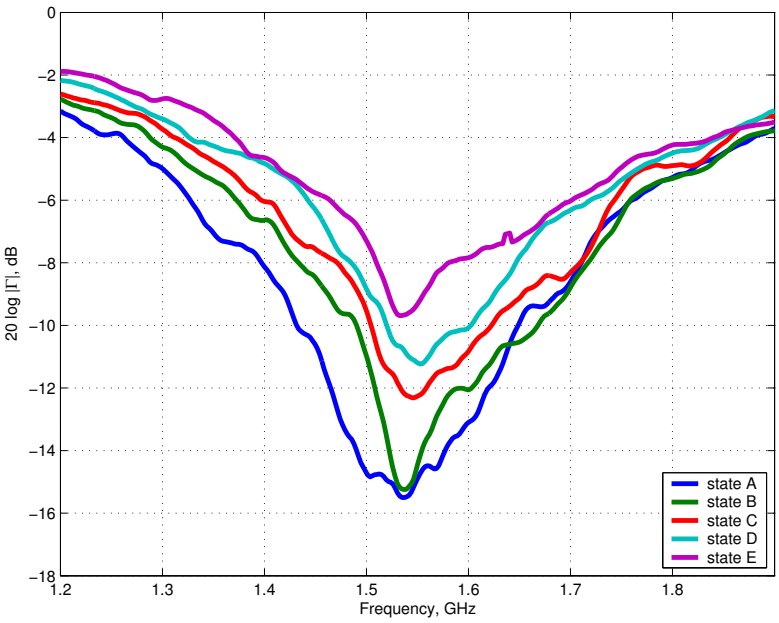

Figure 5.15 Measured return loss for the reconfigurable PIFA in all states.

5.4.2 Pattern Measurements

Radiation patterns were measured in the VTAG indoor anechoic chamber using the near-field scanner. The antenna patterns were measured with the system operating in spherical scanning mode. The pattern measurement test setup consisted of the same equipment used in the impedance measurements of Section 5.4.1. However, for the pattern measurements the AUT was connected to the near-field scanner through the AUT positioner. Additional absorber was placed behind the test antenna and around the AUT tower to minimize any reflections from the test equipment. Prior to performing the final pattern measurements on the AUT, the setup was validated by measuring the radiation patterns of a known 1.5 GHz $\lambda/4$ monopole antenna. The radiation patterns obtained from this validation measurement confirmed that the measurement setup provided a suitable test environment.

The results presented here are for 1.55 GHz. The measured patterns are presented along with the simulated results in Figures 5.16, 5.17, and 5.18. Figures 5.19, 5.20, 5.21 and 5.22 provide pattern comparisons for all ground plane length states. Typically, the radiation behavior of the PIFA is viewed as operating in either a top-hat loaded monopole mode or a dipole mode. The mode of operation is dictated by the selected PIFA geometry and the frequency of operation. The radiation pattern behavior of the RPIFA is similar to that of a z-directed dipole antenna. The pattern is primarily omnidirectional in the azimuth (x-y) planes as is seen in the conical E_θ and E_ϕ cuts of Figures 5.16 and 5.17. Unlike the dipole however, the RPIFA does not exhibit a well defined null in the elevation pattern in the x-y plane ($\theta = 90°$.) Figure 5.18 shows the elevation patterns and a reduction in radiated energy is present below the ground plate. The nulls that would be present at $\theta = \pm 90°$ in a dipole are shifted down slightly to $\theta = \pm 120°$.

Figures 5.16 and 5.17 show the measured conical cut radiation patterns at the elevation angles of $\theta = 10°$ and $\theta = 90°$, respectively. As predicted by the simulations, the radiation pattern behavior of the antenna remains fairly constant from one switch state to the next. This is a desired behavior of the antenna in order to maintain predictable performance while selecting the antenna bandwidth. There is a slight decrease in maximum directivity as the length of the ground plane increases. Figure 5.16(a) shows the

maximum value for state A was 1.1 dB and Figure 5.16(e) shows a value of −0.7 dB for state E. This effect is attributed to the lengthening of the ground plate. The measured elevation patterns are shown in Figure 5.18. The measured patterns exhibit primarily z-directed radiation as was predicted by the simulated patterns. However, there is considerable ripple seen in the measured pattern. This ripple is most likely caused by the z-directed AUT positioner where the antenna was mounted. Unfortunately, this behavior often results when measuring electrically small antennas operated without a ground plane to block the positioner interaction. Figure 5.22 shows a comparison between the measured elevation patterns for each switch state. There is relatively good agreement between the measured patterns between the switch states with only a few dB of deviation between the maximum and minimum ground plane lengths.

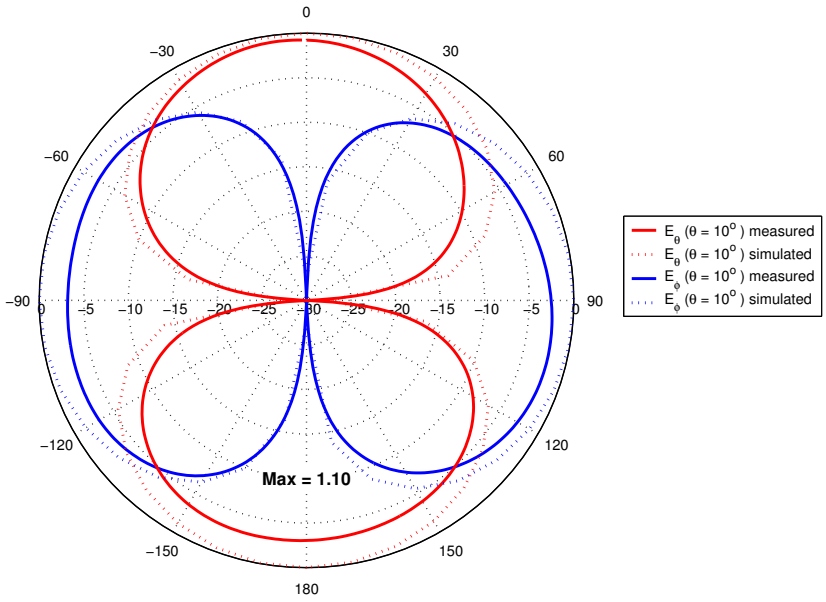

(a) switch state A

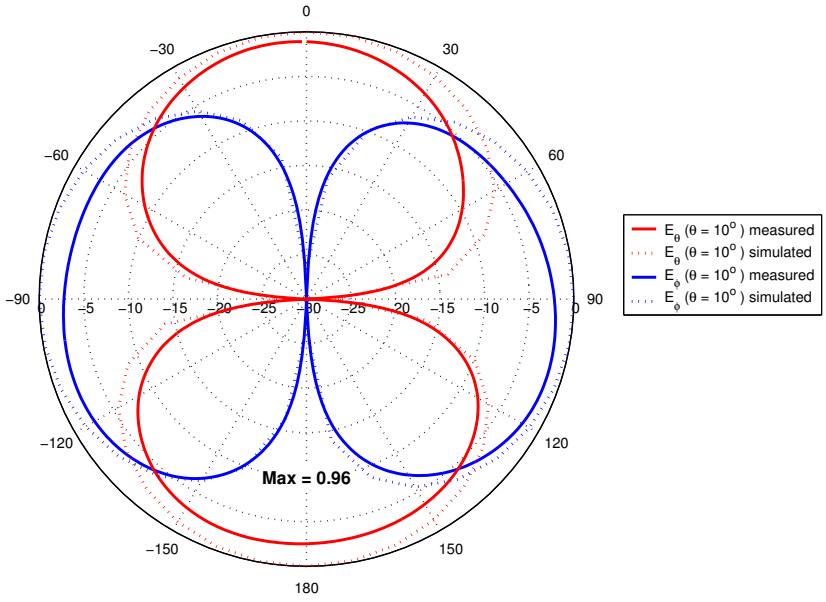

(b) switch state B

Figure 5.16 Measured and simulated conical radiation patterns for the RPIFA.

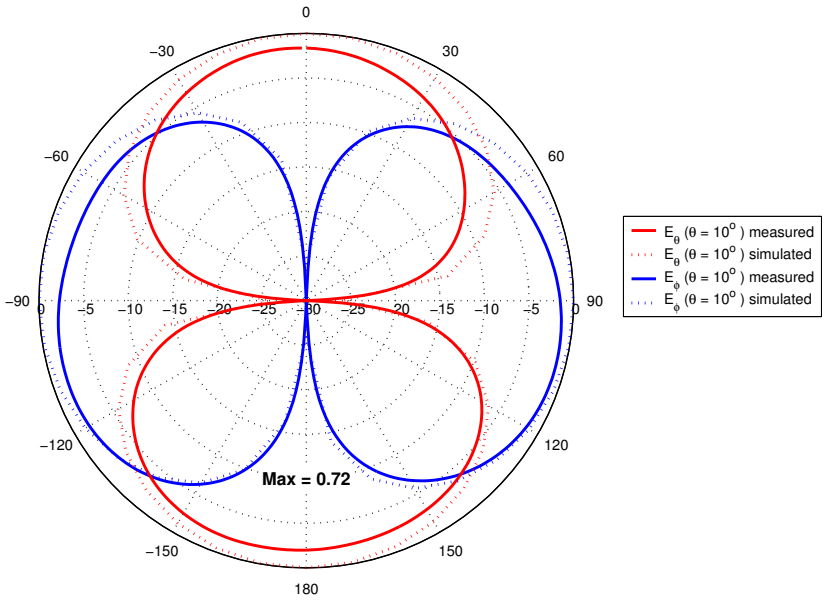

(c) switch state C

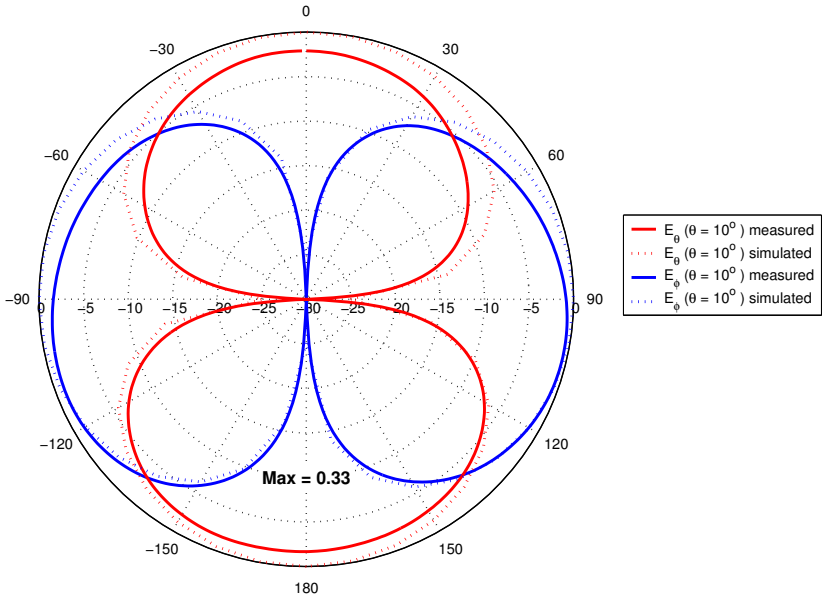

(d) switch state D

Figure 5.16 Measured and simulated conical radiation patterns for the RPIFA (cont.)

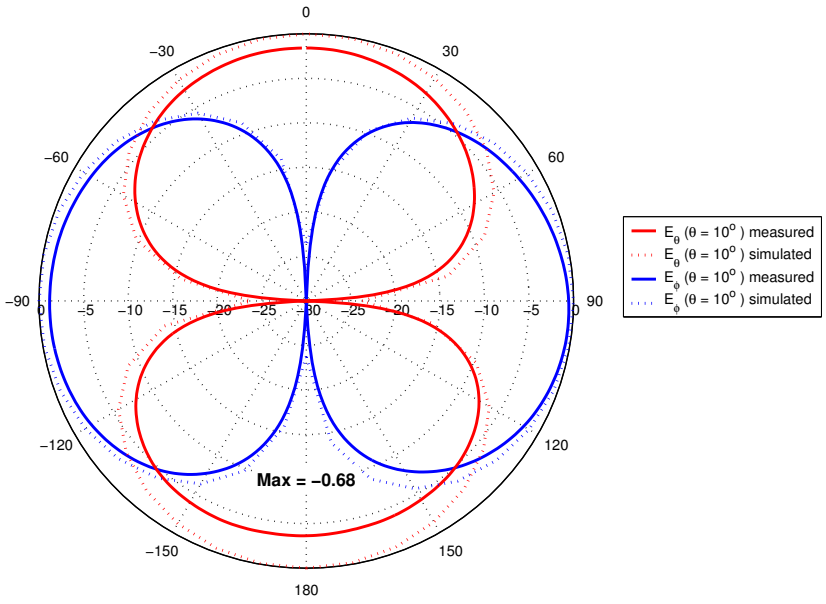

(e) switch state E

Figure 5.16 Measured and simulated conical radiation patterns for the RPIFA (cont.)

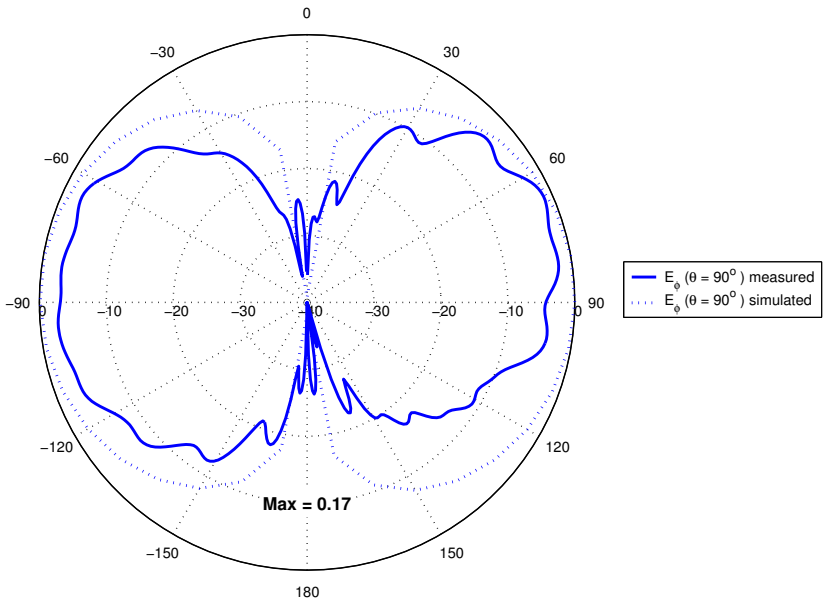

(a) switch state A

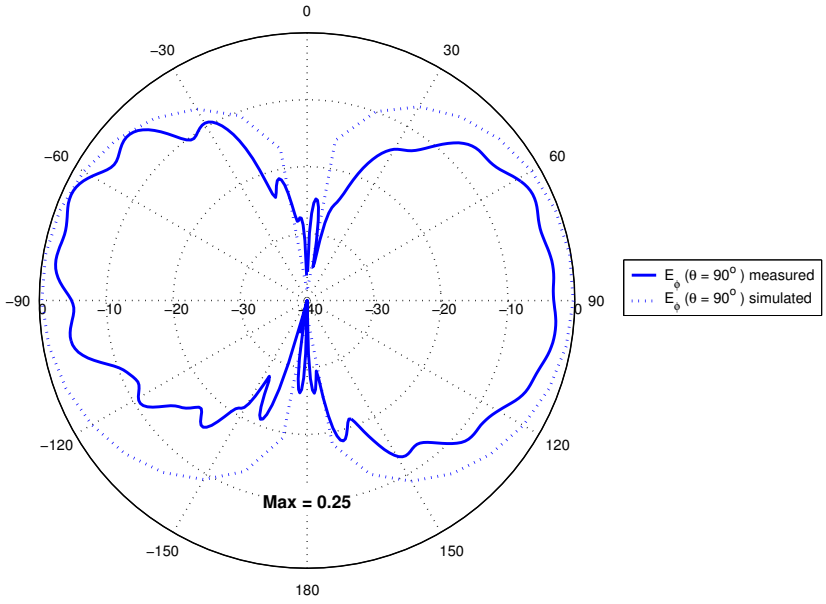

(b) switch state B

Figure 5.17 Measured and simulated conical radiation patterns for the RPIFA.

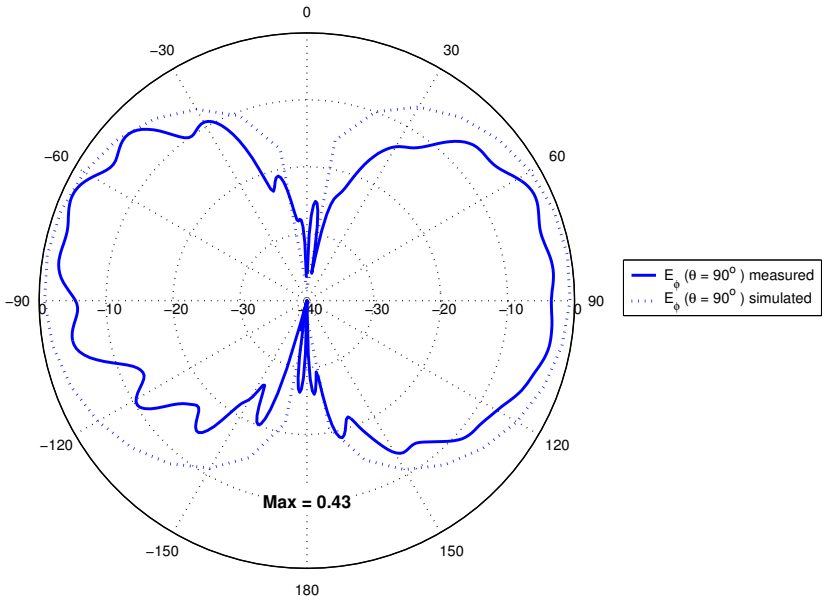

(c) switch state C

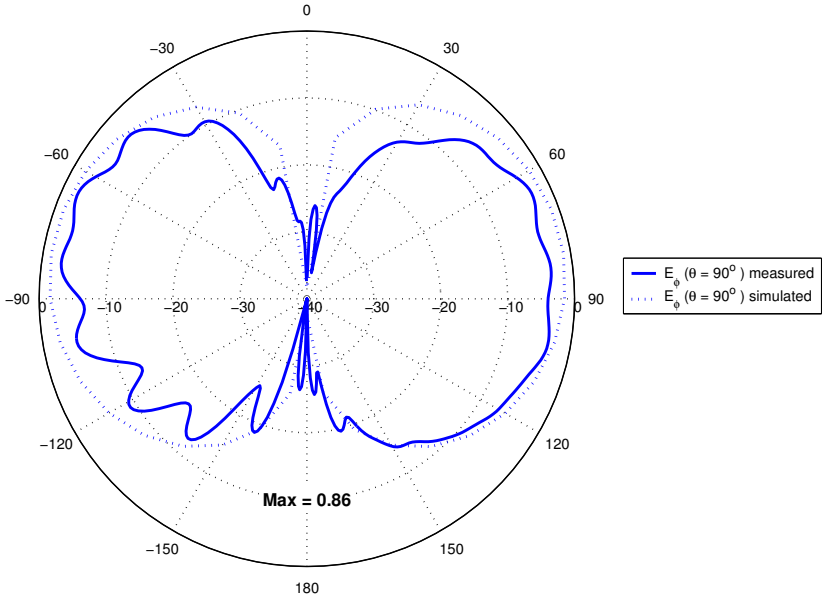

(d) switch state D

Figure 5.17 Measured and simulated conical radiation patterns for the RPIFA (cont.)

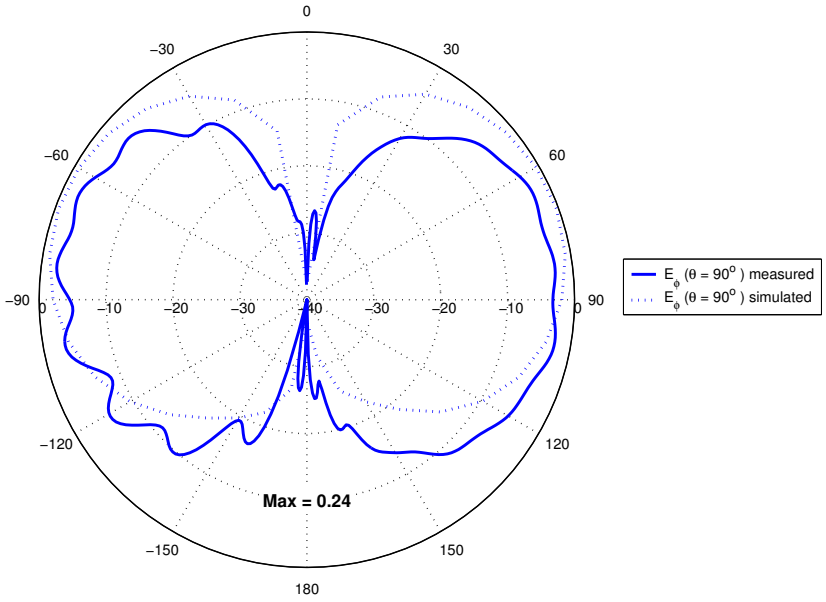

(e) switch state E

Figure 5.17 Measured and simulated conical radiation patterns for the RPIFA (cont.)

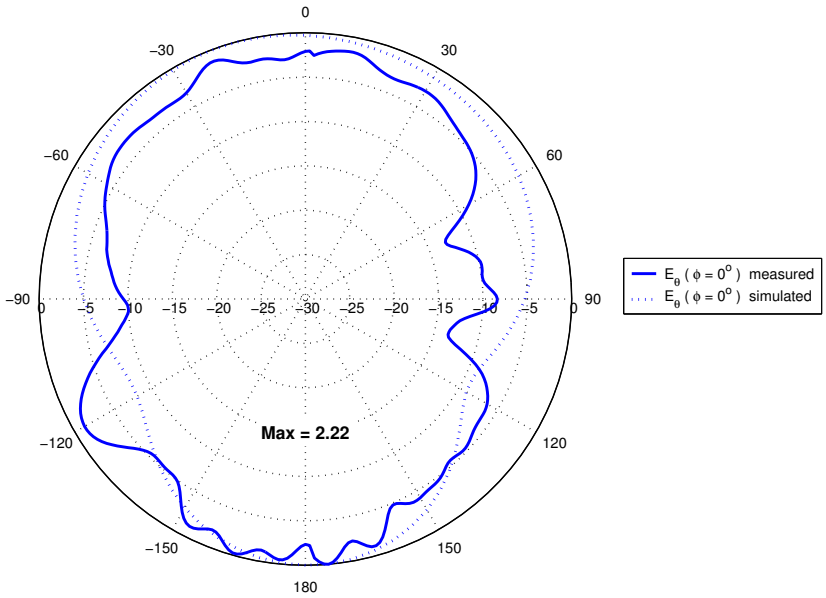

(a) switch state A

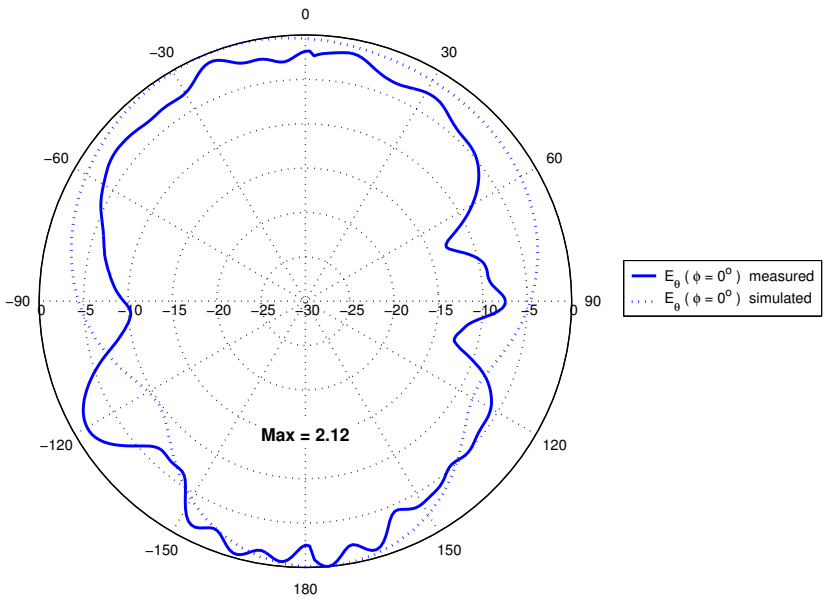

(b) switch state B

Figure 5.18 Measured and simulated elevation radiation patterns in the x-z plane for the RPIFA.

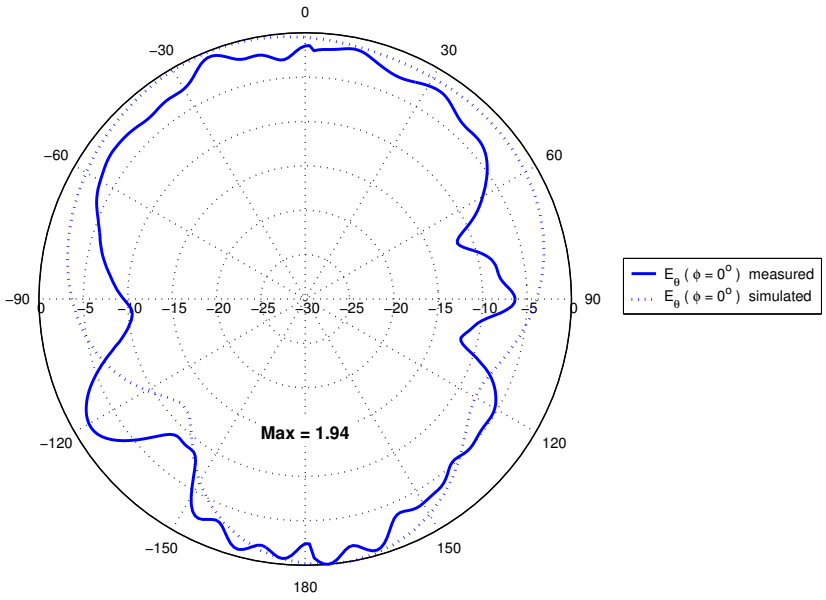

(c) switch state C

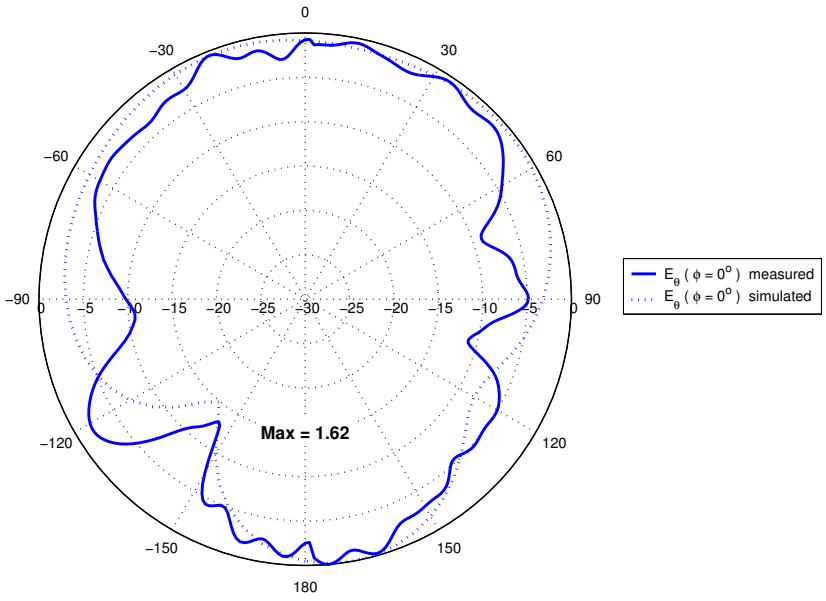

(d) switch state D

Figure 5.18 Measured and simulated elevation radiation patterns in the x-z plane for the RPIFA (cont.)

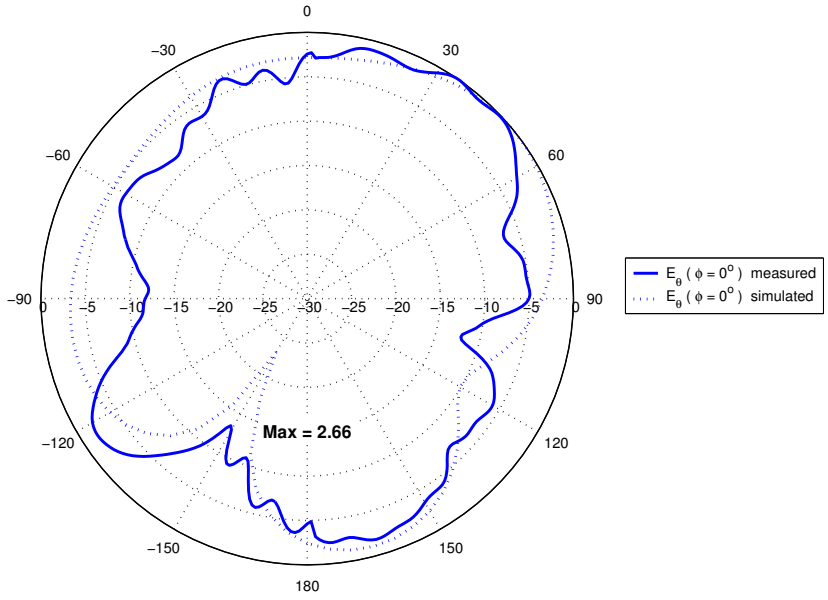

(e) switch state E

Figure 5.18 Measured and simulated elevation radiation patterns in the x-z plane for the RPIFA (cont.)

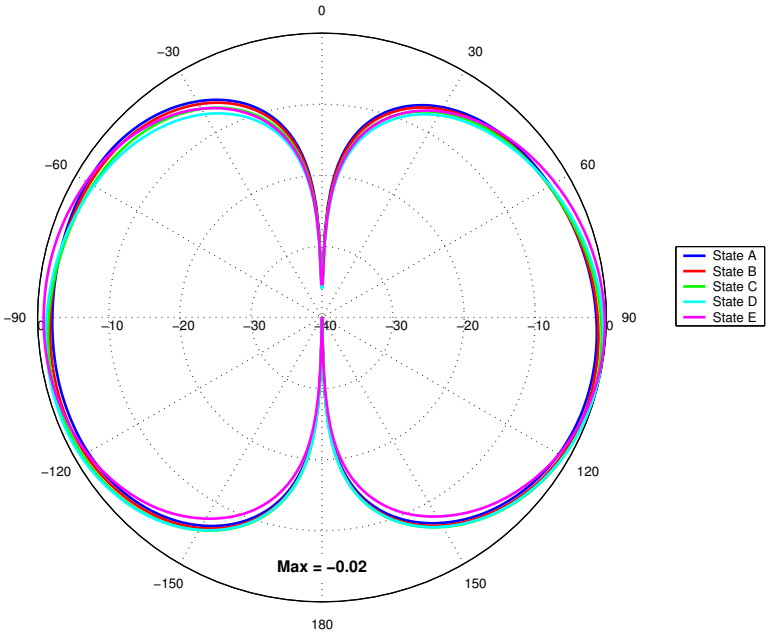

Figure 5.19 Comparison of measured azimuth directivity patterns for all switch states of the reconfigurable PIFA, E_ϕ ($\theta = 10°$).

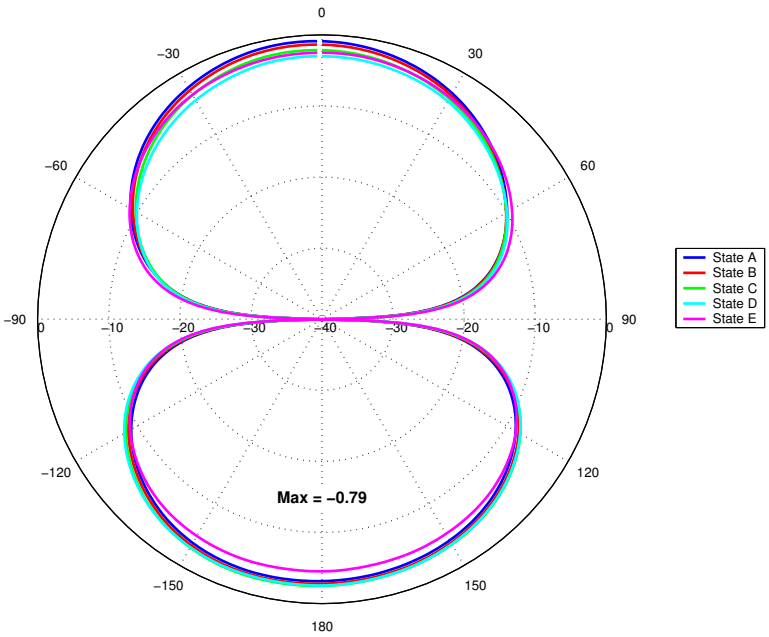

Figure 5.20 Comparison of measured azimuth directivity patterns for all switch states of the reconfigurable PIFA, E_θ ($\theta = 10°$).

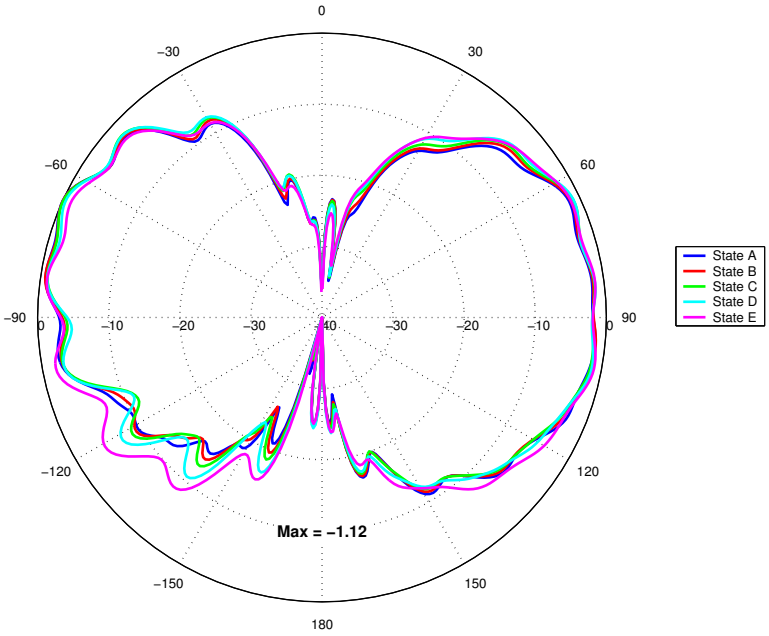

Figure 5.21 Comparison of measured azimuth directivity patterns for all switch states of the reconfigurable PIFA, E_ϕ ($\theta = 90°$).

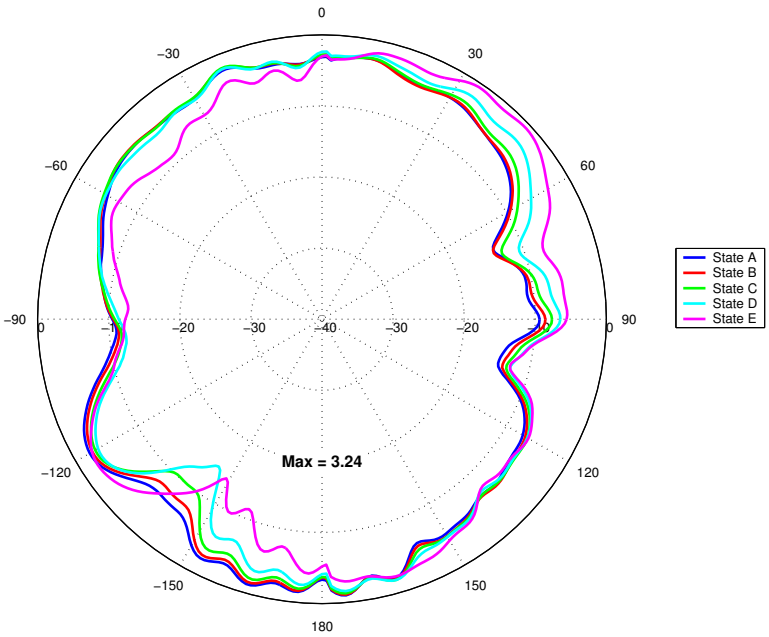

Figure 5.22 Comparison of measured elevation directivity patterns for all switch states of the reconfigurable PIFA, E_θ ($\phi = 0°$).

5.5 Summary

The development, design computer simulation and measurement of the reconfigurable planar inverted-F antenna was presented in this chapter. The ground plate influence on the RPIFA bandwidth was included in the RPIFA design to obtain discrete bandwidth states. A antenna in five discrete steps covering a bandwidth of 0-16% was achieved with only minimal impact on the other radiation properties of the antenna. The bandwidth steps were realized with three conducting inter connects per band that simulated embedded switches. A total of 12 RF switch locations were incorporated into the reconfigurable antenna design to achieve the desired selectable bandwidth behavior. Table 5.5 summarizes the selectable bandwidth characteristics of the RPIFA. The measured antenna performance was shown to be similar to the computed performance. A slight deviation in measured pattern behavior was seen in the elevation pattern most likely due to AUT positioner interference.

Table 5.5 Selectable bandwidth performance for the reconfigurable planar inverted-F antenna with switch states of Figure 5.6.

	Center Frequency	Minimum	Bandwidth 2:1 VSWR	
State	f_o (GHz)	VSWR	(MHz)	(%)
A	1.53	1.13	242	15.8
B	1.54	1.30	191	12.4
C	1.54	1.51	145	9.4
D	1.54	1.76	79	5.1
E	1.53	2.10	0	0

Chapter 6

Analysis and Measurement of Reconfigurable Folded Dipole

This chapter presents the design and analysis of the reconfigurable folded dipole antenna. First, the antenna structure is presented along with the methods used for controllable bandwidth reconfiguration. Next, an explanation of how the antenna structure radiates and what aspects of its geometry allow for bandwidth reconfiguration. A description of the computer antenna computer model then follows along with the computational results. Then, the antenna prototype measurement setup and the associated antenna measured results are presented. Finally, an overall analysis of the reconfigurable antenna is given which relates the theory to the computed performance and compares these results to the measured data.

6.1 Introduction

The folded dipole was studied extensively the 1960s [20, 21]. The antenna is attractive because of its favorable input impedance characteristics and relatively simple and robust construction. The input impedance of the folded dipole is higher than that of an equivalent half-wave dipole and it has a larger impedance bandwidth than the typical wire half-wave dipole. Its input impedance is very close to that of standard 300 Ω twin-lead coax transmission line and it can be easily constructed from twin-lead by

separating the conductors and folding back over themselves, making it a natural choice for an antenna connected to common twin-lead transmission line. Slot versions of the folded dipole are popular in embedded applications because of the ease of printing on microwave substrates.

The folded dipole antenna has also experienced considerable popularity as wire array antenna element. Its favorable input impedance qualities and simplistic construction make it ideally suited to a variety of array applications. It is frequently used as the feed element in Yagi-Uda arrays and as the dipole element in log-periodic array configurations. The folded log-periodic dipole array (FLPDA) is popular because of the convenient feeding mechanism provided by the folded dipole. A phase reversal is required between adjacent elements in the LPDA and in conventional dipole LPDAs this phase reversal is accomplished by crossing or twisting the transmission line path between adjacent elements. This twisting is often undesirable for antennas constructed on planar printed surfaces because it requires vias to the opposite side to cross the transmission line paths. Using a reentrant folded dipole as the LPDA element, it is not necessary to twist the transmission line paths and is suitable for printing on only one side of a planar structure. A further extension of the folded log-periodic dipole array is the FLPDA using parasitically loaded slot elements [86]. This variation has a smaller radiating slot inside the folded dipole element. The parasitic elements allow for individual control of the phase progression between adjacent elements.

During the author's design of a folded log-periodic dipole array [87] it was determined that the parasitic phasing slots not only contribute to the phase progression between array elements, they contribute to the bandwidth of the individual element. Thus, when a parasitically loaded folded dipole is operated by itself, the parasitic slot plays a critical role in antenna impedance bandwidth. The size and shape of the parasitic slot can be modified to achieve bandwidth controllable behavior. These findings lead to the invention of the reconfigurable folded parasitic dipole antenna (RPFDA). The antenna performs similar to the folded dipole antenna but with the ability to control the bandwidth of operation. The new antenna is described in detail in this chapter.

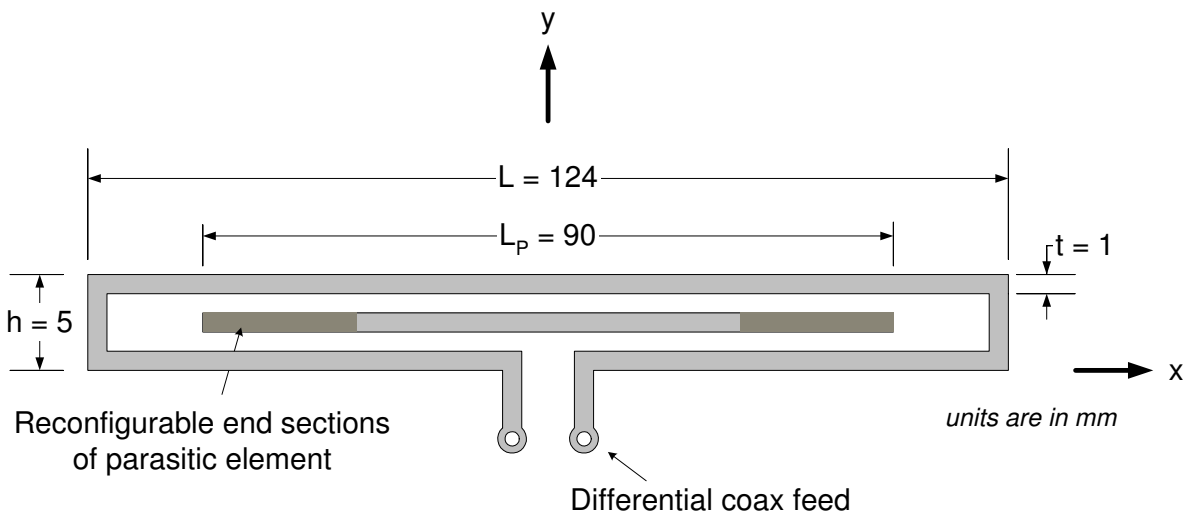

Figure 6.1 Geometry of the reconfigurable parasitic folded dipole antenna that operates at 1.05 GHz. Units are in mm.

6.2 Antenna Structure

This section presents the reconfigurable parasitic folded dipole antenna geometry. The geometry of the RPFDA is shown in Figure 6.1. It is a single sided printed antenna designed to operate at 1.05 GHz. It uses a two-port balanced feed and can be constructed on any suitable microwave substrate. The particular design presented here is printed on a 60 mil thick microwave substrate with a dielectric constant of 3.0. The outer dimensions of the folded dipole are $L = 124$ mm long by $h = 5$ mm high. The main antenna conductor and the parasitic element both have a width of $t = 1$ mm and there is a 1 mm gap between the parasitic element and the main conductor. The primary reconfigurable feature of the antenna is the parasitic slot element located inside the folded dipole structure. The parasitic slot has a maximum length of 90 mm and is responsible for controlling the impedance bandwidth of the antenna. The slot geometry construction and details are addressed in Sections 6.2.1 and 6.2.2.

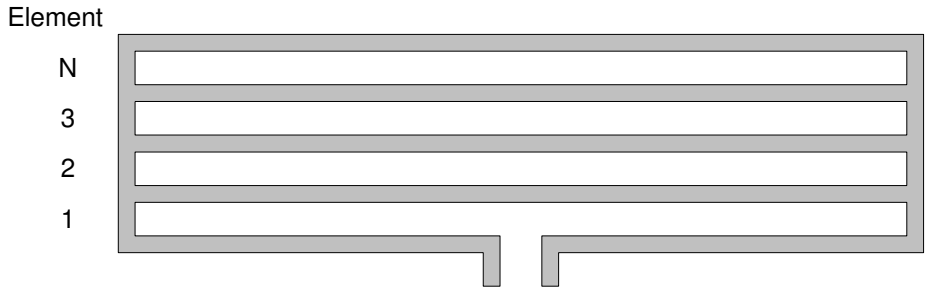

Figure 6.2 Geometry of the N-element folded dipole antenna.

6.2.1 Parasitic Element Length Influence On Bandwidth

A numerical investigation was conducted using IE3D to determine the effect of the parasitic element on antenna performance. The results obtained from this investigation are used in the subsequent sections to determine discrete parasitic element lengths for the controllable bandwidth states of the reconfigurable parasitic folded dipole antenna geometry. The length of the parasitic element, L_p, was varied symmetrically around the dipole center and all other antenna geometry parameters were held constant to explore the effect on input impedance and ultimately the impact on impedance bandwidth bandwidth.

The folded dipole has been investigated extensively since the 1960s [20, 22]. The parasitically loaded folded dipole antenna can be viewed as a modification of the N-element folded dipole as shown in Figure 6.2. The PFDA is a three-element folded dipole with a shortened middle element. It is well known that the input impedance of a N-element folded dipole is given by [88]

$$Z_{in} = N^2 Z_{dipole} \tag{6.1}$$

where the input impedance of a dipole in free-space at its first resonance is $Z_{dipole} \approx 70\ \Omega$.

Figure 6.3 shows the input impedance of the antenna from Figure 6.1 as a function of parasitic element length, L_p, computed using IE3D at the design frequency of 1.05 GHz. When $L_p = 122$ mm the parasitic element extends the entire length of the folded dipole and the element touches the ends of the folded dipole and the antenna

becomes the three-element folded dipole. The input reactance becomes zero and the resistance $\approx 560\ \Omega$, or $3^2 \times 70\ \Omega$, as predicted from Equation (6.1). The input resistance drops sharply and the reactance grows quickly as the length of the parasitic element is reduced. The reactance vanishes when L_p is about 100 mm and 25 mm. The input resistance nearly vanishes as well when $L_p = 105$ mm. The resistance climbs back to favorable values for $L_p < 80$ mm.

Figure 6.4 shows the antenna bandwidth versus parasitic element length from 0 to 100 mm referenced to 300 Ω for the antenna geometry of Figure 6.1. The antenna has a maximum bandwidth of 16% for $L_p = 0$ mm. The bandwidth decreases slowly to 13% where $L_p = 60$ mm. The bandwidth then rapidly decreases to 0% for $L_p = 85$ mm. Figure 6.5 shows the calculated VSWR for parasitic element lengths of 25 to 85 mm. The center frequency of the antenna is lowered when the parasitic element becomes shorter than 55 mm. Figures 6.4 and 6.5 give the usable limits for the length of the parasitic element. If the parasitic element is longer than 85 mm, the impedance bandwidth is reduced to 0% and the antenna is effectively turned off. Parasitic element lengths shorter than 55 mm cause the center frequency of the antenna to deviate from the design frequency of 1.05 GHz and are thus undesirable even though the antenna impedance bandwidth is increased. Table 6.1 summarizes the electrical performance of the parasitic folded dipole antenna from Figure 6.1 based on different parasitic element lengths simulated using IE3D.

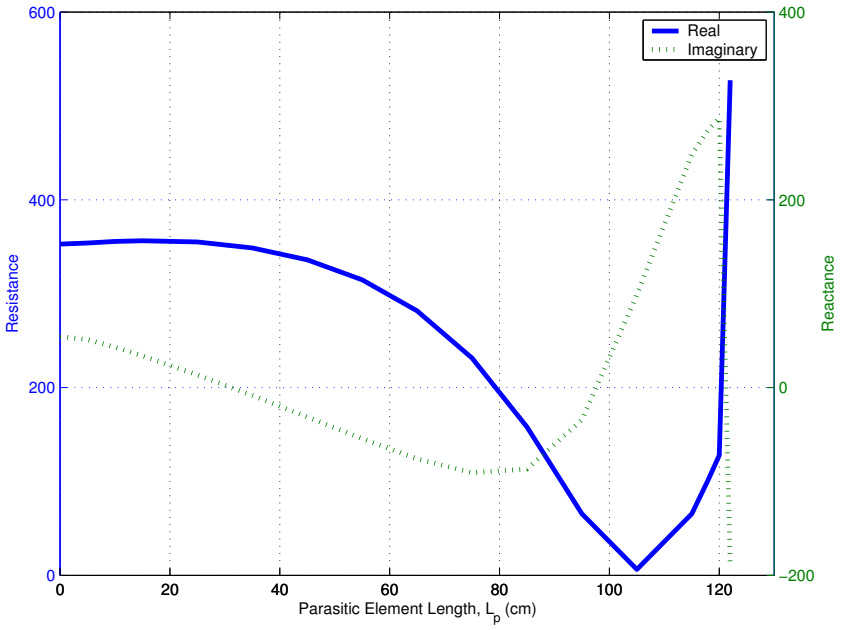

Figure 6.3 Input impedance versus parasitic element length for the geometry in Figure 6.1 at 1.05 GHz computed using IE3D.

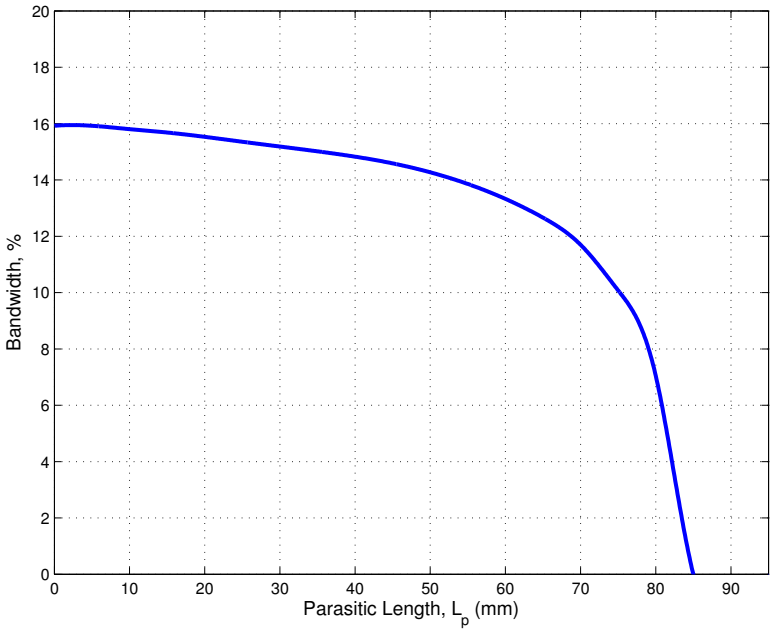

Figure 6.4 Bandwidth versus parasitic element length for the geometry in Figure 6.1 computed using IE3D.

Table 6.1 Electrical performance based on parasitic element length, L_p, for the PFDA of Figure 6.1 simulated using IE3D.

Parasitic length, L_p		Center frequency	Minimum	Bandwidth
(mm)	(wavelengths)	f_0 (GHz)	VSWR	2:1 VSWR (%)
25	0.088	1.03	1.04	15.4
35	0.123	1.04	1.06	15.0
45	0.158	1.04	1.11	14.6
55	0.193	1.05	1.18	13.9
65	0.228	1.05	1.30	12.7
70	0.245	1.05	1.40	11.7
75	0.263	1.05	1.53	10.1
80	0.280	1.05	1.75	7.0
85	0.298	1.05	2.10	0
95	0.333	1.01	4.00	0
105	0.368	0.94	11.5	0
115	0.403	1.12	6.08	0

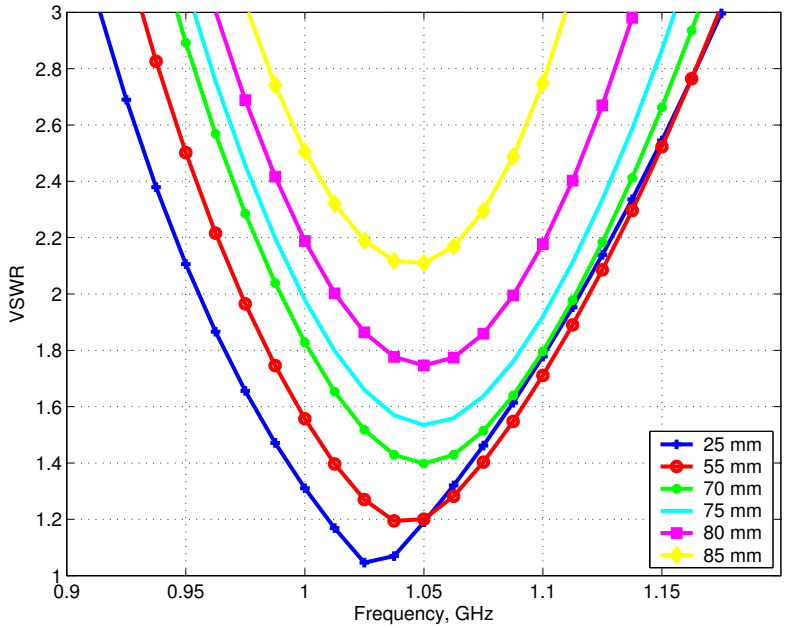

Figure 6.5 VSWR versus frequency of the parasitic loaded folded dipole antenna of Figure 6.1 for various parasitic element lengths, L_p, computed using IE3D.

6.2.2 The Reconfigurable Parasitic Folded Dipole Antenna

Specific parasitic element lengths, L_p, were selected for discrete antenna bandwidth values based on the investigation performed in Section 6.2.1. These parasitic element length states are used in the subsequent work to accomplish the desired reconfigurable bandwidth performance. Five parasitic element lengths were selected to achieve discrete bandwidth states from 0% (effectively off) to 13% (maximum bandwidth). Table 6.2 summarizes the element lengths chosen for the selectable bandwidth states along with the predicted bandwidth values based on the the element length study in Section 6.2.1.

Table 6.2 Discrete parasitic element lengths, L_p, as shown in Figure 6.6 for selected antenna bandwidth states based on simulations from Section 6.2.1.

	Length, L_p		Bandwidth for
State	(mm)	(wavelengths)	$\leq$ 2:1 VSWR (%)
A	62.0	0.217	13
B	69.0	0.242	11
C	76.0	0.266	9
D	83.0	0.291	5
E	90.0	0.315	0

With the parasitic element lengths selected, the design task becomes how to physically vary the length of the element to achieve the desired reconfigurable operation. The solid parasitic element is replaced by a new structure with reconfigurable components. The sub-elements and the main element are connected together with RF MEMS switches as shown in Figure 6.7. The single, solid 90 mm parasitic element is replaced by a shorter 62 mm parasitic element and four 3.2 mm sub-elements on either side. There is a 0.3 mm gap separating the adjacent sections to accommodate the RF switching elements as described in Section 3.3. The electrical length of the parasitic element is varied by selectively activating the interconnecting switches between the sub-elements and a variable impedance bandwidth of 0-13% is obtained.

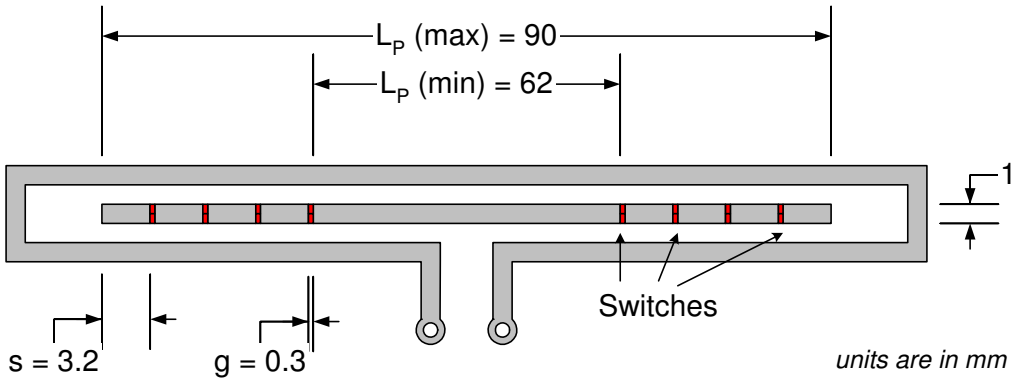

Figure 6.6 Reconfigurable parasitic folded dipole antenna with active parasitic element and RF switch locations. Units are in mm.

(a) state A, $L_p = 62.0$ mm

(b) state B, $L_p = 69.0$ mm

(c) state C, $L_p = 76.0$ mm

(d) state D, $L_p = 83.0$ mm

(e) state E, $L_p = 90.0$ mm

Figure 6.7 Reconfigurable PFDA active parasitic element switch configuration states. Switches in *on* position are shown in dark, switches in *off* position are shown in light.

6.3 Simulation of RPFDA

This section describes the computer simulation and associated numerical results for the reconfigurable parasitic folded dipole antenna presented in Section 6.2.2. The commercial code IE3D was the primary simulation tool used for studying the RPFDA. IE3D is a full-wave frequency-domain package utilizing a laterally-open moment method engine capable of simulating arbitrary metalization geometries and was described in Section 4.3. The simulation model of the RPFDA contains dielectric substrate layer used for supporting the antenna structure. As was previously described, the 2.5 dimensional substrate limitation of finite extent substrates as was seen in the ring patch model applies to the modeling of the RPFDA. However, the radiation mechanism of this RPFDA is not a microstrip fringing mechanism as was present in the operation of the ring patch antenna. Experience shows that the finite extent of the supporting substrate of the hardware model RPFDA will not present a significant problem for accurate simulation of the antenna.

Figure 6.8 shows the computed input impedance for the antenna switch states of Figure 6.7. The real part of the impedance varies between 100 Ω for state E and and 300 Ω for state A, while the imaginary part remains nearly constant at -100 Ω over all switch states at 1.05 GHz. The desired antenna bandwidth control is facilitated primarily by altering the real part of the input impedance as seen in Figure 4.7. Figure 6.9 shows the corresponding VSWR for the switch states referenced to 300 Ω. As was predicted from Figure 6.4, the widest bandwidth is seen with the parasitic element in switch state A with a length of 62 mm. Table 6.3 summarizes the computed 2:1 VSWR impedance bandwidth and geometry parameters for the RPFDA with switch states of Figure 6.7.

Table 6.3 Impedance bandwidth performance and reconfigurable parasitic element geometry for the RPFDA of Figure 6.6 with switch states of Figure 6.7 computed using IE3D

State	Parasitic length, L_p (mm)	Center frequency, f_o (GHz)	Bandwidth for $\leq$ 2:1 VSWR (%)	Minimum VSWR
A	62.0	1.05	13.1	1.28
B	69.0	1.05	11.5	1.40
C	76.0	1.05	9.3	1.60
D	83.0	1.05	2.0	1.98
E	90.0	1.03	0	2.80

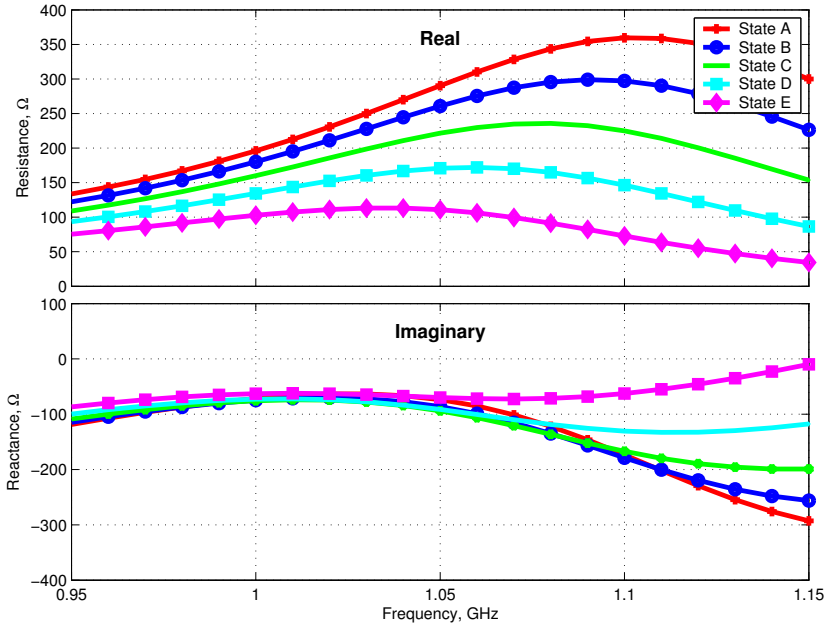

Figure 6.8 Input impedance versus frequency of the reconfigurable parasitic folded dipole antenna for switch states of Figure 6.7 for the RPFDA of Figure 6.6 simulated using IE3D.

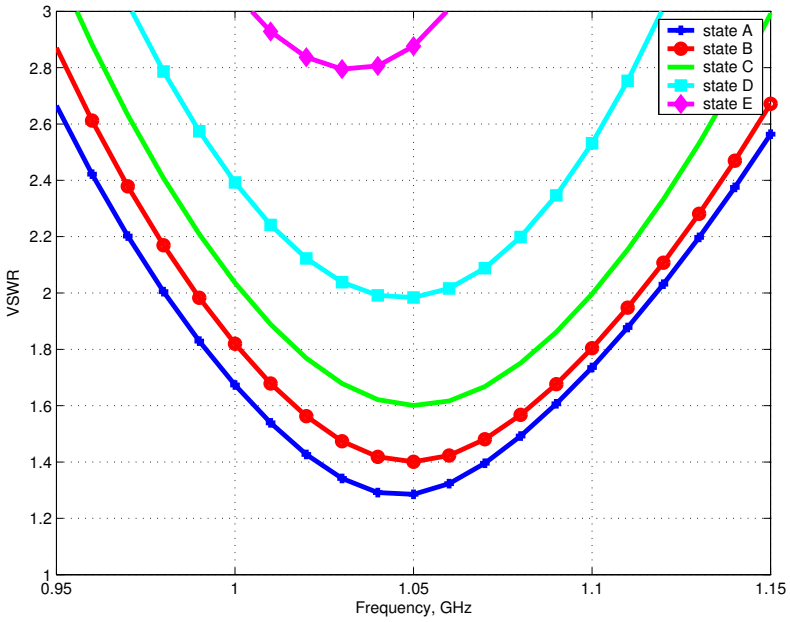

Figure 6.9 VSWR versus frequency of the reconfigurable parasitic folded dipole antenna referenced to 300 Ω for switch states of Figure 6.7 for the RPFDA of Figure 6.6 simulated using IE3D.

6.4 Experimental Results for RPFDA

This section discusses the construction and measurement of the hardware test model RPFDA. The prototype RPFDA of Figure 6.10 was constructed and its electrical performance characteristics were measured in order to verify the theoretical and simulated results. The prototype antennas were printed on Rogers RO3003 [89] microwave material using standard photo-etching processes. The RO3003 material has a dielectric constant of 3.0 and a thickness of 60 mils. The overall substrate size was 7×1.5 inches. Two holes were drilled through the substrate at the feed locations to accommodate the feed network. The feed network was constructed from two pieces of 141 semi-rigid coax formed into a Y–shaped connector as shown in Figure 6.10. The coax connector used two standard SMA plugs. At the antenna side of the Y–connector, the outer shield and dielectric were stripped back and the center conductors were fed though the RO3003 material and soldered to the circular pads at the feed points.

To achieve the five separate antenna states in absence of the actual MEMS switches, five individual antennas were printed as substitutes. The five printed antennas are shown in Figures 6.11 and correspond to the switch states specified in Figure 6.7.

6.4.1 Impedance Measurements

All measurements of the RPFDA ware performed at the Virginia Tech Antenna Group's antenna test facility. Impedance measurements were made using an HP 8510C vector network analyzer. The measurement unit consisted of the printed reconfigurable parasitic folded dipole and coax Y–feed as shown in Figure 6.10. The test unit was mounted on the near-field scanner AUT positioner inside the anechoic chamber. While the impedance measurements were being performed, the AUT positioner was pointed toward the closed chamber door to minimize any external disturbances and maintain test repeatability between measurements. RF absorber was placed around the metal AUT tower to minimize any reflections from the mounting fixture. Considerable effort was taken to minimize any unwanted reflection in the test environment and to ensure repeatability between antenna measurements. Before the final impedance measure-

Figure 6.10 Hardware test model of the RPFDA with coaxial feed network.

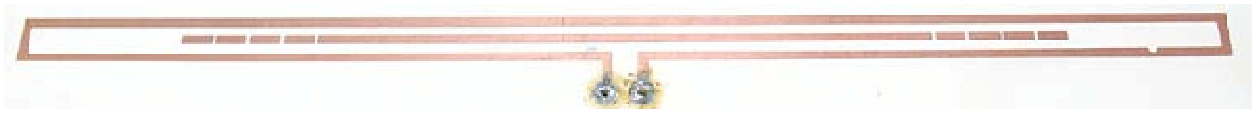

(a) Switch state A

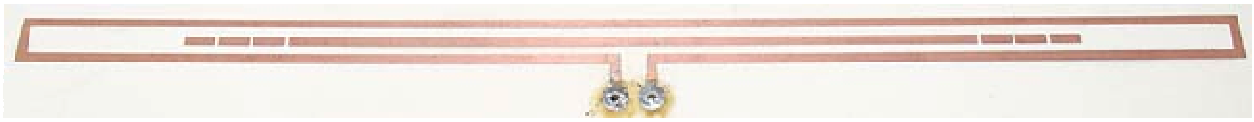

(b) Switch state B

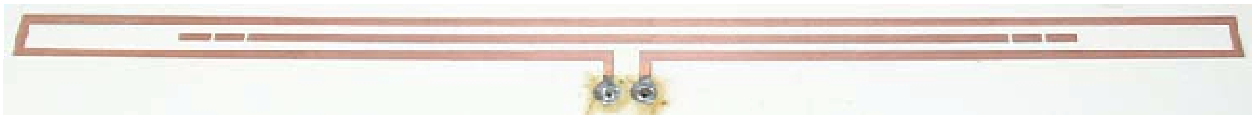

(c) Switch state C

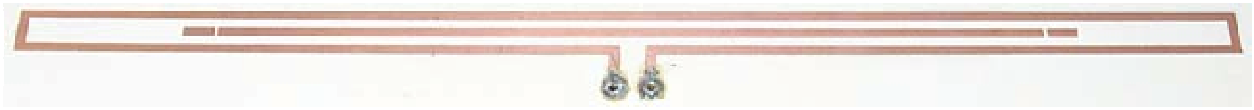

(d) Switch state D

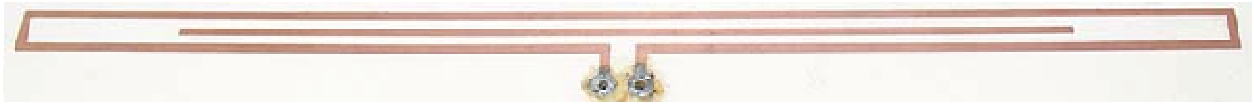

(e) Switch state E

Figure 6.11 Hardware test model for each of the switch states of Figure 6.7.

ments were performed, the setup was validated by measuring the input impedance of a known 1.0 GHz printed half-wave dipole antenna. The S-parameter values and input impedance values obtained from this measurement confirmed that the measurement setup provided a suitable test environment.

The input impedance measurements of the RPFDA were made using the 2-port impedance measurement technique developed by Davis [90]. The technique uses standard two-port scattering parameters for balanced antenna. Each half of the balanced antenna input port is fed as one port of a two port network. This method eliminates the need for a balun or wideband 180° hybrid when measuring the input impedance of a balanced antenna. Impedance is estimated by measuring the two port response of the antenna and is given by [90]

$$Z_{AUT} = 2Z_0 \frac{1 - s_{11} + s_{21}}{1 + s_{11} - s_{21}} \tag{6.2}$$

where Z_0 is the characteristic impedance and s_{11}, s_{21} are the two-port response measurements from the network analyzer.

The measured impedance data is plotted along with the respective IE3D simulated results for each antenna switch state. The measured impedance referenced to 300 Ω is shown in Figure 6.12. Figures 6.13 and 6.14 show the measured VSWR and Figure 6.15 shows the measured return loss for the antennas; all figures are referenced to 300 Ω. Reasonable agreement is obtained between the measured and simulated data, particularly at the design frequency of $f_o = 1.05$ GHz and for antenna switch states A-D (Figures 6.12(a)-6.12(d)). Both the measured resistance and reactance deviate slightly from the simulated cases away from the design frequency. In Figures 6.12(a)-6.12(d), both the real and imaginary parts of the measured input impedance are nearly identical to the simulated values for frequencies up to f_o. For the higher frequencies, the measured input resistance is somewhat higher than the simulated resistance. The discrepancy in measured input impedance is also visible in the measured VSWR and return loss plots of Figures 6.13 and 6.15, respectively. The measured VSWR is slightly lower than the simulated values but within the measurement tolerances that would be expected for small antennas at this operating frequency. However, several mechanisms may be responsible for the discrepancies noted in the impedance plots. As with any high-frequency device, antenna performance is very sensitive to construction dimen-

sional tolerances. The production of hardware models that perform as predicted relies heavily on careful construction techniques. The Y–coax feed network was not included in the simulation models and is likely a source of some measurement error. There is also a small amount of noise observed in the VSWR and return loss plots. Noise of this type is normally due to mismatch reflections from the connecters. Table 6.4 provides a summary and comparison of the measured and simulated performance for the RPFDA. As can be seen, the center frequency remained constant at $f_o = 1.05$ GHz over all switch states and the measured values agreed with the simulated values for all switch states except for state E where it decreased slightly to 1.03 GHz.

Table 6.4 Summary of the measured and simulated 2:1 VSWR impedance bandwidth performance for the RPFDA of Figure 6.6.

	Bandwidth 2:1 VSWR (%)		Center Frequency f_o (GHz)		Minimum VSWR	
State	measured	simulated	measured	simulated	measured	simulated
A	10.6	13.1	1.05	1.05	1.23	1.28
B	9.8	11.5	1.05	1.05	1.30	1.40
C	8.0	9.3	1.05	1.05	1.42	1.60
D	7.3	2.0	1.05	1.05	1.53	1.98
E	2.3	0	1.05	1.03	1.8	2.80

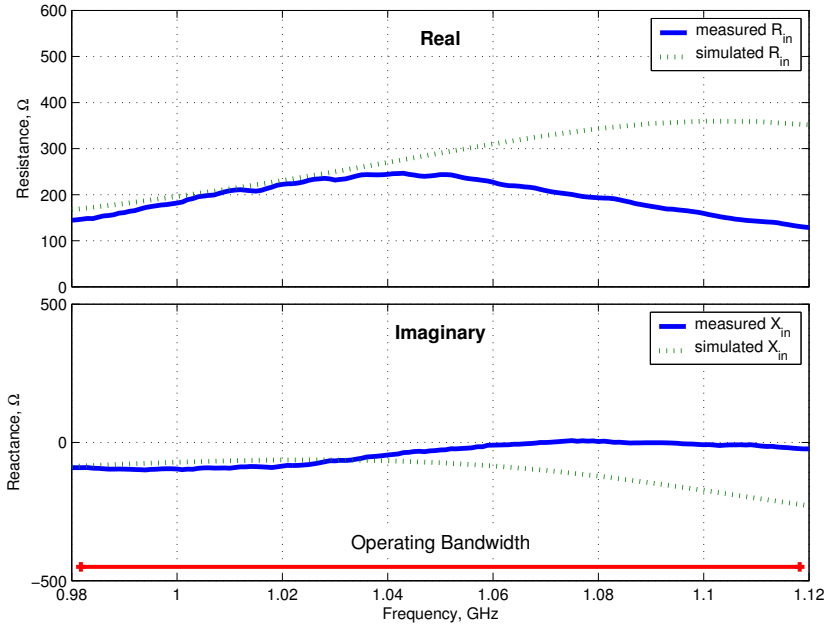

(a) switch state A

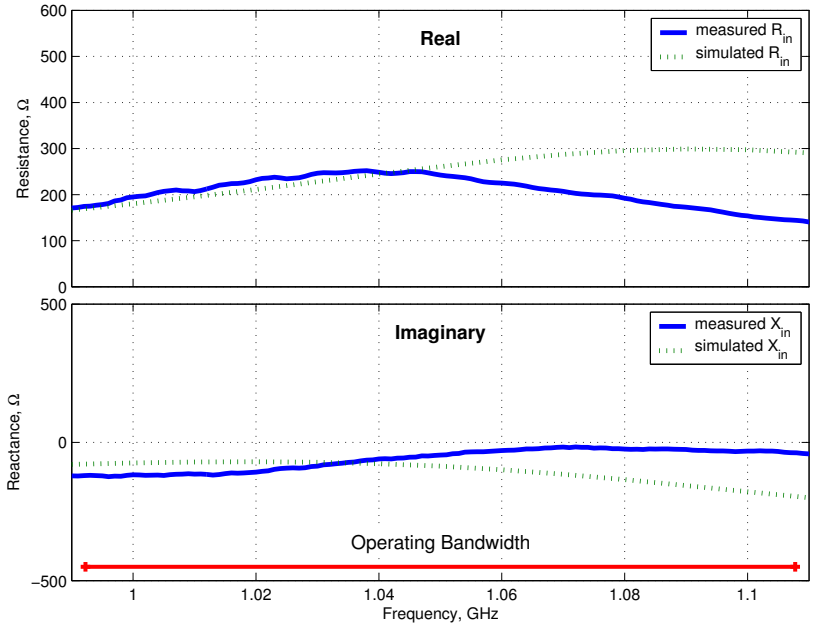

(b) switch state B

Figure 6.12 Measured and simulated input impedance for the reconfigurable folded dipole.

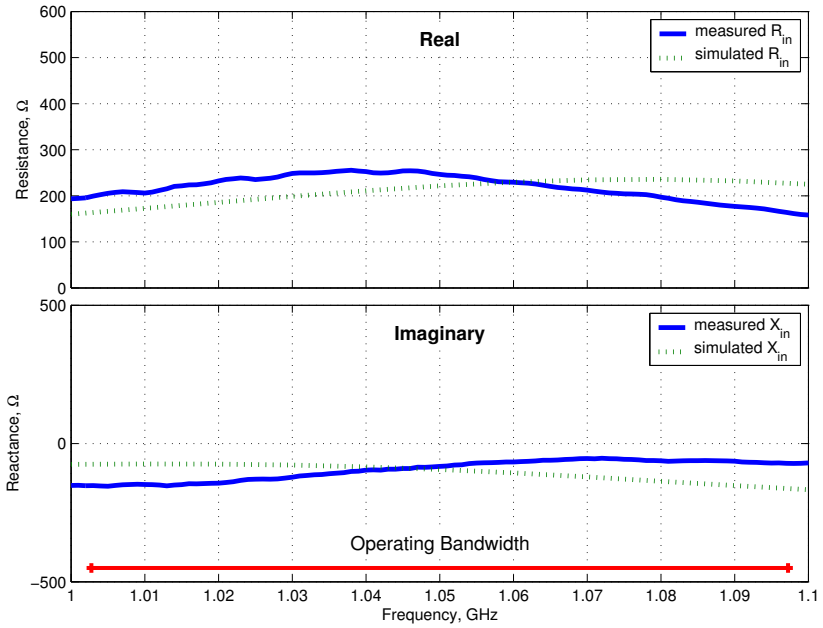

(c) switch state C

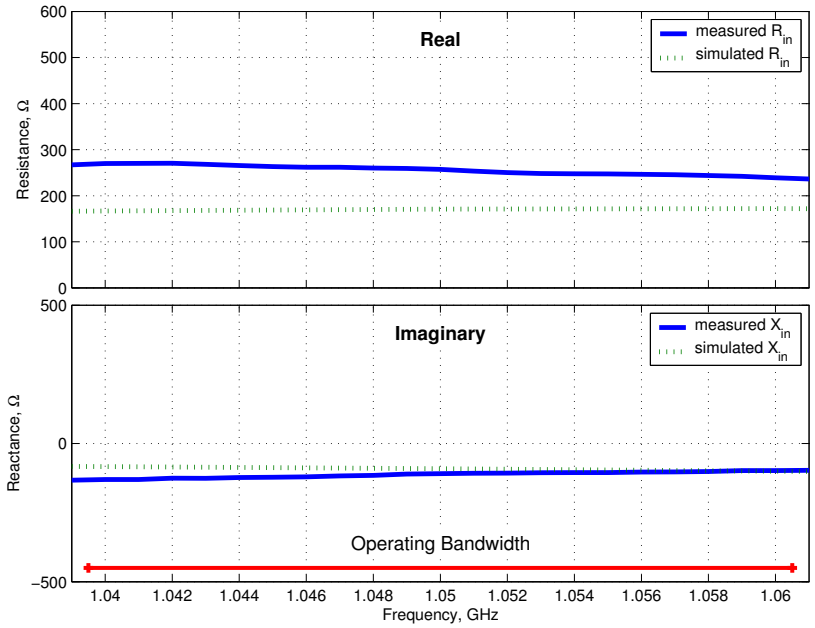

(d) switch state D

Figure 6.12 Measured and simulated input impedance for the reconfigurable folded dipole (cont.)

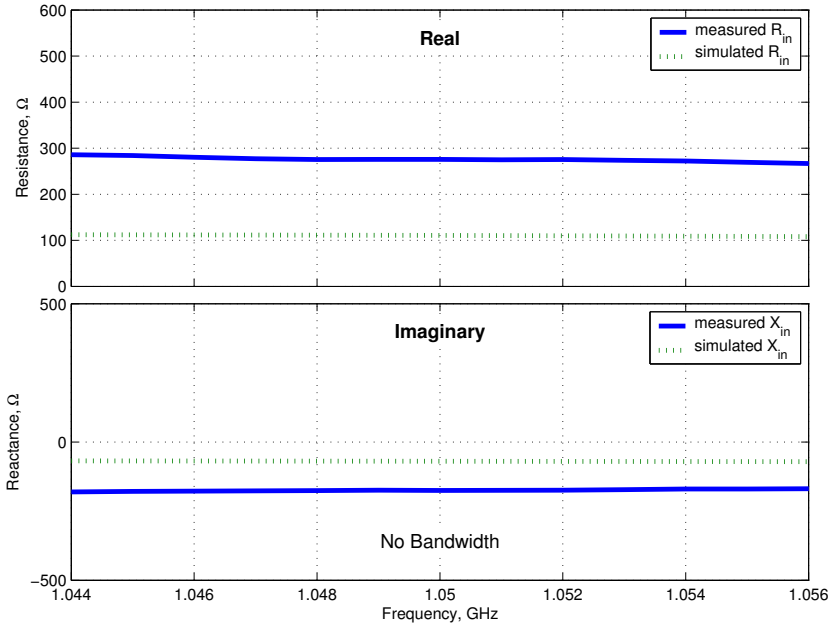

(e) switch state E

Figure 6.12 Measured and simulated input impedance for the reconfigurable folded dipole (cont.)

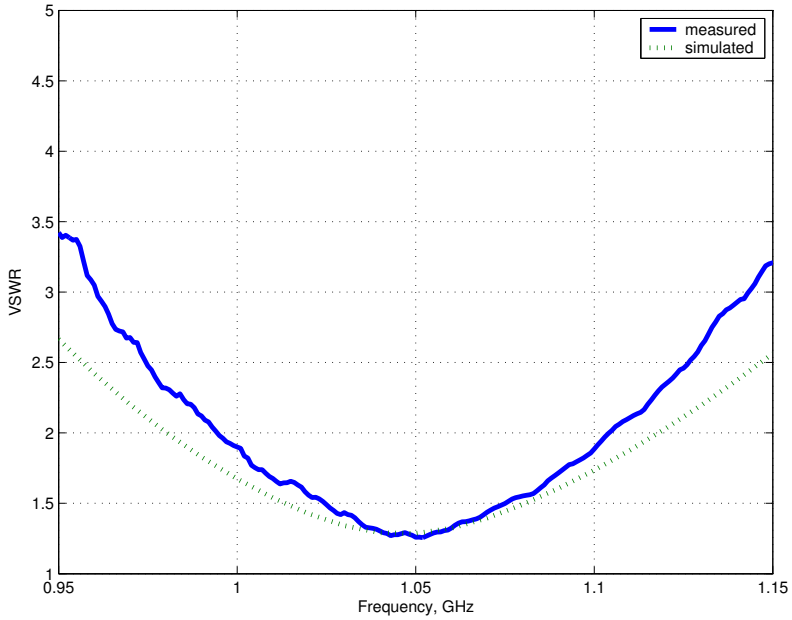

(a) switch state A

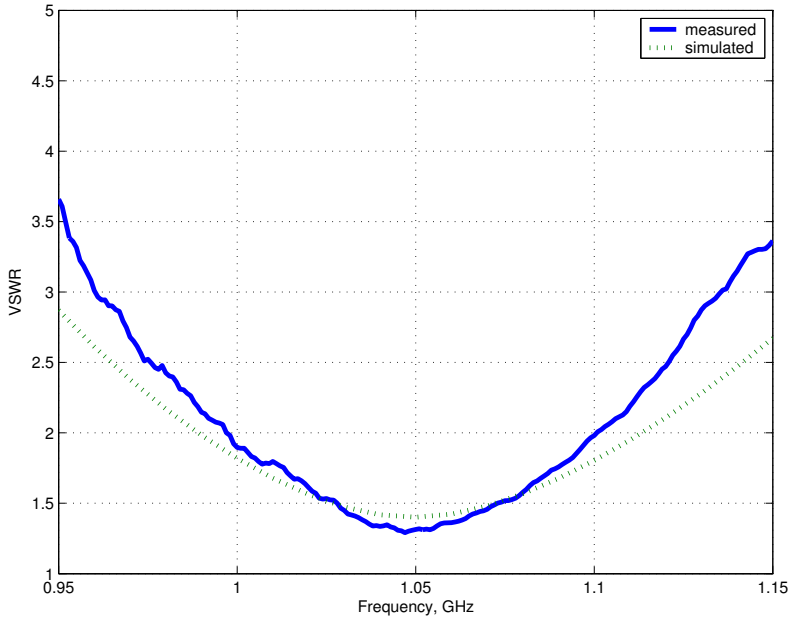

(b) switch state B

Figure 6.13 Measured and simulated voltage standing wave ratio for the reconfigurable folded dipole.

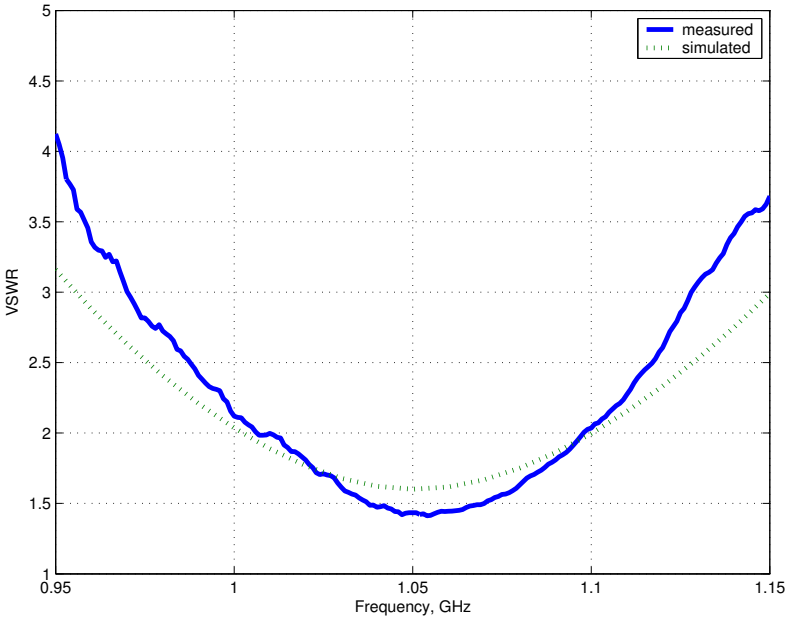

(c) switch state C

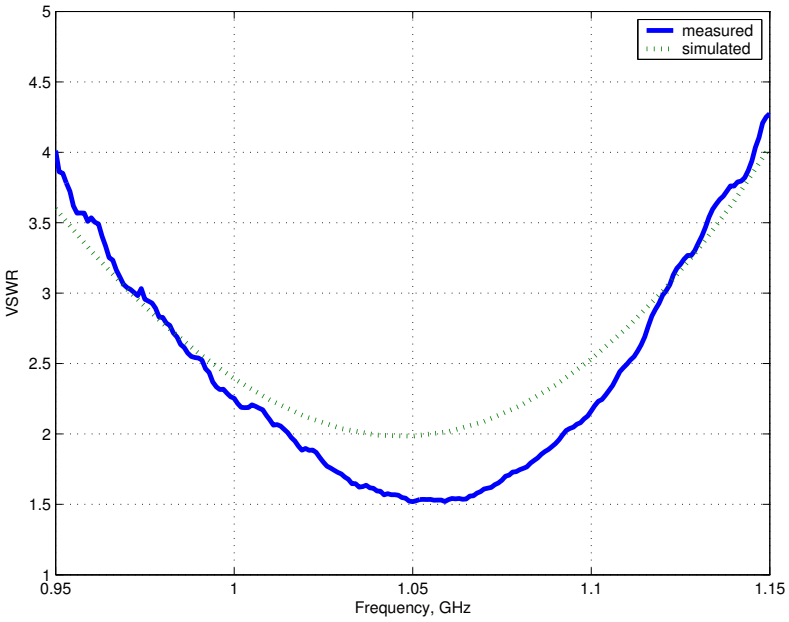

(d) switch state D

Figure 6.13 Measured and simulated voltage standing wave ratio for the reconfigurable folded dipole (cont.)

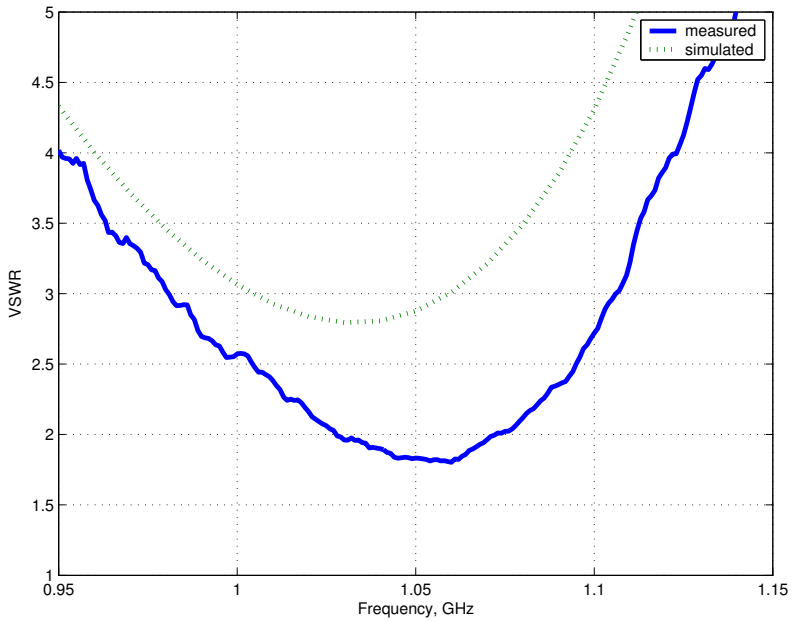

(e) switch state E

Figure 6.13 Measured and simulated voltage standing wave ratio for the reconfigurable folded dipole (cont.)

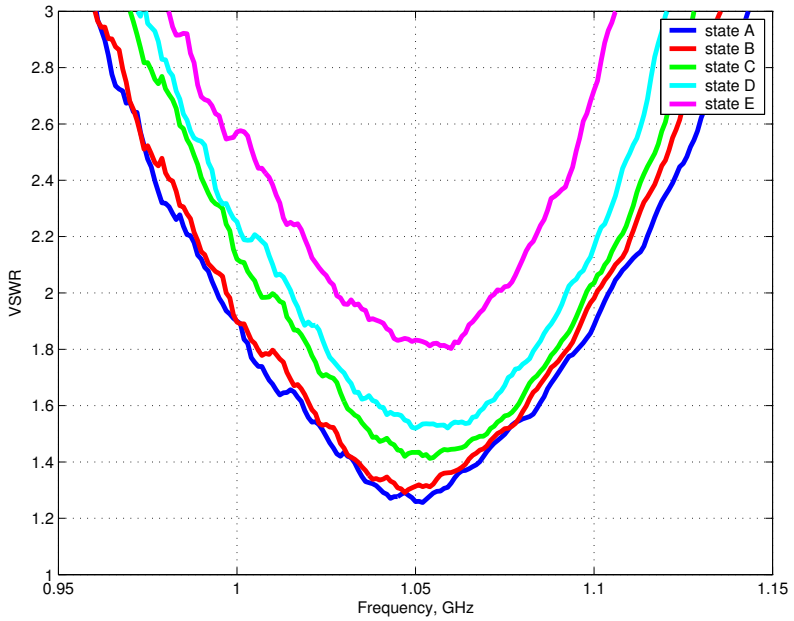

Figure 6.14 Measured voltage standing wave ratio for the reconfigurable folded dipole in all states.

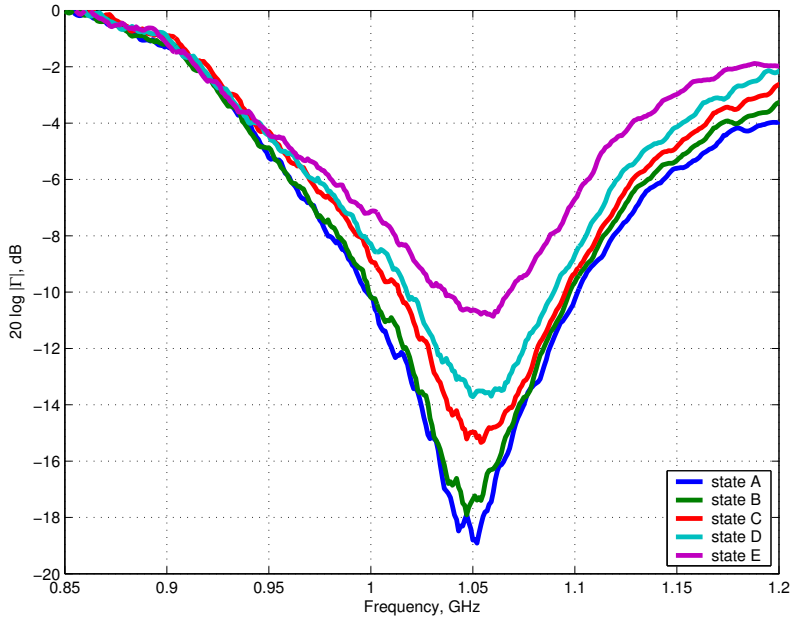

Figure 6.15 Measured return loss for the reconfigurable folded dipole in all states.

6.4.2 Pattern Measurements

Radiation patterns were measured in the VTAG indoor anechoic chamber using the near-field scanner. The patterns were made with the system operating in spherical scanning mode. The pattern measurement test setup consisted of the same equipment used in the impedance measurements of Section 6.4.1. However, for the pattern measurements the AUT was connected to the near-field scanner through the AUT positioner. The measurement unit consisted of the printed reconfigurable parasitic folded dipole and coax Y–feed as shown in Figure 6.10. Additional RF absorber was placed behind the test antenna and around the AUT tower to minimize any reflection from the test equipment. Prior to performing the final pattern measurements of the AUT, the setup was validated by measuring the radiation patterns of a known 1.0 GHz printed half-wave dipole antenna. The radiation patterns obtained from this validation measurement confirmed that the measurement setup provided a suitable test environment.

The results presented here are for 1.05 GHz. The measured patterns are presented along with the simulated results in Figures 6.16, 6.17, 6.18 and 6.19. Figures 6.20 - 6.25 provide pattern comparisons for all parasitic element length states. The radiation pattern behavior for the RPFDA is like that of a simple x-directed $\lambda/2$ dipole antenna. The pattern is primarily omnidirectional in the azimuthal and conical cuts. Excellent agreement is seen between the measured and simulated radiation patterns. The pattern is primarily omnidirectional in the conical E_θ and E_ϕ cuts of Figures 6.17 and 6.18 and the conical E_{total} cuts of Figure 6.19. Figure 6.16 shows the x-z and y-z plane elevation patterns for E_θ and E_ϕ.

As was predicted by the simulations, the radiation pattern behavior of the antenna remains nearly constant from one switch state to the next. This is a desired behavior of the antenna in order to maintain predictable performance while selecting the antenna bandwidth. This consistency can be seen clearly in the pattern comparisons of Figures 6.20 - 6.25. Examining the maximum directivity values for each pattern cut also illustrates the pattern consistency. There was only 0.1 dB difference in the maximum directivity for the both the elevation pattern cuts and the conical pattern cuts. Due to the difficulty in measuring the gain for electrically small antennas, absolute gain measurements were not made. However, the close agreement between

computed and measured performance for pattern and impedance leads to a high level of confidence in the predicted gain obtained from the IE3D simulations even though absolute gain was not measured. In the absence of gain standard measurements, the near-field measurement software reports only directivity measurements.

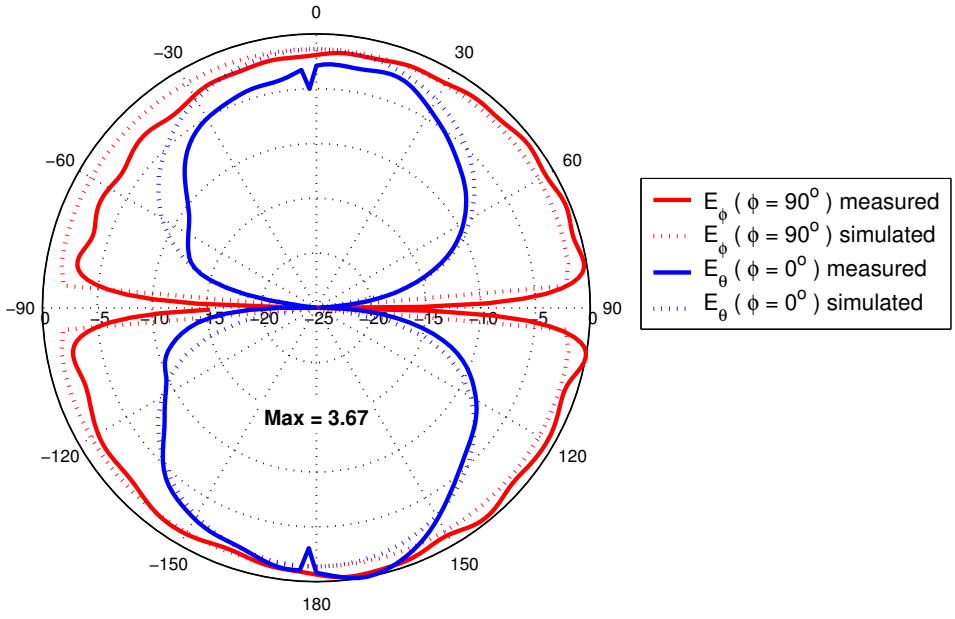

(a) switch state A

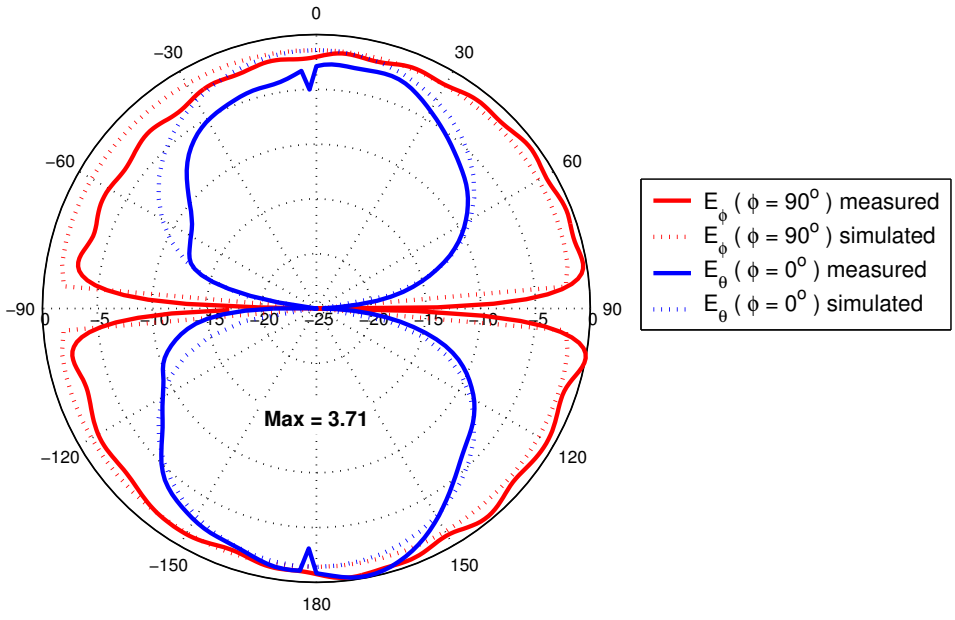

(b) switch state B

Figure 6.16 Measured and simulated elevation radiation patterns in the principal planes for the RPFDA.

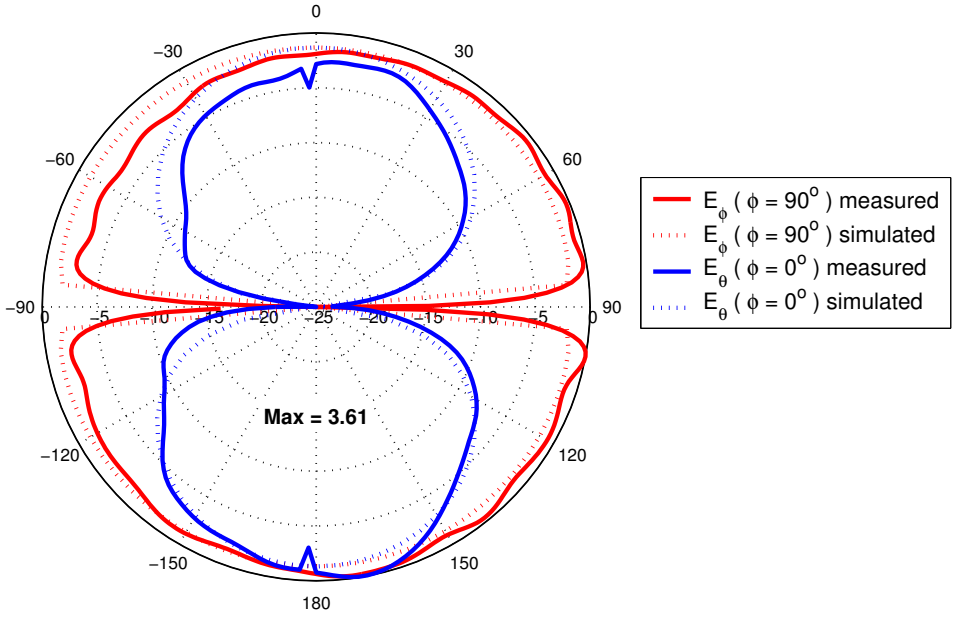

(c) switch state C

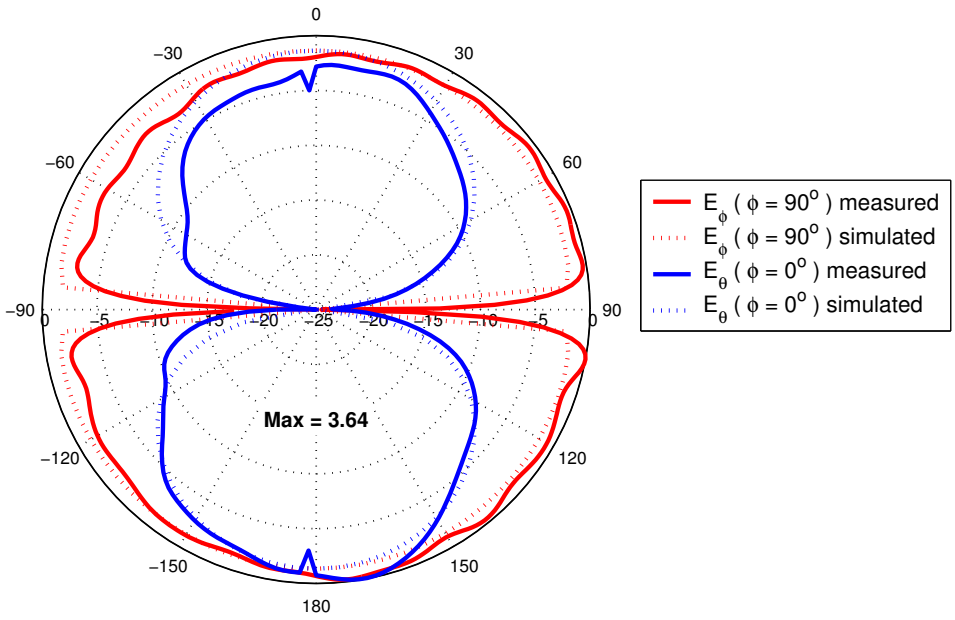

(d) switch state D

Figure 6.16 Measured and simulated elevation radiation patterns in the principal planes for the RPFDA (cont.)

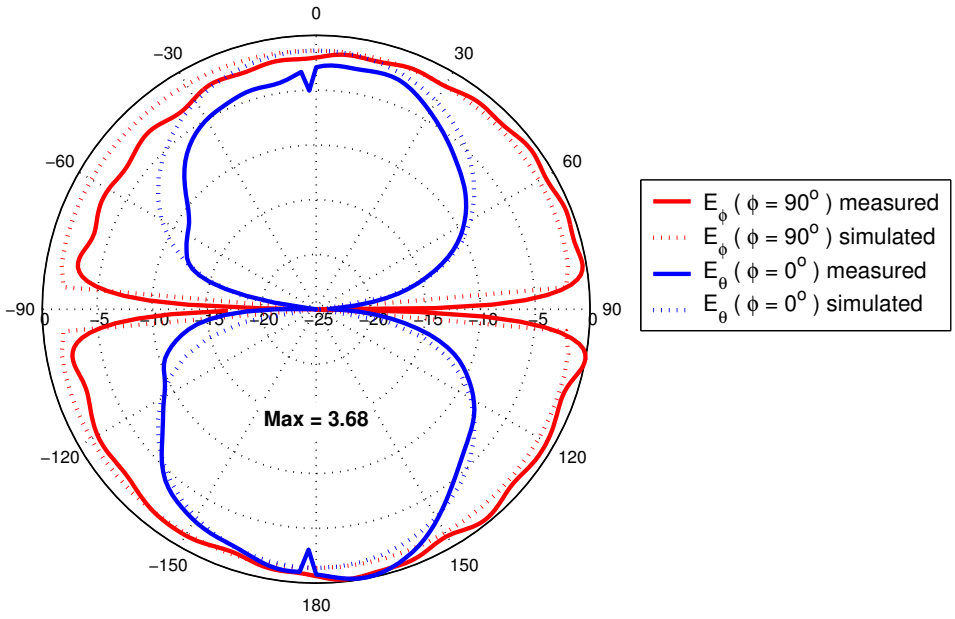

(e) switch state E

Figure 6.16 Measured and simulated elevation radiation patterns in the principal planes for the RPFDA (cont.)

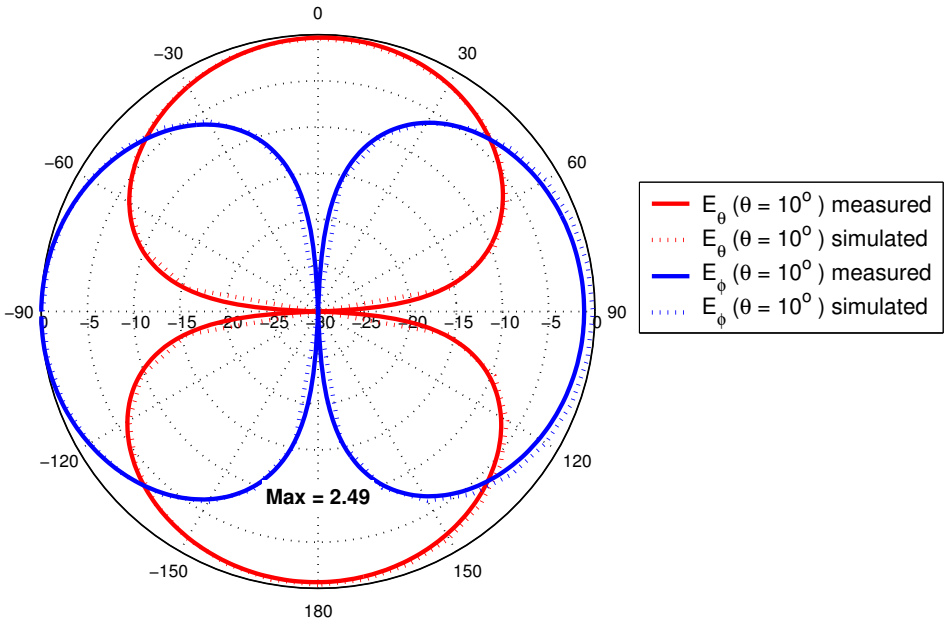

(a) switch state A

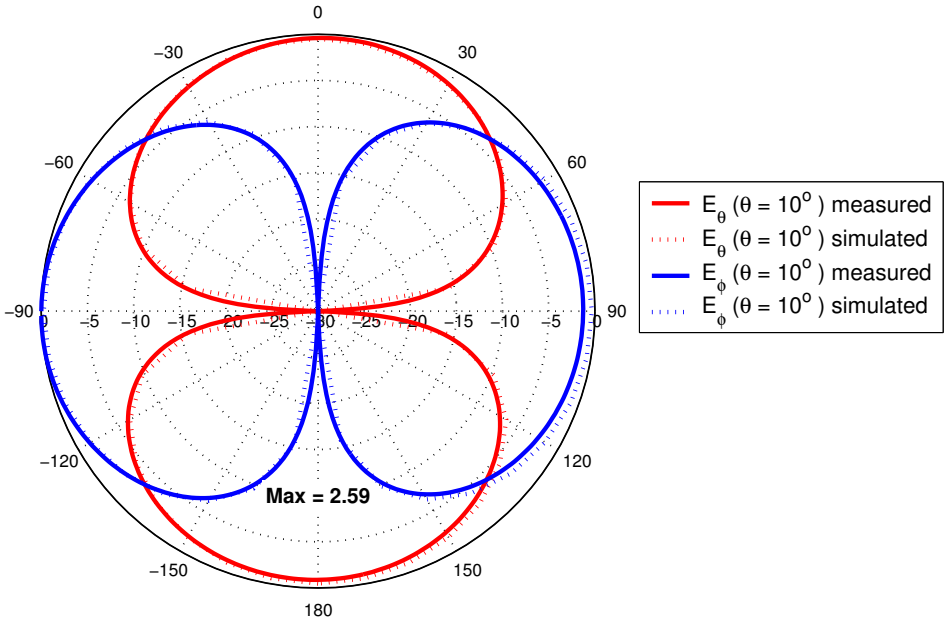

(b) switch state B

Figure 6.17 Measured and simulated conical radiation patterns ($\theta = 10°$) for the RPFDA.

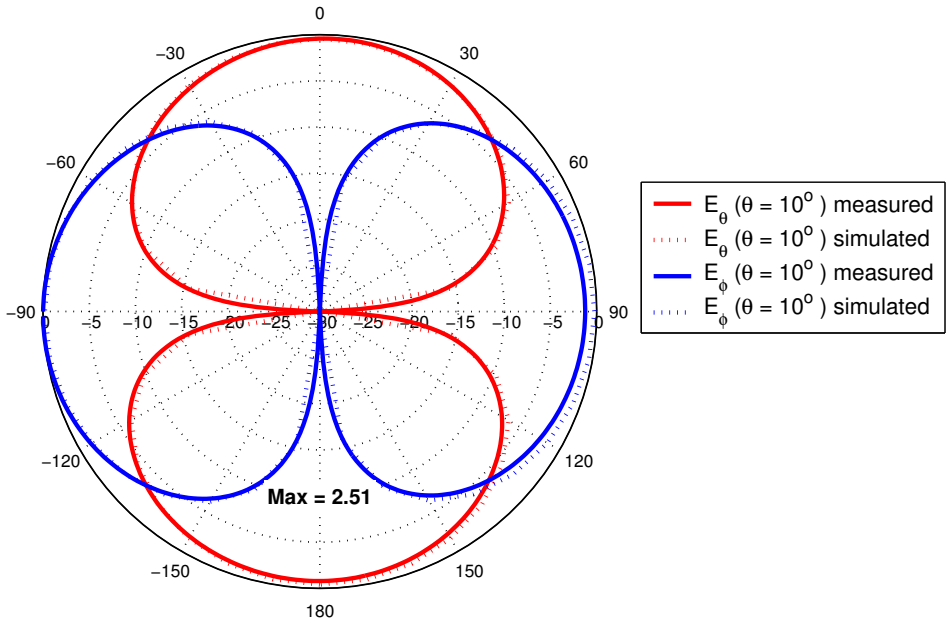

(c) switch state C

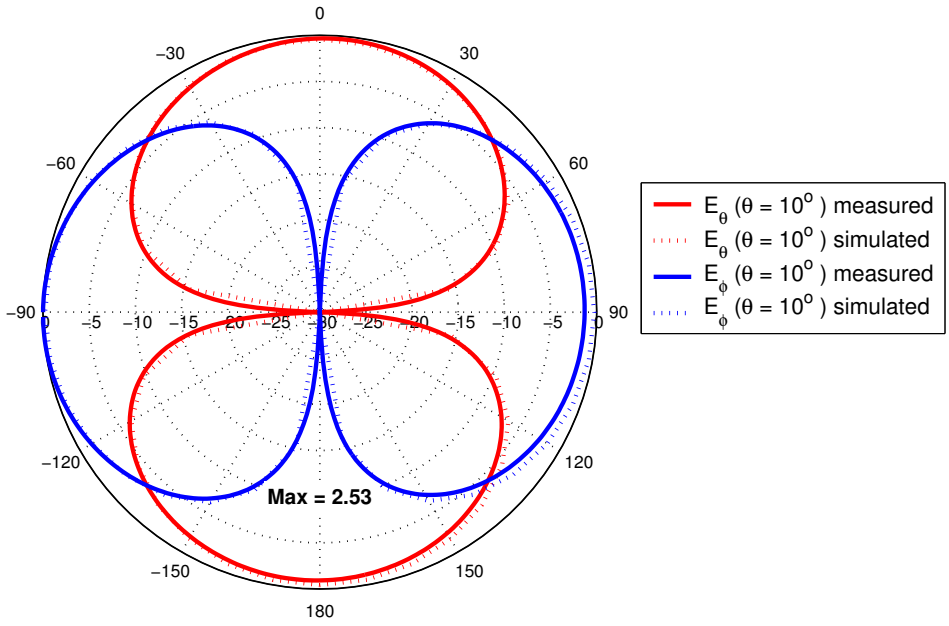

(d) switch state D

Figure 6.17 Measured and simulated conical radiation patterns ($\theta = 10°$) for the RPFDA (cont.)

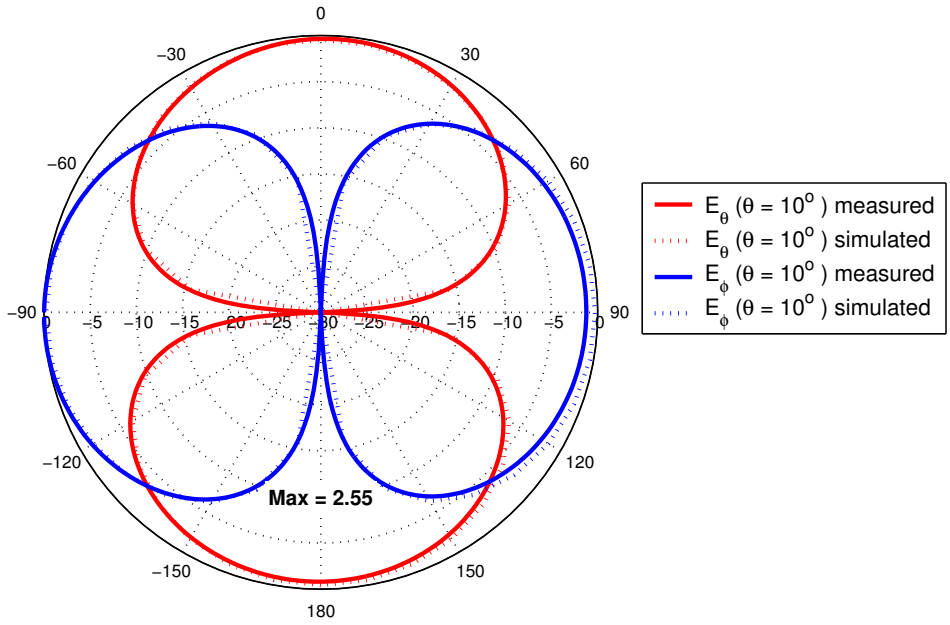

(e) switch state E

Figure 6.17 Measured and simulated conical radiation patterns ($\theta = 10°$) for the RPFDA (cont.)

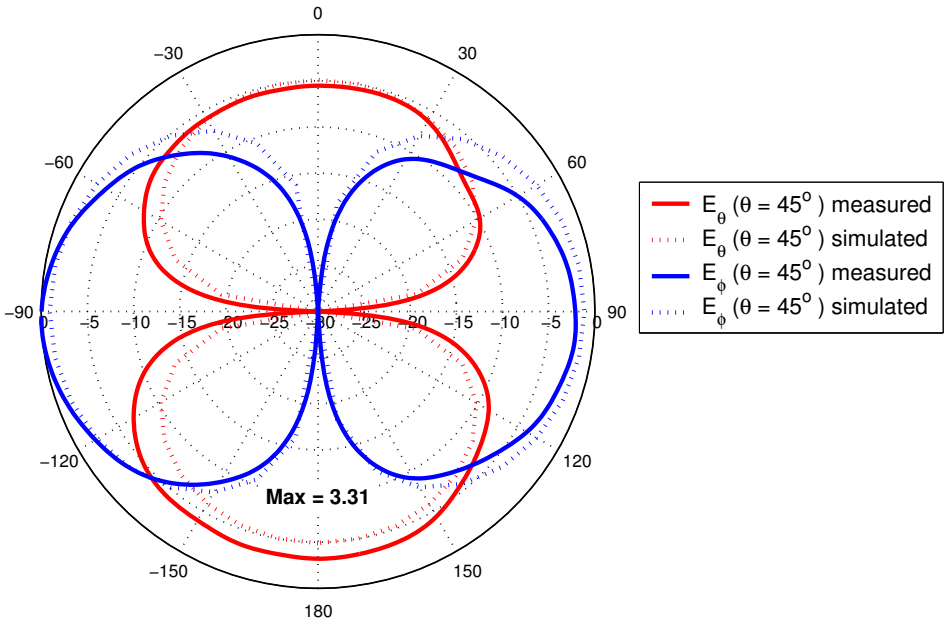

(a) switch state A

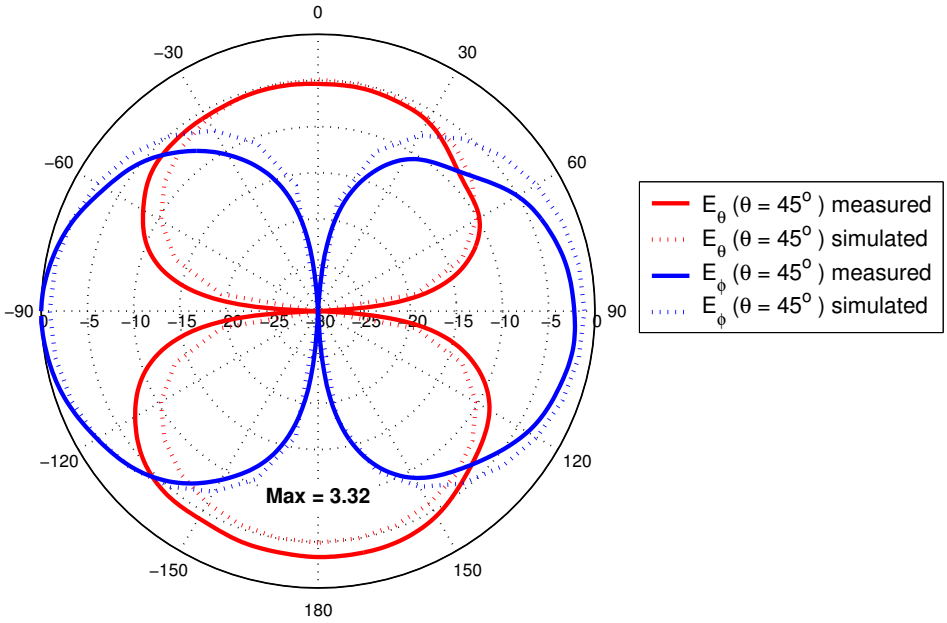

(b) switch state B

Figure 6.18 Measured and simulated conical radiation patterns ($\theta = 45°$) for the RPFDA.

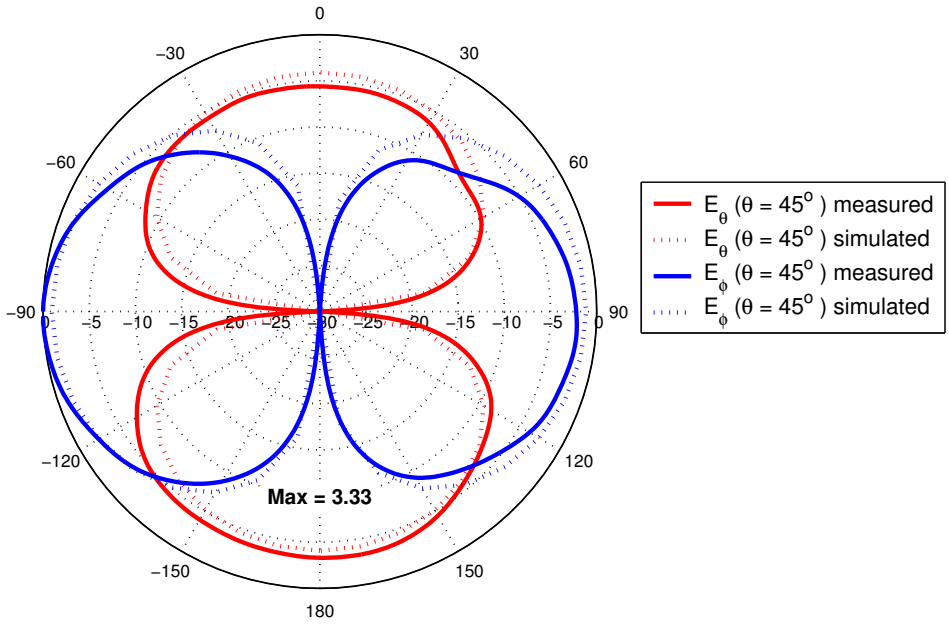

(c) switch state C

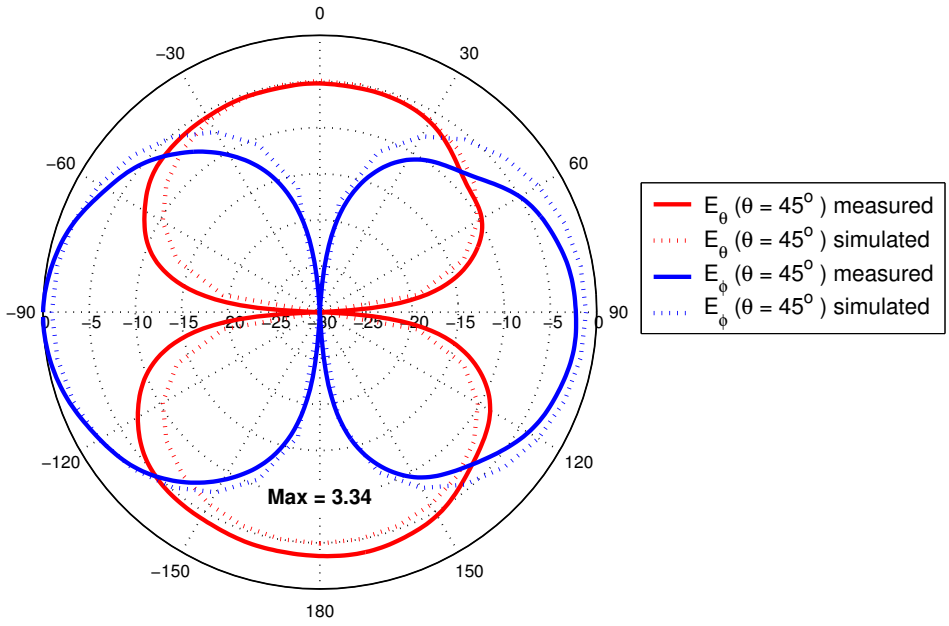

(d) switch state D

Figure 6.18 Measured and simulated conical radiation patterns ($\theta = 45°$) for the RPFDA (cont.)

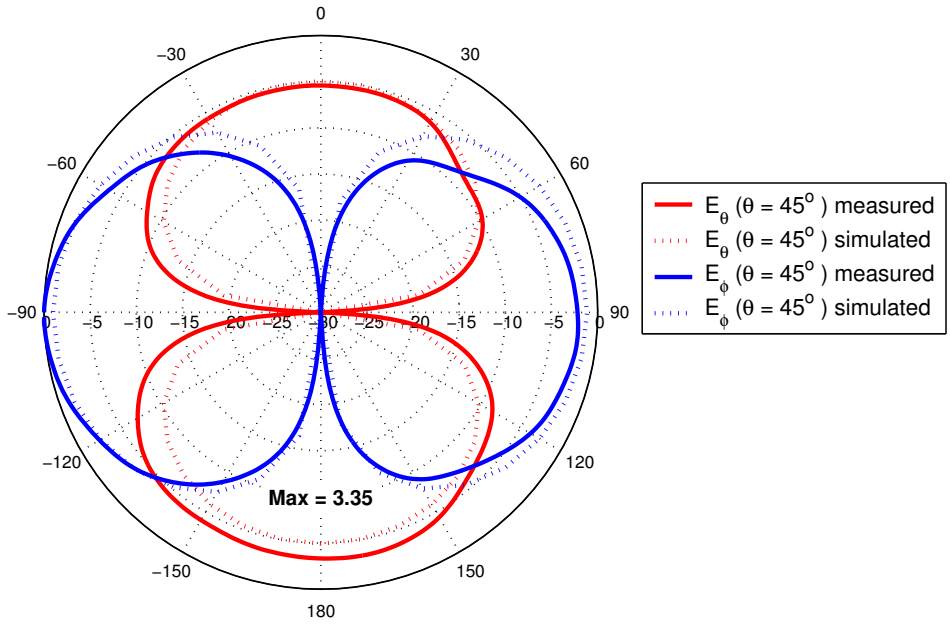

(e) switch state E

Figure 6.18 Measured and simulated conical radiation patterns ($\theta = 45°$) for the RPFDA (cont.)

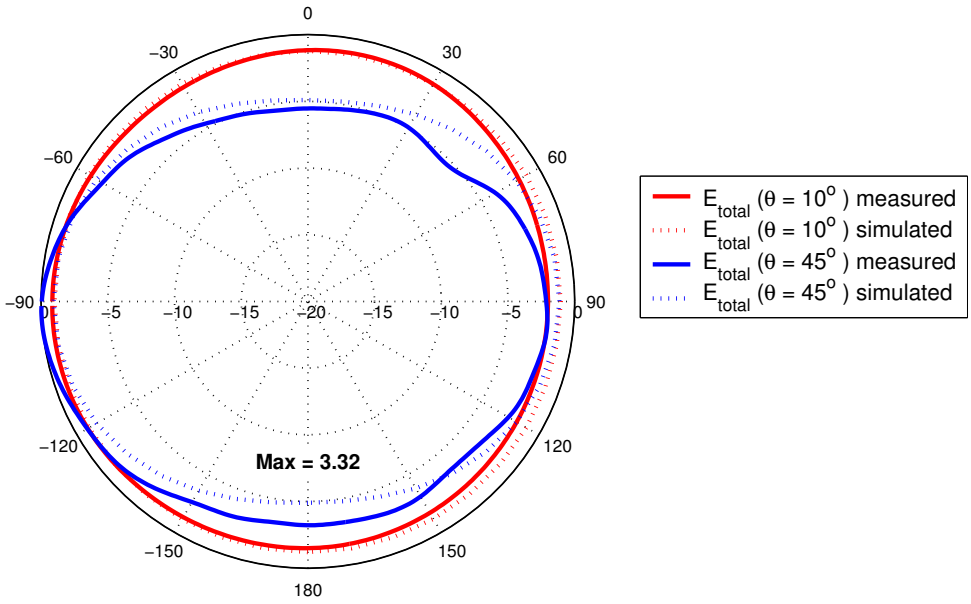

(a) switch state A

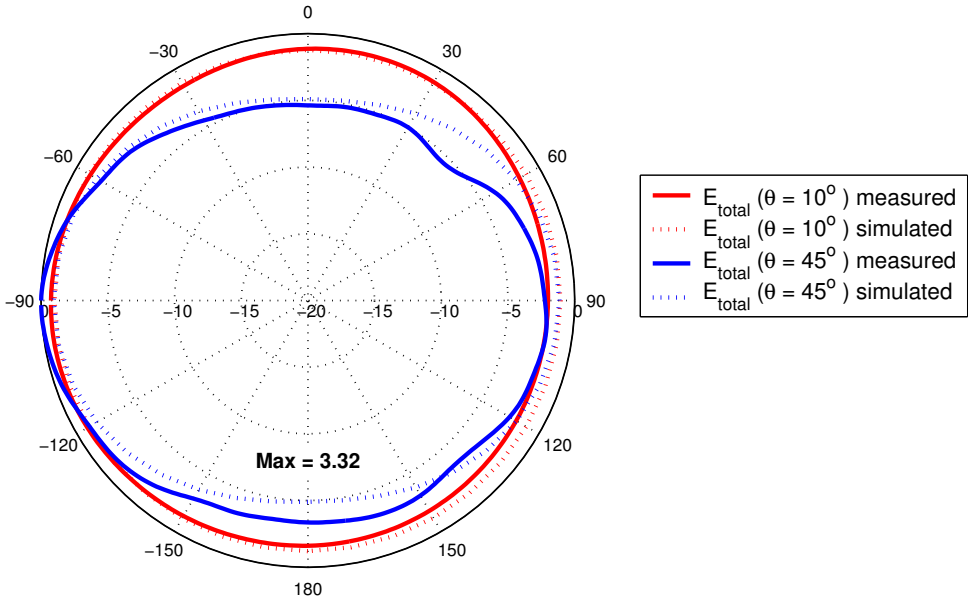

(b) switch state B

Figure 6.19 Measured and simulated conical E_{total} radiation patterns for the RPFDA.

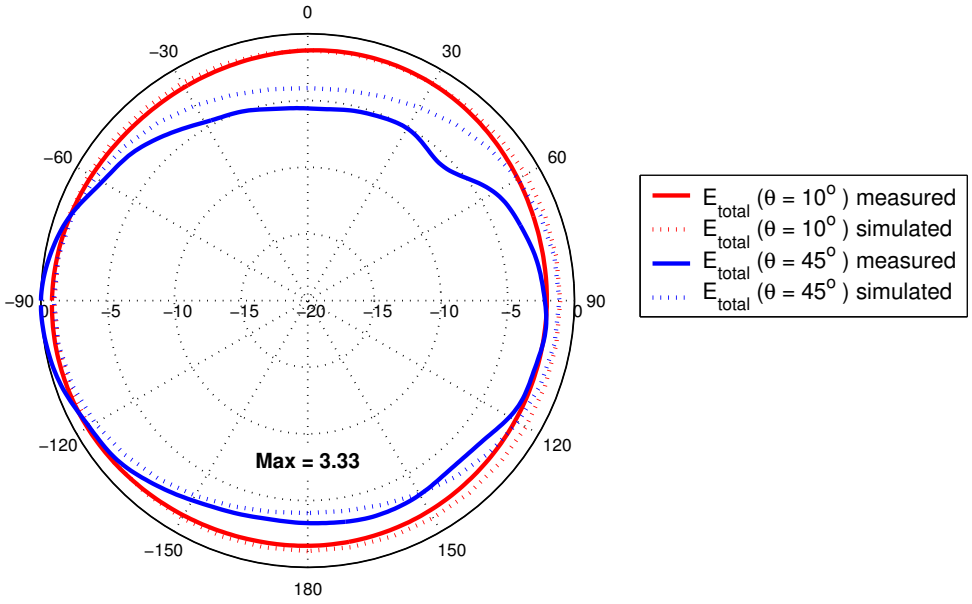

(c) switch state C

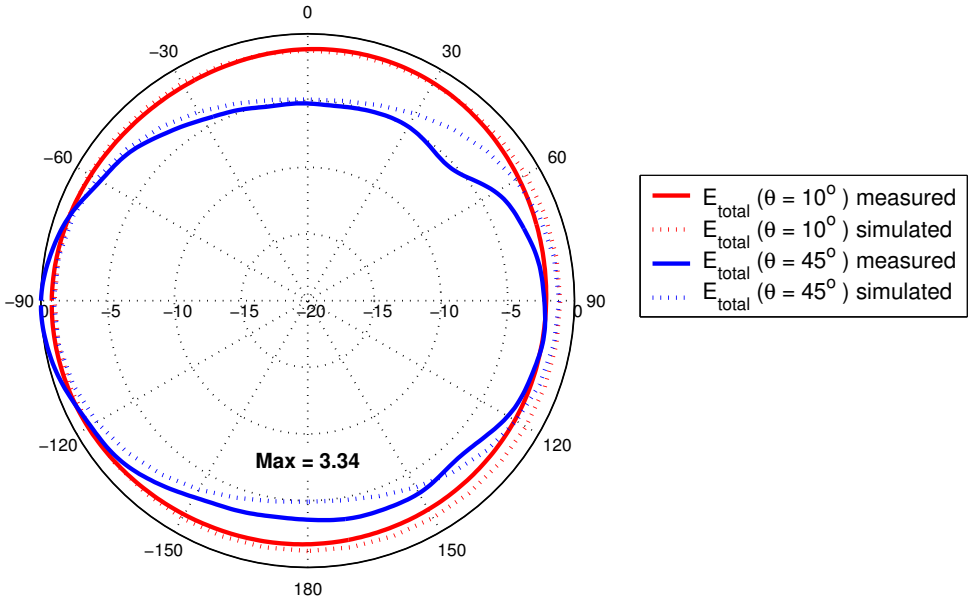

(d) switch state D

Figure 6.19 Measured and simulated conical E_{total} radiation patterns for the RPFDA (cont.)

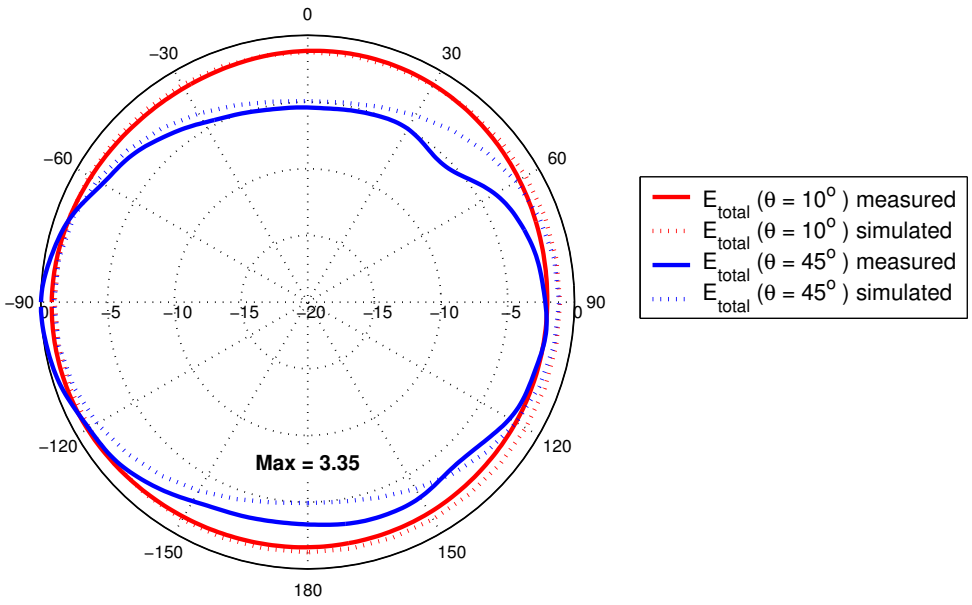

(e) switch state E

Figure 6.19 Measured and simulated conical E_{total} radiation patterns for the RPFDA (cont.)

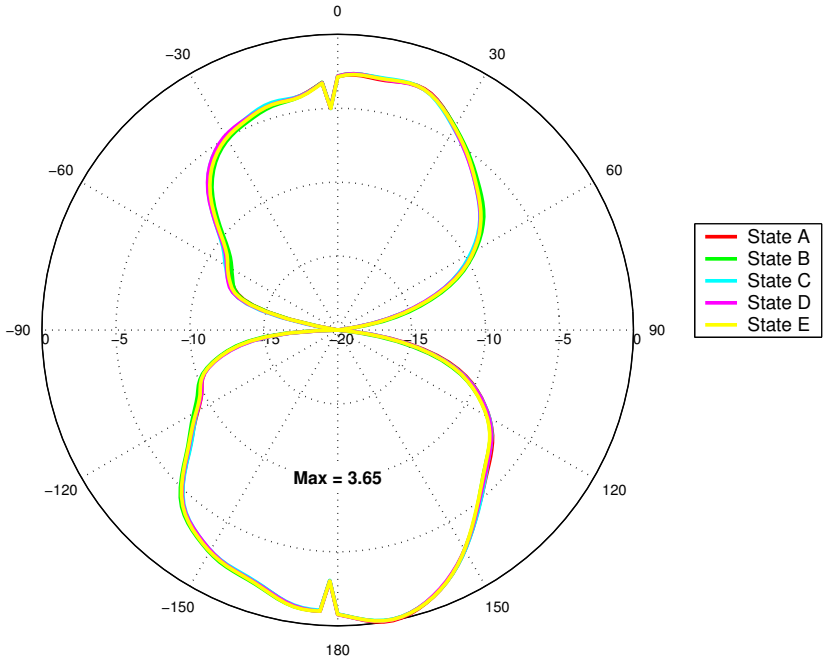

Figure 6.20 Comparison of measured elevation radiation patterns for all switch states of the RPFDA, E_θ ($\phi = 0°$).

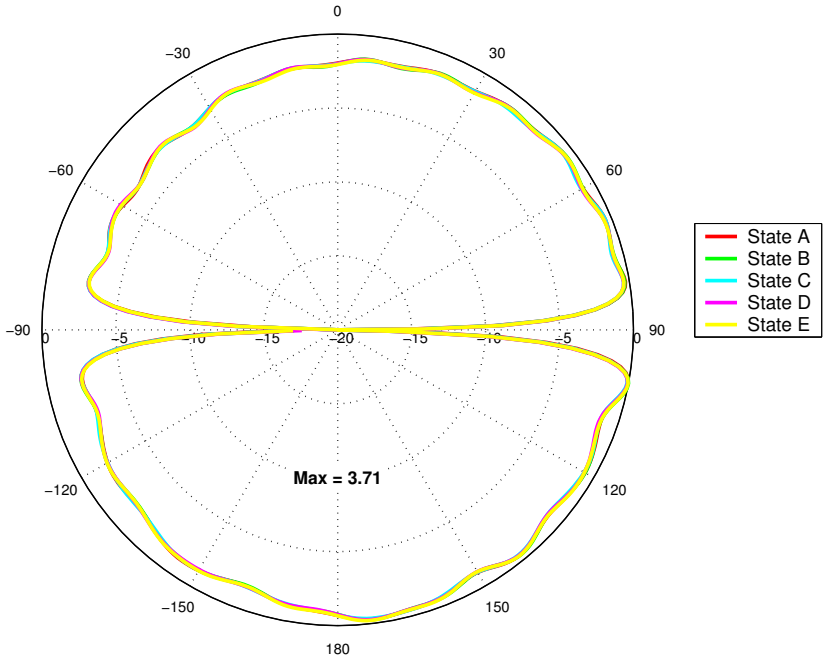

Figure 6.21 Comparison of measured elevation radiation patterns for all switch states of the RPFDA, E_ϕ ($\phi = 90°$).

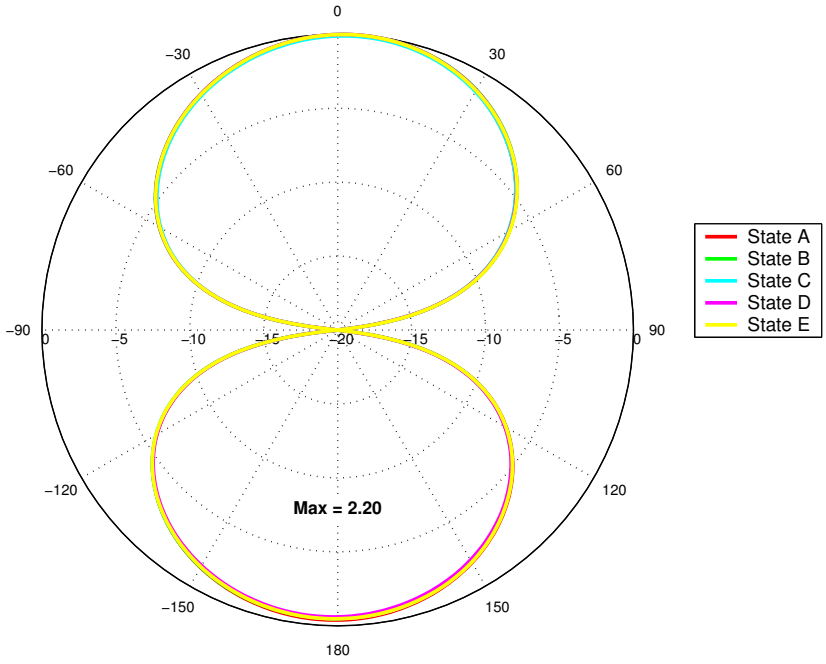

Figure 6.22 Comparison of measured conical radiation patterns for all switch states of the RPFDA, E_θ ($\theta = 10°$).

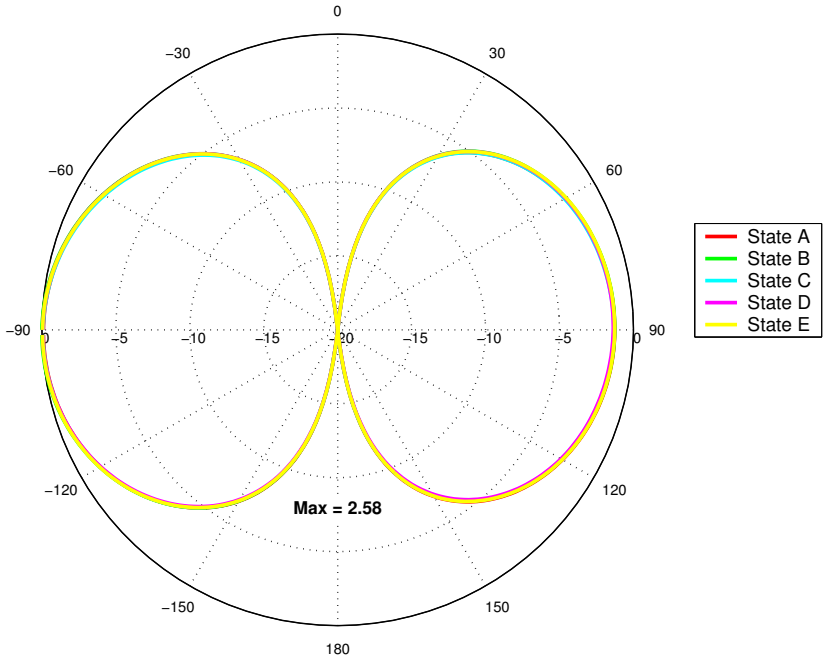

Figure 6.23 Comparison of measured conical radiation patterns for all switch states of the RPFDA, E_ϕ ($\theta = 10°$).

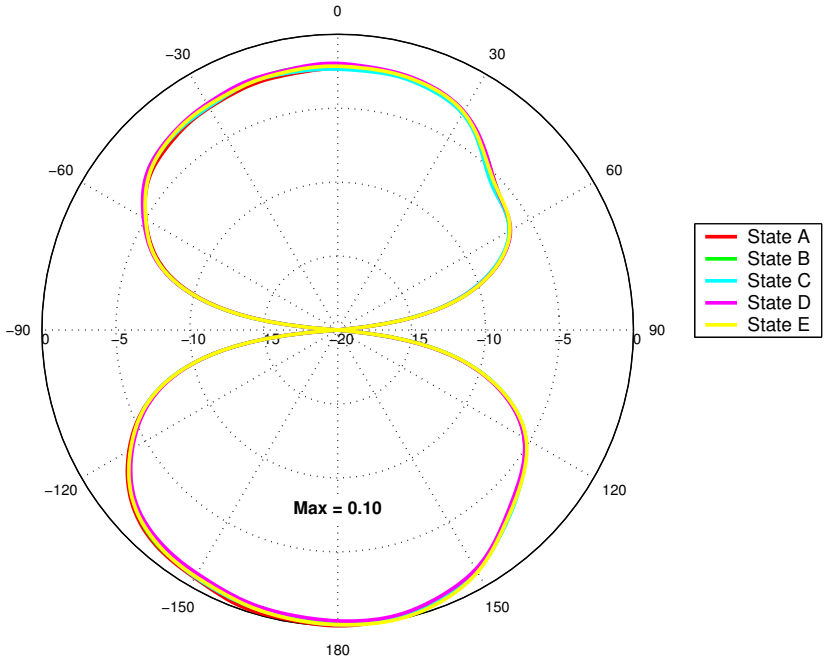

Figure 6.24 Comparison of measured conical radiation patterns for all switch states of the RPFDA, E_θ ($\theta = 45°$).

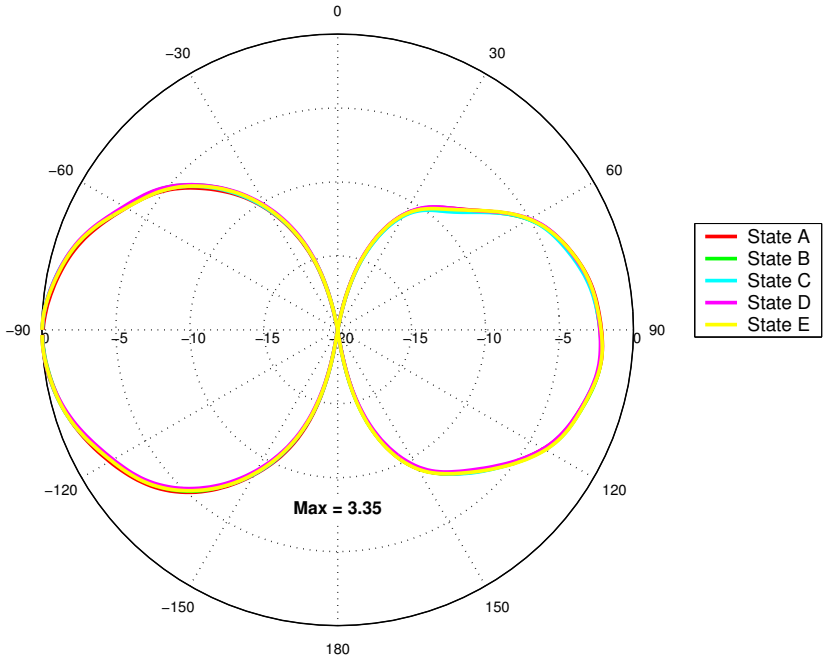

Figure 6.25 Comparison of measured conical radiation patterns for all switch states of the RPFDA, E_ϕ ($\theta = 45°$).

6.5 Summary

The development, design, computer simulation and measurement of the reconfigurable parasitic folded dipole antenna (RPFDA) was presented in this chapter. The RPFDA is a improvement on the conventional folded dipole antenna with bandwidth controllable behavior. A total of 8 RF switch locations were incorporated into the design to achieve the desired reconfigurable bandwidth performance. A selectable bandwidth of 0-13% was attained with minimal impact other antenna radiation characteristics. Table 6.5 summarizes the selectable bandwidth characteristics of the RPFDA. The measured antenna performance was very similar to the computed performance. The simulated and measured data demonstrates that the antenna indeed provides the desired bandwidth control.

Table 6.5 Selectable bandwidth performance for the reconfigurable parasitic folded dipole antenna with switch states of Figure 6.7.

	Bandwidth 2:1 VSWR (%)		Center Frequency f_o (GHz)		Minimum VSWR	
State	measured	simulated	measured	simulated	measured	simulated
A	10.6	13.1	1.05	1.05	1.23	1.28
B	9.8	11.5	1.05	1.05	1.30	1.40
C	8.0	9.3	1.05	1.05	1.42	1.60
D	7.3	2.0	1.05	1.05	1.53	1.98
E	2.3	0	1.05	1.03	1.8	2.80

Chapter 7

Conclusions

The new concept of antenna bandwidth control using reconfigurable antenna elements has been presented in this dissertation. Three new antenna designs have been developed to demonstrate the bandwidth control concept. The new designs presented are the reconfigurable ring patch antenna (RRPA), reconfigurable planar inverted-F antenna (RPIFA) and reconfigurable parasitic folded dipole antenna (RPFDA). This chapter summarizes the important points in this dissertation, details the contributions presented in this dissertation and proposes future work to enhance the existing research.

7.1 Summary

A review of previous work and important background information related to this dissertation was presented in Chapters 1 and 2. Reviews of the square ring patch antenna, the planar inverted-F antenna and the folded dipole antenna were covered in 2. These conventional antenna designs formed the the bases for the newly developed bandwidth reconfigurable antenna designs. Also included in Chapter 2 was a description of the current state of reconfigurable antenna research.

Chapter 3 provided an expanded and detailed analysis of the reconfigurable antenna concept. Descriptions of current and proposed reconfigurable antenna technolo-

gies including the various methodologies employed for achieving antenna reconfiguration were explored. The three broad methods for achieving reconfigurable antenna operation were identified as *total geometry morphing*, *matching network morphing* and *smart geometry reconfiguration*. An overview of RF switch technologies was given and a detailed comparison between the switch technologies was presented. Descriptions of the physical components and switching devices used in reconfigurable antennas was given along with the relevant electrical switch characteristics and mathematical models necessary for simulating the switches in an RF environment.

The next three chapters presented the newly developed antenna designs capable of reconfigurable bandwidth control. Chapter 4 presented the development, design, computer simulation and measurement of the reconfigurable ring patch antenna. The RRPA is an extension of the conventional square ring patch antenna with reconfigurable bandwidth control. A total of 80 RF MEMS switches were incorporated into the new design to give the antenna selectable bandwidth control. Six discrete antenna states were designed with for a controllable bandwidth performance of up to 15%. The inclusion of the selectable bandwidth behavior resulted in a very minimal impact on the other important radiation properties of the antenna. The measured antenna performance was very similar to the predicted computer simulation performance and demonstrated that the antenna provides the desired bandwidth control.

The development, design, simulation and measurement of the reconfigurable planar inverted-F antenna was presented in Chapter 5. A total of 24 RF MEMS switches were incorporated into the new design to give the antenna selectable bandwidth control. Five discrete antenna states were designed for a controllable bandwidth performance of up to 16%. The reconfigurable behavior of the RPIFA resulted in only a minor influence on the other important radiation characteristics of the antenna. The measured antenna performance was similar to the computed performance and demonstrated that the antenna achieves the desired bandwidth control.

Chapter 6 presented the development, design, computer simulation and measurement of the reconfigurable parasitic folded dipole antenna. The RPFDA is an improvement on the conventional printed folded dipole antenna with reconfigurable bandwidth behavior. A total of eight RF MEMS switches were integrated into the

antenna design to achieve the reconfigurable bandwidth control. Five discrete antenna states were designed for a selectable bandwidth control of 13%. The bandwidth reconfigurable behavior of the antenna resulted in only very minimal impact on the other radiation characteristics of the antenna. The measured antenna performance was very similar to the computed performance and demonstrated that the antenna achieves the desired reconfigurable antenna behavior.

7.2 Contributions

The major contribution of this dissertation is twofold. First the new concept of active antenna bandwidth control using reconfigurable antenna elements was developed. Recent advances in RF switch technology have allowed for the development of new classes of dynamically reconfigurable antenna. Until now, the primary areas of interest in reconfigurable antenna designs has been confined to radiation pattern control and steering, frequency of operation selection, and array applications.

The second significant contribution presented here encompasses the three new antenna designs created to achieve the active bandwidth control. The new designs developed in this dissertation are the reconfigurable ring patch antenna (RRPA), the reconfigurable planar inverted-F antenna (RPIFA) and the reconfigurable folded parasitic dipole antenna (RPFDA). These antennas all exhibit the desired bandwidth control while maintaining nearly constant performance over all other critical electrical characteristics. Table 7.1 provides a summary of the important performance characteristics for the three antennas developed in this work.

Table 7.1 Bandwidth reconfigurable antennas performance comparison.

Antenna	Number of Switches	Number of States	Maximum Bandwidth (%)	Selectable Bandwidth States (%)
RRPA	80	6	15.0	0, 5.0, 9.0, 11.0, 13.0, 15.0
RPIFA	12	5	15.8	0, 5.1, 9.4, 12.4, 15.8
RPFDA	8	5	13.1	0, 2.0, 9.3, 11.5, 13.1

7.3 Future Work

The research presented in this dissertation may be extended in several ways. The examination and development of additional antenna designs which incorporate reconfigurable elements to achieve bandwidth control is the first extension to the work already presented here. Additionally, construction and measurement of the designs presented here using actual RF MEMS switches and the subsequent comparison of these measurements to the results presented in this dissertation is a logical extension of the present work. In particular, the MEMS switch control biasing details should be examined more closely to verify that the assumptions presented here are valid. While it is believed that the biasing effects can be minimized through the use of high impedance control lines and judicious trace routing, these details should be examined before production level units can be developed.

References

[1] S. Licul, "Time-domain antenna characterization and design," Ph.D. dissertation, Virginia Tech, Blacksburg, VA, 2004.

[2] J.-C. Chiao, Y. Fu, I. M. Chio, M. DeLisio, and L.-Y. Lin, "MEMS reconfigurable Vee antenna," in *Microwave Symposium Digest, 1999 IEEE MTT-S International*, M. Matloubian and E. Ponti, Eds., vol. 4. IEEE, June 1999, pp. 1515–1518.

[3] J. H. Schaffner, D. F. Sievenpiper, R. Y. Loo, J. L. Lee, and S. W. Livingston, "A wideband beam switching antenna using RF MEMS switches," HRL Laboratories, Malibu, CA, USA, Tech. Rep., 2001.

[4] W.-S. Chen, C.-K. Wu, , and K.-L. Wong, "Square-ring microstrip antenna with a cross strip for compact circular polarization operation," *IEEE Transactions on Antennas and Propagation*, vol. 47, no. 10, pp. 1566–1568, October 1999.

[5] W.-S. Chen and H.-D. Chen, "Single-feed circularly polarized square-ring microstrip antennas with a slit," in *IEEE Antennas and Propagation Society International Symposium, 1998*, vol. 3, Atlanta, GA, June 1998, pp. 1360–1363.

[6] V. Palanisamy and R. Garg, "Analysis of circularly polarized square ring and cross-strip microstrip antennas," *IEEE Transactions on Antennas and Propagation*, vol. AP-34, no. 11, pp. 1340–1346, November 1986.

[7] W. L. Stutzman and G. A. Thiele, *Antenna Theory and Design*. New York: John Wiley & Sons, Inc., 1998.

[8] P. M. Bafrooei and L. Shafai, "Characteristics of single- and double-layer microstrip square-ring antennas," *IEEE Transactions on Antennas and Propagation*, vol. 47, no. 10, pp. 1633–1639, October 1999.

[9] P. Moosavi and L. Shafai, "Stacked square ring resonators for bandwidth enhancment," in *IEEE Antennas and Propagation Society International Symposium, 1997*, vol. 2, Montreal, July 1997, pp. 944–947.

[10] J. Gómez-Tagle and C. G. Christodoulou, "Extended cavity model analysis of stacked ring microstrip antennas," *IEEE Transactions on Antennas and Propagation*, vol. 45, no. 11, pp. 1626–1635, November 1997.

[11] A. Gobien, "Investigation of low profile antenna designs for use in hand-held radios," Master's thesis, Virginia Polytechnic Institute and State University, August 1997.

[12] Z. Liu, P. Hall, and D. Wake, "Dual-frequency planar inverted-F antenna," *IEEE Transactions on Antennas and Propagation*, vol. 45, no. 10, pp. 1451–1458, October 1997.

[13] T. Taga, *Analysis, Design, and Measurement of Small and Low-Profile Antennas*. Boston: Artech House Publishers, 1992, ch. 5: Analysis of Planar Inverted-F Antennas and Antenna Design for Portable Radio Equipment, pp. 161 – 180.

[14] *IE3D User's Manual*, 8th ed., Zeland Software Inc., 2001.

[15] C. R. Rowell and R. D. Murch, "A capacitively loaded PIFA for compact mobile telephone handsets," *IEEE Transactions on Antennas and Propagation*, vol. 45, no. 5, pp. 837–842, May 1997.

[16] M. A. Jensen and Y. Rahmat-Samii, "Performance analysis of antennas for hand-held transceivers using FDTD," *IEEE Transactions on Antennas and Propagation*, vol. 42, no. 8, pp. 1106–1113, August 1994.

[17] K. Virga and Y. Rahmat-Samii, "An enhanced-bandwidth integrated dual-L antenna for mobile communications systems–design and measurement," in *Antennas & Propagation Society International Symposium Digest*. Newport Beach, CA: IEEE, 1995.

[18] Z. Liu and P. Hall, "A novel dual-band antenna for hand-held po[r]table telephone," in *Antennas & Propagation Society International Symposium Digest*, vol. 1. Baltimore, MD: IEEE, July 1996, pp. 54–57.

[19] M. A. Jensen and Y. Rahmat-Samii, "FDTD analysis of pifa diversity antennas on a hand-held transceiver unit," in *Antennas & Propagation Society International Symposium Digest*, vol. 2. Ann Arbor, MI: IEEE, July 1993.

[20] C. Harrison and R. King, "Folded dipoles and loops," *IRE Transactions on Antennas and Propagation*, vol. 9, pp. 171–187, March 1961.

[21] H. Jasik, Ed., *Antenna Engineering Handbook*. McGraw-Hill, 1961.

[22] H.-S. Tsai and R. A. York, "FDTD analysis of cpw-fed folded-slot and multiple-slot antennas on thin substrates," *IEEE Transactions on Antennas and Propagation*, vol. 44, no. 2, pp. 217–226, February 1996.

[23] T. M. Weller, L. P. B. Katehi, and G. M. Rebeiz, "Single and double folded-slot antennas on semi-infinite substrates," *IEEE Transactions on Antennas and Propagation*, vol. 43, no. 12, pp. 1423–1428, December 1995.

[24] M. W. Nurnberger, J. L. Volakis, J. A. Mosko, and T. Özdemir, "Analysis of the log-periodic folded slot array," *IEEE Antennas and Propagation International Symposium Digest, 1994*, vol. 3, pp. 1282–1285, June 1994.

[25] H. K. Schuman, "Modeling folded dipoles and feedlines for radiation and scattering," *IEEE Transactions on Antennas and Propagation*, vol. 38, no. 1, pp. 30–39, January 1990.

[26] W. T. Whistler, "The microstrip dual folded dipole as a phased array element," *IEEE International Antennas and Propagation Symposium Digest, 1987*, vol. 25, pp. 1024–1027, June 1987.

[27] D. Peroulis, K. Sarabandi, and L. Katehi, "A planar VHF reconfigurable slot antenna," in *Antennas and Propagation Society, 2001 IEEE International Symposium*, vol. 1, Boston, MA, July 2001, pp. 154 – 157.

[28] J.-C. Chiao, "MEMS RF devices for antenna applications," in *Microwave Conference, 2000 Asia-Pacific*. Sydney: IEEE, December 2000, pp. 895–898.

[29] J.-C. Chiao, Y. Fu, D. Choudhury, and L.-Y. Lin, "MEMS millimeterwave components," in *Microwave Symposium Digest, 1999 IEEE MTT-S International*, M. Matloubian and E. Ponti, Eds., vol. 2. IEEE, June 1999, pp. 463–466.

[30] B. Cetiner, L. Jofre, and F. De Flaviis, "Reconfigurable miniature multielement antenna for wireless networking," in *IEEE Radio and Wireless Conference, 2001. RAWCON 2001*, August 2001, pp. 203–206.

[31] L. Jofre, B. Cetiner, and F. De Flaviis, "Miniature multi-element antenna for wireless communications," *IEEE Transactions on Antennas and Propagation*, vol. 50, no. 5, pp. 658–669, May 2002.

[32] B. Cetiner, L. Jofre, G. Li, and F. de Flaviis, "A packaged reconfigurable multielement antenna for wireless networking," in *2001 Asian-Pacific Microwave Conference. APMC 2001*, vol. 2, Taipei, Taiwan, December 2001, pp. 705–708.

[33] B. Chang, Y. Qian, and T. Itoh, "A reconfigurable leaky mode/patch antenna controlled by pin diode switches," in *IEEE Antennas and Propagation Society International Symposium, 1999*, vol. 4, Orlando, FL, July 1999, pp. 2694–2697.

[34] Y. Qian, B. Chang, M. Chang, and T. Itoh, "Reconfigurable leaky-mode multifunction patch antenna structure," *Electronic Letters*, vol. 35, no. 2, pp. 104–105, January 1999.

[35] C.-K. C. Tzuang, "Leaky mode perspective an printed antenna," *Proceedings of National Science Council ROC(A)*, vol. 23, no. 4, pp. 544–549, 1999.

[36] C.-W. Baek, S. Song, C. Cheon, Y.-K. Kim, and Y. Kwon, "2-D mechanical beam steering antenna fabricated using MEMS technology," in *IEEE MTT-S International Microwave Symposium Digest, 2001*, Phoenix, AZ, May 2001, pp. 211–214.

[37] J. Bernhard, R. Wang, R. Clark, and P. Mayes, "Stacked reconfigurable antenna elements for space-based radar applications," in *IEEE Antennas and Propagation Society International Symposium, 2001*, vol. 1, Boston, MA, July 2001, pp. 158–161.

[38] R. Simons, D. Chun, and L. Katehi, "Reconfigurable array antenna using micro-electromechanical systems (MEMS) actuators," in *IEEE International Symposium Antennas and Propagation Society, 2001*, vol. 3, Boston, July 2001, pp. 674–677.

[39] J. Maloney, M. Kesler, L. Lust, L. Pringle, T. Fountain, P. Harms, and G. Smith, "Switched fragmented aperture antennas," in *IEEE Antennas and Propagation Society International Symposium, 2000*, Salt Lake City, July 2000, pp. 310–313.

[40] L. Pringle, D. Denison, P. Frederich, E. Kuster, *et al.*, "Micro-switched fragmented reconfigurable apertures," workshop presentation, July 2000, gTRI RECAP Symposium 2000.

[41] L. Pringle, P. Friederich, S. Blalock, G. Kiesel, P. Harms, D. Denison, E. Kuster, and G. Smith, "GTRI reconfigurable aperture design," in *IEEE Antennas and Propagation Society International Symposium, 2002*, vol. 1, San Antonio, June 2002, pp. 473–476.

[42] W. H. Weedon, W. J. Payne, and G. M. Rebeiz, "MEMS-switched reconfigurable antennas," in *IEEE Antennas and Propagation Society International Symposium, 2001*, vol. 3. Boston: IEEE, July 2001, pp. 654–657.

[43] C. Bozler, R. Drangmeister, S. Duffy, M. Gouker, J. Knecht, L. Kushner, R. Parr, S. Rabe, and L. Travis, "MEMs microswitch arrays for reconfigurable distributed microwave components," in *IEEE Antennas and Propagation Society International Symposium, 2000*, vol. 2. Salt Lake City: IEEE, July 2000, pp. 587–591.

[44] ——, "MEMs microswitch arrays for reconfigurable distributed microwave components," in *Microwave Symposium Digest. 2000 IEEE MTT-S International*, vol. 1. Boston: IEEE, June 2000, pp. 153–156.

[45] C. Coleman, E. Rothwell, J. Ross, and L. Nagy, "Self-structuring antennas," *IEEE Antennas and Propagation Magazine*, vol. 44, no. 3, pp. 11–23, June 2002.

[46] J. H. Schaffner, D. F. Sievenpiper, R. Y. Loo, J. L. Lee, and S. W. Livingston, "A wideband beam switching antenna using RF MEMS switches," in *IEEE Antennas and Propagation Society International Symposium, 2001*, vol. 3, Boston, MA, July 2001, pp. 658–661.

[47] J. Schaffner, R. Loo, D. Sievenpiper, F. Dolezal, G. Tangonan, J. Colburn, J. Lynch, J. Lee, S. Livingston, R. Broas, and M. Wu, "Reconfigurable aperture antennas using RF MEMS switches for multi-octave tunability and beam steering," in *IEEE Antennas and Propagation Society International Symposium, 2000*, Salt Lake City, UT, July 2000, pp. 321–324.

[48] J. Veihl, R. Hodges, D. McGrath, and C. Monzon, "Reconfigurable aperture decade bandwidth array," in *IEEE Antennas and Propagation Society International Symposium, 2000*, vol. 1. IEEE, July 2000, pp. 314–317.

[49] F. Dobias and J. Gunther, "Reconfigurable array antennas with phase-only control of quantized phase shifters," in *Vehicular Technology Conference, 1995 IEEE 45th*, vol. 1, Chicago, IL, USA, July 1995, pp. 35–39.

[50] B. Norvell, R. Hancock, J. Smith, M. Pugh, S. Theis, and J. Kriatkofsky, "Micro electro mechanical switch (mems) technology applied to electronically scanned arrays for space based radar," in *IEEE Aerospace Conference Proceedings, 1999*, vol. 3, Snowmass at Aspen, CO, March 1999, pp. 239–247.

[51] V. K. Varadan, K. J. Vinoy, and K. A. Jose, *RF MEMS and Their Applications*. West Sussex, England: John Wiley & Sons, 2003.

[52] *Applications of PIN Diodes*, Hewlett-Packard, 1997.

[53] *PIN Diode Designers' Handbook*, Microsemi Corp., Watertown, MA, 1998.

[54] C. A. Liechti, "Microwave field-effect transistors–1976," *IEEE Transactions on Microwave Theory and Techniques*, vol. MTT-24, no. 6, pp. 279–300, June 1976.

[55] R. A. Gaspari and H. Yee, "Microwave GaAs FET switching," in *Microwave Symposium Digest, MTT-S International*, vol. 78, no. 1, June 1978, pp. 58–60.

[56] H. J. D. L. Santos, *RF MEMS Circuit Design for Wireless Commuications*, ser. Artech House Microelectromechanical Systems Series. Boston: Artech House Publishers, 2002.

[57] E. R. Brown, "RF-MEMs switches for reconfigurable integrated circuits," *IEEE Transactions on Microwave Theory and Techniques*, vol. 46, no. 11, pp. 1868–1880, November 1998.

[58] C. Goldsmith, J. Randall, S. Eshelman, T. Lin, D. Denniston, S. Chen, and B. Norvell, "Characteristics of micromachined switches at microwave frequencies," in *Microwave Symposium Digest, 1996., IEEE MTT-S International*, vol. 2, June 1996, pp. 1141 – 1144.

[59] G. M. Rebeiz, *RF MEMS: Theory, Design, and Technology*. Hoboken, NJ: Wiley-Interscience, 2003.

[60] D. Hyman and M. Mehregany, "Contact physics of gold microcontacts for MEMS switches," *IEEE Transactions on Components and Packaging Technologies*, vol. 22, no. 3, September 1999.

[61] D. Peroulis, K. Sarabandi, and L. Katehi, "Low contact resistance series MEMS switches," in *Microwave Symposium Digest, 2002 IEEE MTT-S International*, vol. 1, Seattle, WA, June 2002.

[62] R. Mihailovich, M. Kim, J. Hacker, E. Sovero, J. Studer, J. Higgins, and J. DeNatale, "MEM relay for reconfigurable RF circuits," *IEEE Microwave And Wireless Component Letters*, vol. 11, no. 2, pp. 53 – 55, February 2001.

[63] J. Poon, L. C. Ling, and N. Karmakar, "Investigations into RF MEMS switches for reconfigurable phased antenna arrays," in *Antennas and Propagation Society International Symposium, 2002*, vol. 2. IEEE, 2002, pp. 18–21.

[64] G. M. Rebeiz, "RF MEMS switches: Status of the technology," in *TRANSDUCERS, Solid-State Sensors, Actuators and Microsystems, 12th Innational Conference on*, vol. 2, June 2003, pp. 1726 – 1729.

[65] J. Yao and M. Chang, "A surface micromachined miniature switch for telecommunications applications with signal frequencies from dc up to 4 ghz," in *Solid-State Sensors and Actuators, 1995 and Eurosensors IX. Transducers '95. The 8th International Conference on*, vol. 2, June 1995, pp. 384 –387.

[66] A. De Silva, C. Vaughan, D. Frear, L. Liu, S. Kuo, J. Foerstner, J. Drye, J. Abrokwah, H. Hughes, C. Amrine, C. Butler, S. Markgraf, H. Denton, and S. Springer, "Motorola mems switch technology for high frequency applications," in *Microelectromechanical Systems Conference, 2001*, Berkeley, CA, 2001, pp. 22 – 24.

[67] C. T.-C. Nguyen, L. P. Katehi, and G. M. Rebeiz, "Micromachined devices for wireless communications," *Proceedings of the IEEE*, vol. 86, no. 8, pp. 1756 – 1768, 1998.

[68] G. M. Rebeiz and J. B. Muldavin, "RF MEMS switches and circuits," *IEEE Microwave Magazine*, pp. 59–71, December 2001.

[69] D. Peroulis, S. P. Pacheco, K. Sarabandi, and L. P. B. Katehi, "Electromechanical considerations in developing low-voltage RF MEMS switches," *IEEE Transactions on Microwave Theory and Techniques*, vol. 51, no. 1, pp. 259–270, January 2003.

[70] N. Bushyager and M. Tentzeris, "Modeling and design of RF MEMS structures using computationsally efficient numerical techniques," in *Electronic Components and Technology Conference, 2001. Proceedings., 51st*, Orlando, May 2001, pp. 327 – 330.

[71] J. B. Muldavin and G. M. Rebeiz, "Inline capacitive and DC-contact MEMS shunt switches," *IEEE Microwave And Wireless Component Letters*, vol. 11, no. 8, pp. 334 – 336, August 2001.

[72] ——, "High-isolation CPW MEMS shunt switches–part 1: Modeling," *IEEE Transactions on Microwave Theory and Techniques*, vol. 48, no. 6, pp. 1045 – 1051, June 2000.

[73] J. Gómez-Tagle and C. G. Christodoulou, "Extended cavity model analysis of stacked microstrip ring antennas," *IEEE Transactions on Antennas and Propagation*, vol. 45, no. 11, pp. 1626 – 1637, November 1997.

[74] J. W. Mink, "Circular ring microstrip antenna elements," in *Antennas and Propagation Society International Symposium, 1980*, vol. 18, June 1980, pp. 605 – 608.

[75] W. C. Chew, "A broad-band annular-ring microstrip antenna," *IEEE Transactions on Antennas and Propagation*, vol. AP-30, no. 5, pp. 918–922, September 1982.

[76] "RT/duroid 5870 datasheet," Rogers Corp., http://www.rogerscorporation.com/mwu/pdf/5000data.pdf; accessed June, 2003.

[77] "Rohacell HF31 datasheet," Degussa, http://www.rohacell.com; accessed June, 2003.

[78] M.-C. Huynh and W. Stutzman, "Ground plane effects on planar inverted-F antenna performance," *IEE Proceedings - Microwaves, Antennas and Propagation*, vol. 150, no. 4, pp. 209 – 213, August 2003.

[79] K.-L. Wong, *Planar Antennas For Wireless Communications*. Hoboken, NJ: John Wiley & Sons, Inc., 2003.

[80] P. Song, P. Hall, H. Ghafouri-Shiraz, and D. Wake, "Triple-band planar inverted-F antenna," in *Antennas and Propagation Society, 1999. IEEE International Symposium 1999*, vol. 2, Orlando, FL, July 1999, pp. 908 – 911.

[81] K.-L. Wong and T.-W. Chiou, "Finite ground plane effects on broad-band dual polarized patch antenna properties," *IEEE Transactions on Antennas and Propagation*, vol. 51, no. 4, pp. 903 – 904, April 2003.

[82] J. H. Richmond, "Monopole antenna on circular disk," *IEEE Transactions on Antennas and Propagation*, vol. 12, no. AP-32, pp. 1282 – 1287, December 1984.

[83] J. Huang, "Finite ground plane effect on the microstrip antenna radiation patterns," *IEEE Transactions on Antennas and Propagation*, vol. AP-31, no. 4, pp. 649 – 653, July 1983.

[84] M. M. Weiner, "Monopole element at the center of a circular ground plane whose radius is small or comparable to a wavelength," *IEEE Transactions on Antennas and Propagation*, vol. 35, no. 5, pp. 488 – 495, May 1987.

[85] M.-C. T. Huynh, "A numerical and experimental investigation of planar inverted-F antennas for wireless communication applications," Master's thesis, Virginia Tech, Blacksburg, VA, October 19 2000.

[86] J. W. Greiser, "Log-periodic antenna structure," U.S. Patent 3 369 243, Feb. 18, 1968.

[87] N. P. Cummings and W. L. Stutzman, "UHF Subscriber and Hub Antenna Designs," Virginia Tech Antenna Group, Blacksburg, VA, Final Report to Spike Broadband Systems, R00-4, October 2000.

[88] C. A. Balanis, *Antenna Theory: Analysis and Design*. New York: John Wiley & Sons, 1982.

[89] "RO3003 datasheet," Rogers Corp., http://www.rogerscorporation.com/mwu/pdf/3000data.pdf; accessed June, 2003.

[90] W. Davis, J. Nealy, G. Ricciardi, and W. Stutzman, "Techniques for the measurement of the impedance of wideband balanced antennas," in *Antenna Measurement Techniques Association Symposium*, no. 95-7, Williamsburg, VA, November 1995, pp. 60 – 63.

Vita

Nathan P. Cummings was born in January 1975 in Parkersburg, West Virginia. He spent his entire precollegiate life on the same street in the town of Vienna, a suburb of Parkersburg. He graduated from high school in 1993 and began his studies in Electrical Engineering at Virginia Polytechnic Institute & State University in the fall of that year. His undergraduate tenure included a co-op position with G.E. Fanuc Automation, North America in Charlottesville, Virginia. He received his B.S. in electrical engineering from Virginia Tech in May of 1998. Upon completion of his undergraduate degree he joined the Virginia Tech Antenna Group. Nathan received his M.S. in electrical engineering in December of 2001 and his Ph.D. in electrical engineering in December of 2003, both from Virginia Tech.